Dublin City University

School of Physical Sciences

Photoemission studies of *in-situ and ex-situ* surface cleaning and electronic properties of ZnO surfaces

Kumar Kumarappan, M.Sc.

A thesis presented for the degree of

Doctor of Philosophy

December, 2014

Supervised by Prof. Greg Hughes

Declaration

I hereby certify that this material, which I now submit for assessment on the programme of study leading to the award of doctor of Philosophy is entirely my own work, that I have exercised reasonable care to ensure that the work is original, and does not to the best of my knowledge breach any law of copyright, and has not been taken from the work of others save and to the extent that such work has been cited and acknowledged within the text of my work.

Signed :..... (ID No. : *56115652*), Date : .....

Dedicated to my parents

எப்பொருள் எத்தன்மைத் தாயினும் அப்பொருள் மெய்ப்பொருள் காண்பது அறிவு.
குறள்: 355

- திருவள்ளுவர்
(தமிழ் அறிஞர், 200 கி.மு.)

Translation in English

Knowledge is truth of things to find in every case of every kind. *(Verse: 355)*

- Thiruvalluvar
(Tamil Scholar, 200 BC)

Acknowledgement

I would like to express my gratitude to my supervisor Prof. Greg Hughes, for giving me this great opportunity, helps, support, respect throughout my PhD years in DCU. His continuous inspiration, constant motivation, flashing ideas, encouragement to explore new paths which all made me to grow, learn and enjoy the research. Further he gave complete freedom to designing my project, executing the experiments, learning things in my own way and especially in my final stage of research allowed extra time with funding is highly appreciable. My special thanks to Dr. Enda McGlynn gave opportunity to learn more about ZnO, for his supports and advices during my PhD.

My heartfelt thanks to all my friends in Surface and Interface Research Group: Robert, Ian, Stephen, Barry, Patrick, Justin, Lalit, Rajesh, Antony, Lee, Conor, Anita, Venkat for helped me in discussions, doing experiments, having fun chats, visiting places and being so friendly for these many years. Thanks to my project mate Mahua Biswas for growing sample for me, doing experiments and discussions during the PhD. I deeply thank Mr. Pat Wogan for his dedicated assistance in helping in my experimental setups. I would like to thank DCU staff members: Dr. Lisa Looney, Prof. Colette McDonagh, Dr. Claire Bohan, Ms. Helena Ahern, Ms. Susan Madigan and Ms. Lynn O Toole all who helped me and were very supportive during my difficult times in my PhD.

I am highly thankful to Prof. R. Chandramohan, Prof. K. Sankaranarayan and Prof. K. Ramamoorthy from India who all were the inspiration to do my PhD and to become a researcher. I would like to take this opportunity to thank all of my Indian and European friends who all helped me in different occasions and made it possible to complete my doctoral degree.

Most importantly, many more thanks to my Father Kumarappan and Sister Vallimayil both were very affectionate, believed so much on me, scarified lot for me and highly supportive throughout my life. No more words are enough to fulfil the thanks to them. The most loved person for me was my mother Saradha, who passed away in middle of my PhD, and she is guiding me with her divine soul light. Her blessing only gave courage and power to complete the PhD.

Finally, I would like to acknowledge the financial support from Science Foundation Ireland, School of Physical Sciences and DCU.

Publications

1. **Atomic hydrogen cleaning of $In_{0.53}Ga_{0.47}As$ studied using synchrotron radiation photoelectron spectroscopy**
   Barry Brennan, Kumar Kumarappan, and Greg Hughes
   Physica Status Solidi RRL, 7 (2013) 989-992.

2. **Microscopic origins of the surface exciton photoluminescence peak in ZnO nanostructures**
   Mahua Biswas, Yun Suk Jung, Hong Koo Kim, Kumarappan Kumar, G. J. Hughes, S. Newcomb, Martin O. Henry, and Enda Mc Glynn
   Physical Review B, 83 (2011) 235320.

3. **A study of drop-coated and chemical bath-deposited buffer layers for vapour phase deposition of large area, aligned, Zinc oxide nanorods arrays**
   D. Bryne, E. McGlynn, M. O. Henry, K. Kumar and G. Hughes
   Crystal Growth and Design, 10 (2010) 2400-2408.

4. **A novel, substrate independent three-step process for the growth of uniform ZnO nanord arrays**
   D. Bryne, E. McGlynn, M. O. Henry, K. Kumar and G. Hughes
   Thin Solid Films, 518 (2010) 4489-4492.

Conferences

1. **High resolution photoemission comparison study of atomic hydrogen cleaned and decapped InGaAs substrates**
   Barry Brennan, Kumar Kumarappan, Lalit Chauhan, Greg Hughes
   38 th International Symposium on Compound Semiconductors (ISCS -2011), Berlin, Germany. (22 - 26, May 2011).

2. **Photoemission studies of atomic hydrogen cleaning of ZnO (0001) surface**
   Kumarappan Kumar and Greg Hughes
   BOC Poster Competition, Dublin City University, Ireland. (24 September 2010).

3. **SIMS characterisation of ZnO and MgO thin films**
   Kumarappan Kumar, Patrick Casey and Greg Hughes
   BOC Poster Competition, Dublin City University, Ireland. (23 September 2009).

4. **XPS study of cleaning procedure of ZnO (0001), (000-1), (10-10) surfaces**
   Kumarappan Kumar, Greg Hughes, Enda McGlynn and Mahua Biswas
   14 th International Conference on Solid Films and Surface (ICFS-14), Trinity College, Dublin, Ireland. (29 June - 4 July, 2008).

5. **XPS study of ZnO single crystal, thin films and nanorods**
   Kumarappan Kumar, Greg Hughes, Mahua Biswas, Brendan Doggett, J-P. Mosner and Enda McGlynn
   12 th European Conference on Surface and Interface Analysis (ECASIA-07), Universite Libre de Bruxelles, Belgium. (9 - 14, September 2007)

Additional projects done

1. **SIMS characterisation of the surface chemical composition of polypropylene pipe**
   (Collaborated with *Qualflow Systems*, Funded by *Enterprise Ireland*)

2. **Electrical characterisation of ZnO nanorods (ZnO NR) for ultra-violet (UV) sensor applications**
   (Collaborated with *Tyndall National Institute*, Funded by *SFI Ireland*)

Abstract

The aim of this research project was to undertake the surface characterisation of (0001)-Zn, (000-1)-O, polar and (10-10), (11-20) non-polar ZnO surfaces by x-ray photoelectron spectroscopy (XPS) and to develop surface cleaning procedures to make these surfaces suitable for subsequent device processing. Conventional XPS and synchrotron radiation based photoelectron spectroscopy (SRPES) were used to undertake binding energy calibrations, estimations of surface contamination, stoichiometric analysis and electronic band alignment measurements for the different ZnO surfaces. A wide range of cleaning procedures including *ex-situ* organic solvent cleaning, *in-situ* ultra-high vacuum (UHV) annealing, *in-situ* atomic hydrogen and atomic oxygen cleaning as well as *in-situ* high temperate molecular oxygen annealing treatments were systematically investigated and evaluated as to their effectiveness at preparing contamination free surfaces. The *ex-situ* wet chemical cleaning resulted in only a small reduction in the carbon contamination signal and a corresponding increase in the surface hydroxide signal. On all ZnO surfaces investigated, the contamination was reduced at different rates, depending up on the surface termination. The *in-situ* surface cleaning studies showed that while in general it is possible to remove the carbon contamination by a variety of methods, the surface hydroxide species cannot be removed, due to the bond strength of O-H. The OH presence may well reflect the re-adsorption of hydroxide groups in the UHV environment. It was found that the effective carbon removal temperature for the ZnO surfaces using atomic hydrogen cleaning was 600 °C, using molecular oxygen thermal cleaning it was 700 °C and for atomic oxygen, the cleaning temperature was 400 °C. As the result of removing carbon contamination on all ZnO surfaces, the natural surface downward banding was reversed into upward band bending.

Keywords: Semiconductor surfaces, Electronic properties, ZnO, Surface cleaning, XPS, SRPES

Contents

List of Figures

Acronyms\Abbreviations

UHV Ultra high vacuum

PES Photoemission Spectroscopy

XPS X-ray photoelectron spectroscopy

SRPES Synchrotron radiation based photoemission spectroscopy

SIMS Secondary mass ion spectrometry

TCO Transparent conductive oxide

TFTs Transparent thin film transistors

SAW surface acoustic wave resonators

VLS vapour-liquid-solid technique,

PVD physical vapour deposition

CVD chemical vapour deposition

MOCVD Metal-organic chemical vapour deposition (MOCVD)

FEs field-emitters

VBM Valence band maximum

SX-PES soft-X-ray photoemission spectroscopy

UPS Ultraviolet photoelectron spectroscopy

ARPES Angle resolved photoemission spectroscopy

LIXPS low intensity x-ray photoemission spectroscopy

TDS Thermal desorption spectroscopy

TPD Temperature Programmed Desorption

EELS Electron energy loss spectroscopy

UV Ultra violet

IR Infra-red

ICs Integrated circuits

TXRF Total X-ray Fluorescence Spectroscopy

SEM Scanning Electron Microscopy

EDX Energy Dispersive X-Ray Spectroscopy

ToF-SIMS Time of flight - Secondary ion mas spectrometry

TD-GCMS Thermal desorption - Gas Chromatograph-Mass Spectrometry

FTIR Fourier transform infrared spectroscopy

VPD Vapour Phase Decomposition

LPD Liquid Phase Decomposition

ICPM Inductively coupled plasma mass spectrometry

AAS Atomic absorption spectroscopy

PL photoluminescence spectroscopy

LPE Liquid phase epitaxy

AFM Atomic force microscopy

RCA Radio Corporation of America

IMEC Interuniversity Microelectronics Centre

e-beam electron beam

c.p.s counts per second

LPES Laser based photoemission spectroscopy

HAXPES, HXPS Hard X-ray photoemission spectroscopy

APPES Ambient Pressure photoemission spectroscopy

RPD Realtive depth profile

ARXPS Angle Resolved X-ray photoelectron spectroscopy

RSF Relative sensitivity factor

FWHM Full width half maximum

IMFP Inelastic mean free path

B.E. Binding energy

K.E. Kinetic energy

EAL Effective attenuation length

MED Mean escape depth

ID information depth

NIST National Institute of Standards and Technology

BW Band width

ASTRID Aarhuas Stroage Ring in Denmark

ISA Institute of Storage Ring

linac linear accelerator

$\mathbf{E}_g$ Energy band gap of the material

$\mathbf{E}_F$ Fermi level position

$\mathbf{E}_{VBM}$ valence band maximum position

$\mathbf{E}_{Vac}$ vacuum level position

W Valence band width

LBE Lower binding energy

HBE Higher binding energy

BB Band bending

DMSO Dimethyl sulfoxide

VPT Vapour phase transport

XRD X-ray Diffraction

SCVT hydrothermal seeded chemical vapour

MBE Molecular beam epitaxy

PLD Pulsed laser deposition

VPE vapour phase epitaxy

ACG Aqueous chemical growth

IPA Iso-Propyl Alcohol

a.u. Arbitrary unit

FEOL front-end-of-line

BEOL back-end-of-line

AHC Atomic Hydrogen cleaning

EUV Extreme Ultraviolet

VB Valence band spectra

RMS Root mean squared

TAMH Tetra methyl ammonium hydroxide

Chapter 1

Introduction

This introduction will discuss the importance of surface cleaning of ZnO for reliable device fabrication which is the focus of this thesis. A brief review of both the surface science of ZnO and semiconductor surface cleaning in general will also be discussed.

1.1 Zinc Oxide

1.1.1 Technological applications

ZnO is a key emerging technological material, due to its versatile semiconducting, optoelectronic, piezoelectric, and pyroelectric properties and it is bio-compactable [1–4]. For more than 150 years, ZnO has been widely used in a range of chemical and industrial applications. ZnO was the first man made zinc compound and was formed as a by-product of copper smelting [4]. In the beginning of the 19^{th} century, ZnO power was used in pharmaceuticals and cosmetics because of its anti-bacterial and non-toxic properties. ZnO is still an important materail in many industrial manufacturing processes including paints, cosmetics, pharmaceuticals, plastics, batteries, electrical equipment, rubber, soap, textiles and even floor coverings [1]. In the 1950s more scientific applications of ZnO and related to its, semiconductor, piezoelectric, luminescent, ultraviolet (UV) absorption, ferrite, photoconductive and photochemical properties were discovered [5]. This research further widened the possibilities of ZnOs application in the fabrication of electronics, photonics, acoustic and sensing devices [6]. More recently, the growth of nanotechnology accelerated ZnO research further, since it can be grown as a nanomaterial suitable for fabrication of various nanoscale devices and sensors. Currently, 100,000 tonnes of ZnO is produced annually making it an easily available material for both current and and future applications [3]. The diverse fields (biological, chemical to physical) of applications of ZnO are illustrated in figure 1.1.

ZnO has a direct band gap of 3.37 eV (II-VI) wide band gap, n- type semiconductor), which makes it transparent to visible light and it is being considered of

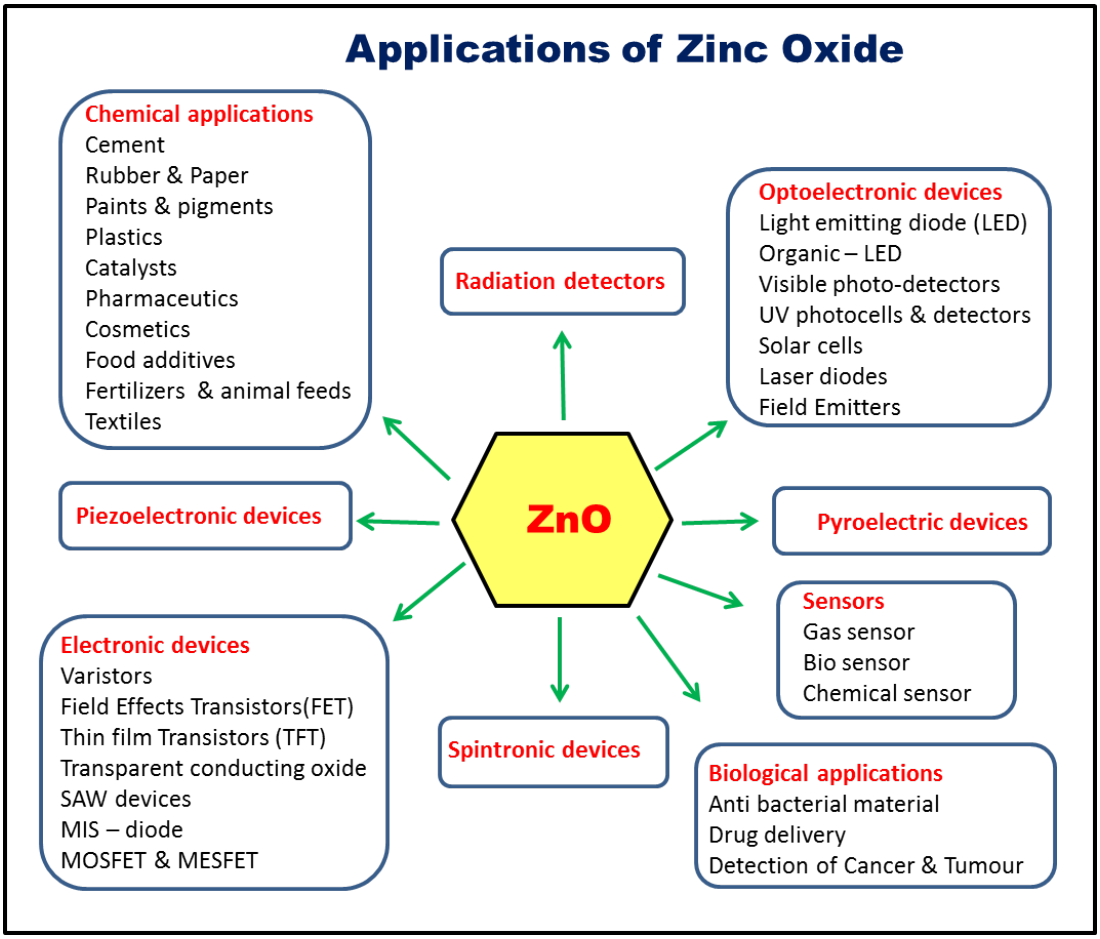

Figure 1.1: Some of the range of applications of Zinc Oxide

optoelectronic applications in the near UV wavelength range. ZnO has an exciton binding energy of ≈60 meV and this high binding energy enhances the luminescence efficiency of light emission [1]. The wurzite (at room temperature) structured ZnO crystals have non-central symmetry ions which produces a piezo electric potential due to polarisation of the ions by applying an external mechanical stress [7]. Furthermore, pyroelectricity can also be obtained from ZnO crystals resulting from the differential change in polarisation caused by heating the crystals [8]. ZnO also has excellent thermal properties, with a high melting point of 2000 °C, high heat capacity, high heat conductivity and low thermal expansion [9] which all makes ZnO a suitable material for developing thermally stable devices. Early ZnO electronic and photonic devices were reported in the later 1950s [2]. In 1965, ZnO based Schottky diodes [10] were made with gold contacts. ZnO LEDs [11] were demonstrated with Cu_2O as p-type material in 1967. Metal - insulator - semiconductor (MIS) structures [12] were fabricated in 1974. The p-n junctions [13] of ZnO/ZnTe were successfully formed in 1975 and Al/Au contacts [14] were investigated in 1978. More recently doped ZnO has been investigated for application as a possible transparent conductive oxide (TCO) alternative to indium tin oxide (ITO) and transparent thin film transistors (TFTs) [15]. Pulsed laser deposition grown ZnO epitaxial layers has also been used to fabricate

LEDs and laser diodes. For technological applications, melt grown and hydrothermal grown 4 inch ZnO single crystal wafers are now commercially available as semiconductor substrates for homo and heterostructures. The breadth of application for ZnO based applications is captured in figure 1.2.

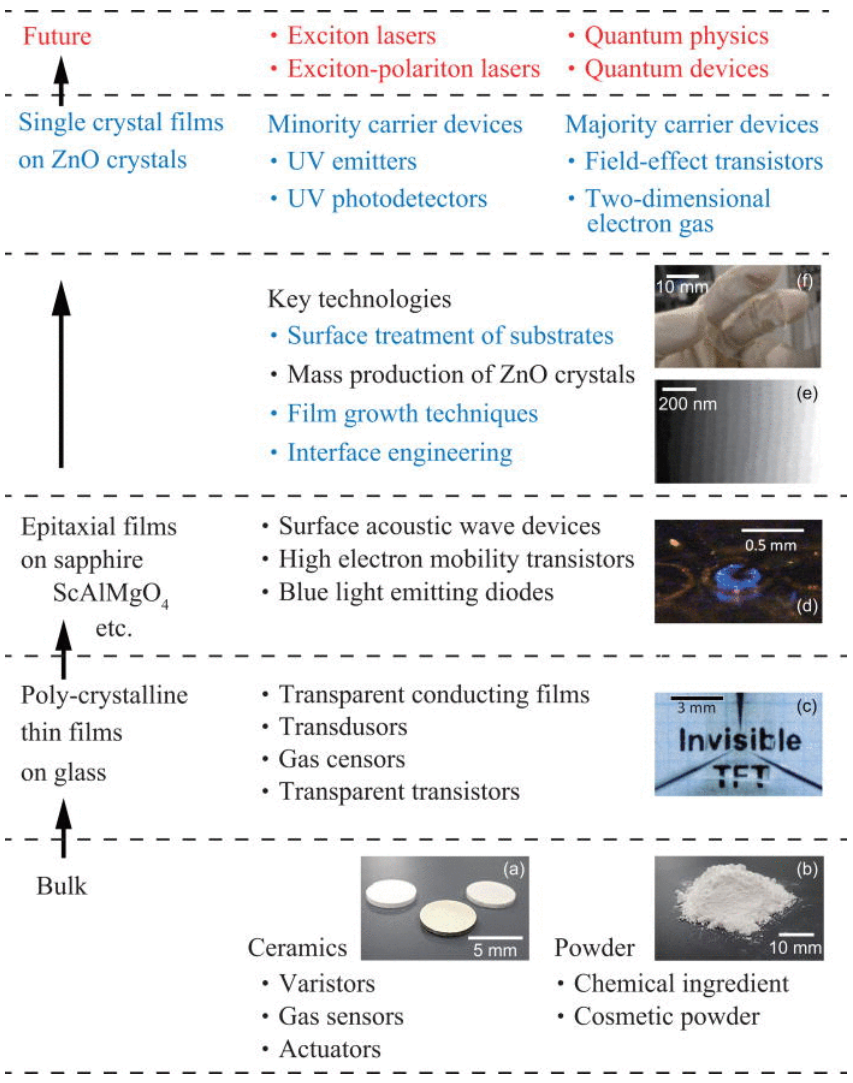

Figure 1.2: A historical stream for research topics and electronic, optoelectronic applications of ZnO. The inset pictures are (a) sintered ceramics, (b) powders, (c) a transparent transistor made on glass, (d) a blue light emitting diode made of ZnO p-n junction, (e) and atomic force microscope image of a ZnO single crystal substrate surface that exhibits step and terrace structure, and (f) a commercially available ZnO single crystal wafer with a diameter of 2 inch [16].

Room temperature ferromagnetism can be achieved in ZnO by doping with 3d transition metals (e.g. Mn, Co, V, Ni, Ti, Fe, etc) making ZnO a dilute magnetic semiconductor (DMS) for spintronic device applications [2]. By utilizing the piezoelectric properties of ZnO, bulk acoustic wave and surface acoustic wave resonators (SAW), filters and sensors have been fabricated [2]. A new field of research, piezotronics and piezo-phototronics as proposed by Wang [7], is emerging which aims to develop self-powered nanodevices and nanosystems based on ZnO nanostructures. Due to the

pryoelectric property of ZnO, thin film pyroelectric sensors were manufactured for applications in pollution monitoring, hot image detectors, intruder alarms and gas analysis [17]. Additionally, the radiation hardness of ZnO to MeV proton irradiation makes it an ideal candidate for applications in space [18]. Application of ZnO as semiconductor based scintillators [19] and pulsed radiation detectors for X-ray, Gamma rays were also under development [20].

In nanotechnology, ZnO is one of the most studied nanomaterial in terms of growth, characterisation, and device applications. ZnO nanostructures can be grown by a variety of physical and chemical methods including a vapour-liquid-solid (VLS) technique, physical vapour deposition (PVD), chemical vapour deposition (CVD), metal-organic chemical vapour deposition (MOCVD), and multiple hydrothermal methods [21]. These nanostructures were grown in different shapes and sizes by controlling growth process conditions. A wide range of morphologies have been reported in the literature ranging from nanorods, nanoplates, to nanopropellers and nanoflowers [22] and SEM images showing a selection of these structures are displayed in Figure 1.3 [21]. The large surfaceto-volume ratio of nanostructures makes them more suitable for sensors and photovoltaic devices like UV detector, solar cells, etc. ZnO nanostructures have become fundamental building blocks for applications such as nano-lasers, field-effect transistors, ultrasensitive nano-gas sensors, nano-resonators, transducers, actuators, nano-cantilevers, and field-emitters (FEs) [2].

The ZnO surface is inherently very reactive due to the presence of oxygen vacancies. It has a tendency to absorb gas and bio-molecules onto the surface which affect the electrical conductivity or change in resistance of ZnO thin film or nanowire leads making it suitable for sensor applications. ZnO based nano-gas sensors have demonstrated sensitivity to NO_2, NH_3, NH_4, CO, H_2, H_2O, O_3, H_2S, and C_2H_5OH [15]. Selectivity of a particular gas is a very important parameter in gas sensors and this is achieved in ZnO gas sensors by sensing at different temperature for different gas molecules [23]. Similar to gas molecules, biological molecules also react with ZnO surface. Hence ZnO has shown potential application as biosensors with the added advantages of stability in air, non-toxicity, chemical stability, electrochemical activity, ease of synthesis, and bio-safety [2]. ZnO nanorods structures have been used as pH, cholesterol and glucose sensors [23].

ZnO is a biodegradable material and is being considered as a possible biocompatible material suitable for medical and biological applications. ZnO nanoparticles have been recognised as having anti-bacterial properties due to the emission of UV light remittance on illumination of laser light of the current wavelength. It has been used for cholesterol sensing, hydrolysis activity for controlling diabetes, hyperlipaemea, cell imaging, modulating allergic reactions, and other antimicrobial applications [24]. ZnO nanomaterials below 100 nm size have been found to be the most suitable for biocompatibility. These nanostructures are easily biodegradable by dissolving into ions, which can be absorbed by body. ZnO hallow nano-tube structures have been

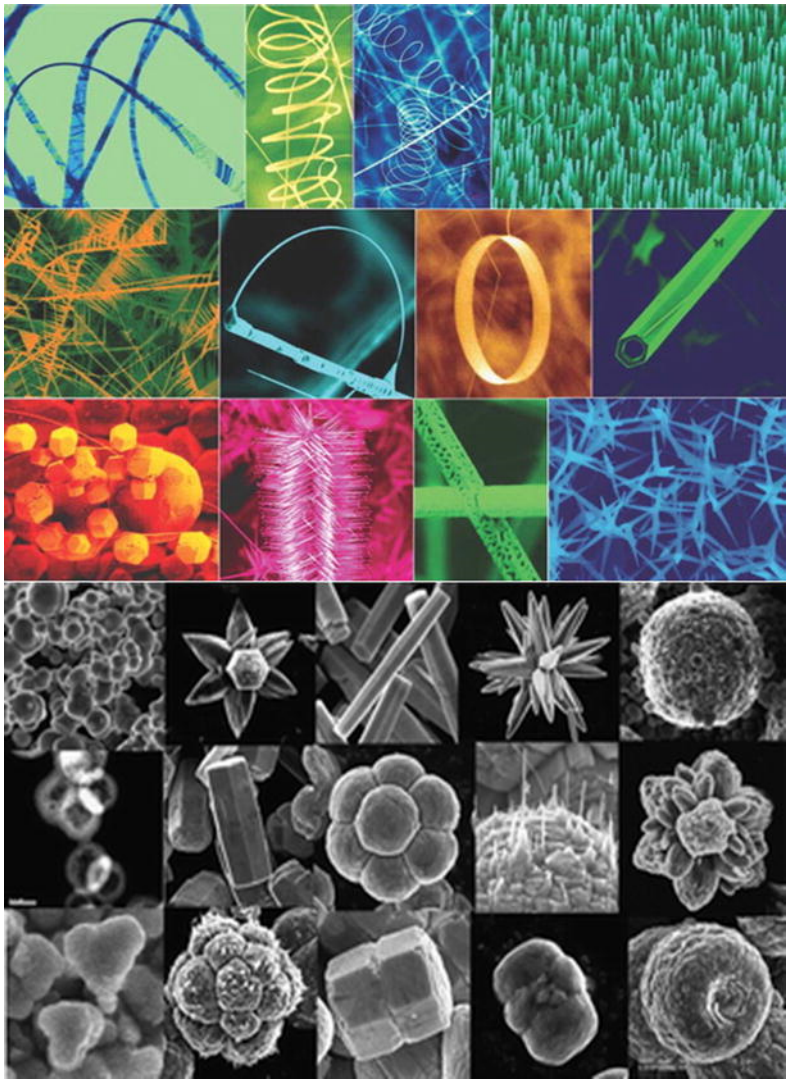

Figure 1.3: SEM images of various ZnO nanostructures [21]

found to be suitable for drug delivery and slow drug release applications. Among all other metal oxide nanoparticles, the ZnO nanoparticles have been shown to be effective as a cancer treatment because of its cytotoxicity. The cytotoxic property of ZnO nanoparticle has been shown to increase with the reduction in nanoparticles size. Several studies show ZnO nanoparticles have been effective in treating different types of cancers like glioma, breast, bone, colon and lymphomas [24].

1.1.2 Surface properties of ZnO

The surface science of ZnO has become an important field of research due to the different chemical and physical properties of its polar and non-polar surfaces. These surface properties are very important for applications like catalysis, electronic devices, sensors and nanostructure based devices. The four most common face terminations of wurtzite ZnO as schematically illustrated in figure 1.4 are the polar Zn- terminated (0001) and O terminated (000-1) faces (c-axis oriented), and the non-polar (11-20)

(a-axis) and (10-10) (m-axis) faces. The polar faces are known to possess different chemical and physical properties, and the O-terminated (000-1) face possesses a slightly different electronic structure to the other three faces. The non-polar surfaces (11-20) and (10-10) both contains equal number of Zn and O atoms on the surface termination [25] [25]. A detailed review of surface chemistry of the ZnO polar and non-polar surface was reported by C.Woll [25]. In the case of the non-polar surface there is no dipole moment and hence the surface is chemically stable. For polar surface terminations with the cation Zn^{2+} or anion O^{2-} the surface is not chemically stable [26]. The geometric structure, electronic structure and molecular adsorption properties are discussed in this chapter.

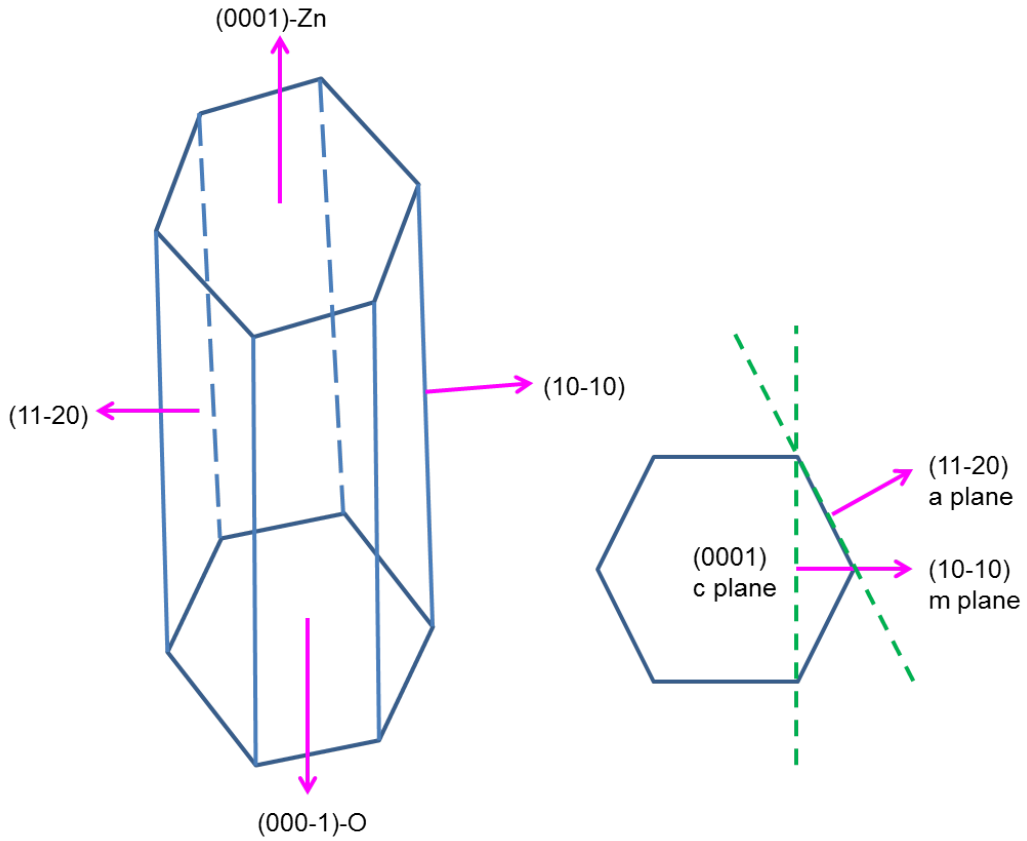

Figure 1.4: Morphology of the ZnO single crystal with different surfaces.

1.1.2.1 Crystal Structure

Zno being a II-VI compound semiconductor whose ionicity resides at the borderline between the covalent and ionic semiconductors. Hence, ZnO crystal structure was shared by three types (a) wurzite (B4), (b) zinc blende (B3) and rocksalt(NaCl) (B1) were shown in figure 1.5. Under ambient pressure and temperature ZnO forms the stable phase of wurzite symmetry. The zinc blende ZnO structure can be stabilized only by growth on cubic substrates, and the rocksalt or Rochelle salt (NaCl) structure may be obtained at relatively high pressures, as in the case of GaN [2]

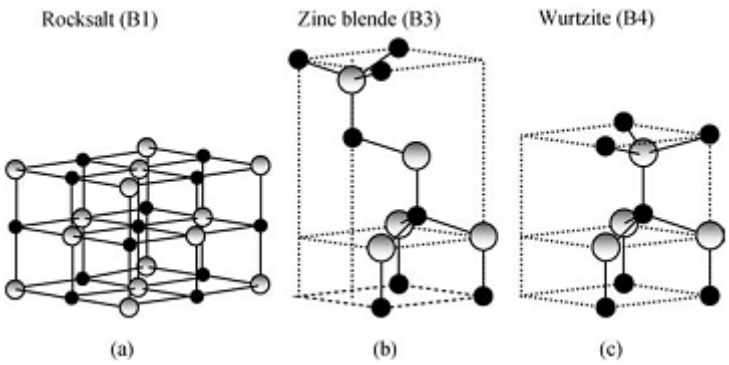

Figure 1.5: ZnO crystal structures: (a) cubic rocksalt (B1), (b) cubic zinc blende (B3), and (c) hexagonal wurtzite (B4). Shaded gray and black spheres denote Zn and O atoms, respectively. [2]

1.1.2.2 Geometric structure

When a single crystal of ZnO is cleaved normal to the c-axis in such a way as to break the fewest number of inter atomic bonds, two different polar surfaces are formed on opposing crystal faces, each having only one type of ion in its outermost plane. The cation (Zn^+) plane is outer most for the (0001) surface and anion (O^-) plane is outer most for the (000-1) surface. These orientations are also basal planes in that they are perpendicular to the c-axis of the crystal. The (0001) Zn terminated and (000-1) O terminated surfaces behave very differently due to different atomic species that are outermost on the two faces as illustrated in figure 1.6(a,b). The different termination of these two faces can be deduced by their response to etching with hydrochloric acid (HCl) solutions. The (0001) face is relatively unaffected, while the (000-1) face is rapidly etched and becomes visibly roughened. In the growth of ZnO thin films, the dominant natural grown surface is (000-1) oxygen terminated face. The ideal bulk terminations of these two surfaces are energetically unfavourable and there are a number of possibilities to remove these instabilities. The first one is a charge transfer between the two different polar surfaces without a significant rearrangement of the geometric positions. The second one is a reconstruction changing the geometry of the surface and the third one involves the adsorption of additional charged particles on the surface resulting in stabilisation [27]. Both (10-10) and (11-20) surfaces are atomically flat and have equal numbers of cations and anions in the surface plane as shown in figure 1.6(c,d). The planes can be thought of in terms of Zn-O pairs or dimers in that on the (10-10) face these dimers bond to ions in the plane below rather than directly to each other, while on the (11-20) face they bond to each other as well as to the plane below and are arranged in zigzag rows parallel to the c-axis. Among all four surfaces, the (10-10) is the most stable one for ZnO, while (11-20) was the least stable [27].

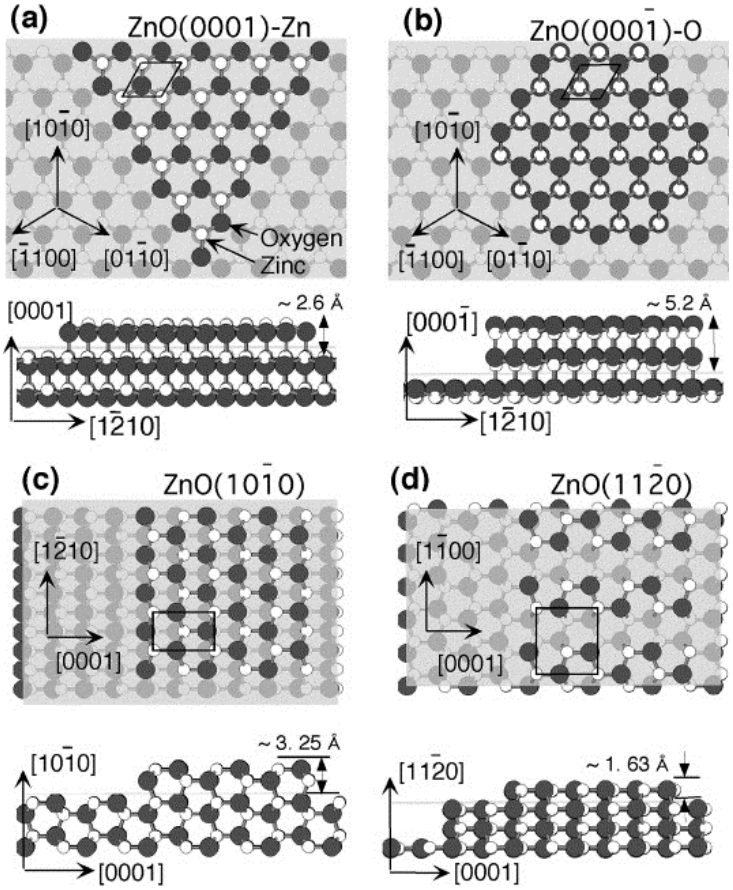

Figure 1.6: Top and side views of atomic models for the bulk-terminated ZnO surfaces (0001), (b) (000-1), c) (10-11) and (d) (11-20) [28].

1.1.2.3 Electronic structure

The electronic structure of the different ZnO surface terminations were calculated by theoretical methods and also measured by photoemission spectroscopy [29]. Electronic properties such as valence band maximum (VBM), work function (ϕ), electron affinity (χ) and density of states were measured by ultraviolet photoelectron spectroscopy (UPS) and soft-X-ray photoemission spectroscopy (SX-PES) showed that the electronic structure of ZnO is highly surface sensitive. The valence band spectra displayed in figure 1.7 measured by UPS for all four ZnO surfaces have a large peak about 10 eV binding energy which originates from the filled Zn 3d energy level [30]. The ZnO valance band feature extending from 3 to 8 eV binding energy is attributed from theoretical predictions to relate to emission from the non-bonding O 2p orbitals while the emission from 5 to 8 eV is a bonding combination of O 2p and Zn 4s orbitals [27]. There are large differences in the relative intensity of these valence band features for the different surface terminations as illustrated in figure 1.8.

By determining the position of the valence band maximum with respect to the Fermi level position of a metal in contact with the sample, the upward or downward band bending at the surface can be determined. Recently reported, angle resolved photoemission (ARPES) study VBM measurement for both clean (0001)Zn and (000-

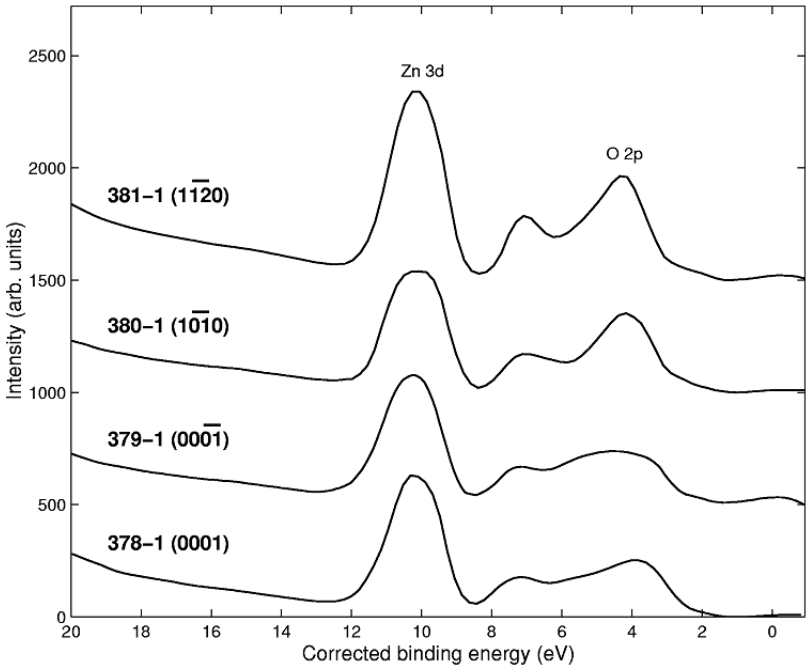

Figure 1.7: UPS spectra for the all four different ZnO surfaces [30].

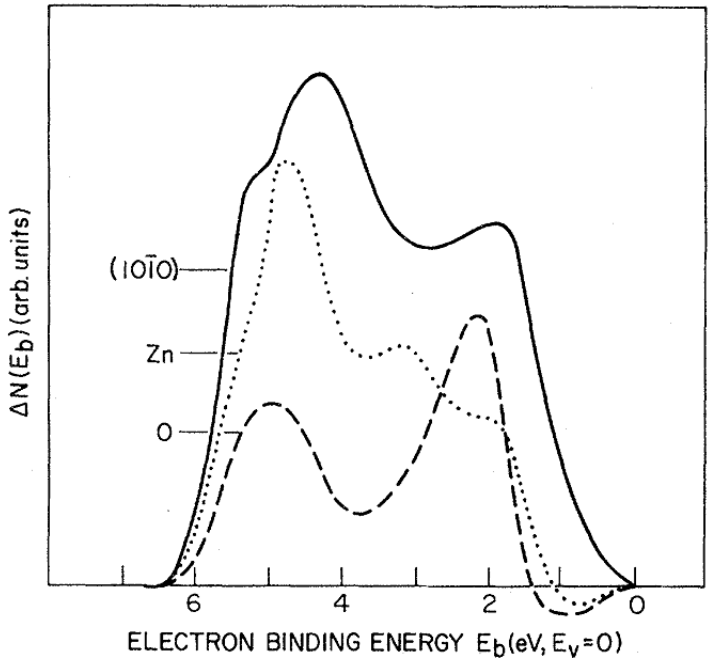

Figure 1.8: Difference between UPS spectra take at surface sensitive photo energies for the (10-10), (0001)-Zn, and (000-1)-O surfaces [31].

1)O surface is 2.9 eV, which leads to upward band bending [32]. The cleaned non-polar surface (10-10) has VBM at 3.3 eV which is of downward band bending [32]. The work function (ϕ) is an important electronic property to predict the Ohmic or Schottky behaviour of metal - semiconductor interfaces. The work function of ZnO

single crystal faces has been measured by several techniques on surfaces prepared in various ways. In 1976, an initial study of the work function value for ZnO (0001) was reported as 3.15 eV and the value for the ZnO (000-1) is 4.85 eV [33]. The Kelvin probe method was used to measure the work function for different freshly cleaved ZnO surfaces and gave the following values (0001) - 4.25 eV, (000-1) - 4.95 eV and (10-10) - 4.64 eV [34]. However, for UHV cleaved samples it was reported that different cleaves gave different values of ϕ for same crystal plane and that the values also depended upon the temperature at which the sample was cleaved. The work functions for the faces studied followed the trend and the work function of the cleaved surface changed irreversibly upon annealing [35].

$$\Phi(000-1) > \Phi(10-10) > \Phi(0001)$$

An accurate work function measurement determined by low intensity x-ray photoemission spectroscopy (LIXPS) for nano-crystalline ZnO surfaces was reported as 4.1 eV. In comparison with LIXPS measurement, the reduction of work function of 0.35 eV by UPS measurement due to arc effect also reported [36]. The variation of work function based on surface processing (annealing, oxygen plasma, wet chemical treatment) was also widely reported. The ability to alter the ZnO work function was demonstrated by adding strong electron acceptor molecules 2,3,5,6-tetrafluoro-7,7,8,8-tetracyanoquinodimethane [(F4TCNQ) on ZnO surface which increased the work function of the (000-1)O surface from 4.5 eV to 5.9 eV similarly for the (0001)Zn surface from 3.7 eV to 6.5 eV [37].

1.1.2.4 Molecular adsorption on ZnO

As clean ZnO is a reactive surface, it readily reacts with water, carboxyl and other organic molecules. There are many studies reported about the adsorption of H, H_2O, O_2, CO, CO_2 on the different crystallographic surfaces of ZnO [25]. In experimental studies, TDS, TPD, XPS, EELS and IR-spectroscopy techniques have been employed to identify and estimate amount of the adsorbates. The two major applications relating to this property of molecular adsorption on the ZnO surface are industrial catalysis and gas sensors. In the industrial large scale synthesis of methanol, ZnO is used as a component of the heterogeneous catalyst. In gas sensing, the surface conductivity of ZnO is changed on adsorption of molecules on the surface. Thus, the change in surface conductivity happens by either the transfer of electrons from adsorbate to the ZnO surface or vice-versa. The variety of polar and non-polar surfaces available, the presence of acidic Zn and basic O sites, the complex and imperfectly understood defect chemistry and the possibility of electron and oxygen-atom transfer are all factors which impact on the adsorption process. The ambient exposure of any ZnO crystallographic surface leads to adsorption of hydroxyls and water. Furthermore, the interaction of ZnO with NH_3 and organic chemicals such as benzene, pyridine,

alkynes, alcohols, aldehydes, carbolic acids have also been studied [27, 38, 39].

1.1.3 Challenges in the realization of ZnO devices

In research and development processes, ZnO scientist have had made enormous progress in the making electronics, photonics, acoustics, and sensing devices. But there remain a number of important technical challenges which need to be addressed to realise the fabrication of commercial devices [15]. Amongst these issues, there are two major issues, the formation of stable p-type ZnO and reliable Schottky contacts to ZnO.

1.1.3.1 p-type ZnO

To fabricate short wavelength optoelectronic devices like light emitting diodes and lasers diodes, p-type ZnO is need to form homostructure p-n junctions. ZnO is unintentionally a n-type semiconductor by its native point defects (donor type) and hydrogen donors. The natural n-type carrier concentration of ZnO is 10^{14}cm^{-3} but for both n-type and p-type semiconductor the potential carrier concentration required is typically of the order of 10^{17}cm^{-3}. The n-type carrier concentration can be enhanced by doping with elements such as Al, Ga, In, on zinc sites and Cl and I on oxygen sites. On the other hand, for p-type conductivity group I, IV, V elements Li, Na, K, Cu, Ag on Zinc sites and N, P, Sb, As on oxygen sites were doped to make acceptors [2]. But native point defects and hydrogen responsible for n-type conductivity compensate the acceptors making p-type ZnO a challenging task. Research on the limiting factors to achieve p-type doping include (i) point defects (V_{zn}, V_o vacancies), self-interstitials (Zn_i and O_i), anti-sites (Zn_o and O_{zn}), impurities were found to be the cause self-compensation in p-type doping [4]. By doping of Li with ZnO turn as semiconducting material to semi-insulating material and Na, K doping with ZnO creates defects, vacancies because of larger bind length. Nitrogen was found to be a genuine candidate for doping ZnO in that it provides the shallowest acceptor impurities and has an ionic radius similar to the oxygen atom [2]. The problem in N doping was the low dopant solubility and precipitation formation. Yamamot et al, recommended a co-doping method and also ion implantation of pure N [40]. P-type conductivity of 10^{18}cm^{-3} by N doping was recently reported [41]. In device fabrication process the stability of p-type ZnO was affected by heat treatments, injection of high currents, applied electric fields, etc. Further complex decomposition and inversion of p-type to n-type conductivity happened over time were also reported [2]. So still extensive research and deep understanding of ZnO is still needed for making commercial grade p-tye ZnO.

1.1.3.2 Schottky contacts on ZnO

Metal contacts are crucial for the fabrication of ZnO based transparent thin film transistors, blue/ UV light-emitting diodes, high electron mobile transistors and spin-

tronic devices. Schottky diodes prepared even with high work function metals (Pd, Au) on ZnO exhibit lower Schottky barrier heights than expected [4]. Normally, the problems associated with Schottky contacts are (1) chemical reactions between the metal and semiconductor, (2) surface states, (3) contaminants, (4) defects in the surface layer and (5) the diffusion of the metal into the semiconductor, etc [2]. For ZnO, a wide variation of Schottky barrier heights as function of surface treatments (air exposed, UHV cleaved) have been reported. Studies have shown that adsorbed gases induced charge transfer and opposite behaviour on different polar surfaces (Zn and O surface) for the same gas treatment have been reported. This strong dependence on surface preparation indicates that extrinsic factors such as crystal quality and surface treatment have a large effect on ZnO barrier heights [4]. The surface elemental composition and its bonding will also affect the interface property of metal/semiconductor junctions. ZnO is naturally a reactive surface resulting in strong adsorption of ambient contaminants which have a large impact on metal/semiconductor behaviour. Therefore, researchers have employed different surface cleaning methods before the deposition of metal on ZnO surface. A significant rise in Schottky barrier heights as function of surface cleaning methods was also reported [42]. Other problems such as surface states, impurities and native point defects need to be addressed to make reliable Schottky contacts [4].

1.2 Semiconductor Surface cleaning

The objective of semiconductor surface cleaning is the removal of particulate and chemical impurities from the semiconductor surface without damaging or negatively altering the properties of the substrate surface. In semiconductor nomenclature cleaning is the process that removes from the wafer surface particles, metallic contaminants, organic contaminants, and native/chemical (spontaneously grown) oxide [43]. For industrial scale surface preparation, wet-chemical and gas-phase methods have been developed to achieve these objectives. Nearly all semiconductor surface cleaning processes were initially developed specifically for silicon for the fabrication of integrated circuits (ICs). Later novel cleaning procedures were developed for germanium and III-V compound semiconductor materials [44].

1.2.1 Significance of semiconductor surface cleaning

The importance of clean substrate surfaces in the fabrication of semiconductor microelectronic devices has been recognized since the development of solid state device technology in the 1950s. It is now well known that the device performance, reliability, and product yield of semiconductor devices are critically affected by the presence of chemical contaminants and particulate impurities on the wafer or device surface. In modern device processing the surface cleaning procedures are more important than ever before because of the nanometre sizes of the device features [45]. Proper surface

preparation is an absolutely critical first step in semiconductor device fabrication in order to achieve optimum results. The consequences of improper surface cleaning are numerous leading to less than optimized results through increased epitaxial defect densities (dislocations and stacking faults), lower dielectric breakdown voltages, higher densities of interface states, variations in threshold voltage, increased ohmic contact resistance, and variations in Schottky barrier heights. All of these effects lead to a significant reduction in the device performance. In turn, these observations, have led to numerous studies of the surfaces of technologically important semiconductors surfaces such as Si, Ge, GaAs, and InP. These studies have shown that the chemical, electrical, and structural properties of a semiconductor surface can be significantly influenced by surface cleaning processes [46].

1.2.2 Contaminants

The semiconductor surface contaminant originates in different ways such as air exposure, processing gas molecules, handling chemicals, water etc. Furthermore the contaminants can come from the laboratory equipment or industrial tools. The contaminants exist on the surface in different forms such as adsorbed ions, elements, thin films, discrete particles, clusters and adsorbed gases. These contaminates are classified based on detection methods as follows: metallic contaminants, particles, organic contaminants, surface defectively and atmospheric molecular contamination [45]. Metallic contaminant originates from liquid chemicals, water and metal parts of processing equipment. Organic contaminants are volatile in nature and come from clean room air, ambient air and storage containers. Organic contamination will lead to gate oxide break down and thermal oxide film thickness variation [47]. The detection techniques for contaminants which is based on their size is shown in the figure 1.9.

1.2.3 Surface cleaning methods

The mechanisms of surface cleaning include chemical, physical force (mechanical or thermal) and using electromagnetic radiation to remove the contamination from a surface methods are shown in figure 1.10. The surface cleaning methods were classified based on these different mechanisms. Primarily surface cleaning methods were branched into two type (1) wet cleaning methods and (2) dry cleaning methods. In wet cleaning method the contaminant is converted into soluble compound and easily removed from the surface. Dry cleaning method involves the contaminant being converted into volatile compound and removed [43].

The aqueous chemicals, organic solvents or mixtures of these were used in used in wet-chemical process. The treatment of semiconductor surfaces with these chemicals leads to the chemical reaction dissolution of contaminants which can then be removed. Based on the semiconductor substrate and the various types of contamination several different chemical and process / methods were used and a few important process are

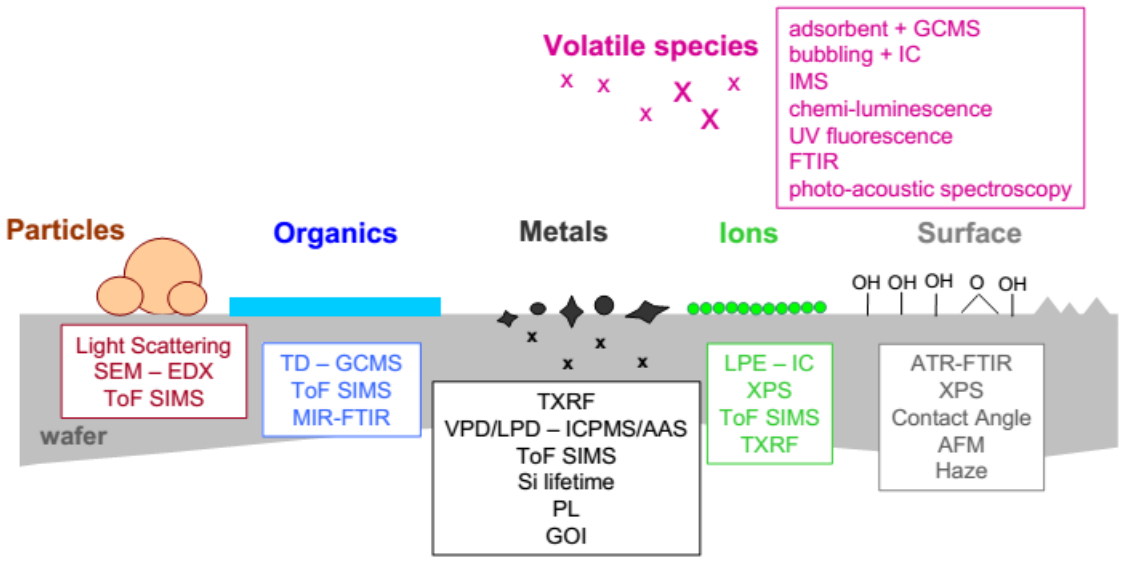

Figure 1.9: The meteorology of contaminations and detection techniques in semiconductor surface cleaning [48].

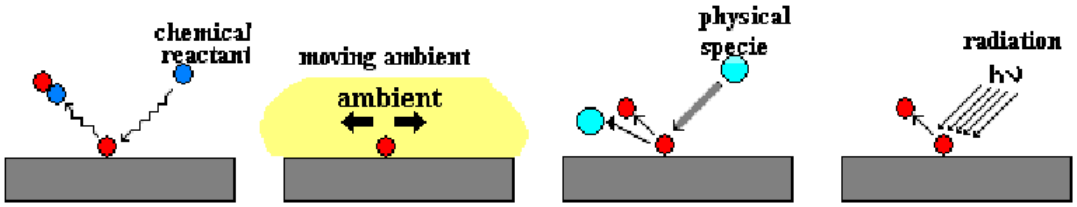

Figure 1.10: The meteorology of contaminations and detection techniques in semiconductor surface cleaning [48].

listed here: (1) hydrofluoric acid solutions (2) sulfuric acid/hydrogen peroxide mixtures (3) original RCA cleaning process (4) modifications of the (Radio corporation of America) RCA cleaning process (5) ohmic clean (6) IMEC clean (7) Diluted dynamic clean.

The traditional approach of wafer cleaning is based on wet-chemical processes, which use mostly acid and hydrogen peroxide based solutions. Successful results have been achieved by this approach for large scale manufacturing of semiconductor devices for a number of decades. However, the relatively large consumption of chemicals required by these processes, the disposal of chemical waste, and the incompatibility with advanced concepts in integrated processing are the main reasons why methods based on gas-phase cleaning have been and continue to be developed. So more recently the dry cleaning methods were mostly encouraged in industrial environment rather than wet chemical cleaning methods. The dry cleaning methods have used the energy sources: heat, light, particle beam and combination of gas, chemical vapours

etc. to clean the surfaces. The different types of dry cleaning methods used for removal contamination are shown in figure 1.11. The other dry cleaning methods used in the research laboratories for semiconductor surface cleaning are: (1) argon ion sputtering (2) reactive ion bombardment (3) electron cyclotron resonance plasma reactions, (4) pulsed laser radiation particle removal, (5) reduction annealing in H_2, (6) RF sputtering treatments [45].

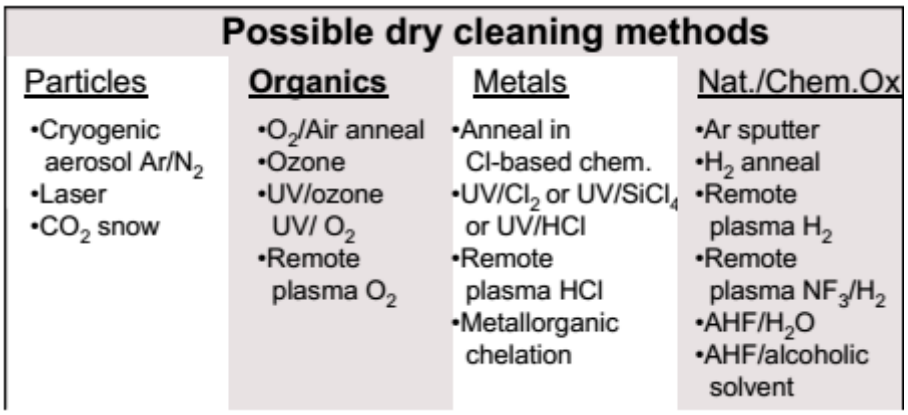

Figure 1.11: 10 Dry cleaning methods employed for surface cleaning of various types of contaminations [45].

1.3 Thesis Organisation

In chapter 2 there will be a detailed discussion of characterisation techniques used in these studies. These techniques include conventional x-ray and synchrotron radiation based photoemission spectroscopy and secondary mass ion spectrometry.

Chapter 3 will discuss the different ultra-high vacuum systems employed for the study. Surface cleaning methods include organic solvent cleaning, atomic hydrogen and oxygen cleaning and molecular oxygen thermal cleaning.

Chapter 4 presents the XPS characterisation of Zinc metal, ZnO single crystal polar and non-polar surfaces, thin film and angle resolved XPS studies of ZnO nanorods. The aim is to establish reference spectra and calculate stoichiometry with contamination analysis for ZnO surface. Chapter 5 focuses on the UHV thermal cleaning of ZnO(0001) surface and the cleaning of ZnO (0001) surface by atomic hydrogen with in-situ XPS and SRPES characterisation. The successful removal of carbon by atomic hydrogen without any change in ZnO stoichiometry is reported. The valence band and work function measurements for (0001)-Zn terminated as a function of hydrogen cleaning of surface are discussed.

Chapter 6 deals with the initial organic solvents (acetone, dimethyl sulfoxide (DMSO), toluene) surface cleaning of ZnO polar and non-polar surfaces. Using conventional XPS the effectiveness of each organic solvent is analysed. The effect of ethanol surface cleaning on different ZnO (0001), (000-1), (10-10) and (11-20) sur-

faces and sequent characterisation by synchrotron radiation based photoemission with measurement of surface banding and work function are reported.

Chapter 7 details the results of high temperature molecular oxygen cleaning of four ZnO surfaces and in-situ characterisation by synchrotron radiation based photoemission spectroscopy. The efficacy of surface cleaning on valence band spectra and the work function of ZnO (0001), (000-1), (10-10) and (11-20) surfaces are reported. An explorative study of applying atomic oxygen for surface cleaning of ZnO at both elevated temperatures and room temperatures are discussed.

In Appendix A the SIMS characterisation of e-beam grown ZnO thin films also discussed.

1.4 Bibliography

[1] C. Jagadish and S. J. Pearton(Eds.), Zinc Oxide bulk, thin films and nanostructures, first ed., Elsevier, 2006.

[2] H. Morkoc and U. Ozgur, Zinc Oxide fundamentals, materials and device technology, first ed.,Wiley-VCH, 2009.

[3] C. F. Klingshrin, B. K. Meyer, A. Waag, A. Hoffmann, J. Geurts, Zinc Oxide from fundamental properties towards novel applications, first ed., Springer-Verlag, 2010.

[4] C. W. Litton, D. C. Reynolds, T. C. Collins, Zinc Oxide materials for electronic and optoelectronic device applications, first ed., John Wiely and sons, 2011.

[5] H. E. Brown, Zinc oxide rediscovered, New Jersey Zinc Company, 1957.

[6] C. Klingshirn, J. Fallert, H. Zhou, J. Sartor, C. Thiele, F. Maier-Flaig, D. Schneider, and H. Kalt, Phys. Status Solidi B 247 (2010) 1424.

[7] Z. L. Wang, Adv. Mater., 24 (2012) 4632.

[8] C-C. Hsiao and S-Y. Yu, Sensors, 12 (2012) 17007.

[9] F. Porter, Zinc Handbook: Properties, processing and use in design, CRC Press, 1991.

[10] C. A. Mead, Phys. Lett., 18 (1965) 218.

[11] I. T. Drapak, Semiconductors 2 (1968) 624.

[12] T. Minami, M. Tanigava, M. Yamanishi and T. Kawamura, Jpn. J. Appl. Phys., 13 (1974) 1475.

[13] A. E. Tsrkan, N. D. Fedotova, L. V. Kicherman and P. G. Pasko, Semiconductors 6 (1975) 1183.

[14] L. J. Brillson, J. Vac. Sci. Tech. 15 (1978) 1378.

[15] U. Ozgur, D. Hofsteller and H. Morkoc, Proc. Of IEEE, 98 (2010) 1255.

[16] Y. Kozuka, A. Tsukazaki, and M. Kawasaki, Appl. Phys. Rev. 1 (2014) 011303.

[17] C-C Hsiao, K-Y Huang, and Y-C Hu, Sensors 8 (2008) 185.

[18] D. C. Look, D. C. Reynolds, J. W. Hemsky, R. L. Jones and J. R. Sizelove,Appl. Phys. Lett. 75 (1999) 811.

[19] T. Yanagida, Y. Fujimoto, K.Yamanoi, M.Kano, A. Wakamiya, S. Kurosawa, N. Sarukura, Phys. Status Solidi C 9 (2012) 2284.

[20] M Yan-Liang, O Xiao-Ping, Z Jing-W en, Z Zhong-Bing, P Hong-Bo, C Liang, L Lin-Yue, Chinese Physics C 34 (2010) 354.

[21] D. Panda, T-Y. Tseng, J. Mater. Sci. 48 (2013) 6849.

[22] A. Moezzi, A. M. McDonagh, M. B. Cortie, Chem. Engg. J. 185-186 (2012) 1.

[23] Y. Umasankar, S-M. Chen, Sensors, 8 (2008) 290.

[24] J. W. Rasmussen, E. Martinez, P. Louka and D. G. Wingett, Expert Opin. Drug Deliv. 7 (2010) 1063.

[25] C. Woll, Prog. Surf. Sci. 82 (2007) 55.

[26] U. Diebold, S-C. Li, and M. Schmid, Annu. Rev. Phys. Chem. 61 (2010) 129.

[27] V. E. Henrich and P. A. Cox, The Surface Science of Metal Oxides, 2nd edition, Cambridge University Press, 1996.

[28] O. Dulub, L. A. Boatner, U. Diebold, Surf. Sci. 519 (2002) 201.

[29] K. Horn and M. Scheffler, (Eds.) Hand book of surface science, Vol: 2 Electronic structure, Elsevier, 2000.

[30] E. I. Solomon and V. E. Henrich, Surf. Sci. Spectra, 5 (1998) 186.

[31] W. Gopel, J. Pollmann, I. Ivanov, and B. Reihl, Physical Review B, 26 (1982) 3144.

[32] K. Ozawa, and K. Mase, Phys. Rev. B, 83 (2011) 125406.

[33] J. Marien, Physica Status Solidi (a), 38 (1976) 513.

[34] H. Moormann, D. Kol and G. Heiland, Surf. Sci., 80 (1979) 261.

[35] K. Jacobi, G. Zwicker and A. Gutmann, Surf. Sci., 141 (1984) 109.

[36] S. Gutmann, M. Conrad, M. A. Wolak, M. M. Beerbom, and R. Schlaf, J. Appl. Phys. 111 (2012) 123710.

[37] R. Schlesinger, Y. Xu, O. T. Hofmann, S. Winkler, J. Frisch, J. Niederhausen, A. Vollmer, S. Blumstengel, F. Henneberger, P. Rinke, M. Scheffler, and N. Koch, Phys. Rev. B, 87 (2013) 155311.

[38] D.P. Woodruff (Ed.), The Chemical Physics of Solid Surfaces, Vol. 9, Oxide surfaces, Elsevier, 2001.

[39] H. P. Bonzel, (Ed.) Group III: condensed matter, Vol. 42: Physics of Covered Solid Surfaces, Sub. Vol. A: Adsorbed Layers on Surfaces. Part 5: Adsorption of molecules on metal, semiconductor and oxide surfaces, Landolt Brnstein Series, Springer-Verlag, 2006.

[40] J. C. Fan, K. M. Sreekanth, Z. Xie, S. L. Chang, and K. V. Rao, Prog. Mater. Sci. 58 (2013) 874.

[41] J. G. Reynolds, C. L. Reynolds Jr., A. Mohanta, J. F. Muth, J. E. Rowe, H. O. Everitt, and D. E. Aspnes, Appl. Phys. Lett. 102 (2013) 152114.

[42] L. J. Brillson, and Y. Lu, J. J. Appl. Phys. 109 (2011) 121301.

[43] J. Ruzyllo, Semiconductor cleaning and conditioning challenges beyond planar silicon technology, 22nd Symposium on Microelectronics Technology and devices (SBMICRO 2007), Rio de Janeiro, Brazil, Sept. 4, 2007.

[44] W. Kern, "Handbook of semiconductors wafer cleaning technology", Noyes Publications, 1993.

[45] K. A. Reinhart, Werner Kern, Handbook of silicon wafer cleaning technology, 2nd, Willian Anderw, 2008.

[46] S. W. King, J. P. Barnak, M. D. Bremser, K. M. Tracy, C. Ronning, R. F. Davis,and R. J. Nemanich, J. Appl. Phys., 84 (1998) 5248.

[47] Leading Edge Semiconductor Cleaning Technologies. Sony Corp.CX-News 36 (2004).

[48] A. Danel, "Metrology for contamination", UCPSS Tutorial, Belgium, September 18-20, 2006.

Chapter 2

Experimental Techniques

The principle surface characterisation technique employed in this thesis is photoemission spectroscopy and the background and principle of the technique are outlined in the following sections.

2.1 Photoemission Spectroscopy (PES)

Photoelectron spectroscopy, often referred to simply as photoemission, has its fundamental origin in the photoelectric effect [1]. Photoemission is the process of ejecting an electron from atoms (solid material) by incident photons (light) on it. It is one of the most extensively used method for surface chemical analysis and investigating the electronic structure of solid surfaces.

2.1.1 History and development

In 1887, Heinrich Hertz observed the photoelectric effect which was partially explained by Max Plank through his understanding of black body radiation. Max Planck received the Nobel Prize in 1918 for his concept of quantification energy [2]. Later this phenomenon was successfully explained by Albert Einstein which led to the award of a Nobel Prize in 1921 [1]. This was key to the later development of the photoelectron spectroscopy as a technique for studying the composition and electronic structure of matter. In 1946-1950, Steinhardt and Serfass revived research into photoemission spectroscopy research and they were instrumental in proposing X-ray Photoelectron spectroscopy (XPS) as a viable surface analysis tool by demonstrating the quantitative analysis of elements present in a material by comparing the intensities in the photoemission spectrum [3]. Finally, X-ray Photoelectron spectroscopy (XPS) technique was fully developed by Prof. Kai Siegbahn in Uppsala University, Sweden who recorded the first high resolution (1 eV) spectra for NaCl in 1954 and his comprehensive study on XPS was published in 1957 [4]. Siegbahn received the Nobel Prize

in 1981 to acknowledge his extensive efforts to develop XPS into a useful analytical tool [5]. In 1969 Hewlett-Packard in USA produced the first commercial XPS instrument which was marketed as a surface analysis technique that measured the chemical composition and provides information on the chemical state of elements that exist within the material.

2.1.2 Principle and Working

In photoemisson, the kinetic energies of photoemitted electrons are measured by an experimental set-up similar to that schematically shown in figure 2.1

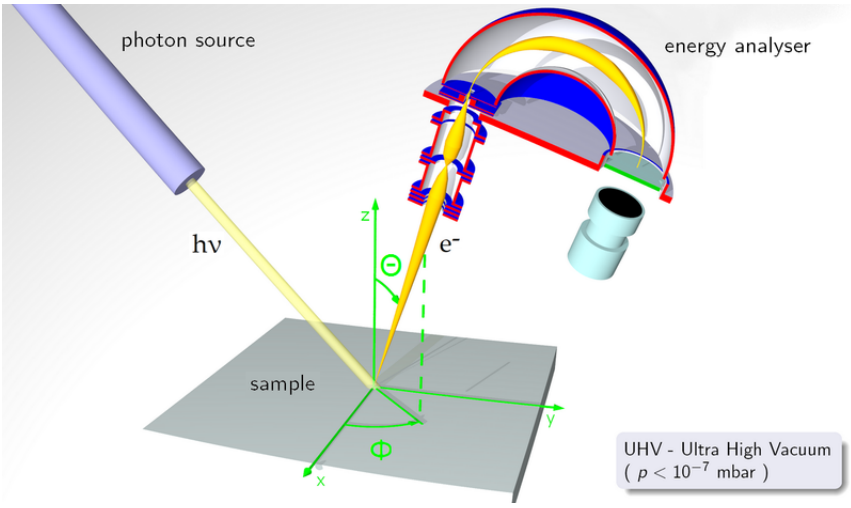

Figure 2.1: Photon ($h\nu$) excite electrons (e^-) which are emitted from the sample and the kinetic energies of these electrons are measured by an electron energy analyser [6].

From the Einstein equation for photoelectric effect with Planks constant (h) [7]

$$E_B = h\nu - E_{kin}^T \tag{2.1}$$

The above equation implies that the binding energy (E_B) of the photoexcited electron is equal to the energy of incident photons($h\nu$) minus the kinetic energy(E_{kin}^T) of the emitted electron. The incident photon energy($h\nu$) is fixed and the kinetic energy (E_{kin}^T) of the emitted electron is measured by an electron energy analyser. From the periodic table / XPS Hand Book, we know the electronic configuration of each element is unique. So, the emitted electrons from every element will have particular binding energies. This unique binding energy is utilized for the identification of elements, in photoemission spectroscopy.

To understand the full photoemission process and accurate measurement of binding energy of emitted photo-electron, the schematic energy level diagram (figure 2.2) below is used.

The binding energy in photoemission is referenced with respect to the Fermi level. The work function is defined as the energy difference between the Fermi level and the vacuum level($E_{Vac} - E_F$) Now the equation 2.1 modified as (where E_{kin}^T is the

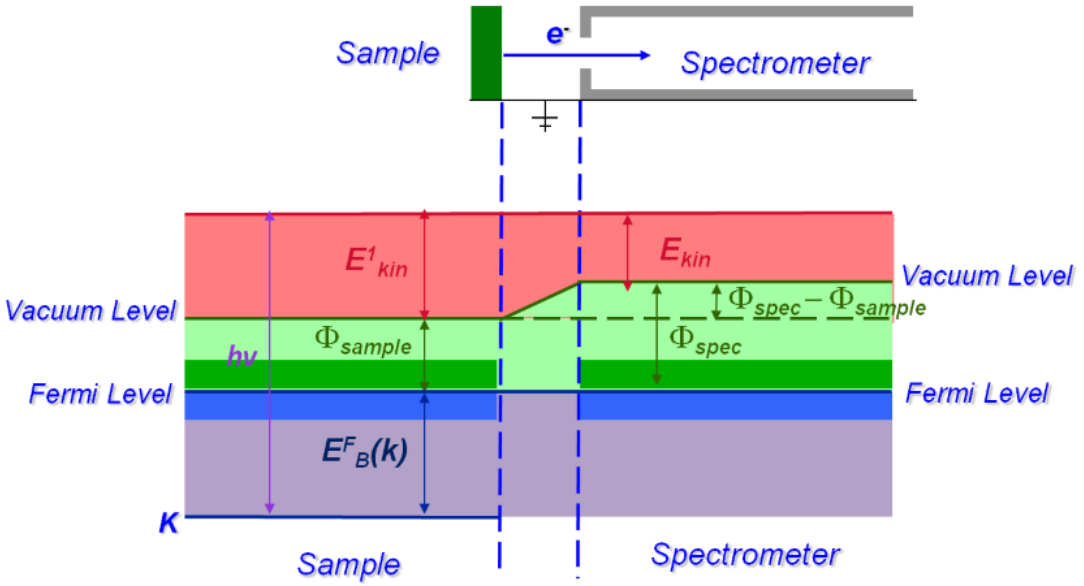

Figure 2.2: An energy level diagram for a sample and spectrometer in electrical contact during an XPS experiment [9].

kinetic energy after emission of photoelectrons which is not equal to photon energy of incidencing X-rays).

$$E_B^F = h\nu - (\Phi_{Sample} + E_{kin}^1) \tag{2.2}$$

In figure 2.2, the Fermi level for the sample and the spectrometer are aligned as both are in electrical contact [10]. So when the photo-electron entre the spectrometer they will experience a potential difference equal to the work function difference between spectrometer and the sample $(\Phi_{Spec} - \Phi_{Sample})$

$$E_{Kin}^1 = E_{kin} + (\Phi_{Spec} - \Phi_{Sample}) \tag{2.3}$$

Substituting equation 2.3 in equation 2.2

$$E_B^F(k) = h\nu - \Phi_{Sample} + E_{kin} + (\Phi_{Spec} - \Phi_{Sample}) \tag{2.4}$$

$$E_B^F(k) = h\nu - E_{kin} - \Phi_{Spec} \tag{2.5}$$

Using the above equation, the binding energy is obtained by knowing the incident photon energy $(h\nu)$, the kinetic energy (E_{kin}) of the emerging photoelectrons and the work function (Φ_{Spec}) of the spectrometer is measured by scanning gold sample in Photoemission spectroscopy. The gold and copper were used as reference sample to calibrate the spectrometer. By using the known binding energy of the gold (Au 4f = 83.98 eV), with measured spectra being shifted to compensate this value. The spectrometer work function is measured.

2.1.3 X-ray Photoelectron spectroscopy (XPS)

XPS can provide elemental information from the surface of a sample. It can detect all elements expect H and He. The atomic concentration it is able to detect is approximately >0.1 atomic%. The X-ray penetration depth will be in the order of few micrometres and the photoelectron emission will be from less than 10 nm into the surface. The detailed view of recording XPS spectra from a sample is shown in figure 2.3. A beam of X-ray is incidence on sample of 10 nm thickness and only form top 20 atomic layers of the sample the electrons revolving around the nucleus got excited (see figure 2.3). Those excited photoelectrons from particular atomic orbital (like 1s, 2s, 2p) forms a corresponding 1 s, 2 s, 2p core level XPS peaks and photoelectrons with minimum energy forms the background of XPS spectra.

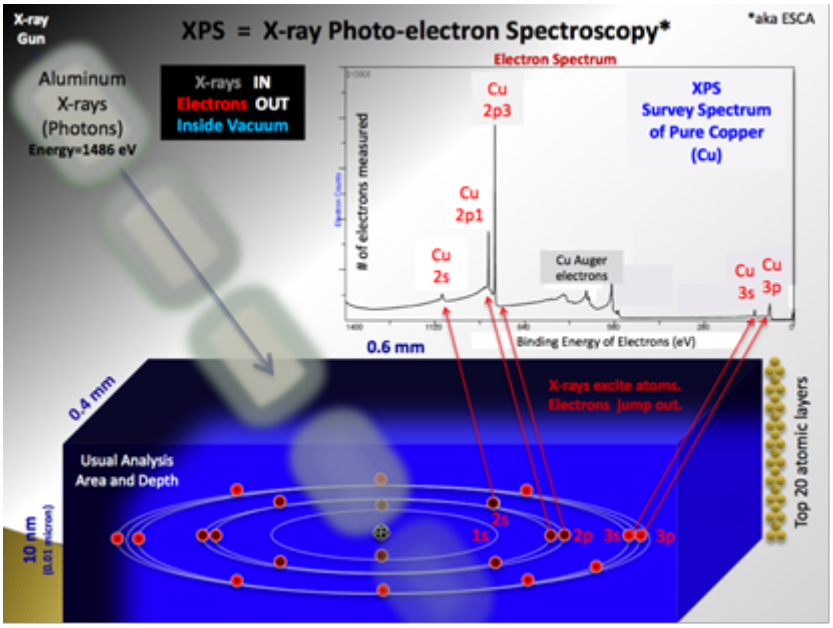

Figure 2.3: Detailed views of generating and recording the XPS spectra from the sample surface [11].

The primary instrumental set up for XPS system is (1) X-ray source (2) electron lens (3) electron energy analyser (4) detection system (5) vacuum system (6) external computer to plot the data as graph. The schematic diagram of a twin anode X-ray source is illustrated in figure 2.4. The X-ray peak energy for aluminium target is 1486.7 eV with a line width of 0.85 eV and for magnesium target is 1253.6 eV with a line width of 0.7 eV [12]. By using the different anode materials, it is possible to produce high energy or hard X-rays above 2000 eV as tabulated in table 2.1.

The X-ray photo-emitted electrons from the sample surface are collected and focused by an electrostatic lens (see figure 2.5). The acceptance angle of the lens depends on the analyser design and while increasing this angle would increase the overall electron yield it would result in a trade-off between the total sampling areas with an increased angle taking electrons from a wider surface area [14]. The photoelectrons

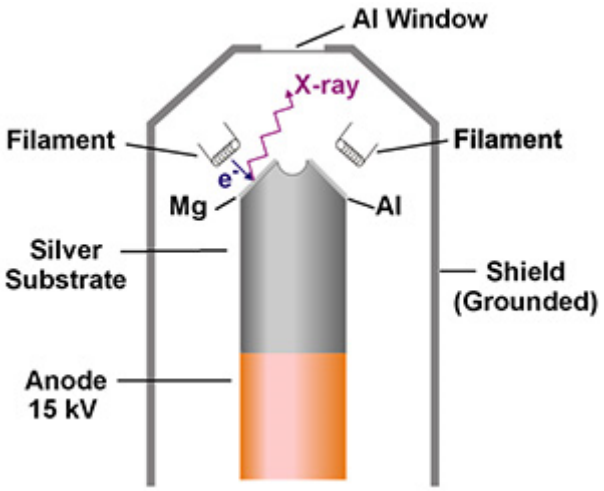

Figure 2.4: Twin anode conventional X-ray source [13].

Table 2.1: 2 Different anode metals with their respective X-ray peak energy and line width [7].

Anode	**Radiation**	**Photon Energy (eV)**	**Line Width (eV)**
Mg	Kα	1253.6	0.7
Al	Kα	1486.6	0.85
Si	Kα	1739.5	1
Zr	Lα	2042.4	1.6
Ag	Lα	2984	2.6
Ti	Kα	4510	2
Cr	Kα	5415	2.1

passing through the lens system enter the electron energy analyser where they can be separated based on their kinetic energy. An hemispherical electron energy analyser is the most common analyser used in XPS. Hemispherical analyser consists of two concentric segments of spheres of radii $R_1$and R_2. The mean radius between these plates will be R_0, as illustrated in figure 2.5.

The electrons going from the lens to the analyser will have the energy of $E_0 = eV_0$, (where V_0 is the retardation voltage applied to the grid). The voltage on the two hemispheres is adjusted in such a way that it matches the pass energy. This will allow the electrons to travel in trajectory of radii R_0 as shown in figure 2.5. This adjustment of voltage to hemisphere plates is attained by applying the negative voltage V_2 to the outer hemisphere, which repels the electrons and a positive voltage V_1 to the inner hemisphere, which will attract the electrons. The relationship between the applied voltages V_1 and V_2 to radius of hemispheres is express as:

$$V_1 = V_0 \left(3 - 2\frac{R_0}{R_1}\right) \tag{2.6}$$

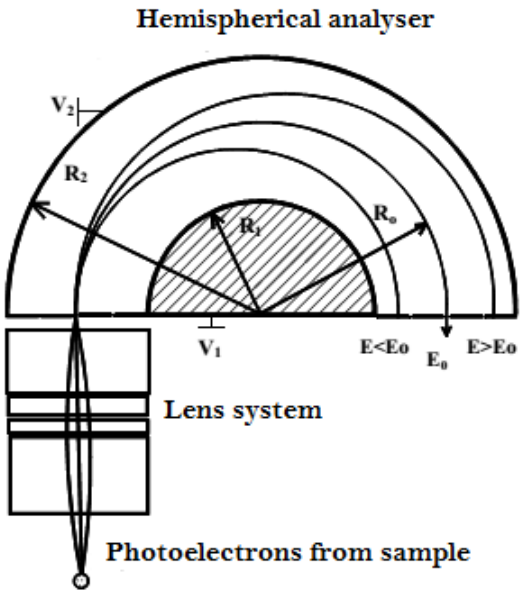

Figure 2.5: Schematic diagram of the electrostatic lens and hemispherical electron energy analyser [15].

$$V_2 = V_0 \left(3 - 2\frac{R_0}{R_2}\right) \tag{2.7}$$

Then the voltage between the hemispherical plate is

$$V_2 - V_1 = V_0 \left(\frac{R_2}{R_1} - \frac{R_1}{R_2}\right) \tag{2.8}$$

The final vales for $V_1 = 0.5(V_0)$ and $V_2 = (-1.33)V_0$
Electrons with large energy variation from will be lost to collision with the hemispheres before they are able to transverse the full distance to detector [15].

The channeltron multiplier is used in spectrometer to amplify the incoming photoelectrons obtain good XPS spectra and it is placed inside the XPS Analyser. The channeltron multiplier is made of semiconducting glass tube with wide funnel shaped entrance to accepted the electrons from the analyser. To amplify the number of electrons inside the channeltron, a potential difference of 2 - 4 kV is applied to the channeltron. This will create an electron cascade effect and incoming electrons are multiplied as shown in fig 2.7. The output of the multiplier is then measured as a pulse, providing an electron gain of 10^6 - 10^8 and potential count rates of greater than 10^6 counts per second (c.p.s.). The output from the pulse counter is then fed into analysis software that is able to plot the (c.p.s) as function of the electron binding energy [15].

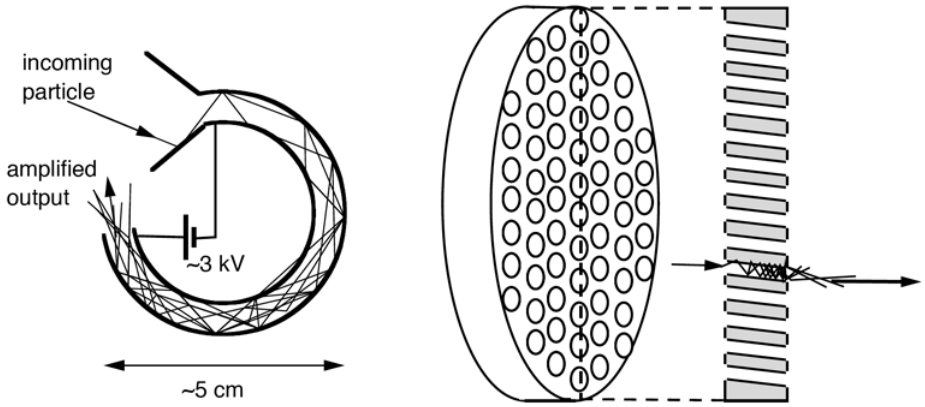

Figure 2.6: Single channeltron detector and channel plate consisting of a series of electron multipliers oriented in parallel [16].

2.1.4 Different types of photoemission spectroscopy

Kai Siegbahn and co-workers developed a successful X-ray photoelectron spectrometer in 1950. XPS has emerged as powerful tool to study the chemical composition and electronic structure of matter. To further explore the matter in detail the scientists were in continuous development of the new methods, sophisticated instrumentation such as high resolution spectrometer, spin-resolved spectrometer, electron microscopes. The principle behind different types of photoemission spectroscopy were reviewed in detail by C. S. Fadley et al [17–20].

Different versions of photoelectron spectroscopy were developed by tuning the photon energy of the photoemission source as following: (1) UV (UPS) and Laser (LPES) are used to record valance band and molecular spectra (2) X-ray photoemission (XPS) is used for study of core levels (3) Synchrotron radiation photoemission spectroscopy (SRPES) is emerged as a prominent techniques to study the electronic structure of the surface and interfaces. An additional synchrotron radiation variation is hard X-ray photoemission (HAXPES) where high energy X-rays (above 2kV) are used to generate photo-emitted electrons which have significantly higher sampling depths than conventional XPS. Then by replacing a conventional analyser by a spin resolved electron analyser has been used to characterise magnetic materials in spin resolved photoemission spectroscopy (SRPES). By replacing the vacuum environment for the sample able to record photoemission spectra from samples in ambient condition is technique called Ambient pressure XPS (APPES).

In figure 2.7 the different types photoemission spectroscopy based techniques are illustrated. These different techniques are classified into four groups based on the instrumental modification (source, analyser) as well as method of doing the experiment (time, sample, vacuum and other ways). The details of instrumental modification and their specific application in characterisation of material are tabulated in table 2.2.

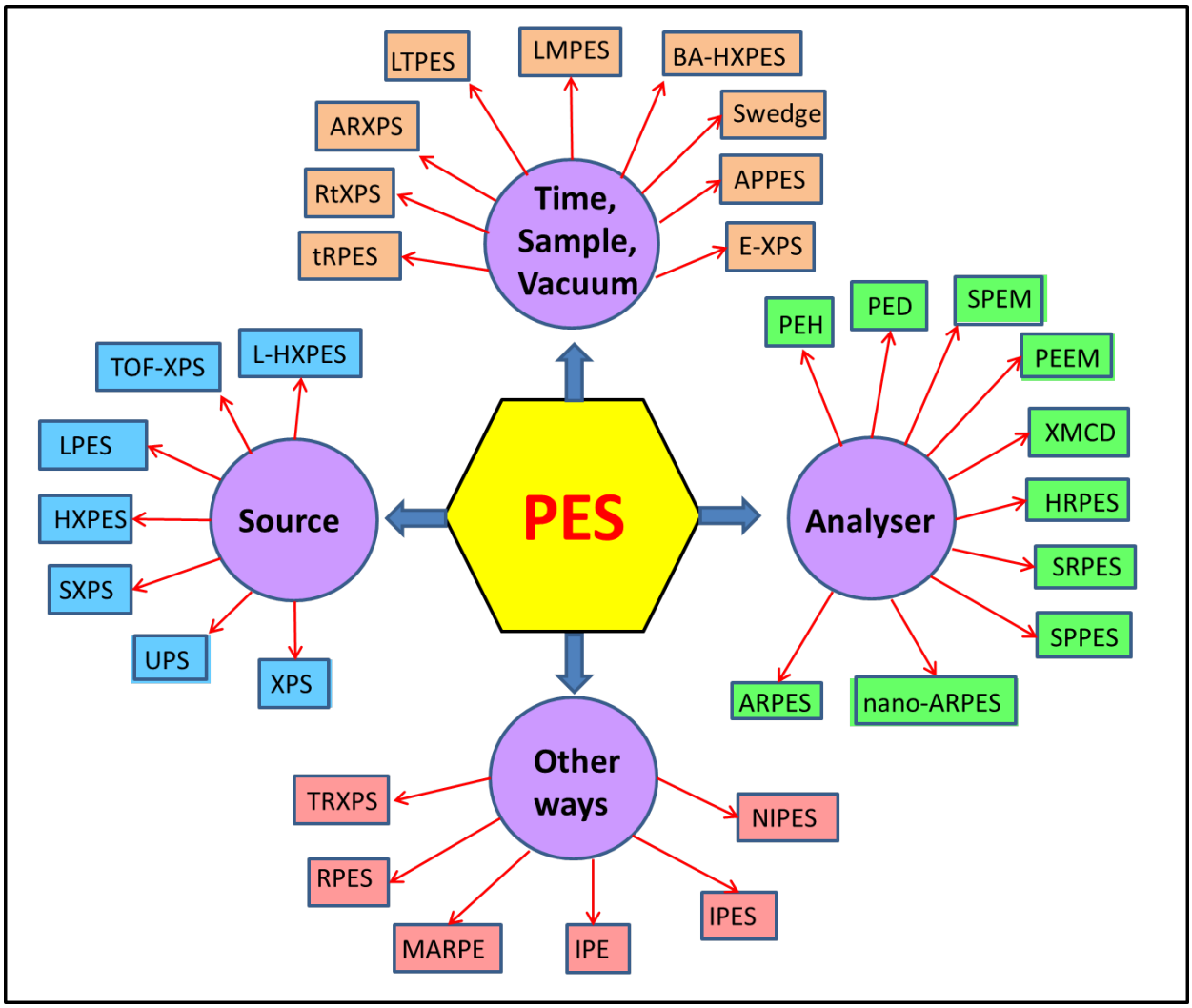

Figure 2.7: Branch of photoemission spectroscopy as different types of materials characterisation techniques.

Table. 2. 1(a). Different types of Photoemission spectroscopy based materials characterisation techniques with instrumentation and applications details

S.No	Technique	Abbreviation	Instrumental modification	Application	Ref.
1	X-ray photoelectron spectroscopy	XPS	Source – X-ray (Al and Mg)	Surface chemical composition, bonding of atoms, and thickness of ultra-thin films	1
2	Ultraviolet photoemission spectroscopy	UPS	Source – UV lamp	Valence band, Work function, Fermi level	2, 3
3	Soft X-ray photoemission spectroscopy	SXPS	Source – Synchrotron radiation (>2 KeV)	Surface chemical composition, valence band, work function, Fermi level, film thickness measurement	4
4	Hard X-ray photoemission spectroscopy	HXPES	Source – Synchrotron radiation (5 – 15 KeV)	Bulk chemical composition, bulk electronic states, multiple layer thin films composition	5
5	Laser based photoemission spectroscopy (also called Molecular photoelectron spectroscopy) a) Two Photon photoemission spectroscopy b) Zero-kinetic-energy photoelectron spectroscopy c) Resonantly enhanced multi photon ionization	LPES 2PPE ZEKE REMPI LAPE	Source – Laser, XUV Anlayser – TOF electron analyser	Ionic states, electronic structure of bonding electrons, mostly organic materials, gases. a) Occupied and unoccupied electronic states in a metal or semiconductor. b) Vibrational structure c) Materials in gas phase and their ionic states d) Electron dynamics in atoms, atom	6 7 8 9 10 11

	spectroscopy d) Laser-assisted photoemission			dynamics in molecules.	
6	Time of flight – photoemission spectroscopy	TOF – PES	Source – X-ray or laser released in pulsed mode , Pump-probe method, Analyser – TOF spectrometer	Electron dynamics on semiconductors, Understand the chemical reactions, Vibrational dynamics of molecules, and dynamics of organic and biological molecules.	12, 13
7	Laboratory scale hard X-ray photoemission	L-HXPES	Source – X-ray (Zr, Ag, Ti, Cr, 2 – 5 KeV)	Bulk chemical composition, film thickness, Multi-junction semiconductor structure	14
8	Angle resolved photoemission spectroscopy	ARPES	Analyser – angle resolved spectrometer	Energy and momentum of electrons, Electronic structure of solid surface	15, 16
9	Nano – angle resolved photoemission spectroscopy	Nano – ARPES	Lens – Zone plate to focus X-ray to small spot, Analyser - angle resolved spectrometer	Electronic band structure of nano-sized samples as well as nano spots on sample	17
10	Spin polarized photoemission spectroscopy	SPPES	Analyser – spectrometer with Spin Polari meter	Spin-polarized electronic band structure of thin films and magnetic materials. Obtain the magnetic properties of materials.	18, 19
11	Spatially resolved photoemission spectroscopy	SRPES	Analyser – spectrometer with 2D detector, Lens – photoelectron Transfer or focusing lenses	Chemical state distribution on surface and for surface chemical photoelectron imaging.	20
12	Ultra high resolution photoemission spectroscopy	HRPES	Analyser – high resolution spectrometer (energy resolution < 10 meV)	Electronic structure off surface (Simultaneous determination of energy and momentum of electrons)	21

13	X-ray Magnetic circular dichroism	XMCD	Source – Polarised X-rays Analyser – Electron microscope	Detection of electronic structure of both the ground states and excited states, especially magnetic properties (spin and orbital magnetic moment).	22
14	Photoemission electron microscopy	PEEM	Analyser – Electron microscope	Study the growth, chemical and magnetic interactions, properties of micro or nanostructured materials	23
15	Scanning photoelectron microscopy	SPEM	(X-ray focusing) Fresnel zone plates optic system, Analyse – Scanning and imaging system	To study the surface chemical inhomogeneity in sub-micrometer scale or spatially resolved electronic structure variation of nanomaterials	24
16	Photoelectron diffraction	PED or PhD	Analyser – Spectrometer and diffractometer	Surface structure determination of adsorbates / surfaces	25, 26
17	Photoelectron Holography	PEH	Analyser - High speed multi-channel detector	Study the surface structure of single crystal and thin films.	27
18	Standing wave photoemission spectroscopy	Swedge	Source – synchrotron soft X-rays, Analyser – Spectrometer and detector Samples – In the shape of a wedge	Structural and chemical properties of multilayer structure	28
19	Time resolved photoemission spectroscopy (Femto /Atto / Pico second photoelectron spectroscopy)	tRPES	Source – laser or XUV Analyser – TOF spectrometer	Exploring the gas-phase systems, electronic process occur on below mirco second	29, 30, 31
20	Real-time X-ray photoelectron spectroscopy	RtXPS	Source – Synchrotron soft X-rays, Analyser – multichannel	Determination of the composition and structure of gas–solid surface interface at	32

			electron energy analyser	different stages of surface reactions	
21	Angle resolved X-ray photoelectron spectroscopy	ARXPS	Same as for XPS	Find chemical and electronic properties of thin films and substrate	33, 34
22	Low temperature photoemission spectroscopy	LTPES	Novel apparatus – electrospray ionization source, 3D Paul trap for ion accumulation and cooling, a TOF mass spectrometer, and a magnetic-bottle photoelectron analyzer	To investigate the complex anions in the gas phase, including multiply charged anions, solvated species, and biological molecules	35
23	Liquid microjet photoemission spectroscopy	LMPES	Special apparatus – Micro liquid beam apparatus for high pressure environment.	Detecting the local electronic structure, and chemical composition for monitoring ultrafast dynamical processes in aqueous solution	36
24	Bias voltage application in hard X-ray photoemission spectroscopy	BA-HXPES	Source – Synchrotron sample – bias voltage applied to sample vertically.	Find the interface electronic states in the semiconductor device in operation.	37
25	Atmospheric pressure photoemission spectroscopy	APPES	New apparatus – Electrostatic lens, X-ray window, differential pumping system, special load lock.	The study of liquid and solid surfaces / interfaces, particularly in areas such as atmospheric, environment and catalysis sciences	38
26	Environmental X-ray photoelectron spectroscopy	E-XPS	electrostatic lens system (up to 0.4 Torr), 2D detector (imaging and angle resolved capability)	To study the surfaces exposed to gases or liquids at different pressures (Catalysis and environmental science)	39
27	Gracing incidence angle X-ray	GIXPS	Sample holder – high precision	To measure the thickness, density of	40,

	photoelectron spectroscopy Or Total reflection X-ray photoelectron spectroscopy	or TRXPS	multi-axis rotatable	layers, and chemical state of ultrathin films or adsorbate on surface	41
28	Resonant photoemission spectroscopy	RPES	Source – Synchrotron	To determine the electronic structure of surface (unoccupied states)	42, 43
29	Multiple atom resonant photoemission	MARPE	Source – Synchrotron, Analyser – Multichannel electron spectrometer	For the study of near-neighbour atomic identities, bonding, and magnetism in alloys or at interfaces	44
30	Internal photoemission spectroscopy	IPE	Source – Xenon Lamp Analyser – Detector and electrometer	To determine the electron energy barrier heights and band structure between solid interfaces	45
31	Inverse photoemission spectroscopy	IPES	Source – electron gun, Analyser – Photon detector	To study the unoccupied electronic structure of surfaces, thin films, and adsorbates.	46
32	Negative ion photoemission spectroscopy	NIPES	Source – UV laser, Ion gun Analyser – Mass spectrometer and electron energy analyser	To obtain electronic state, electron affinity and vibrational frequencies of organic molecules	47

2.1.5 XPS in semiconductor industry

Traditionally, XPS has been used as a surface characterisation tool in chemical, chemical engineering and the metallurgical industries. Due to growing demand for powerful, portable chips for future computing, smartphones and other electronic devices the semiconductor industries has kept reducing the size of transistors and other semiconductor devices to few (90, 65, 45, 32, 16) nanometers. Another approach adopted by the semiconductor industries is moving towards new materials for semiconductor device fabrication. This all leads to new demands of the metrological tools in chip production line [22]. In general, metrological tools in production line will use reflectometers to measure gate oxide (SiO_2) thickness. In this case, in addition to the thickness measurement, now chemical composition mapping was also needed as the distribution of N in SiO_2 is crucial in maintaining the dielectric constant of the gate oxide [23]. A new gate material HfO_2 on silicon wafers is now used in microprocessor fabrication and this also need a metrological tool for the confirmation of proper chemical composition of the oxide layer along with thickness [24]. Similarly changing the Al interconnect to Cu metal in semiconductor devices has happened. The problem here is that Cu has the property of both quick oxidation and diffusion into active device region, which requires introduction an additional barrier layer such as Co between the copper and dielectric. Here also metrological tool is needed to monitor the thickness as well as chemical composition of the substrate Cu interconnects layers [25]. Hence modern XPS with lateral resolution of 10 μm emerged as promising meteorological tool to measure the thickness of these ultra-thin film (gate oxides, interconnects) and map the chemical composition to the scale of large area (200 mm 300 mm) wafers [26]. Further modern XPS has been automated to load of wafers, acquiring data in different locations, spectral area analysis and creating elemental composition percentage table, etc so as to match with fast moving production lines [25]. The thickness of ultra-thin oxide films were measured by comparing the peak ratios of oxide to substrate. Parallel angle resolved XPS (ARXPS) were also used for non-destructive depth profiling of ultra-thin films on large wafers (<10 nm) [25, 27]. This non-destructive depth profiling was done by Relative depth profile (RPD) method, a simplistic approach intended to indicate which elements (or chemical states, if identified) in an acquired XPS spectrum are, on average, nearer the surface and which further away [25]. A typical industrial XPS system used for in-line metrology for large scale wafers is shown in fig. 2.10 [26]. An example of how the in-line XPS maps the composition of silicon wafer with ultra-thin layers of silicon oxide, aluminium oxide and on top HfO_2 deposited by ALD is shown in figure [24].

2.2 Analysis of XPS spectra

The analysis and understanding of XPS spectra needs a special appreciation of spectral features. Basic chemical compositional analysis, with depth profiling of sample,

Figure 2.8: VeraFlex III XF Industrial XPS as metrological tool to characterise the large scale wafers [26].

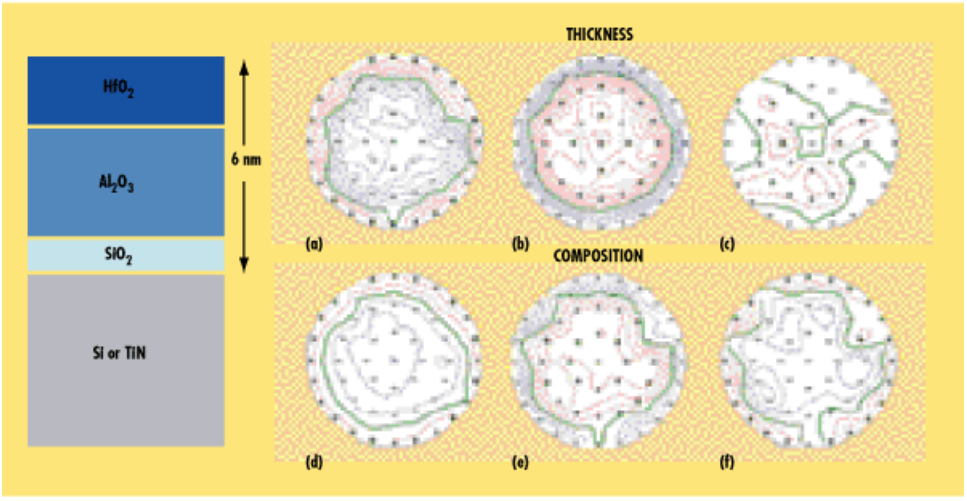

Figure 2.9: Schematic diagram at left shows a stack with film thicknesses and compositional uniformities illustrated in the wafer maps at the left: (a) HfO_2 thickness (3.93%), (b) Al_2O_3 thickness (6.13%),(c) SiO_2 thickness (1.68%), (d) hafnium uniformity (0.75%), Aluminium uniformity (6.07%), and (f) oxygen uniformity (2.28%) [24]

thickness calculations and important fundamental parameters helpful in understanding XPS spectra are discussed in this section.

2.2.1 Element Identification

From the initial scans, the XPS survey spectra were used to identify the elements present on the surface at atomic percentage leve1 (0.1 1%) based on detection limit. Generally, these elements were found by appearance of the strong peaks in the survey spectra, for example: in Figure 2.10 we can see the survey spectra of ZnO nanorods grown using a gold catalyst. All the peaks indicative of zinc, oxygen and carbon were found. These positions of the peaks (binding energy) is not always unique for particular element, other elements can also have similar positions and thus overlap with each other. Such a case was also seen in Figure 2.10 where the gold peak Au 4f typically overlapped with a zinc peak Zn 3p. Like this cases, other core level peaks (such as Zn 3d, Zn 2p) were used to confirm the presence of the element in the sample.

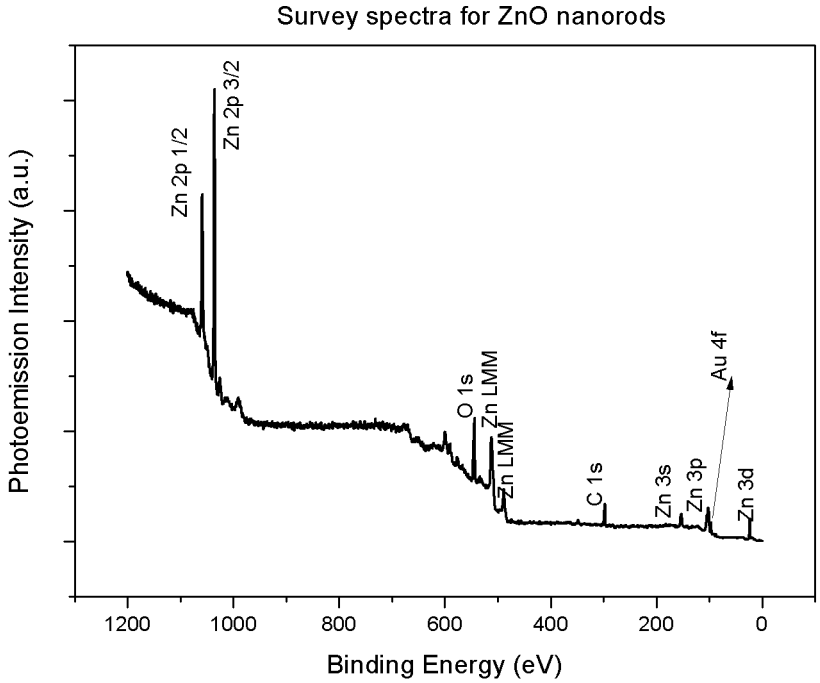

Figure 2.10: XPS Survey scans obtained for ZnO nanords grown using gold catalyst. The elements Zn, O, C, and Au were identified by their photoemission peaks binding energy position.

2.2.2 Chemical Shifts

In parallel to identifying the elements present on the surface, one of the most important aspects of XPS is the ability to distinguish between different chemical environments of the same element. This is possible because the binding energy of an electron within an atom depends on the bonding environment of that atom. Therefore, changes in chemical bonding can result in changes in the charge density around the atoms, which causes a chemical shift in the binding energy of the electrons which

emerge from these atoms [28]. This process is described in greater detail with reference to the zinc oxide/zinc hydroxide system, using the Zn 2p spectrum in figure 2.11 which shows a Zn 2p spectrum taken from a hydrogen cleaned ZnO (0001) surface. It can be seen that electrons excited from the Zn substrate appear at a binding energy of 1022 eV, while those from the $Zn(OH)_2$ layer appear at a higher binding energy position, chemically shifted by ≈1.0 eV. This is due to the different bonding environment present within the two chemical species on the surface. Zn atoms at the surface bonded to OH are in a different chemical environment that those bonded to oxygen in ZnO. This difference is reflected in the different binding energies of the Zn 2p photoemitted electrons as $Zn(OH)_2$ is more ionic than ZnO. Therefore the kinetic energy of electrons emitted from ZnO is higher than those emitted from Zn atoms in the $Zn(OH)_2$ bonding environment. This means that the relative electronegativity values of the elements within a sample can be used to identify chemical environments in which they exist.

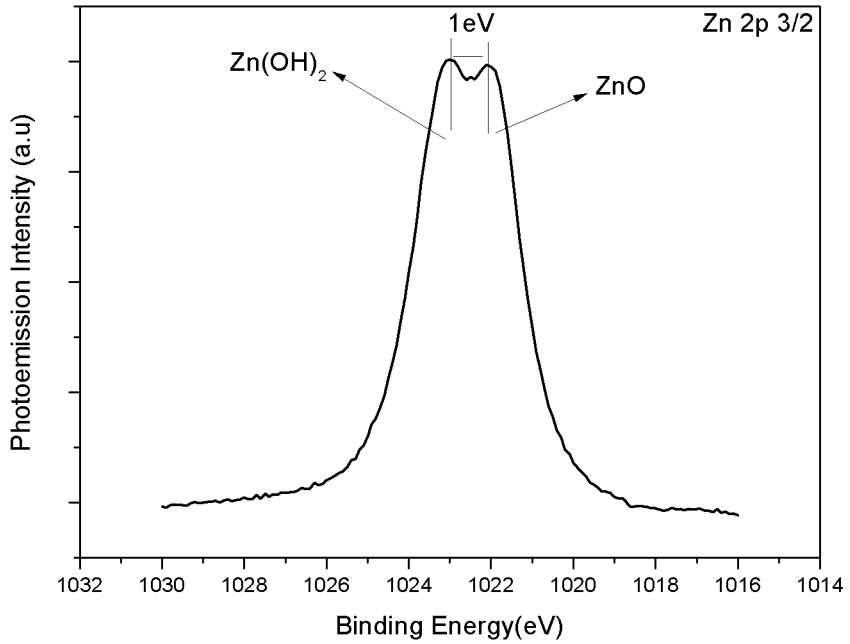

Figure 2.11: Zn 2p 3/2 core level peak having two component peaks for ZnO and $Zn(OH)_2$ separated by 1.0 eV chemical shift.

2.2.3 Quantification

Quantification of the chemical composition of a surface can be easily achieved by the comparison of the relative intensity of the core levels belongs to different elements present on the same surface. For accurate prediction of chemical composition of surface several other factors have to be taken into account in addition to XPS peak

intensities. The way of doing quantification analysis was explained further in detail from the figure 2.12 with reference to the Zn 2p and O 1s core level spectra obtained for ZnO thin films grown on Si(111) wafer.

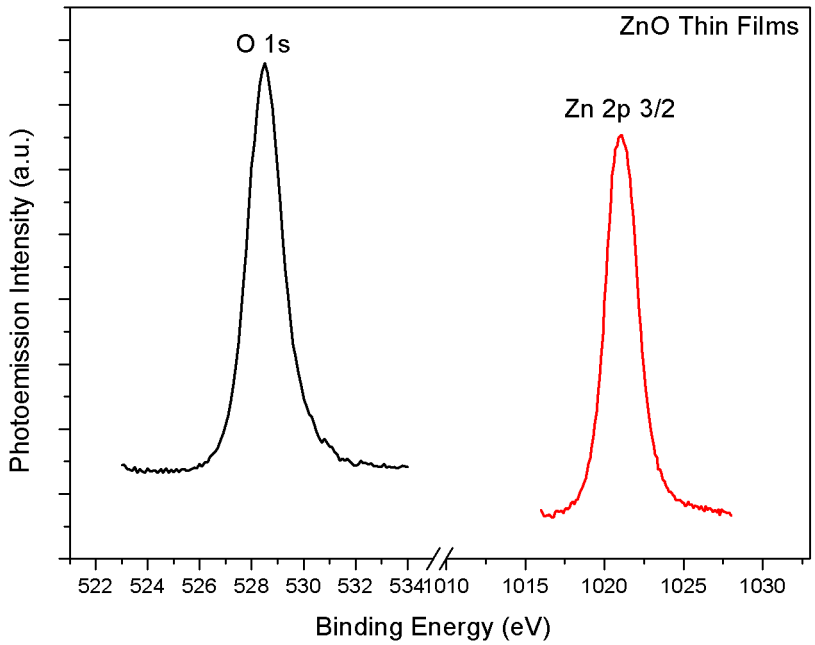

Figure 2.12: Zn 2p 3/2 and O 1s core level peak for ZnO thin films grown on Si(111) surface.

Before determining the Zn and O stoichiometry for ZnO thin films (from figure 2.12). First we need to assume the ZnO thin films is homogenous, if the thin film surface is non-uniform perpendicular to the XPS sampling depth, it is difficult to determine the exact elemental ratios. The main three factors that have to taken into account were inelastic mean free path (IMFP), photoionization cross section and the transmission function of analyser. The (IMFP) is dependent on the kinetic energy of the peak which is obtained from binding energy of the peaks as follows. For Zn 2p peak binding energy is 1022 eV, then its Kinetic energy is, K.E. = 1486 - 1022 = 464 eV and similarly for O 1s B.E. is 531 eV, then K.E. = 1486 531 = 955 eV, where 1486 eV is the photo-excitation energy. From the K.E. values obtained, the O 1s peak will represent electrons further deep into the sample than the Zn 2p peak. The photoionization cross section is the probability that an electron will be photoexcited. The transmission function of the analyser determines the sensitivity of the analyser to electrons of that particular kinetic energy [28, 29]. The relative sensitive factor (RSF) for the particular core level of a element was obtained based on three factors explained above. By using these RSF values the chemical composition was calculated. The RSF values for all elements were tabulated in the XPS Hand Book [30]. For the spectra shown in figure 2.12, the RSF values were 3.726 and 0.711 for Zn 2p and O

1s respectively. The stoichiometry of ZnO thin film is achieved by taking the ratio of peak intensity to the RSF value and then adding all ratios, equating to 100%. Form this we can get exact atomic% (up to 1% acuracy) of oxygen and zinc as shown in table 2.2.

Table 2.2: Quantification of chemical composition of Zn and O in ZnO thin films using RSF.

Element	**Peak**	**Intensity**	**RSF**	**Ratio**	**Stoichiometry in atomic %**
Zinc	Zn 2p	418651	3.726	112359	54%
Oxygen	O 1s	67802	0.711	95361	46%
Total				207720	100%

2.2.4 Peak fitting

From the XPS core level spectra of an element the binding energy position, peak width and intensity were easily obtained. This information only gives the single chemical state of that element in given sample. But it is very common; the element can exist in more than one chemical state within the same sample. In XPS core level spectra the binding energy position of two different chemical states of an element does not vary by more than 5 eV. Hence their will overlapping two peaks meant for two different chemical states of an element can be possible. Then final core level spectra obtained will be combination of all those chemical state peaks.

To distinguish those overlapped peaks and to obtain information of individual peaks meant for each chemical state of elements, cure-fitting/ peak-fitting of raw core level spectra was usual. The special software Aanalyser [31] was used to perform peak-fitting in this thesis work. Initially the known core-level parameters of a selected peak were applied and adjusted as required to get realistic peak fit. All parameters were independent of chemical state and can be a varied as well as fixed as needed. The no. of peaks to fit was chosen from possible chemical state can be present in the sample. The full width half maximum (FWHM) is key parameter in peak fitting is made up of two coordinates. Firstly, the Lorentzian line width is intrinsic to the particular core-level and is independent of chemical state. Secondly, the Gaussian line width is dependent on the instrumental peak broadening and as well as the form the sample (like crystalline or amorphous) [10]. The peak fitting details of core level peaks of Zn, O and C for ZnO are explained in chapter 4.

2.2.5 XPS Parameters

The XPS data analysis depends on the sensitivity, spatial resolution, data-acquisition time and morphology of the sample. The chemical compositions also vary based on the depth of measurement and position of the sample. In order to use the XPS effectively and efficiently for qualitative analysis, such as measurement of over layer / ultra-thin film thickness and estimation sampling depth, etc, It is necessary to obtain the four

key parameters: IMFP, EAL, MED and ID as discussed below [32]. In addition to this photoionization cross section and Auger parameter are briefly explained.

2.2.5.1 Inelastic mean free path (IMFP) and Sampling depth

In the photoemission process, if X-rays of energy 1 kV irradiated on the sample. The depth that X-rays will penetrate into sample is 1m and the photoelectron depth from which the electron can be emitted from the sample is about 10 nm. Then the emitted electrons will lose the kinetic energy by inelastic collisions before reaching the top surface or comeing out of the sample. The probability of these electron interactions can be predicted based on the inelastic mean free path (IMFP) of given material, which depends on the kinetic energy of the emitted electrons and kind of material [16]. This is commonly represented as the universal mean free curve in figure 2.13

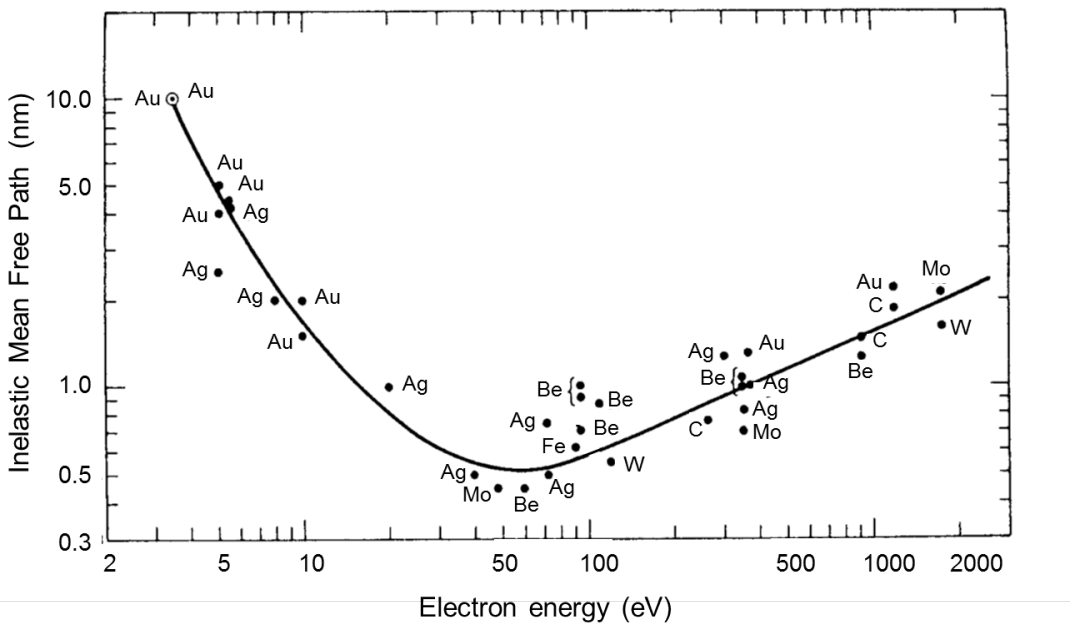

Figure 2.13: Universal mean free path (MFP) curve, showing a range of materials [33].

The inelastic elastic mean free path is defined as the average distance that an electron with a given energy travels between inelastic collisions [32]. Mathematically expressed as

$$P(d) = exp\left(-\frac{d}{\lambda}\right) \tag{2.9}$$

Where $P(d)$ is the probability of an electron travelling a distance d, through a solid without undergoing scattering; and λ is the IMFP for the electrons of a given energy. The probability of electron decay with respect to depth of the sample is illustrated in figure 2.14

From the figure 2.14 it seems the great amount of unscattered electrons are from a

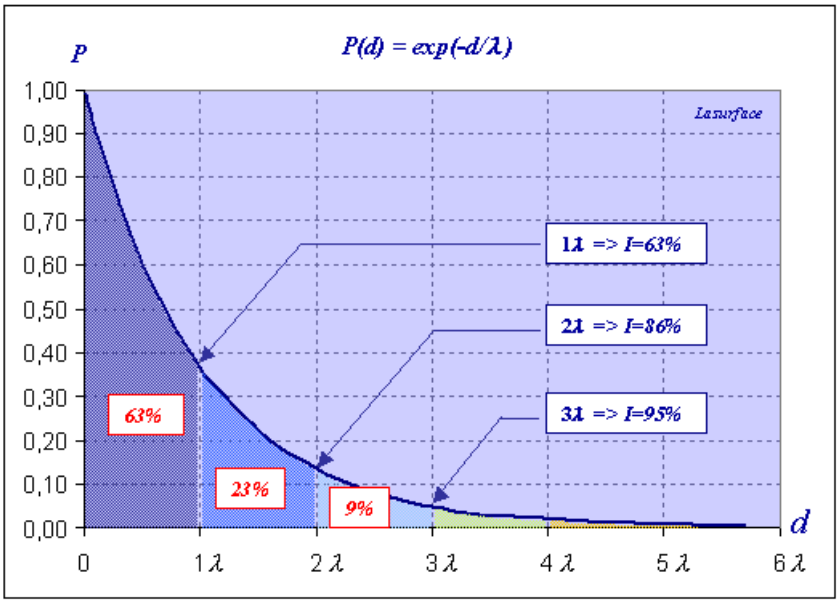

Figure 2.14: Graph for the probability of scattered electron emission as a function of depth [34]

depth of 3λ. This is described as the sampling depth. So roughly the sampling depth is three times of the inelastic mean free path (d = 3λ). The sampling depth for ZnO compound core levels including carbon is calculated by using the NIST Electron EAL Database [35] and shown in figure 2.15 for the two X-ray excitation lines used in this study, Al Kα (1486 eV) and Mg Kα (1253 eV).

2.2.5.2 Effective Attenuation Length (EAL)

This is the parameter which, when introduced in place of the IMFP into an expression derived for XPS on the assumption of that elastic scattering effects were negligible for a given quantitative application, will correct the expression for elastic scattering effects [36]. The EAL is generally intended as a measure of opacity of a given solid for single electrons of interest. Values were obtained from measurements of XPS spectra intensities as a thin film of increasing thickness was deposited on a substrate. The EAL expressions for the determination of thickness of over layer films on planar substrate. If we neglect the elastic scattering of the signal electrons for the moment, the intensity of XPS photoelectrons emitted form a substrate I_S, covered by a uniform overlayer film of thickness t would be given by

$$t = -\lambda \cos\theta \ \ln\left(\frac{I_S}{I_S^0}\right) \tag{2.10}$$

Where I_S^0 is the signal intensity from bare substrate (t = 0) and λ_{in} is the IMFP for the substrate-signal electrons in the overlayer material. A thickness t could then simply calculated from measurement of I_S^0 and and data for λ_{in} [32].

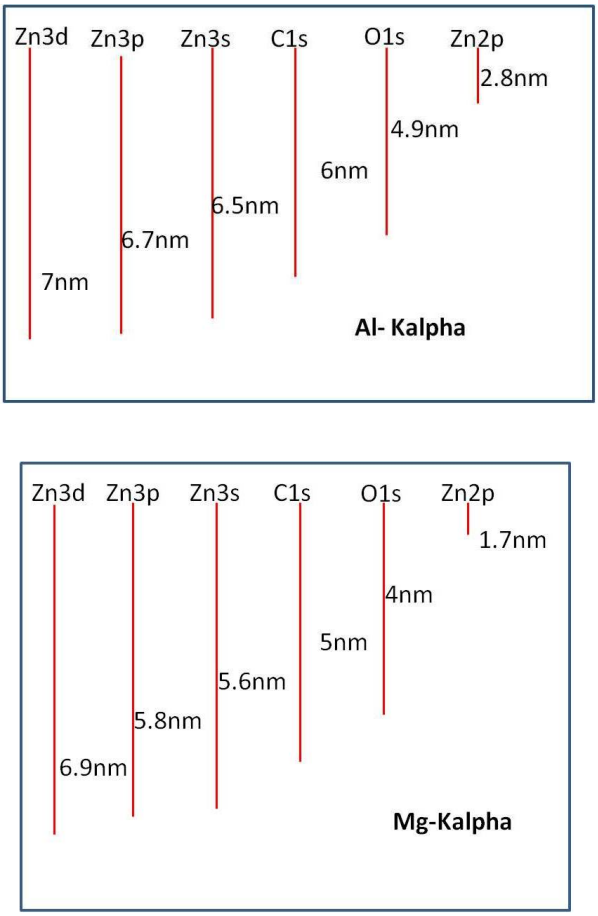

Figure 2.15: XPS effective sampling depth for ZnO compound for AlKα (1486.7 eV) and Mg Kα (1253.76 eV) X-rays.

2.2.5.3 Mean escape depth (MED)

It is defined as the average depth normal to the surface from which electron escape from the sample. It is express as

$$MED = \frac{\int_0^\infty Z\Psi(Z,\Theta)dz}{\int_0^\infty \Psi(Z,\Theta)dz} \tag{2.11}$$

Where $\Psi(Z,\Theta)$ is the emission depth distribution function for depth (Z), from the surface to material and for angle of emission,Θ, with respect to surface normal. (Z - Sample depth, Ψ - angle of X-ray incidence, Θ - angle of electron emission) [21].

2.2.5.4 Information depth (ID)

The information depth is defined as the maximum depth, normal to surface, from which useful information of sample is obtained [32]. It also depends on the nature of the sample and can be identified by the sample thickness from which the specified percentage of (eg. 95% or 99%) from which the detected signal originates. Based on the figure 2.13 the information depth will be about 3 - 5 times of inelastic mean free path (3λ to 5λ) [21].

2.2.5.5 Photoionization cross section

The photoionization cross section is the probability that an electron will be photo excited by a photo-excitation energy for a particular core-level. The photoionization cross section depends on both the photo-excitation energy as well as the core-shell of the atom (nature of material). In synchrotron photoemission spectroscopy there is a possibility of tuning the photoemission energy as required for a core-level of the particular elements. Hence the photoionization cross section values were helpful to find the right photoemission energy for different core-levels to get maximum intensity of spectra. For ZnO compound the core levels of Zn, O, C, the highest photoionization cross-section and respective photoemission energy is tabulated in table 2.3. The values were obtained from online database of Sincrotrone Trieste ScpA [37]

Table 2.3: The range of photoemission energies for getting maximum photoionzation cross section (high intense photoemission spectra) for core levels of elements Zn, O and C.

Core level	**Photoexcitation energy range**	**Photoionization cross section**
Zn 2p	1055 - 1065	0.92 - 0.91
Zn 2s	1160 - 1165	0.12 - 0.11
Zn 3d	60 - 70	9.35 - 9.32
Zn 3p	200 - 210	0.77 - 0.77
Zn 3s	135 - 145	0.31 - 0.29
Zn 4s	10.2	0.66
O 1s	540 - 550	0.51 - 0.47
O 2p	16.7 - 25	10.77 - 10.12
O 2s	45 - 55	0.86 - 0.87
C 1s	295 - 305	0.91 - 0.82

2.2.6 Auger Parameter

In XPS spectra the two types of peaks were obtained one photoemission peak due to core - level photoionization and other the Auger electron emission peaks induced by X-rays. By referencing the binding energy position of the photoemission peaks the respective elements were identified. But these Auger lines can be also used to find the chemical state of the compound using the Auger parameter. These Auger lines were easily distinguished from photoemission line by changing the photoemission excitation energy (change of X-ray source Mg Kα to Al Kα). After changing the photoemission energy the Auger lines will stay at same position while photoemission lines will move due to their kinetic energy change. By the combination of both photoemission line and Auger emission line Wanger et al [38] coined the Auger parameter to precisely predict the chemical state of a compound. The Auger parameter is simply defined as the difference in binding energy between two chemical states. The Auger parameter (α) is the sum of the binding energies of the photoemission peak (E(K)$_{BE}$) and the kinetic energy of the Auger emission peak (E(KLL)$_{KE}$) of particular compound. (α = E(KLL)$_{KE}$ + E(K)$_{BE}$). The Auger parameters for all elements and their chemical

compounds were tabulated and graphically present in the Appendix - A of the XPS Hand Book [30]. Detailed investigations of Auger parameters for zinc oxide based compounds were reported by L. S. Dake et al [39].

2.2.7 Depth Profiling and Angled resolved XPS (ARXPS)

Surface sensitive techniques like XPS can still be used to find the chemical composition of thicker films by depth profiling from the surface. This can be achieved, when the surface of the material is removed by etching or ion-bombarding, this makes it possible to examine the underlying layer. If the amount of material being removed can be controlled then it is possible to determine an accurate chemical composition (%) versus depth (m) profile [10]. Normally for *in-situ* XPS depth profiling of materials, Argon ions were used for bombardment of the the sample in a controlled way. By knowing the argon ion sputtering rate and measuring the sample current due to the incidence of the charged ions, it was possible to calculate the rate of removal of material with respect to the sputtering time, but it will vary differently for different material. Then by recording XPS spectra in successive intervals of sputtering time it is possible to give a chemical depth profile of the material.

Another way of doing depth profiling of ultra-thin films is non-destructive angled resolved XPS (ARXPS). This method is also used to estimate the thickness of ultra-thin films. In the photoemission spectroscopy the analyser is kept perpendicular to sample surface in order to capture the photoelectrons coming from maximum sampling depth. As per IMFP, the emitted electrons will escape in the shortest path which is perpendicular to the surface. But to analyse top surface, the sample can be rotated relative to the analyser position in order to detect the electrons emitted at a swallow angle from the top surface. Such a photoemission measurement is illustrated in figure 2.16(a) and the comparative photoelectron spectra in reference to that also shown in figure 2.16(b). From the figure 2.13(a) we can see the electrons emitter form perpendicular to the surface have same sampling depth at angled ($\Theta = 70°$) emission. But the perpendicular depth d_2 will be less than d_1(see figure 2.16). Hence the spectra acquired at angle ($\Theta = 70°$) is more surface sensitive than normal ($\Theta = 0°$). As an evidence for that in figure 2.16(b) the O 1s core level spectra the (ZnO) bulk peak is equal to normal ($\Theta = 0°$) and Angled ($\Theta = 70°$) emissions. Further the (OH) surface peak have high intensity for the angle resolved XPS ($\Theta = 70°$) measurement.

2.2.8 Thickness calculations

XPS can be used to approximately measure the thickness of ultra-thin films or contamination layers on the substrate by comparing the intensity of core level peaks taken from the substrate and over layers respectively. XPS thickness calculations used in this study can be divided into two categories. The overlayer thickness can be estimated based on the suppression of the substrate peak by the presence of an overlayer.

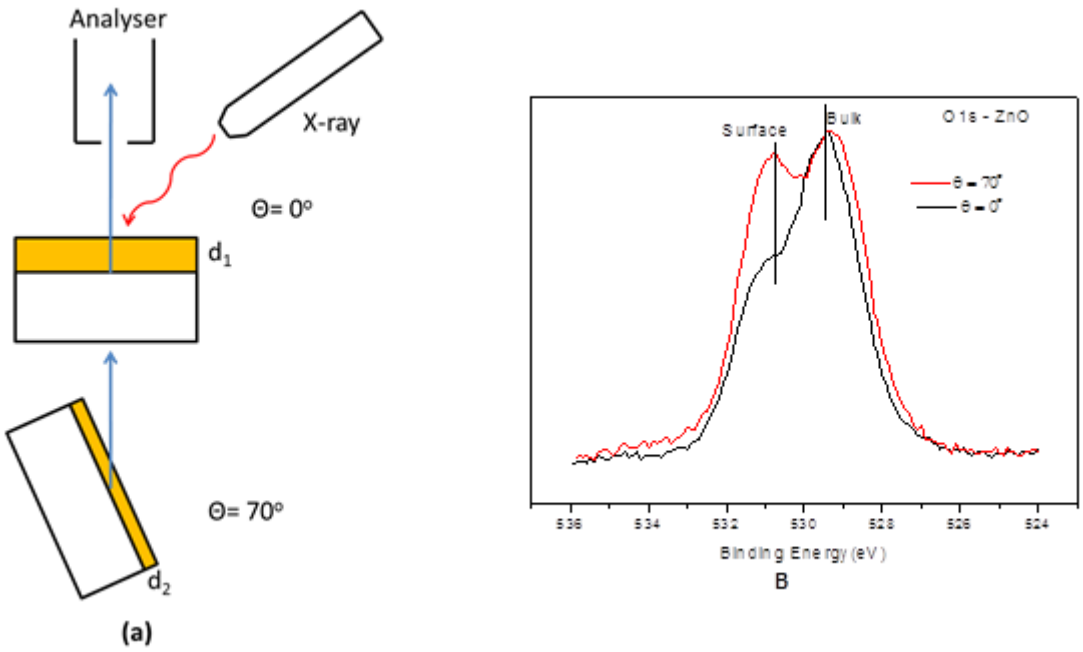

Figure 2.16: (a) The variation of sampling depth with respect to the angle ($\Theta = 70°$) and (b) O 1s spectra taken for OH on ZnO at both normal and angle resolved photoemission.

Alternatively, when the same element is present in distinguishably different chemical environments in the over layers and substrate, the over layer thickness calculations were simplified. In this Thesis, the calculation of thickness was done by the first way, different material overlayer on substrate [28].

For a sample of material A which forms a thin uniform layer of thickness d on a substrate of material S, the following equation can be written for the relative intensity of the substrate I_S and overlayer I_A XPS signals (assuming exponential attenuation of the overlayer) [16].

$$\frac{I_S}{I_a} = \frac{I_A^{\infty}\left\{1 - exp\left[\frac{-d}{\lambda_{A,A}\cos\theta}\right]\right\}}{I_S^{\infty}\left\{1 - exp\left[\frac{-d}{\lambda_{S,A}\cos\theta}\right]\right\}} \tag{2.12}$$

The angle Θ in this equation is the emission angle of the excited electrons and is measured with respect to the surface normal. Factors I_A^{∞} and $I_S^{\infty}$are peak intensities taken from samples of materials A and B of effectively infinite thickness. The parameters $\lambda_{A,A}$ and $\lambda_{S,A}$ are the effective attenuation lengths of electrons emerging from the overlayer and the substrate respectively [40]. The effective attenuation length (EAL) is known to differ from the inelastic mean free path (IMFP) due to elastic-scattering which causes the photoelectrons signal to decay in a non-exponential manner [41] . This variation from the IMFP value is dependent on the composition of the sample but, in general, changes in physical properties such as an increased density will result in a reduction of the EAL. Thickness calculations based on this method can be achieved using software such as NIST Electron EAL Database [35, 42].

2.3 Synchrotron radiation photoemission spectroscopy (SRPES)

Synchrotron radiation photoemission spectroscopy is similar to X-ray photoelectron spectroscopy. The only change is that difference is the photoemission source is synchrotron radiation which can enhances the resolution and surface sensitivity possibly. The important feature of SRPES is the ability to tune the photoemission energy from a few electron volts to thousands of electron volts (22 eV - 2000 eV), which makes it possible to probe the material exclusively and exactly look into one or two atomic layers to several nano metres (1 - 10 nm). In this section the introduction, operation of synchrotron radiation source and determination of surface electronic properties by SRPES were discussed.

2.3.1 Synchrotron Radiation - A Light source

When electrons or other charged particles moving at relativistic speeds (speed of light, c) are forced by magnetic fields (perpendicular to the direction of motion) to follow curved trajectories they emit electromagnetic radiation in the direction of their motion, known as synchrotron radiation. This synchrotron radiation were extremely intense and extends over a wide range from infrared, through the visible the infrared through the visible and ultraviolet, into the soft and hard X-ray regions of the electromagnetic spectrum [43]. The special characteristics of the synchrotron light source are listed below [14]:

- High brightness and high intensity, many orders of magnitude more than with X-rays produced in conventional X-ray tubes
- High brilliance, exceeding other natural and artificial light sources by many orders of magnitude: 3rd generation sources typically have a brilliance larger than 10^{18} $photonss^{-1}mm^{-2}mrad^{-2}0.1\%$BW, where 0.1%BW denotes a bandwidth 10^{-3} centred around the frequency ν.
- High collimation, i.e. small angular divergence of the beam
- Low emittance, i.e. the product of source cross section and solid angle of emission is small
- Widely tunable in energy/wavelength by monochromatization (sub eV up to the MeV range)
- High level of polarization (linear or elliptical)
- Pulsed light emission (pulse durations at or below one nanosecond) Powerful synchrotron radiation techniques with these peculiar characteristics were used to investigate the properties of matter by range of spectroscopic, microscopic and diffraction techniques.

A synchrotron light source consists of the following components: electron gun, linear accelerator, booster, storage ring with array of magnets as illustrated in figure 2.17. The electron emitted from the electron gun were fed into the linear accelerator (linac) where the high energy microwaves and radio waves split the stream into pulses and accelerate the beam to 99% the speed of light [16]. The electrons are then passed into the booster ring, here the electrons will travel in the closed loop as forced by the magnetic field and further the radio waves will increase the speed of electrons close to the speed of light. Now the energy of the electron stream is between 1.5 - 2.9 GeV which is sufficient to produce synchrotron light (electromagnetic wave range of infra-red to hard X-rays). Then, the electron streams are fed into the storage ring which is made up of series of straight tube sections connected in the shape of polygon arrangement. These straight sections have the focusing magnets which keep the electron beam small and more intense, well defined with the brighter radiation.

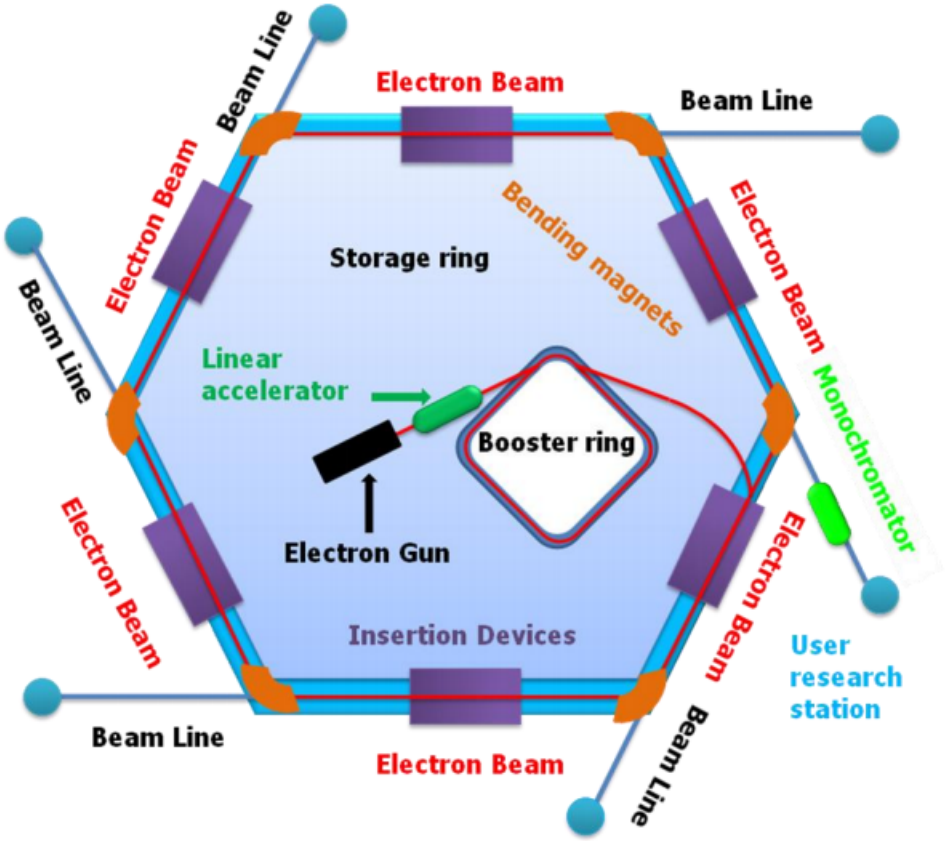

Figure 2.17: (a) Schematic diagram of Synchrotron radiation light source [16].

If undulators are placed in the straight sections they cause the electrons to oscillate and radiate energy before reaching the corner sections of the storage ring [44]. These undulators will generate the highly intense and coherent beam of light. Finally, bending magnets deviate the electrons by several degrees and allow the beam to negotiate the curved corners of the ring. The change in electron momentum which occurs at the

curved corners of the ring results in the tangential emission of a broad spectral range of synchrotron radiation by the electrons [16]. This synchrotron radiation is split into several beam lines for different types of material characterisation techniques. For photoemission spectroscopy technique the monochromators were employed to allow selected photoemission energy to get maximum surface sensitivity and specific photon energy were chosen particular core level based on the XPS parameters.

All synchrotron photoemission experiments for this thesis work were done at the Aarhuas Stroage Ring in Denmark (ASTRID), University of Aarhus. The schematic diagram of ASTRID is shown in figure 2.18 and beam line SX700 was used for all studies. The photon energies were varied between 20 eV to 600 eV to obtain the high surface sensitive spectra for different core levels, valence band and work function of zinc oxide samples.

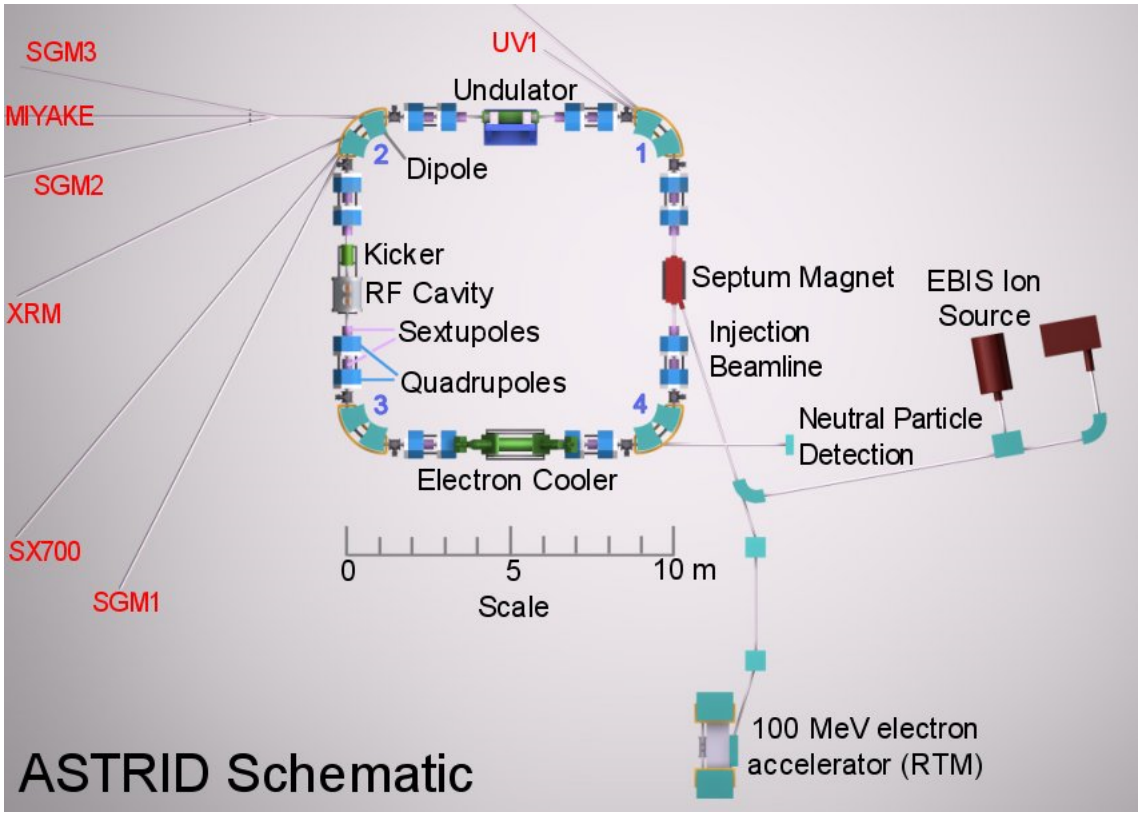

Figure 2.18: Schematic of the ASTRID synchrotron source at the University of Aarhus, Denmark [45].

2.3.2 Determination of energy level band alignment in semiconductor surface

Energy band alignment is the important electronic property of a semiconductor surface, by which only it is able to tell the nature of surface (n-type or p-type) of the semiconductor hetero-structure. For example after depositing a metal contact on a semiconductor surface, by energy band alignment it is possible to find the contact is

either Ohmic or Schottky. The energy band alignment at the interfaces of semiconductors is of direct relevance for the electrical function of electronic devices made with such materials [46]. The key parameters which constitute the energy band alignment are the energy band gap of the material (E_g), Fermi level position (E_F), valence band maximum (E_{VBM}), work function (Φ), electron affinity (χ), vacuum level position (E_{Vac}), etc. Based on the above parameters (obtained by experiment) the energy level band diagram is drawn as shown in figure2.19. The photoemission technique is a straight forward method to measure the Fermi level position, work function and to calculate the other parameters. The UPS and SRPES techniques were used to obtain the energy band alignment of semiconductor surface or interfaces. Since these techniques were more surface sensitive than conventional XPS. Even in UPS the photon energy is fixed (21.2 eV) where as in SRPES the photon energy is tuneable (20 eV 2000 eV) as required for the material and the spectra obtained was in high resolution. The procedure to determine energy band alignment using photoelectron spectroscopy (PES) has been outlined by Waldrop et al [47].

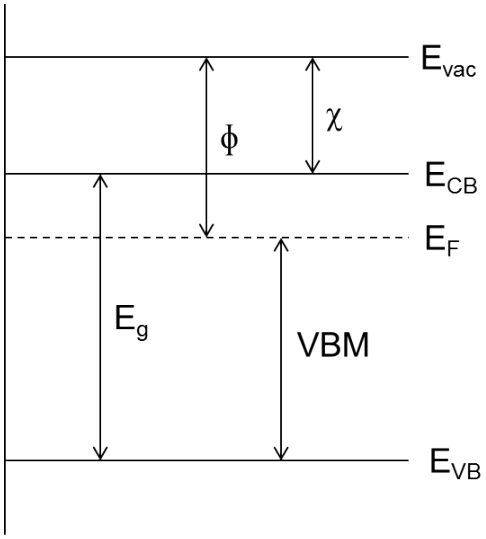

Figure 2.19: Energy level band diagram of a semiconductor surface.

The energy band gap (Eg) and Fermi level position of the bulk semiconductor was determined by the Hall effect measurements [48]. For the surface of the semiconductor the valence band maximum (E_{VBM}) and work function (Φ) were found from photoemission valence band spectra (see figure 2.20).

The binding energy of the photoemission peaks were found with respect to the Fermi level position of the spectrometer. By setting the spectrometer Fermi level position at zero, the lower binding energy offset in valence band spectra is called valence band maximum (E_{VBM}). It corresponds to the difference between the conduction band to the surface Fermi level position (E_{VB} - E_F). The distance from the lower binding energy cut-off to the higher binding cut off is called valence band width (W). The work function value is obtained from the difference of photon energy ($h\nu$) to valence band width (W). Then simple mathematics the electron affinity and surface

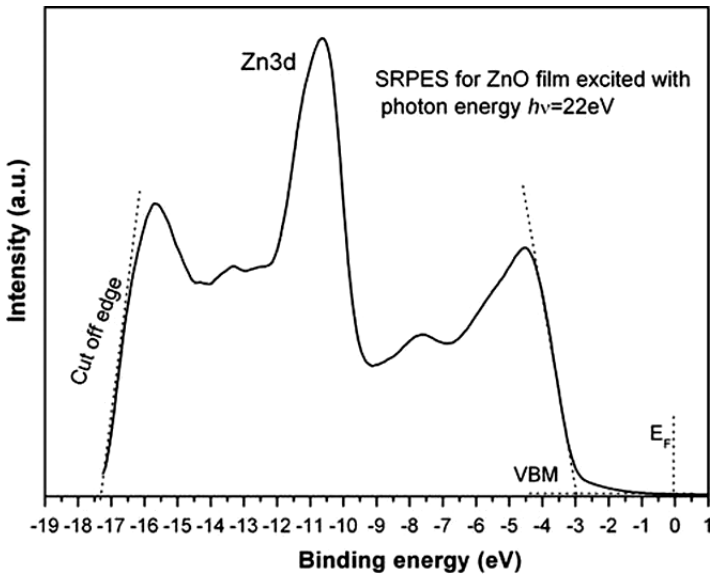

Figure 2.20: Valence band spectra of ZnO surface. [49].

band bending were calculated.

Calculation of parameters for energy level band alignment from photoemission valence band spectra (where LBE is lower binding energy and HBE is higher binding energy)

$$Valence\ band\ maximum\ (E_{VBM}) = E_F - LBE_{cut-off} \tag{2.13}$$

$$Valence\ band\ width\ (W) = HBE_{cut-off} - LBE_{cut-off} \tag{2.14}$$

$$Work\ function\ (\Phi) = h\nu - W \tag{2.15}$$

$$Electron\ affinity\ (\chi) = \Phi - (E_g - E_{VBM}) \tag{2.16}$$

$$Band\ bending\ (BB) = E_g - E_{VBM} \tag{2.17}$$

2.4 Secondary Mass Ion Spectrometry (SIMS)

2.4.1 Principle

Secondary mass ion spectrometry (SIMS) is an analytical technique that can be used to characterize the chemical composition of the surface and near surface ($\approx 30\mu$m) region of solids. The technique uses a beam of energetic (0.5 - 20 keV) primary ions to sputter the sample surface, producing ionized secondary particles that are detected using a mass spectrometer as schematically shown in Fig. 2.11. The primary beams can be O_2^+, O^-, Cs^+, Ar^+, Xe^+, Ga^+. The angle of incidence of the primary beam

with the surface can vary with a typical range from normal to 60° degrees (mostly 45° degrees is used). The sputtering process is not just a surface layer phenomenon but consists of the implantation of the primary species into the sample and the removal of surface atoms by the energy loss of the primary species in the form of a collision cascade. Many secondary species are formed by the interaction of the beam with the sample, but the positive and negative secondary ions are the species of interest for SIMS. The secondary ions are extracted by electric fields and mass analyzed. Detection is done by an electron multiplier, Faraday cup, or an ion sensitive image amplifier for imaging.

2.4.2 Instrumentation

SIMS instruments differ in their complexity, performance, generation and detection of ions, but always contain three basic components:

- A chamber to mount the sample to be analyzed,
- A device to produced primary ions and direct a focused ion beam at the sample,
- A mass spectrometer to separate the secondary ions according to their mass/charge ratio,

The ion optics used to direct the beam to the sample may be able to focus the beam to a diameter as small as 100 nm in some cases, but primary ion beam diameters of 10 to 100 μm are more commonly used. The vacuum in the sample chamber ranges from 10^{-7} mbar to ultra high vacuum (UHV) pressures of 10^{-11} mbar. Mass analyzers for SIMS instruments are any one of three types, namely magnetic sector, quadrupole, or time-of-flight (TOF).

A mass spectrum consists of the secondary ion intensities of the species detected as function of mass which are produced by sputtering a sample. With SIMS, the secondary ion intensities can be measured over a dynamic range as broad as nine orders of magnitude instead of a factor of 100 which is typical for XPS therefore, SIMS spectra are usually displayed on a logarithmic intensity scale and can have significantly enhanced elemental sensitivity compared with almost any other surface analysis technique [50].

Dynamic SIMS involved acquiring SIMS spectra as a function of depth into the material. For rapid data acquisition, only a number of masses are monitored during the etching process rather than acquiring complete spectra. This use of SIMS for depth profiling has become an important method of profiling the composition of multilayer device structures.

2.4.3 Quantification

It has been difficult to provide quantitative results using SIMS. Secondary ion yields for elements can differ by six orders of magnitude for given material or matrix, and can

vary from matrix to matrix [51]. These sensitive variations for the elements cannot be accurately modelled using theoretical models of ion emission. The combination of reference mass spectra and relative sensitive factors (RSF) allows semi-quantitative compositional analysis to be performed.

2.5 Bibliography

[1] Einstein, Ann. Phys., 17 (1905) 132.

[2] http://www.nobelprize.org/nobel$_p$*rizes/physics/laureates*/1918/*planck* − *facts.html*

[3] R. Steinhardt and E. Serfass, X-Ray Photoelectron Spectrometer for Chemical Analysis, Anal. Chem. 23 (1951) 1585.

[4] C. Nordling, E. Sokolowski, and K. Siegbahn, Phys. Rev. 105 (1957) 1676.

[5] http://www.nobelprize.org/nobel$_p$*rizes/physics/laureates*/1981/*siegbahn* − *facts.html*

[6] https://commons.wikimedia.org/wiki/File:ARPESgeneral.png

[7] J. C. Vikerman, Surface Analysis- The Principal Techniques, John Wiley and Sons, 1997.

[8] http://xpssimplified.com/ and J. F. Watts, J. Wolstenholme, An Introduction to Surface Analysis by XPS and AES, John Wiley Sons, 2003.

[9] R. Brindle and A. D. Baker, Electron Spectroscopy: Theory, Techniques and Applications, Vol: 2, Academic Press, 1978.

[10] Stephen McDonnell, Ph.D Thesis, Dublin City University, 2009.

[11] https://commons.wikimedia.org/wiki/File:XPS$_P$*HYSICS.png*

[12] X-ray data booklet - http://xdb.lbl.gov/

[13] http://xpssimplified.com/xray$_g$*eneration.php*

[14] Barrry Brennan, Ph.D Thesis, Dublin City University, 2009.

[15] http://es1.ph.man.ac.uk/research/facilities/HDA.html

[16] Justin Bogan, Ph.D Thesis, Dublin City University, 2010.

[17] C. S. Fadley, Surf. Interface anal., 40 (2008) 1579.

[18] C. S. Fadley, Nucl. Inst. And Meth. A 601 (2009) 8.

[19] C. S. Fadley. J. Electron Spectrosc. Relat. Phenom., 178-179 (2010) 2.

[20] C. S. Fadley , S. Nemsk, J. Electron Spectrosc. Relat. Phenom., 195 (2014) 409.

[21] S. Hofmann, Auger and X-Ray Photoelectron Spectroscopy in Materials Science, Springer-Verlag, Heidelberg, 2013.

[22] C. R. Brundle, Surf. Interface Anal. 42 (2010) 770.

[23] N. Cabuil, A. Le Gouil, O. Doclot, B. Dickson, A. Lagha, M. Amipur, C. Chaton, and J-C. Royer, Solid State Technology, October (2007) 48.

[24] C. T. Larson, E. Gurer, and J. K. Truman, Micro Magazine, April (2005).

[25] C. R. Brundle, G. Conti, P. Mack, J. Electron Spectrosc. Relat. Phenom., 178-179 (2010) 433.

[26] http://www.revera.com/products/veraflex-iii-xf/

[27] B. Pelissier, A. Beaurain, J.P. Barnes,R. Gassilloud,F. Martin,O. Joubert, Microelectr. Eng., 85 (2008) 1882.

[28] Patrick Casey, PhD Thesis, Dublin City University, 2009.

[29] G. Alvarez, H.J. Silverstone, Phys. Rev. A, 40 (1989) 3690.

[30] John F. Moulder, William F. Stickle, Peter E. Sobol, Kenneth D. Bomben, Jill Chastain, Handbook of X-ray Photoelectron Spectroscopy, Perkin-Elmer Corporation, 1992.

[31] A. Herrera-Gmez, A. Hegedus and P. L. Meissner, Appl. Phys. Lett., 81 (2002) 1014.

[32] A. Jablonski and C. J. Powell, Chapter-3, section-3.2.3, E. Wandelt (Ed.), Surface and Interface Science, Vol: 1 Concepts and Methods, Wiley-VCH Verlag, WeinHeim, 2012.

[33] D. Brigggs and J. T. Grant, Surface Analysis by Auger and X-ray photoelectron spectroscopy. IM Publications, 2003.

[34] http://www.lasurface.com/

[35] NIST Electron Effective-Attenuation-Length Database - http://www.nist.gov/srd/nist82.cfm

[36] A. Jablonski and C. J. Powel, J. Alloys Compd. 362 (2004) 26.

[37] http://ulisse.elettra.trieste.it/services/elements/WebElements.html

[38] C.D. Wagner, A. Joshi, J. Electron Spectrosc. Relat. Phenom., 47 (1988) 283.

[39] L. S. Dake, D. R. Baer and J. M. Zachara, Surf. Interface Anal. 14 (1989) 71.

[40] R.G. Vitchev, J.J. Pireaux, T. Conard, H. Bender, J. Wolstenholme, Chr. Defranoux, Appl. Surf. Sci. 235 (2004) 2125.

[41] A. Jablonski, C.J. Powell, Surf. Sci. Rep. 47 (2002) 33.

[42] C. J. Powell, A. Jablonski, W.S.M. Werner, W. Smekal, Appl. Surf. Sci., 239 (2005) 470.

[43] S. Mobilio, F. Boscherini and C. Meneghini, (eds.), Synchrotron Radiation, Basics, Methods and Applications, Springer-Verlag, Heidelberg, 2015.

[44] Wiedemann, Synchrotron Radiation, Springer, 2003.

[45] http://www.isa.au.dk

[46] A. Klein, Thin Solid Films, 520 (2012) 3721.

[47] J. R. Waldrop, R.W. Grant, S.P. Kowalczyk, E.A. Kraut, J. Vac. Sci. Technol. A 3 (1985) 835.

[48] S. M. Sze, Physics of Semiconductor Devices, Wiley, 1964.

[49] C. W. Zou, Y. Y. Wu, B. Sun, W. Gao and P. S. Xu, Surf. Interface Anal. 39 (2007) 865.

[50] F. A. Stevie and D.P. Griffs, Appl. Surf. Sci., 255 (2008) 1367.

[51] C. W. Magee, R. G. Wilson, F. A. Stevie, Secondary Ion Mass Spectroscopy A practical handbook for depth profiling and bulk impurity analysis, John Wiley Sons, 1989.

References for Table 2.1(a)Different types of Photoemission spectroscopy based materials characterisation techniques:

1. S. Hofmann, Auger and X-Ray Photoelectron Spectroscopy in Materials Science, Springer-Verlag, Heidelberg, 2013.
2. J. W. Rabalais,"Principles of Ultraviolet Photoelectron Spectroscopy", Wiley, New York, 1977.
3. W. Turner and M. I. Al Jobory,J. Chem. Phys. 37(1962) 3007.
4. D. E. Eastman, W. D. Grobman, J. L. Freeouf, and M. Erbudak, Phys. Rev. B 9 (1974) 3473.
5. K. Kobayashi, M. Yabashi, Y. Takata, T. Tokushima, S. Shin, K. Tamasaku, D. Miwa, T. Ishikawa, H. Nohira, T. Hattori, Y. Sugita, O. Nakatsuka, A. Sakai and S. Zaima, Appl. Phys. Lett. 83 (2003) 1005.
6. K. Kimuraa, J. Electron Spectrosc. Relat. Phenom., 100 (1999) 273.

7. W. Steinmann, Appl. Phys. A 49 (1989) 365.

8. H. Ueba and B. Gumhalter, Prog. Surf. Sci., 82 (2007) 193.

9. E. R. Grant and M. G. White, Nature 354 (1991) 249.

10. K. Kimura, Int. Rev. Phys. Chem., 6 (1987) 195.

11. G. Saathoff, L. Miaja-Avila, M. Aeschlimann, M. M. Murnane, and H. C. Kapteyn, Phys. Rev. A 77 (2008) 022903.

12. D. W. Lindle, O. A. Hemmers, J. Alloys Comp., 328 (2001) 27.

13. R. Z. Bachrach, F. C. Brown and S. B. M. Hagstrm, J. Vac. Sci. Technol. 12 (1975) 309.

14. K. Kobayashia, M. Kobatac, and H. Iwaid, J. Electron Spectrosc. Relat. Phenom., 190 (2013) 210.

15. R. H. Williams, Rep. Prog. Phys. 43 (1980) 1357.

16. D. Lu, I. M. Vishik, M. Yi, Y. Chen, R. G. Moore, and Z-X Shen, Ann. Rev. Condens. Mater. Phys. 3 (2012) 129.

17. J. Avila, I. Razado, S. Lorcy, R. Fleurier, E. Pichonat, D. Vignaud, X. Wallart and M. C. Asensio, Sci. Rep., 3 (2013) 2439.

18. E. Kisker, J. Phys. Chem 87 (1983) 3597.

19. P. D. Johnson, Rep. Prog. Phys., 60 (1997) 1217.

20. C. J. Bloomfield, J. Electron Spectrosc. Relat. Phenom., 143 (2005) 241.

21. S. Hfner (Ed.), Very High Resolution Photoelectron Spectroscopy, Lecture Notes in Physics - 715, Springer, Heidelberg, 2007.

22. S. Imada, A. Sekiyama and S. Suga, J. Phys.: Condens. Matter 19 (2007) 125204.

23. J. Feng, and A. Scholl, Photoemission Electron Microscopy (PEEM), in: P. W. Hawkes, and J. C. H. Spence (Eds.) Science of Microscopy, Springer, New York, 2007.

24. J-W. Chiou and C-H. Chen, Scanning Photoelectron Microscopy for the Characterization of Novel Nanomaterials, in: J. Guo (Ed.) X-Rays in Nanoscience: Spectroscopy, Spectromicroscopy, and Scattering Techniques, Wiley-VCH, 2010.

25. E. V. Shalaeva and M. V. Kuznetsov, J. Struct. Chem. 44 (2003) 465.

26. D. P. Woodruff, Appl. Phys. A 92 (2008) 439.

27. J. J. Barton, Phys. Rev. Lett., 61 (1988) 1356.

28. S.-H. Yang, B. S. Mun, A. W. Kay, S.-K. Kim, J.B. Kortright, J.H. Underwood, Z. Hussain, C.S. Fadley, Surf. sci., 461 (2000) L557.

29. S. Hellmann, C. Sohrt, M. Beye, T. Rohwer, F. Sorgenfrei, M. Marczynski-Buhlow, M. Kallane, H. Redlin, F. Hennies, M. Bauer, A. Fohlisch, L. Kipp, W. Wurth, and K. Rossnagel, New J. Phys., 14 (2012) 013062.

30. A. Stolow, A. E. Bragg and D. M. Neumark, Chem. Rev., 104 (2004) 1719.

31. A. L. Cavalieri, N. Muller, Th. Uphues, V. S. Yakovlev, A. Baltuska, B. Horvath, B. Schmidt, L. Blumel, R. Holzwarth, S. Hendel, M. Drescher, U. Kleineberg, P. M. Echenique, R. Kienberger, F. Krausz1, and U. Heinzmann, Nature 449 (2007) 1029.

32. A. Baraldi, G. Comelli, S. Lizzit, M. Kiskinova, G. Paolucci, Surf. Sci. Rep., 49 (2003) 169.

33. R. H. Williams, G. P. Srivastava and I. T. McGovern, Rep. Prog. Phys. 43 (1980) 1357.

34. C. S. Fadley, Prog. Surf. Sci. Rep., 16 (1984) 275.

35. X-B Wang, and L-S Wang, Rev. Sci. Instrum., 79 (2008) 073108.

36. B. Winter, Nucl. Instr. and Meth. Phys. Res. A, 601 (2009) 139.

37. Y. Yamashita, K. Ohmori, S. Ueda, H. Yoshikawa, T. Chikyow, K. Kobayashi, e-J. Surf. Sci. Nanotech., 8 (2010) 81.

38. M. Salmeron and R. Schlgl, Surf. Sci. Rep., 63 (2008) 169.

39. F. Mangolini, J. hlund, G. E. Wabiszewski, V. P. Adiga, P. Egberts, F. Streller, K. Backlund, P. G. Karlsson, B. Wannberg and R. W. Carpick, Rev. Sci. Instrum. 83 (2012) 093112

40. J. Kawai, J. Electron Spectrosc. Relat. Phenom., 178-179 (2010) 268.

41. T. Jach and E. Landree, J. Surf. Anal., 9 (2002) 339.

42. F. Sette, P. Perfetti, F. Patella, C. Quaresima, C. Capasso, M. Capozi, and A. Savoia. Phys. Rev. B 28 (1983) 4882.

43. A. Sekiyama, T. Iwasaki, K. Matsuda, Y. Saitoh, Y. nuki, and S. Suga, Nature, 403 (2000) 396.

44. A. Kay, E. Arenholz, S. Mun, F. J. Garca de Abajo, C. S. Fadley, R. Denecke, Z. Hussain, M. A. Van Hove, Science, 281 (1998) 679.

45. V. V. Afanas'ev, Internal Photoemission Spectroscopy: Principles and Applications, Elsevier, Amsterdam, 2008.

46. N. V. Smith, Rep. Prog. Phys. 51 (1988) 1227.

47. P. G. Wenthold and W. C. Lineberger, Acc. Chem. Res., 32 (1999) 597.

Chapter 3

Experimental Details

This chapter describes the ultra-high vacuum (UHV) systems employed in the experimental studies, the surface cleaning methods used on ZnO surfaces and the ZnO sample growth and deposition methods investigated in this work.

3.1 Ultra High Vacuum Systems

In surface science, the experimental study of an atomically clean surface requires a vacuum environment to minimise the interaction of foreign gas molecules which potentially alter the surface composition and geometric structure. The exposure of a clean surface to atmospheric conditions quickly leads to the absorption of carbon and oxygen based contaminants. It is therefore necessary to undertake surface cleaning and subsequent experimentation in a vacuum environment. Generally the concept of vacuum was understood in terms of molecular density, mean free path and time constant to form a monolayer [1]. In ultra high vacuum conditions, inside the vacuum chamber the molecular density is very low which results in the mean free path of the electrons being very high. The operation of x-ray source, ion-source, e-beam evaporators, and spectrometers all needs vacuum conditions [2]. The pressure in a vacuum chamber lower than 10^{-9} mbar is classified as being in the ultra-high vacuum (UHV) range. In this work, different vacuum systems were used based on the required surface characterisation, surface processing and other capabilities.

3.1.1 XPS system 1

The XPS system 1 is an ESCALAB model manufactured by Thermo Fisher Scientific and is shown in figure 3.1. This system consists of three vacuum chambers, a fast entry load lock chamber pumped by a rotary pump with a base pressure of 10^{-3} mbar which is used to load samples. The preparation chamber is diffusion pumped ($>10^{-6}$ mbar) and has a heating stage allowing controlled annealing of samples up

to 500 °C. The analyser chamber has a base pressure of 10^{-9} mbar and is equipped with a twin anode x-ray source (Al and Mg kα) with a VG CLAM 2 hemispherical electron energy analyser with a triple channeltron electron multiplier detector. The analysis chamber also has argon bombarding facilities for surface cleaning applications. Normal operation involves inserting a sample into the load lock and after 30 minutes it can be transferred to the preparation chamber and then into the analysis chamber. UHV is achieved in the analysis chamber by bake out for 12 hours at 150 °C. This system was used to undertake basic XPS studies of the characterisation of different ZnO samples and *ex-situ* surface cleaning investigations of ZnO surfaces.

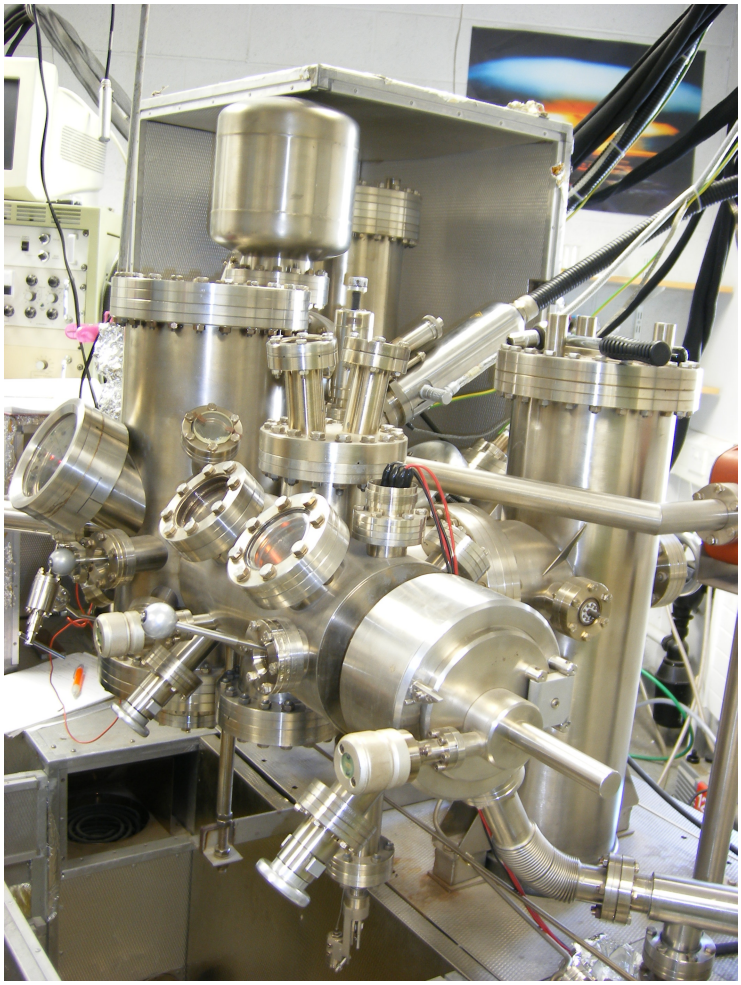

Figure 3.1: XPS system 1 showing the fast entry load lock, preparation and analysis chambers.

3.1.2 XPS system 2

The XPS system 2 shown in figure 3.2 is used for *in-situ* surface preparation, thin film deposition and surface characterisation. It consists of the two chambers, a small fast entry load lock equipped with a turbomolecular pump backed by a rotatory pump with a base vacuum of 10^{-6} mbar. The main chamber is also equipped with a rotary backed turbomolecular pump and a titanium sublimation pump with a base

pressure in the order of 10^{-10} mbar. The chamber is equipped with a twin anode (Al and Mg) x-ray source, a VG CLAM 2 electron analyser, e-beam evaporator, mass spectrometer, and a thermal gas cracker. The annealing of samples is carried out by using a sample holder with an internal resistive heater capable of heating up to 700 °C which was calibrated using a thermocouple. The atomic hydrogen / oxygen cracker was employed for surface cleaning of semiconductor surfaces. The multi-pocket mini e-beam evaporator was used to deposition different metals and metal oxides. The annealing studies of zinc metal and atomic hydrogen cleaning studies of ZnO were carried out in this system.

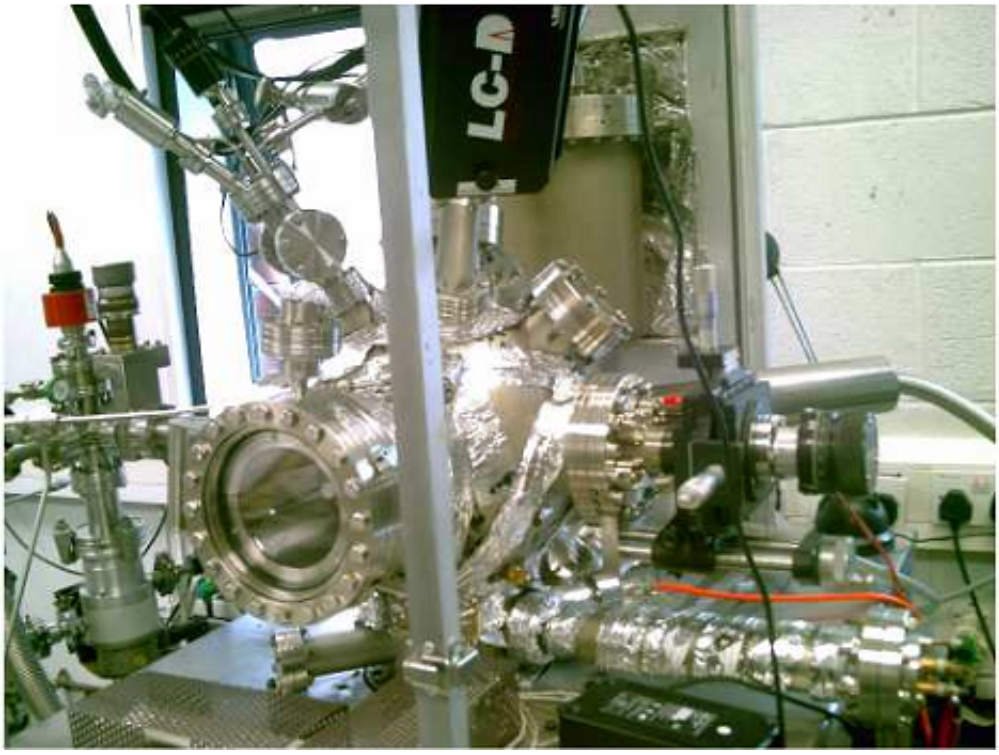

Figure 3.2: XPS system 2 which has the following additional components, e-beam evaporator, thermal evaporator, mass spectrometer, and thermal gas cracker

3.1.3 SIMS systems

The SIMS system (manufactured by Hiden Analytical Ltd) shown in figure 3.3 was used for depth profile analysis of semiconductor materials. The SIMS chamber was pumped by a turbo molecular pump backed by a rotary pump and routinely operated at an ultra high vacuum pressure of 10^{-9} mbar. The chamber contains an IFG200 ion gun, quadrupole mass spectrometer and a sample holder. The E-beam grown ZnO thin films were characterised by SIMS.

Figure 3.3: The SIMS vacuum system

3.1.4 SX700 Synchrotron Radiation Photoemission vacuum system

SX700 is a photoemission beamline (shown in figure 3.4) at the ASTRID synchrotron, Institute of Storage Ring (ISA), University of Aarhus, Denmark. The UHV system on this beamline shown in figure 3.5 consists of load lock and an analysis chamber which has a base pressure of 2 x 10^{-10} mbar. The analysis chamber has a VG CLAM 2 electron energy analyser and a sample holder with e-beam bombardment capable for heating the sample to high temperatures (<1100 °C). The atomic hydrogen cleaning and high temperature oxygen annealing studies of ZnO crystals were performed in this system.

3.2 Surface cleaning methods

The main goal of this work is the development of surface cleaning procedures for ZnO surfaces. Both *ex-situ* and *in-situ* surface cleaning methods were investigated including modifications of wet chemical cleaning treatments previously reported

3.2.1 Ultrasonic organic solvent cleaning

ZnO surfaces have a strong tendency to adsorb ambient contaminants such as carbon and water. The organic solvents were chosen to remove the carbon and hydroxide re-

Figure 3.4: SX700 beamline at the ASTRID synchrotron [3]

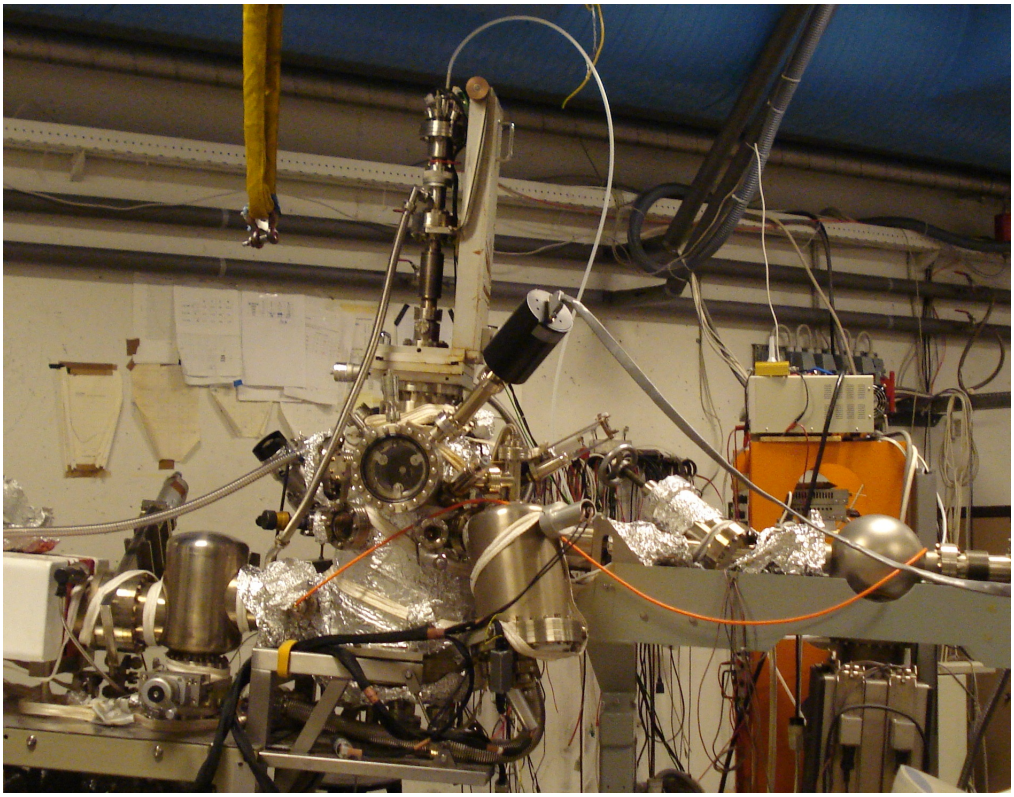

Figure 3.5: UHV photoemission system on the SX700 beamline

lated species. These solvent cleaning results will be reported in Chapter 6. Firstly, the as received ZnO crystals (purchased from Crystal GmbH, Germany) were immersed in acetone ultrasonic bath for 10 minutes to remove organic contamination. Secondly, the crystals were treated in dimethyl sulfoxide (DMSO) in an ultrasonic bath for 10 minutes to remove polar organic contaminants. Thirdly, crystals were ultrasonically cleaned with toluene to remove non-polar organic and water based contaminants. After each solvent treatment the ZnO crystals were blown dry with nitrogen gas and immediately loaded into the vacuum. This study of the effectiveness of organic cleaning was performed by both investigating the changes in chemical composition resulting from the individual treatments and the combined effect of all the organic cleaning steps as shown in figure 3.6.

Seperate Cleaning:

$$Acetone^{Ultrasonic}_{10\ minites} + N_2 drying + vacuum_{3\ hours} ==\gg XPS$$

$$DMSO^{Ultrasonic}_{10\ minites} + N_2 drying + vacuum_{3\ hours} ==\gg XPS$$

$$Toluene^{Ultrasonic}_{10\ minites} + N_2 drying + vacuum_{3\ hours} ==\gg XPS$$

Continuous Cleaning:

$$Acetone^{Ultrasonic}_{10\ minutes} + N_2\ drying + DMSO^{Ultrasonic}_{10\ minutes} + N_2\ drying + Toluene^{Ultrasonic}_{10\ minutes} + N_2\ drying + Acetone^{Ultrasonic}_{10minutes} + N_2\ drying + Vacuum_{5\ hours} == \gg XPS$$

Figure 3.6: Systematic organic solvent cleaning in represented equation format

3.2.2 Atomic hydrogen and oxygen cleaning

The atomic hydrogen cleaning is one of the established *in-situ* surface cleaning techniques for semiconductors like Si, Ge, and III-Vs. Exposure of a surface in vacuum to atomic hydrogen or oxygen at elevated temperature can result in the efficient removal of carbon contamination and surface localised oxides at lower temperatures than thermal annealing alone. The UHV compatible thermal gas cracker used in this project to prepare ZnO surfaces is shown in figure 3.7.

This Oxford Applied Research® thermal gas cracker (TC-50) can efficiently produce the required amount of atomic hydrogen at a power setting of 60 W. The operation of thermal gas cracker is schematically shown in figure 3.8. Hydrogen gas at a background pressure of 1 x 10^{-7} mbar, is passed through a fine bore capillary tube which is connected directly to the gas inlet line. This confines and minimises

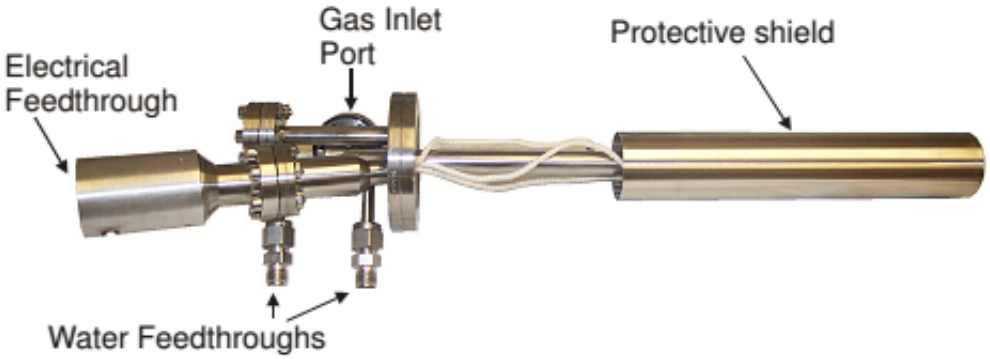

Figure 3.7: TC-50 Thermal gas cracker [5]

the gas flow while also providing a large surface area and path length for the gas, increasing the efficiency of the cracking process. The capillary tube is held at 1 kV so that electrons from a filament at earth potential in close proximity to the tube are accelerated towards it, generating temperatures of 1000 °C. An emitted beam current of 65 mA, allows for a maximum power output of ≈65 W. The power is kept constant throughout by adjusting the temperature of the filament with a feedback loop. Hydrogen molecules impacting on the walls of the capillary are thermally dissociated, achieving atomic fractions of ≈ 50%. This atomic flux is then incident on a sample held at elevated temperature (typically 200 °C - 500 °C), for periods of time up to a few hours. The body of the cracker is water cooled to reduce the thermal strain on the UHV system and prevent out gassing.

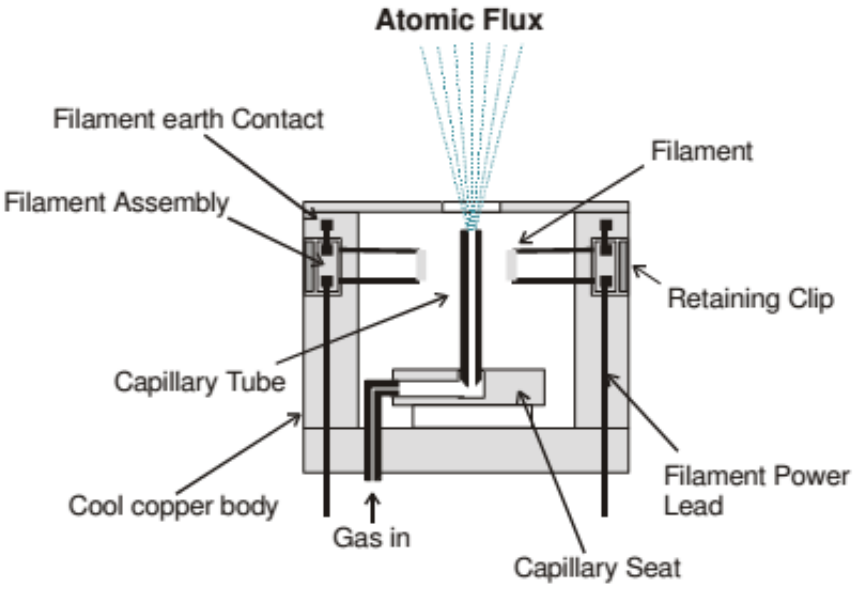

Figure 3.8: Schematic diagram showing the operation of the TC 50 thermal gas cracker system used to produce atomic hydrogen [5]

3.2.3 High temperature oxygen annealing

Annealing a contaminated surface in an oxidizing atmosphere can be effective at removing surface carbon. In chapter 7, high temperature (up to 1000 °C) oxygen annealing was carried out on the four different crystallographic surfaces of ZnO studied in this work. These experiments were carried out at the synchrotron beamline SX700 using high purity oxygen gas.

3.3 ZnO growth and thin film deposition details

In this part of the work, different growth methods were used to deposit ZnO thin films and nanostructures as outlined below.

3.3.1 E-beam deposition of ZnO thin films

E-beam deposition is a form of physical vapour deposition in which a target anode is bombarded with an electron beam generated by a heated tungsten filament under high vacuum. The focussed electron beam generates sufficient heat to cause atoms from the target material to evaporate. These atoms then deposit in solid form, coating everything in the vacuum chamber in line of sight of the source with a thin layer of the anode material as schematically shown in figure 3.9. E-beam evaporation is characterised by high deposition rates from 1.7 nm/s to 170 nm/s, with very high material utilization efficiency.

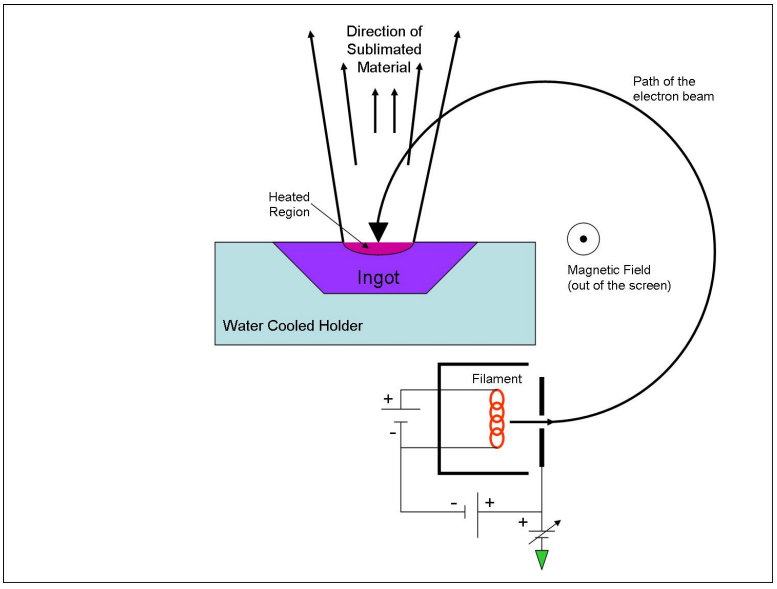

Figure 3.9: Operation of e-beam evaporation [6]

A Leybold Univex deposition chamber was utilized for e-beam deposition (see figure 3.10) and a water cooled quartz crystal thin film thickness monitor was used to determine the deposited film thickness. The ZnO thin films were e-beam deposited from ZnO (99.9%) pure pellets onto silicon substrates. The 4 inch silicon Si(111)

wafer covered by native oxide was cleaned by sequentially immersing the wafer in acetone, methanol and isopropanol in an ultrasonic bath and then dried in flowing nitrogen before being placed in the deposition chamber. The rate of ZnO deposition could be varied between 0.5 $Å s^{-1}$ to 0.7 $Å s^{-1}$ depending on the emission current. The total thickness of the deposited layer as estimated from the quartz thickness monitor to be ≈54 nm. For the SIMS characterisation studies of these materials, ZnO thin films were grown separately using the same deposition method.

Figure 3.10: The e-beam deposition chamber

3.3.2 Pulsed laser depositions of ZnO Thin films

ZnO thin films were grown in a conventional pulsed laser deposition (PLD) apparatus containing a frequency-quadrupled Nd:YAG laser (λ = 266 nm, τ = 6 ns) operated at 10 Hz which provides 140 mJ of laser light energy. The laser targets were made of sintered ZnO powder (99.99%) in 2.54 cm diameter disks. The base pressure of the chamber was 2 x 10^{-8} mbar and 5N-pure oxygen is introduced into the chamber at a rate of ≈40 sccm creating a background pressure of ≈0.1 mbar. Thin films were grown at a laser fluence of 2 Jcm^{-2} and required 4800 shots. All the samples were grown at a substrate temperature of around 700 °C. After growth, the samples were *in-situ* annealed in oxygen atmosphere and subsequently cooled at a rate of 1.0 $°Cs^{-1}$ [7].

3.3.3 ZnO nanorods by VPT method

The vapour phase transport (VPT) is a simple synthesis method widely used for the growth of ZnO nanostructures. In this method, vapour of Zn and oxygen is transported over a sapphire substrate where they react to form ZnO nanorods. There are various growth mechanisms in the VPT method, like direct decomposition of the growing material or using a catalyst for vapour reaction. In this work a vapourliquidsolid (VLS) mechanism [8] was used to grow ZnO nanorods and the experimental setup used is shown in figure 3.11.

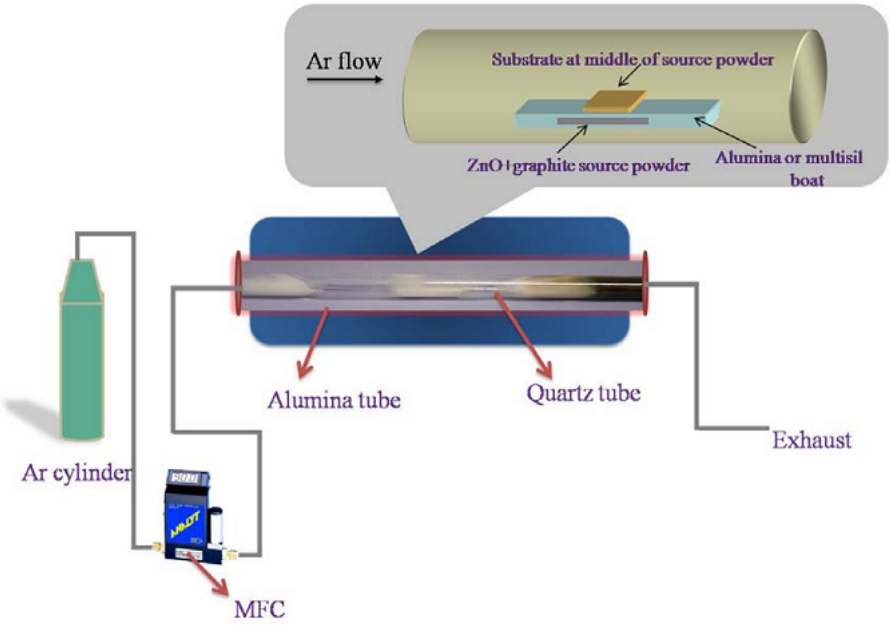

Figure 3.11: Vapour Phase Transport set up for ZnO nanorod growth [9]

Initially, ≈5 nm thin film of Au was thermally deposited on the sapphire substrate as a catalyst metal to initiate nanorod growth. This sample was placed in a tube furnace along with a mixture of graphite and ZnO powder. With an argon flow of 90 sccm and the furnace heated up to ≈900 °C, the Zn vapour forms a Au/Zn alloy which becomes supersaturated resulting in the precipitation of Zn which reacts with oxygen to form ZnO nanorods. By the continuation of this process, the alloy droplet are displaces to the top and the nanorod grows perpendicular to the substrate. A typical growth run duration is 60 minutes with the source of oxygen from the residue oxygen partial pressure in the chamber.

For XPS characterisation, ZnO nanorods were grown on a-plane (11-20) sapphire substrates (1 cm x 1cm). The crystalline nature and texture of the as grown nanorods was characterised by XRD. The result shows nanorods were single crystal with (0002) c-plane orientation. The growth of well aligned straight nanorods with gold on top was also confirmed by SEM morphological studies.

3.4 Bibliography

[1] K. Oura, V. G. Lifshits, A. A. Saranin, A. V. Zotov, M. Katayama, Surface Science - An Introduction, Springer-Verlag, 2003.

[2] J. C. Vikerman, Surface Analysis - The Principal Techniques, John Wiley and Sons, 1997.

[3] http://www.isa.au.dk/photos/photos.asp

[4] J. Dumont, T. Seldrum, S. Couet, C. Moisson, D. Turove, R. Sporken, J. Vac. Sci. Technol. B, 24 (2006) 2124.

[5] Handbook TC-50 Operation and Maintenance (ver 2.1), Oxford Applied Research (www.oaresearch.co.uk).

[6] http://en.wikipedia.org/wiki/Electron beam physical vapor deposition

[7] R. OHaire, A. Meaney, E. McGlynn, M.O. Henry, J.-R. Duclre, and J.-P. Mosnier, Superlatt. Microstruct., 39 (2006) 153.

[8] R. S. Wagner and W. C. Ellis, Appl. Phys, Lett., 4 (1964) 89.

[9] Mahua Biswas, PhD Thesis, Dublin City University, 2010.

Chapter 4

XPS characterisation of differently prepared ZnO surfaces

4.1 Introduction

The surface science of ZnO has become an important field of research due to different chemical and physical properties of its polar and non-polar surfaces [2, 33] as outlined in chapter 1. The adsorption of surface contaminants on ZnO surfaces especially hydroxyls (OH), hydrocarbons (CH) and water during air exposure significantly influence its properties. Application of ZnO surfaces in a wide range of devices from microelectronics to gas sensors [3] requires a deep understanding of ZnO surface behaviour. In nanostructured ZnO, the small length scale and large surface-to-volume ratio mean that surface effects play a stronger role in controlling the observed properties than for dense materials. The physics and chemistry of the ZnO surface has been comprehensively reviewed by Woll [3].

Photoemission studies of ZnO have been reported by many researchers since 1973 [4]. Due to the recent developments in novel growth techniques highly stoichiometric ZnO crystals have been grown by hydrothermal seeded chemical vapour (SCVT), pressurized melt growth and the Bridgman method [5]. 2D ZnO thin films have been grown by e-beam evaporation, RF magnetron sputtering, chemical vapour deposition (CVD), molecular beam epitaxy (MBE) and pulsed laser deposition (PLD) [6], 3D ZnO nanorods have been grown by metalorganic chemical vapour deposition (MOCVD), vapour phase epitaxy (VPE), pulse laser deposition (PLD), vapour-liquid-solid (VLS), aqueous chemical growth (ACG) and electro-deposition techniques [7]. A primary aim of the present study is to evaluate and generate the reference photoemission spectra for the different ZnO surfaces. A number of previous X-ray photoelectron spectroscopy studies for ZnO [8–14] have been reported.

In this work XPS measurements have been undertaken for a range of different ZnO

samples including single crystals, powders, thin film and nanorods. Angle resolved XPS (ARXPS) was employed for nanorods in an attempt to distinguish the photoemission spectra acquired from the top polar surface and hexagonal non-polar sides. The core level spectra of Zn 3d, Zn 2p, O 1s and C 1s were analysed. The binding energy referencing and curve peak fitting were optimised based on standard photoemission spectra from the NIST database [16] and the XPS handbook [17]. These core level spectra were peak fitted to precisely identify the different chemical species present on the surface of the ZnO samples.

4.2 Experimental

4.2.1 Materials

Zinc metal

Reference spectra of zinc metal of purity 99.99% were acquired for a native oxide covered sample and following the mechanical removal of the surface oxide immediately prior to being inserted into the XPS vacuum system. The XPS scans were record for as loaded and vacuum annealed at 100 °C conditions. A zinc metal sample was also subjected to an IPA ultrasonic before being loaded into the vacuum system and annealed at 200 °C for 30 minutes.

ZnO crystals

Four different crystallographic faces of ZnO single crystals, namely the polar Zn and O terminated (0001)-Zn, (000-1)-O surfaces as well as the non-polar (10-10) and (11-20) surfaces, all hydrothermal grown were investigated by XPS measurements as a function of organic solvent cleaning.

ZnO thin films

The PLD growth details of ZnO thin films were described in Chapter 3. ZnO thin films ≈54 nm thick were grown on a silicon dioxide surface by e-beam deposition. The silicon dioxide substrates were cleaned prior to ZnO deposition with acetone, methanol and isopropanol. After deposition films were exposed to air for approximately 10 minutes before being loaded into the XPS system for analysis.

ZnO Pellets

ZnO pellets were also obtained by compressing 99.99% pure ZnO powder (purchased from Sigma-Aldrich Inc, Ireland) into a pellet and further annealed in tube furnace at 400 °C for 1 hour.

ZnO nanrods

Well aligned ZnO nanorods were grown on sapphire substrates by the vapour phase transport (VPT) method as previously reported [18]. The growth details were de-

scribed in chapter 3. For ZnO nanorods, photoemission spectra were acquired at a range of angles between 0° and 60° in steps of 15° to study the angular dependence of the photoemission signals.

4.2.2 XPS characterisation

All XPS spectra were recorded by a VG photoelectron spectrometer using Al-Kα radiation (1486.6 eV) as the X-ray excitation source at a pressure of 10^{-9} mbar. The diameter of the x-ray radiated area was approximately 10 mm and the pass energy of the analyser was set at 20 eV yielding an energy resolution of approximately 1.0 eV. The spectrometer was calibrated by using the photoemission lines of Au (Au 4f7/2 = 84.09 eV, with reference to Fermi level) for the Au 4f7/2 line, the full width at half maximum (FWHM) was 1.02 eV. The calibration of binding energy scale was performed with the C 1s line (285 eV) from the carbon contamination layer. The XPS core levels were analyzed by using AAanlyser [19] in which a Shirley background is assumed and peak fitting of experimental curves were defined by mixed singlet combination of Gaussian and Lorentzian line shapes. The XPS atomic concentrations of Zn, O and C were computed from measuring the area under the fitted photoemission peaks and dividing this area by the relative sensitive factors (Zn: 3.354; O: 0.711; C: 0.296) [17].

4.3 XPS results

4.3.1 Native oxide on zinc metal

XPS is a suitable tool to investigate the oxidation state of metal and semiconductor surfaces [20,21]. Surface oxides will readily form on a clean znic metal surface due to the reactivity of (zinc metal) Zn^{2+} ions with moisture or atmospheric oxygen. The native oxide on zinc metal surfaces is widely used as protective coating for corrosion prevention. In XPS analysis, the oxidation state of a transitional metal can in principle be determined from the 2p core level binding energy. But the change in binding energy of the 2p peak for metallic zinc, partially oxidised zinc, fully oxidised zinc oxide and zinc hydroxide is very small. Therefore careful XPS studies of binding energy positions for metallic Zn, ZnO, $Zn(OH)_2$ are needed and will be compared with previously studies [9, 12, 22–25]. The main aim of this initial work on Zn native oxide is to evaluate the binding energy position of the native oxide states on ZnO and determine the peak fitting parameters and the stoichiometry of the native oxides on Zn metal.

The survey spectra for the differently prepared zinc metal surfaces are shown in figure 4.1 with the core level peaks of Zn 3d, Zn 3p, Zn 3s, Zn 4s, C 1s, O 1s, and Auger peak Zn LMM identified. The binding energy of these peaks are in agreement with the reported reference values for ZnO [17, 26] and are displayed in Table 4.1.

The zinc metal which initially cleaned by iso-propanol and annealed after having high amount of carbon contamination when compared to scraped samples. In all four samples presence of O 1s peak shows existence of ZnO on zinc metal. Even after annealing up to 200 °C no more desorption of oxygen is seen.

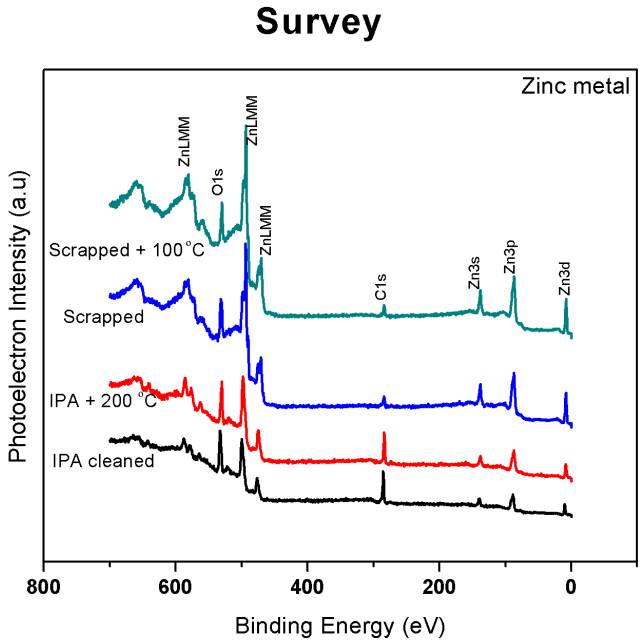

Figure 4.1: Survey spectra of zinc metal with native oxide (1) IPA cleaned, (2) IPA clean with 200 °C annealing, (3) scraped and (4) scraped after 100 °C annealing.

In Figure 4.2 Zn 3d is a bulk sensitive core level peak. This peak is deconvoluted into three peaks by peak fitting (1) zinc metal (9 eV) (2) ZnO (10 ± 0.25 eV) (3) $Zn(OH)_2$ (11.3 ± 0.2 eV). It is clearly seen the zinc metal component is prominent in a scraped sample whereas ZnO component is prominent in an IPA cleaned sample. The spectral intensity of scraped sample is due to the clean metal surface is better than IPA cleaned sample haves a high level of contamination. So IPA treatment will lead to oxidation and contamination instead of cleaning the metal surface. In all samples the existence of zinc hydroxide shows adsorption and reaction of moisture on Zn metal surface. Hence the vacuum cleaving will be the best cleaning method for photoemission study of pure zinc metal surface.

Naturally any surface exposed to air or atmosphere will pick up carbon as contamination layer and can be precisely identified by XPS. Carbon C 1s core level spectra are shown in figure 4.3 and the adventitious carbon peak is found at 285 eV for scraped, IPA cleaned and annealed samples. Further peak fitting revealed the existence of carbon monoxide and dioxide binding energy ranges at (287.2 - 286.4 eV) and (289.2 - 289.9 eV) respectively. In both IPA cleaned and scraped zinc metal sample after annealing the reduction of oxygen bonded carbon is observed by shift of peaks to lower binding energy. In general, the scraped sample having less CO and CO_2 than

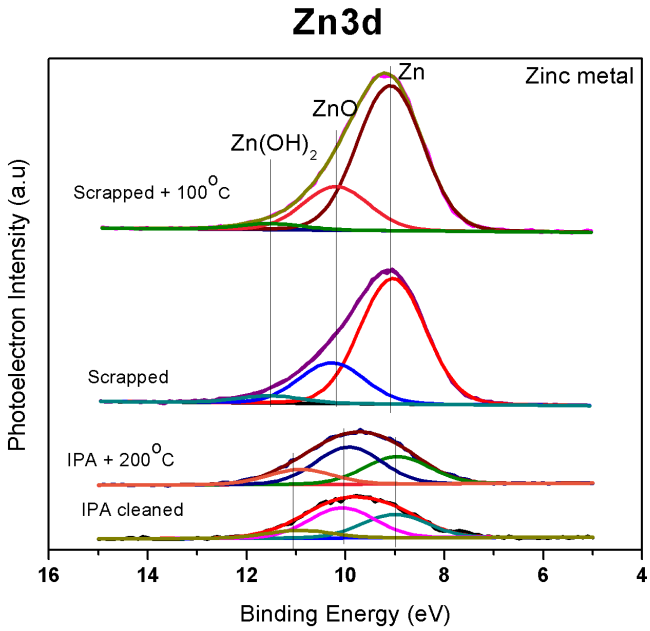

Figure 4.2: Bulk sensitive Zn3d core level spectra for zinc metal both IPA cleaned and scraped.

IPA cleaned sample.

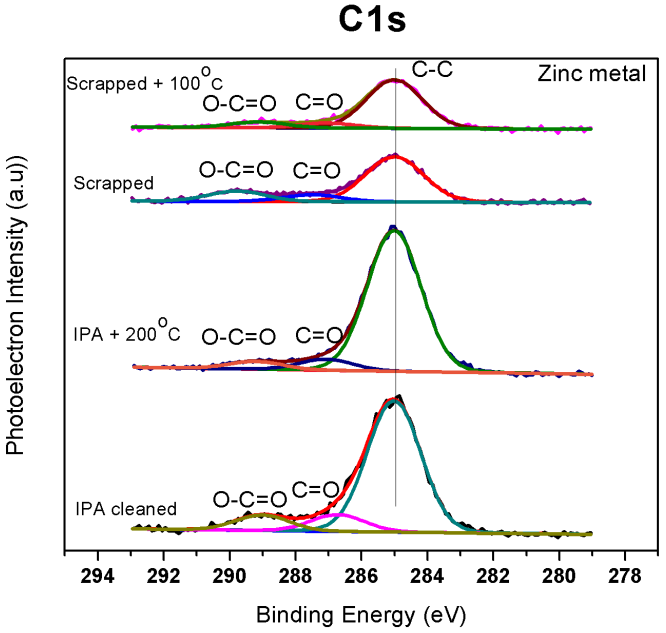

Figure 4.3: Core level spectra for carbon C1s for zinc metal samples.

The Auger peak Zn $L_2M_{45}M_{45}$ obtained for both scraped and IPA cleaned is shown in kinetic energy scale in figure 4.4. It clearly shows the distinction of Zn^0 metallic state and Zn^{2+} oxidised state respectively. In IPA cleaned sample the kinetic energy for ZnO is 988.24 eV and annealing at 200 °C peak moves the feature to 987.77 eV

(K.E.) and is due to further oxidation of Zn atoms. On the other hand the scraped sample peak at 992.91 eV (K.E.) is typical of the zinc metallic state and annealing at 100 °C a movement of the peak to 993 eV shows as it becomes more metallic by desorption of oxygen from zinc. The difference in kinetic energy for Zn to ZnO for the Auger peak is 5 eV. This value is consistent with previously reported XPS studies [10].

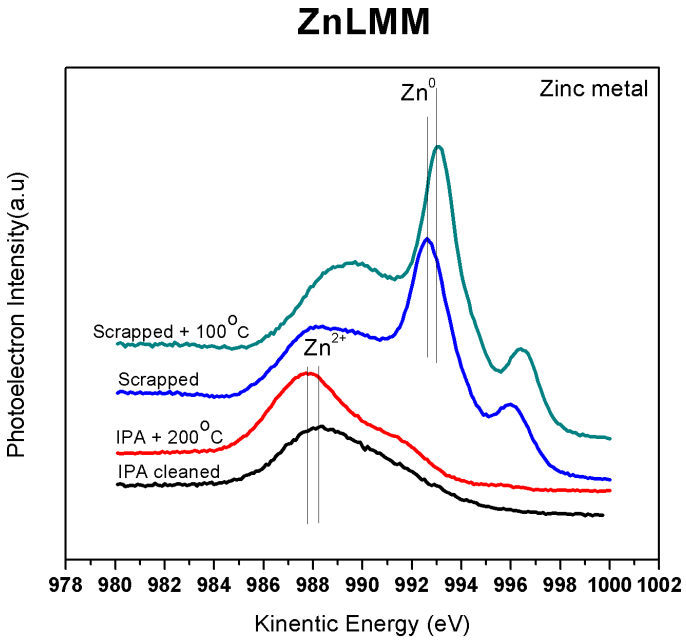

Figure 4.4: Zinc Auger peak Zn $L_2M_{45}M_{45}$ in metallic state for scraped and oxidised state for IPA processed metal sheets.

The oxygen photoelectron feature for zinc oxide in zinc metal is shown in figure 4.5. The position of the zinc bonded oxygen is seen in all spectra at 530.45 eV while the hydroxide is at 532 eV for the scraped sample and 531.76 eV for an IPA cleaned metal. Finally the water as well as carbon bonded oxide is observed at 533.16 eV for scraped, 532.96 eV scraped cum annealed at 200 °C and 533.36 eV for an IPA cleaned. Before annealing on the zinc metal strong coverage of zinc hydroxide is seen for scraped and IPA treated. After annealing the hydroxide was reduced and the ZnO component increases significantly. In all four samples, zinc metal sheets show the presence of ZnO at the surface. The removal of zinc oxide by annealing is not possible here because the melting point of ZnO is 2000 °C while that of zinc metal is 400 °C. So annealing above 200 °C the zinc metal will desorb the Zn atoms from surface.

Zn 2p3/2 core level spectra for the zinc metal sheet is shown in figure 4.6. Because of the surface sensitive peak the chemical composition of the metal surface is revealed here. The large movement of peak positions shows how the surface cleaning as well as annealing influences the surface. The binding energy ranges from as follows (1) zinc metal - 1021.81 eV, (2) ZnO - 1022.53 to 1022.98 eV, (3) $Zn(OH)_2$ - 1023.78 eV to 1024.06 eV and $ZnCO_x$ 1024.96 eV. Similar to the Zn 3p detected an unknown peak

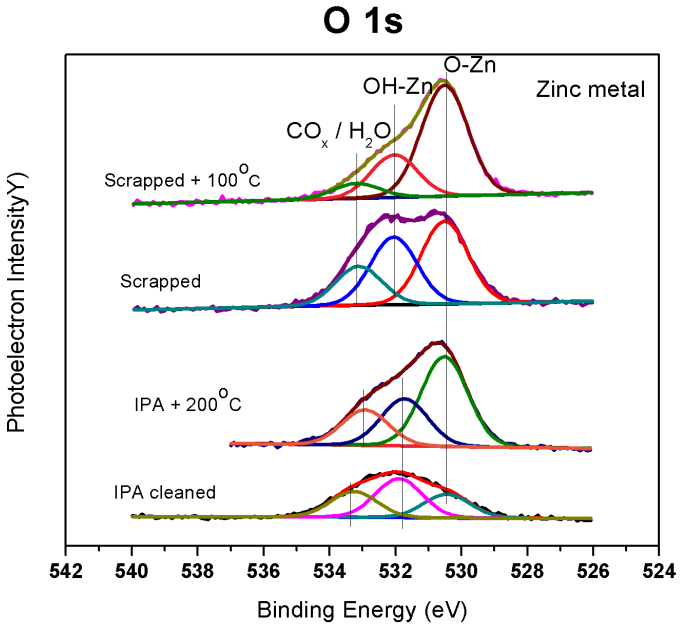

Figure 4.5: O 1s core level spectra for zinc metal sample.

Zn_x is also s-en at a lower binding energy of all XPS spectra. In initial IPA treated spectra $Zn(OH)_2$ and $ZnCO_x$ were seen, further annealing at 200 °C evaporates the of excess hydroxide and the presence of ZnO is observed. In scraped metal similar ZnO and $Zn(OH)_2$ features were seen whereas further annealing at 100 °C leads to the desorption of hydroxide with transformation of zinc metal and ZnO.

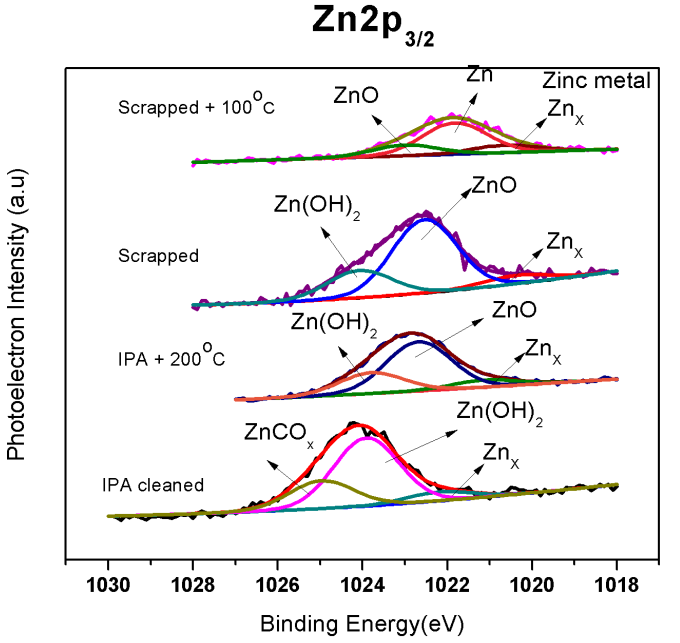

Figure 4.6: Zn 2p3/2 Surface sensitive core level for zinc metal.

4.3.2 ZnO single crystal surfaces, thin films and powders

ZnO single crystal surfaces are of technological importance having a wide range of applications from industrial catalysts to humidity sensing and UV sensors [27]. It has a hexagonal crystal structure with eight outer faces and six inner cut faces (as mentioned in chapter 1). The four crystallographic surfaces (0001)-c plane (top), (000-1)-c plane (bottom), (10-10)-m plane, (11-20)-r plane are the most important for both fundamental studies and for technological applications. Zinc terminated (0001) and oxygen terminated (000-1) surfaces have both semiconductor and optoelectronic device applications [27]. Both surfaces display different chemical and physical properties, while the (10-10), (11-20) surfaces have been used as catalysts for organic chemical manufacturing [28]. A comparative XPS study of these four different ZnO surfaces is presented in this work.

Pulsed laser deposition (PLD) has been shown to be a suitable technique on which to grow ZnO thin films to obtain high stoichiometry with good electrical and optical properties [29]. The strength of PLD growth is that the deposited film directly reflects the chemical composition of the target material. PLD has been used to growth ZnO epitaxial films and nanostructures at room temperature. E-beam deposited ZnO thin films are polycrystalline in nature and are used for making ZnO varistors [27]. XPS comparative study of PLD grown thin films and e-beam grown thin films will give a good understanding of the surface reactivity of ZnO thin films. XPS survey spectra of ZnO single crystals, thin films and powders acquired at normal emission are shown in figure 4.7.

Similar to previous zinc metal survey spectra the peaks for zinc (Zn 3d, Zn 3p, Zn 3s, Zn 2p, Zn-Auger), carbon (C 1s), oxygen (O 1s) were identified in all four polar and non-polar faces, PLD and E-beam grown thin films and pellets. The comparative binding energy value of all peaks was tabulated (Table 1). The survey spectra for the ZnO single crystal surfaces showed in figure 4.7 show low levels of carbon contamination on the O-terminated and (10-10) mixed terminated crystal surfaces. A higher carbon signal was measured on the Zn-terminated (0001) crystal surface which is a naturally more reactive surface. From the survey spectra for ZnO pellets the initial sample spectra show less intensity of all peaks when compared to sintered pellet.

The carbon contamination C 1s core level peak is shown in figure 4.8 for the four single crystal surfaces investigated. The carbon C 1s is peak fitted with three peaks, with the main peak at (285 $\pm$ 0.3 eV) attributed to adventious carbon bonded carbon (C-C) signal which is the reference peak for binding energy calibration. The carbon monoxide (C=O) peak ranges at 286.4 eV - 287.4 eV and a peak at higher binding energy between 288.6 eV - 291.8 eV is attributed to (O-C=O) bonding configurations. The formation of the oxidised carbon species is attributed to the surface reaction of oxygen on surface of ZnO with adventious carbon. The variation of binding energy of C 1s peaks between the different crystal surfaces was $\approx \pm$ 0.5 eV. Analysis of the C 1s core level spectra for the PLD and e-beam deposited thin films show the same spectral

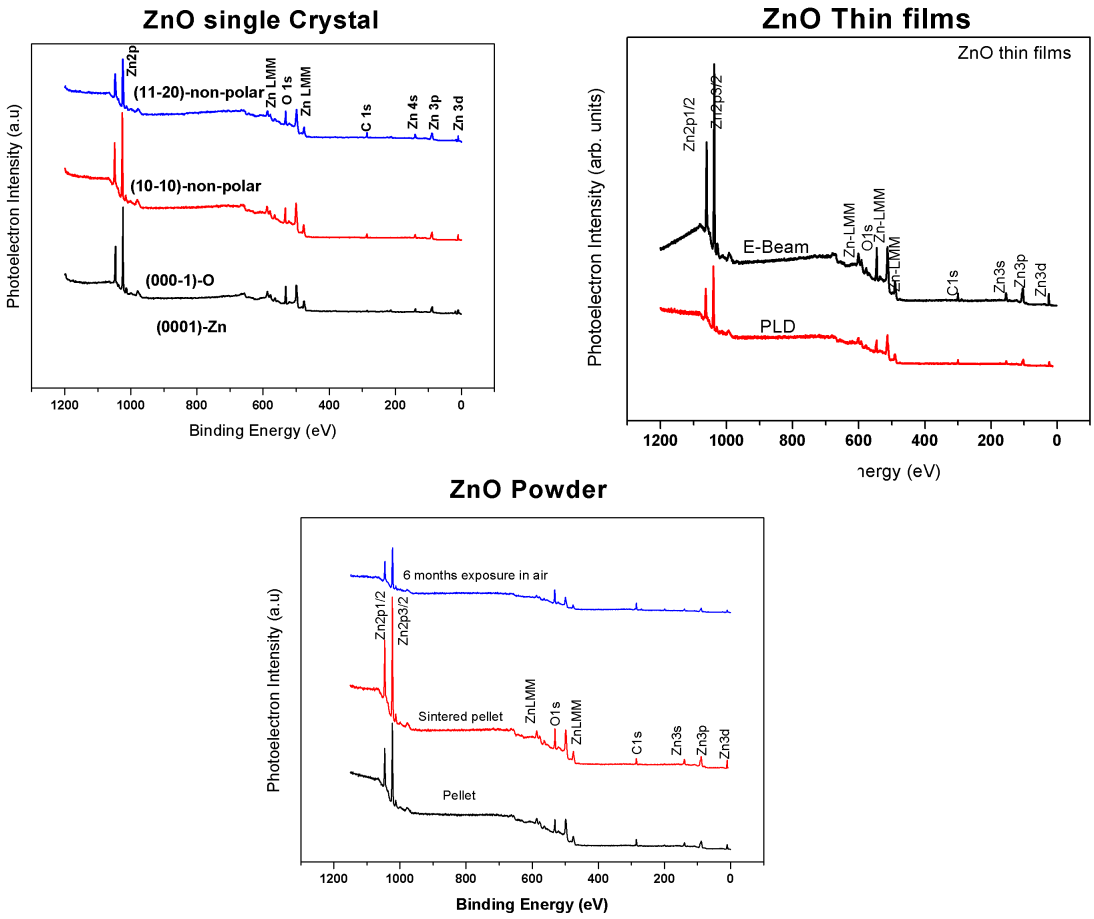

Figure 4.7: Survey spectra for ZnO single crystal of important four faces (0001), (000-1), (10-10), (11-20), ZnO thin films (E-beam and PLD grown) and ZnO powder (pellet, sintered and air exposure).

features as for the single crystal surfaces and no obvious dependence on deposition method.

The oxygen core level for the single crystal ZnO surfaces can be curve fitted with principle peaks at 530.5 eV and 532 eV attributed to zinc oxide and zinc hydroxide species, respectively as shown in figure 4.9. For the Zn-terminated surface the adsorbed hydroxide peak is significantly larger than on the other surfaces and a higher binding energy peak at 533.1 eV is attributed to adsorbed water. The origin of the additional lower binding energy oxygen peak at 529.1 eV is unknown but may be related to other adsorbed impurities consistent with the reactive nature of the Zn-terminated surface. The O 1s spectra for the O-terminated and non-polar (10-10), (11-20) surfaces show similar peak profiles with the zinc oxide related peak at 530.5 eV and the hydroxide peak at 532 $\pm$ 0.2 eV binding energies. For the PLD and e-beam deposited thin films, the O1s core level spectra are ZnO at 530.51 eV, a hydroxide component at 532.04 eV and a H_2O related peak at 533.17 eV in agreement with previous studies [30]. For ZnO powders, the peak attributed to ZnO bonding is at

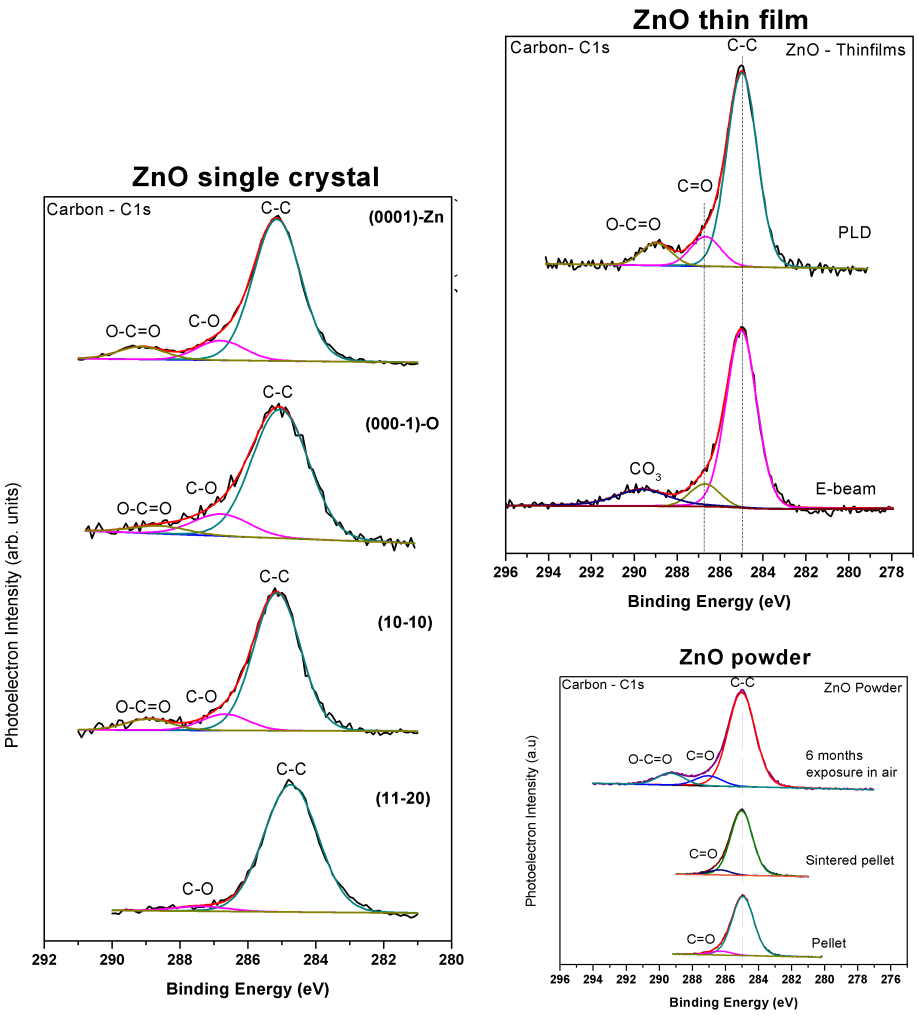

Figure 4.8: Comparative adventitious carbon C 1s core level for polar and non-polar ZnO crystal surfaces, thin films (E-beam and PLD grown) and ZnO pellets with annealing and exposure.

530.9 eV B.E. with the hydroxide and water related component peaks at 532.2 eV - 533.4 eV B.E.

The bulk sensitive Zn 3d photoemission spectra for the ZnO single crystal surfaces shown in fig 4.10 were observed at 9.77 eV to 10.11 eV and corresponding hydroxide also visible at 1 eV higher binding energy than ZnO. Zn 3d spectra confirm that on all four surfaces a hydroxide bonding component forms. The Zn $L_2M_{45}M_{45}$ Auger peak from thin films were shown at figure 4.11 the Kinetic energy (K.E.) of both PLD and E-beam grown film were very close at 987.75 eV and 988.10 eV respectively. This matches the exactly the standard value for ZnO [17].

Zn 2p3/2 core level spectra (figure

The lower binding energy peak below the ZnO is identified in all surfaces which fall below binding energy position of zinc metal. The origin of the peak is unclear which appear for Zn 2p, Zn 3p core levels similarly found in zinc metal. For the PLD grown ZnO thin films the zinc peaks were at (1) ZnO - 1022.51 eV, (2) $Zn(OH)-2$

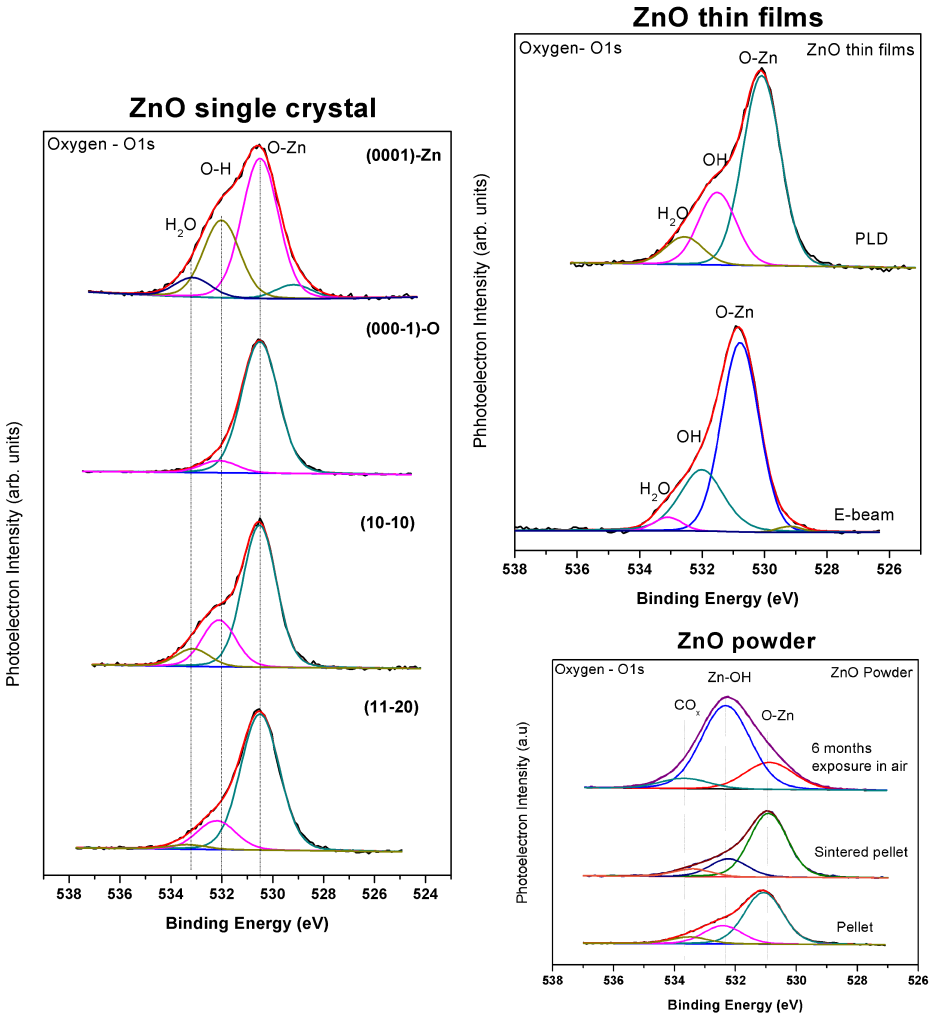

Figure 4.9: Comparative oxygen O 1s core level for the polar and non-polar ZnO crystal surface, thin films (PLD and E-beam grown) and ZnO pellets with processing.

1024.00 eV. For E-beam grown thin films the Zn2p peak for ZnO component is at 1022.30 eV and hydroxide component at 1023.28 eV. Similarly for the ZnO powder also Zn 2p3/2 having three components, the higher binding energy peak at 1023.89 eV is assigned to a zinc hydroxide, the lattice zinc oxide peak is at 1022.60 eV, and a small peak 1020.67 eV at lower binding energy is related to a zinc surface state [31]. This small peak may be due to the conductive free electrons accumulated as a layer on surface of ZnO [32].

4.3.3 Angle resolved XPS studies of ZnO nanorods

ZnO nanostructures can readily be growth using a wide range of techniques ranging from simple chemical preparation methods to the use of sophisticated vacuum deposition methods. The XPS is well established surface analysis technique to determine the chemical composition of two dimensional surfaces. As nanorods are three dimensional surfaces, the angular dependence of the photoemission signal was determined

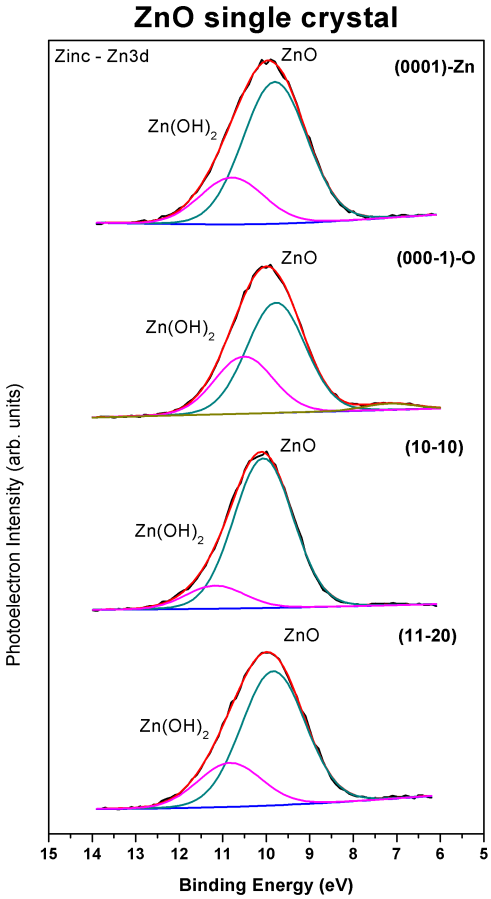

Figure 4.10: Bulk sensitive Zn3d core level for ZnO (the polar and non-polar) crystal Surface.

by acquiring photoemission spectra at a range of angles between 0° and 60° in steps of 15° degree as schematically shown in figure 4.13.

The XRD 2 $(\theta - \omega)$ scans shown in figure 4.14(a) for the nanorod structures on an Al_2O_3 substrate display a peak for ZnO (0002) at 34.58° and a second order (0004) peak at 72.64° indicating the single crystal nature of the nanorods. A strong (11-20) diffraction peak originating from the sapphire substrate also observed at 37.78°. The FWHM of 0.18° for (0002) peak displays the good crystallinity and alignment of the nanorods with [0001] texture. No XRD peaks corresponding to other phases are detected in the scan. The scanning electron micrograph (SEM) of the nanorods shown in figure 4.14(b) indicates the well aligned morphology of ZnO nanorods. These results confirm that the ZnO nanorods employed for photoemission study are well aligned, single crystalline nanostructures.

Figure 4.15 shows the core level spectra of carbon C 1s and oxygen O 1s at different photoemission angles with respect to surface off-normal. For the C 1s, a four component peak fit is used to identify, carbon bonded with hydrogen(C-H) at 284 eV, (C-C) - 285 eV, (C-O) - 286.70 eV and (O-C=O) - 289.3 eV. The FWHM of all

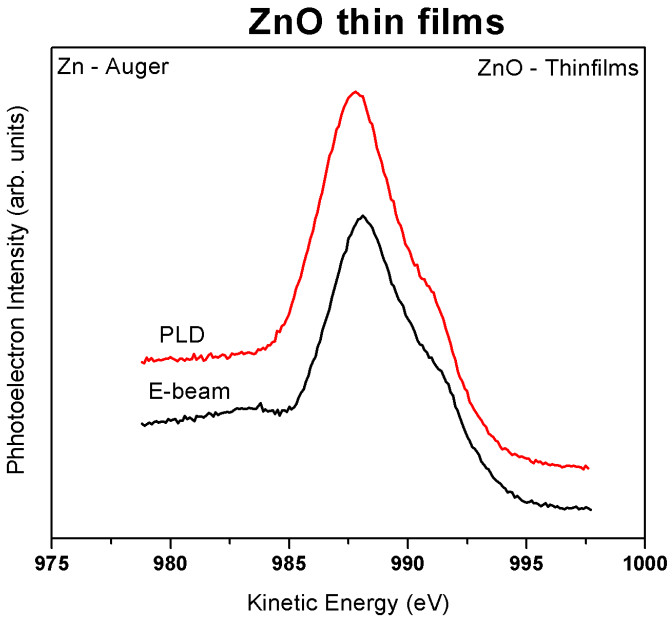

Figure 4.11: Zn $L_2M_{45}M_{45}$ Auger peaks for (PLD and E-beam) thin films.

the peaks with different angle of photoemission is constant at 1.6 eV. O 1s core level spectra were the most useful peak for studying surface the chemical state of ZnO. The oxygen O 1s peak is peak fitted with 4 peaks which are (1) small peak at lower binding energy which is meant to aluminium oxide from substrate at 528.9 eV, (2) O-Zn - 531.1eV, (3) OH - 532.5 eV and H_2O - 533.5 eV. These observed binding energy had a small variation of ± 0.4 eV with respect to different angle of photoemission and are consistent with recently reported values for ZnO nanorod [34]. The FWHM of the all oxygen peaks with different angle of photoemission is constant at 1.6 eV.

The readily visible peak for zinc Zn 2p3/2 is shown in figure 4.16. Similar to oxygen O1s, zinc Zn 2p3/2 is peak fitted with a bulk oxide component oxide (1022.7 eV), hydroxide (1023.6 eV), carboxylates (1025 eV) and small asymmetric peak (1020.89 eV) is attributed to a surface state feature. The FWHM of the all peaks with different angle of photoemission is constant at 1.75 eV. Gold nanoparticles were used as catalyst for nanorods growth and the Au 4f7/2 signal is detected with Zn 3p core level in the XPS spectra is shown in figure 4.16. This peak was deconvoluted with four doublet peaks. Gold Au 4f peak observed at 84.2 eV and Zn 3p peak with three components (i) Zn surface state - 86.35 eV, (ii) ZnO - 89.05 eV, (iii) $Zn(OH)_2$ - 90.55 eV. The FWHM of the all peaks with different angle of photoemission is constant of 0.89 eV and 2.52 eV for gold and zinc respectively.

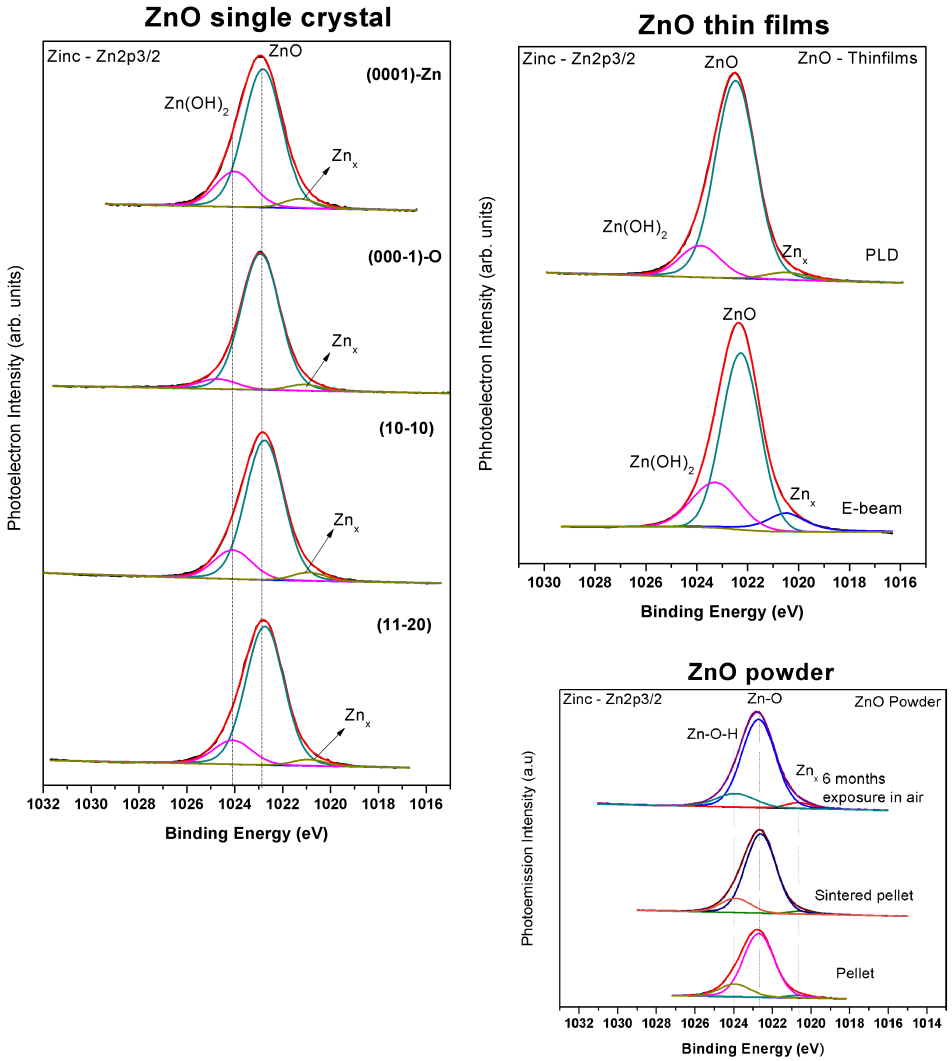

Figure 4.12: Comparative zinc Zn 2p3/2 core level for polar and non-polar ZnO surface, PLD and E-beam grown ZnO thin films and ZnO pellets (initial, sintered, air exposed).

4.4 Analysis

4.4.1 Binding Energy

Binding energy values of the XPS peaks can provide information on the chemical state of the elements present at the surface of the materials. In Table 4.1 the binding energy values of survey spectra of different type of ZnO samples measured were given,

4.4.1.1 Survey Scans:

On comparing these survey binding energy values to standard values for ZnO [26,35], there was not much variation for all samples. The Zn 3d peak B.E. values vary from 9.97 eV to 10.98 eV. In collective view of all samples, the Zn 3d binding energy from 9.97 eV to 10.5 eV is for ZnO and above 10.5 eV is for $Zn(OH)_2$. For Zn 3p and

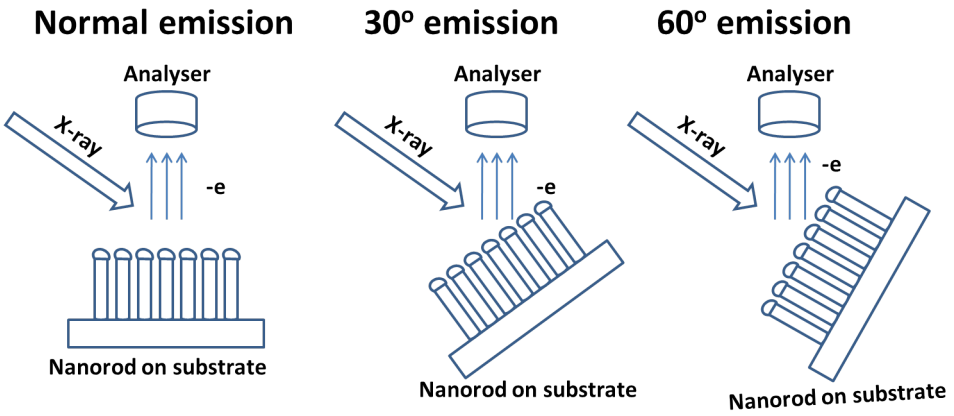

Figure 4.13: Alignment of nanorod with X-ray and analyser when normal, 30, 60 degree angle dependent photoemissions.

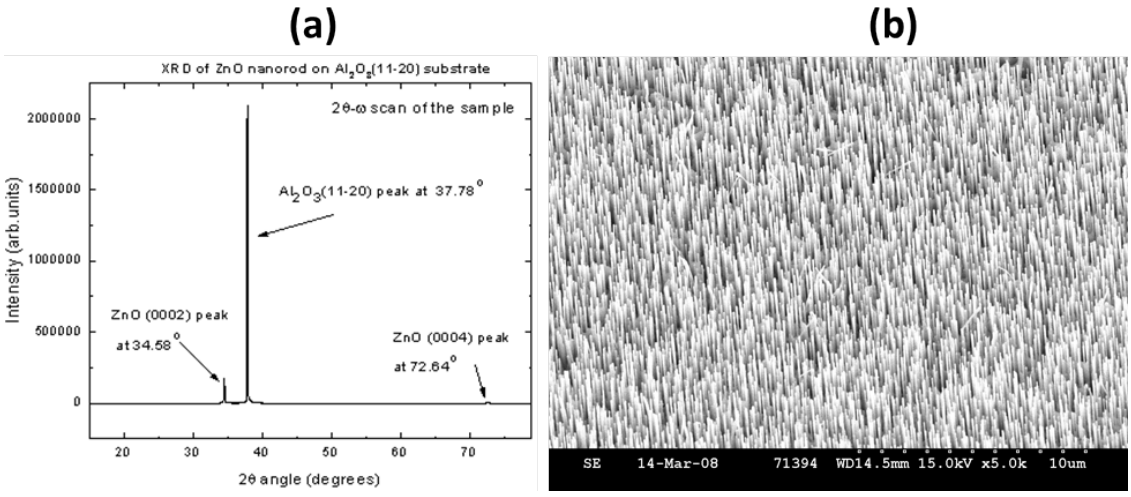

Figure 4.14: (a) X-ray diffractrogram and (b) SEM image of single crystal ZnO nanorod vertically grown on sapphire substrate.

Zn 3s peaks the average values of B.E. were 88.95 eV and 139.96 eV respectively. These peaks have a small variation in B.E. (0.52 eV Zn 3p and 0.32eV Zn 3s) for all samples. The chlorine Cl 2p is found as common contamination in ZnO (199 eV - 200.8 eV) crystals, E-beam thin films and powder samples. The adventious carbon is found around 285 eV in all ZnO samples. Among all Zn LMM Auger peaks the high intensity and prominent peak Zn $L_2M_{45}M_{45}$ is between 497.79 eV - 500.01 eV, which corresponds to ZnO. The O 1s peak is the more sensitive peak in ZnO which found between 530.27 eV 532.03 eV. Based on O1s peak in survey spectra the binding energy for partially oxidised Zn (ZnO_x) is below 530.5 eV, fully oxidised Zn (ZnO) is between 530.5 eV - 531 eV, above 531 eV is for $Zn(OH)_2$. The surface sensitive peak Zn 2p3/2 having average B.E. at 1022.5 eV is for ZnO peak and hydroxide is above 1022.7 eV. To nullify the charged shifts and for perfect identification of compound difference in B.E. of two core levels is used. Difference in B.E. of Zn 2p1/2 - Zn 2p3/2 is around 23 eV and Zn 2p3/2 - O 1s is between at 491.02 eV - 492.23 eV.

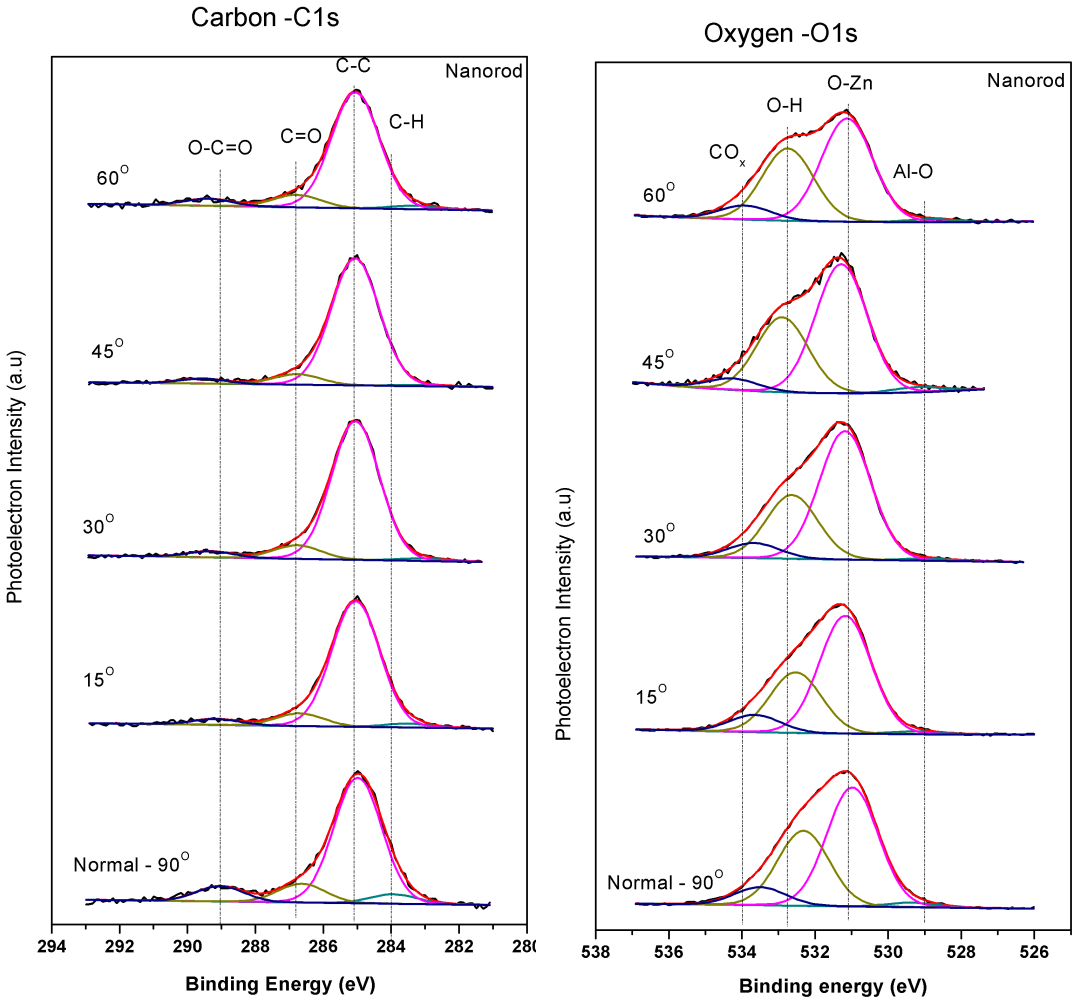

Figure 4.15: The core level spectra of carbon (C 1s) and oxygen (O 1s) of ZnO nanorods from photoemission angles from 0 to 60 degrees in steps of 15 degrees.

4.4.1.2 Narrow Scans:

The binding energy of narrow scans for core levels of C 1s, O 1s, Zn 2p3/2 for Zn metal, ZnO on Zn metal, ZnO crystals, thin films, powder and nanorod were shown in table 4.1. These tabulated binding energy values were reproducible and consistent in-house XPS repeated studies. In table 4.2 following sample B.E. values were not included: (1) initial scraped and IPA cleaned zinc metal, (2) as made and air exposed ZnO pellets and (3) 15°, 45°, 60° degree angle of photoemission for ZnO nanorod. Those samples were omitted because of large amount of contamination, very low photoemission peak intensity and then repetitive results.

The carbon peaks for all samples were found at 285 eV with variation of ± 0.3 eV. The carbon dioxide(C=O) peak for zinc metal sample is having higher B.E. difference of 2 eV from C-C position and other ZnO samples having only 1.6 eV. Carbon trioxide (O-C=O) has B.E. difference of 4 eV from C-C peak for all samples. But the (11-

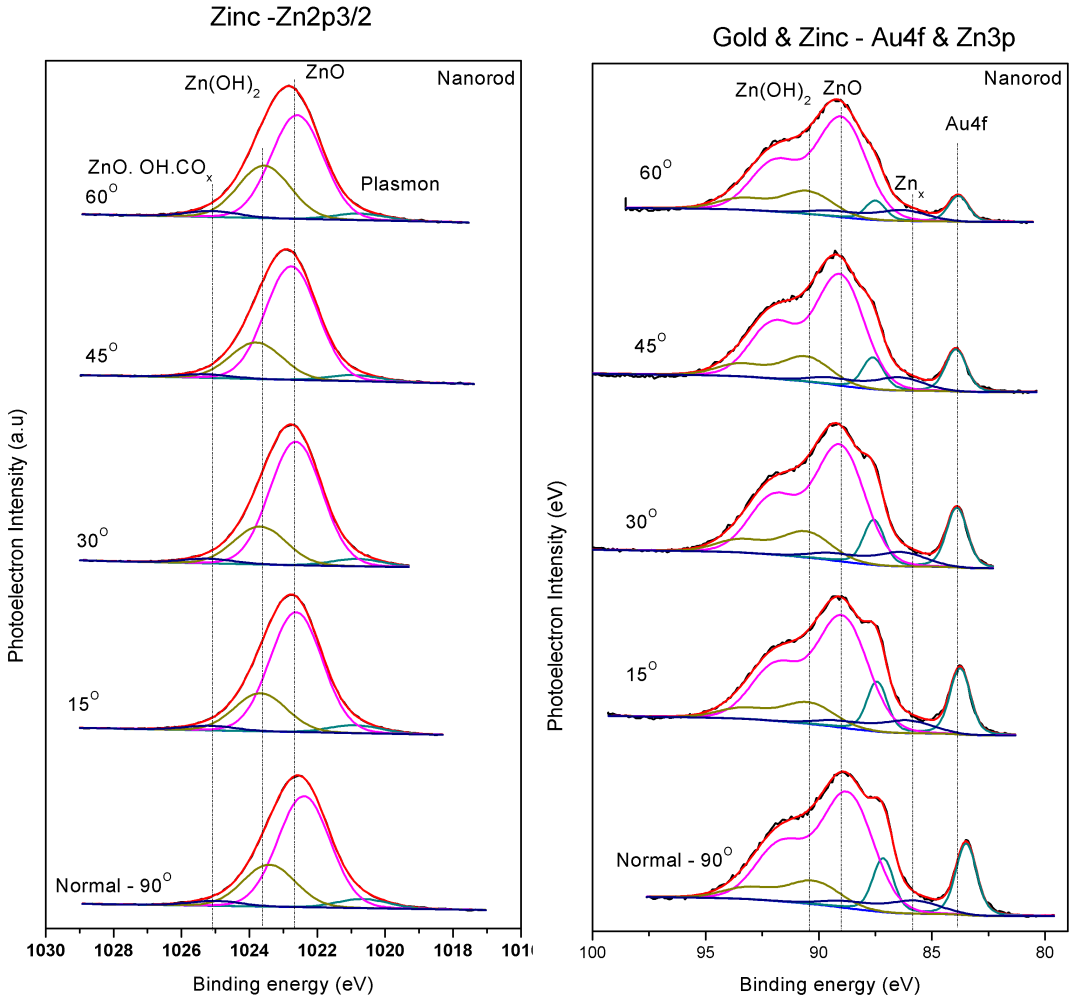

Figure 4.16: The core level spectra of Znic (Zn2p3/2) and (Zn3p3/2 and Zn3p1/2) of ZnO nanorods from photoemission angles from 0 to 60 degrees in steps of 15 degrees.

20) crystal surface has a large B.E. difference of C-C to C-O is 2.63 eV and C-C to O-C=O is 7 eV due to high level of carbon contamination. Most of the O 1s peak for ZnO is perfectly found at 530.5 eV. For e-beam thin films, zinc bonded oxygen (O-Zn) got more oxide or hydroxide on surface. So the peak position slightly moves to 530.77 eV, powder - 530.91 eV and nanorod 530.97 eV. Hydrogen bonded oxide (OH) in the O 1s signal matches with previous reports [35] and is 1.5 ± 0.3 eV away from zinc bonded oxide. The B.E. difference for peak fitted for water (H_2O) to O-Zn is 2.6 ± 0.35 eV. Prominent Zn Auger (Zn $L_2M_{45}M_{45}$) peak for zinc metal is 992.99 eV (K.E.) and for ZnO is between 987 - 988 eV (K.E.) in thin film samples. The zinc surface sensitive peak Zn 2p3/2 ranges from 1022.3 - 1022.9 eV for ZnO, where thin films, powder, nanorod has 0.3 eV less than crystals sample Zn 2p 3/2 peak B.E. Zinc hydroxide ($Zn(OH)_2$) components found at higher B.E. difference of 1 ± 0.35 eV for Zn-O peak. The zinc metallic peak is at 1021.81 eV for zinc metal sheet and $Zn(OH)_2CO_x$ is at 1025.03 eV for ZnO nanrods.

Survey spectra - Binding Energy (eV)															
Peak	**Zinc metal**				**ZnO Crystals**				**ZnO Thin films**		**ZnO Powder**			**ZnO nanorod**	
	IPA Clean	**IPA Clean + 200°C**	**Scraped**	**Scraped + 100°C**	**(0001)-Zn**	**(000-1)-O**	**(10-10)**	**(11-20)**	**E-Beam**	**PLD**	**Pellet**	**Sintered**	**Ageing**	**Normal Θ = 0°**	**Θ = 30°**
Zn3d	10.3	10.0	11.0	10.0	10.0	10.1	10.0	10.0	10.2	10.0	10.7	10.5	10.5	10.5	10.7
Zn3p	89.1	89.0	89.0	89.0	89.0	89.1	89.0	89.0	88.7	88.6	88.9	89.1	89.1	89.0	89.0
Zn3s	140.0	140.0	140.1	140.0	140.1	140.0	140.0	140.0	139.8	140.0	139.8	139.9	139.8	140.0	140.0
Cl2p	--	--	--	--	200.0	--	--	--	200.5	--	199.9	200.8	199.1	--	--
C1s	285.0	285.0	285.0	285.0	285.0	285.0	285.0	285.0	285.0	285.0	285.1	285.1	285.0	285.0	285.0
Zn Auger	476.0	474.7	476.0	476.0	476.5	476.1	476.0	475.0	475.5	475.8	476.2	475.7	476.5	475.8	475.7
Zn Auger ($L_3M_{45}M_{45}$)	499.6	497.8	499.5	499.0	500.0	499.1	499.0	498.1	498.5	498.5	498.8	498.8	499.5	498.5	499.1
O1s	531.0	530.7	530.7	530.3	530.7	530.6	530.5	530.6	530.8	530.5	531.3	531.0	532.0	531.5	531.2
Zn Auger	563.1	563.3	563.3	561.3	563.6	563.8	564.0	562.9	562.7	562.6	562.7	563.8	564.0	563.8	564.3
Zn Auger	578.1	577.3	577.3	575.3	578.5	577.6	577.9	576.9	577.0	576.1	577.3	577.3	578.6	577.6	578.2
Zn Auger	586.6	586.5	586.5	584.8	587.0	587.2	586.9	585.6	586.5	586.6	586.4	586.7	587.1	586.6	586.9
Zn Auger	655.8	654.6	654.6	653.0	656.3	656.7	657.0	658.0	655.7	655.1	656.3	656.8	656.5	656.1	657.3
Zn Auger	664.0	663.8	663.8	662.9	663.2	663.7	663.5	663.2	663.6	663.0	662.3	663.4	663.9	662.7	664.3
Zn2p1/2	1022.5	1022.7	1022.5	1022.5	1022.5	1022.7	1022.5	1022.6	1022.5	1022.7	1022.8	1022.8	1022.5	1022.5	1022.7
Zn2p3/2	--	--	--	--	1045.5	1045.7	1045.5	1045.6	1045.5	1046.0	1046.0	1045.8	1045.8	1045.8	1046.0

Table 4.1 Binding energy of the Survey XP spectra of Zn metal, ZnO: single crystal surfaces, thin films, powders and nanorods (angle resolved)

Core level spectra - Binding Energy (eV)										
Peak	**Zinc metal**		**ZnO single crystals**				**ZnO Thin films**		**ZnO Powder**	**ZnO nanorod**
	Pure Zn*	Native oxide€	(0001)-Zn	(000-1)-O	(10-10)	(11-20)	E-beam	PLD		
Carbon - C1s										
C-C	284.99	285	285.13	285.03	285.13	284.72	284.98	284.93	285.02	284.98
C-O	287.02	287.06	286.79	286.77	286.67	287.35	286.67	286.76	286.35	286.64
O-C=O	289.11	289.18	289.13	288.59	288.91	291.78	288.98	289.70	---	289.08
Oxygen-O1s										
O-Zn	530.5	530.5	530.48	530.49	530.5	530.49	530.77	530.51	530.91	530.97
OH	532.02	531.72	532	532.10	532.10	532.20	532	532.04	532.29	532.30
H_2O	533.17	532.91	533.12	---	533.12	533.33	533.07	533.17	533.40	533.51
Zn $L_2M_{45}M_{45}$ (K.E.)	992.99	987.79	---	---	----	---	988.10	987.75	---	---
Zinc - Zn2p										
Zn	1021.81	---	---	---	---	---	---	---	----	---
ZnO	1022.98	1022.67	1022.81	1022.91	1022.74	1022.73	1022.30	1022.51	1022.60	1022.39
$Zn(OH)_2$	----	1023.78	1023.99	1024.70	1024.07	1024.07	1023.28	1024.00	1023.89	1023.43
$Zn.OH.CO_X$	---	---	---	---	---	---	---	---	---	1025.03

*Scraped + 100°C annealed, € IPA cleaned + 200°C annealed

Table 4.2 Binding energy of core level spectra of Zn metal, ZnO single crystal [(0001), (000-1), (10-10), (11-20)], thin films [E-beam and PLD grown], Powders

4.4.2 Peak fitting

The measured XPS core level peak for a particular element is a collection of several peaks due to different chemical bonding of that element. To separate those individual peaks (for each bond) as a mathematical function used to deconvolute / dissociate the real peak is fitted by combination of several synthetic peaks. The fitted peaks must be meaningful to mention the element or compounds are in existence. The parameters used in peak fitting were (1) expected binding energy separation between peaks (2) full width half maximum (FWHM) of peak, which is combination of Lorentzian and Gaussian functions. Some peaks of s, p, d orbitals will have splitting of two peaks separated by a distance which were called double-let peaks. So peak fitting is a crucial and important part in XPS spectra analysis. The peak fitting were repeated several times and analysis were done to find the best and most meaningful synthetic peaks.

The binding energy separation between fitted peaks of C 1s, O 1s, Zn 2p core levels were easily calculated from table 4.2. The FWHM used in peak fitting for all samples were tabulated here (see Table 4.3). For zinc, all core levels Zn 3d, Zn 3p, Zn 2p were peak fitted with three peaks with an energy separation of nearly 1.0 eV between the each peaks (Zn ZnO $Zn(OH)_2$ $Zn(OH)CO_x$). The FWHM for Zn 3d - 1.5 eV, Zn 3p - 2.5 eV and Zn 2p - 1.75 eV were also mostly similar for all samples. A special case here is Zn 3p which is a doublet peak with 2.9 eV - 3.0 eV splitting and a small peak fitted for Zn surface state has a different FWHM of 1.5 eV and must be used to make a good fit. Further in the ZnO nanorod, a gold peak Au 4f is detected and fitted with a FWHM of 0.89 eV.

For O 1s core level three peaks were fitted with binding energy separation of O-Zn to O-H is 1.5 ± 0.3 eV and O-Zn to H_2O is 2.5 ± 0.3 eV. The FWHM is varied between 1.32 - 1.6 eV the variation range is 0.3 eV, this variation is due to the change in the level of hydroxide and nature of the sample surface area. ZnO thin films and powder have low values of 1.32 - 1.45 eV, next the ZnO crystal has 1.4 - 1.6 eV. Finally metal and nanorod have a stable width of 1.6 eV. This FWHM variation is due to partial oxidation of zinc metal as well as the hydroxide based contaminants. Carbon C 1s core level also peak fitted with three synthetic peaks with binding energy difference of C-C to C-O is 2 ± 0.5 eV and C-C to O-C=O is 4 ± 0.8 eV. The variation of FWHM for carbon is 0.5 eV from 1.42 to 1.92 eV. The wide peak broadening (1.9 eV) implies larger amount and different types of carbon stays on surface.

4.4.3 Comparison of ZnO nanrod photoemission signal as a function of emission angle

The variation in area of peak for ZnO nanorods with respect to different photoemission angles for carbon, oxygen, zinc is shown in figure 4.17 Summaries the comparison, the intensity of C 1s and O 1s peak is very low at normal 0° and 15° emission, is a maximum at 30° emission and reduces again at angles of emission of 45°, 60° (see

Peak	FWHM (eV)									
	Zinc metal		ZnO single crystal				ZnO Thin films		ZnO Powder	ZnO nanorod
	Pure Zn*	Native oxide€	(0001) -Zn	(0001) -O	(10-10)	(11-20)	E-beam	PLD		
Zinc – Zn3d (Zn, ZnO, $Zn(OH)_2$)	1.5	1.5	-	-	-	-	-	-	-	-
Zinc – Zn3p (Zn_x,ZnO, $Zn(OH)_2$)	2.5	-	-	-	-	-	-	-	-	2.52
Carbon - C1s (C-C, C-O, O-C=O)	1.92	1.85	1.58	1.9	1.56	1.81	1.59	1.9	1.42	1.6
Oxygen-O1s (O-Zn, OH, H_2O)	1.6	1.6	1.55	1.57	1.43	1.66	1.46	1.45	1.32	1.6
Zinc - Zn2p (Zn, ZnO, $Zn(OH)_2$, $Zn.OH.CO_X$)	1.75	1.75	1.75	1.75	1.75	1.75	1.75	1.76	1.72	1.75

*Scraped + 100°C annealed, € IPA cleaned + 200°C annealed

Table 4.3 The full width half maximum (FWHM) of core level peaks for carbon, oxygen, zinc.

figure 4.17). In peak area analysis, the ambient carbon (C-C) and carbon monoxide (C=O) signals rise from normal emission to 30o off normal and decrease again up to 60° shows amount carbon on whole surface of nanorod is almost uniform. Further area analysis of carbon trioxide (O-C=O) and hydrocarbon (C-H) decreases at the photoemission angle (O° to 60°) increases implying these were abundant on the top surface of the nanorod. The oxygen peak areas reduce as a function of emission angle except 30° because of the reduction in surface area and scattering of photoelectrons between nanorods. At 30° plenty of photoelectrons emerge out from top and sides of nanorod with less collision rate. The reason why the area of OH peak reduces at 15° and Al-O increases at 45° is unclear. In Zn 2p the maximum intensity was also obtained at 30° of photoemission. In comparison, the intensity of the gold peaks (see figure 4.17) are almost zero at normal emissions, rise to a maximum at 30° and decrease again in intensity at 45° and 60° off normal. The ratio of zinc to gold increases from normal to 60°. Both zinc and gold have attained maximum at 30°.

4.4.4 Surface chemical composition

The surface chemical composition can be obtained by analysis of the XPS spectra in atomic percentage terms. Information on surface contamination and ZnO stoichiome-

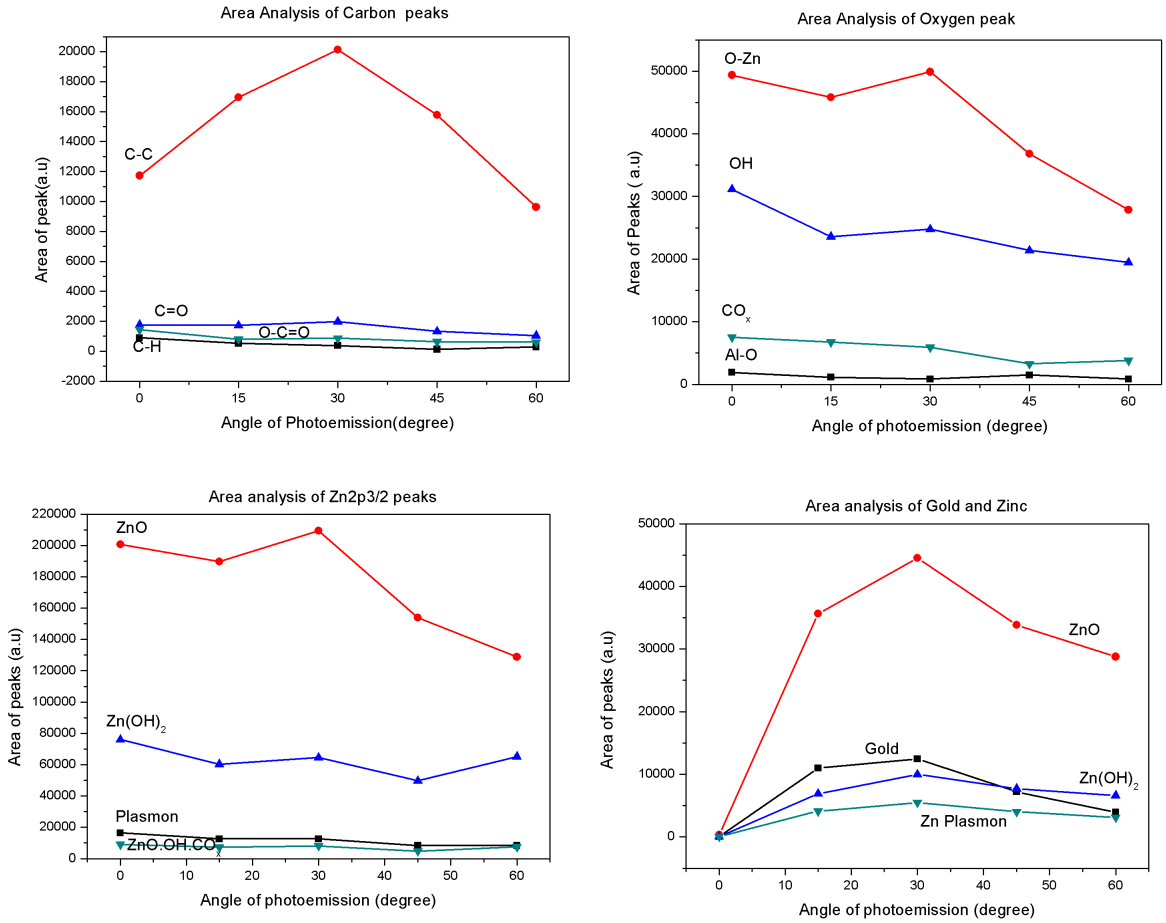

Figure 4.17: Carbon, oxygen, zinc (Zn2p, Zn3d) and gold core level peaks total area analysis in function of angle of photoemission.

try can also be extracted from these measurements [36]. The XPS atomic percentages for the ZnO single crystals, thin films and powders are tabulated in Table 4.4 and for nanords in separate table 4.5. In a collective view (from Table 4.4) of carbon contamination on samples the IPA cleaned Zn metal was having more carbon of 50%, next the ZnO powers and scraped zinc metal having 30%, single crystal having in the order of ≈20% expect (0001)Zn-terminated crystal surface has ≈30% and finally thin films having less amount ≈ 15% of carbon contamination. The oxygen composition is high for (000-1) O-terminated crystal (53.35%), scraped as well as annealed metal (41.22%) and PLD thin films (35.87%) due to top surface of oxygen dangling bonds and growing PLD thin films in O_2 atmosphere will leads to oxygen terminated thin films respectively. The hydroxide contamination found to be very high air exposed pellets (24%) and minimum (4.9%) for (000-1) O-terminated crystal surface. These shows sintered pellets were more reactive to atmospheric moisture. A constant ratio of hydroxide and water is seen along with the lattice oxygen of ZnO. The more amount of water seen in zinc metal sample 7% - 10% and very less of ≈ 1% found in (11-20) crystal, E-beam thin films. The zinc concentration is high (36.44%) for mixed

terminated crystal surface (10-10), sintered pellet (30.29%), e-beam grown thin films (30.5%) where sintered pellet losses oxygen while annealing and E-beam to loose oxygen while evaporation of target. The zinc hydroxide also follows the same trend of the zinc in ZnO.

The chemical composition of ZnO nanords with respect to different angle of photoemission shown in Table 4.5 is analysed here. In addition to primary elements C, O, Zn of ZnO gold Au used for catalyst and Al from sapphire substrate were found. On comparing the atomic percentage with photoemission angle, the maximum value is obtained at angle 0° degree for Al (3.97%), C-H (1.1%), O-C=O (1.78%), O-Al (0.99%), O-Zn (25.55%), O-H (16.11%), H_2O (3.89%), Zn_x(1.62%) were mostly present on substrate. But Zn 2p core levels peaks components, Zn-O (20.29%), Zn(OH)2 (10.26%), $Zn(OH)_2.CO_x$ (1.18%) reach maximum atomic percentage at angle of 60 degree photoemission were on the surface of nanorod. Then, Au (0.71%), C-O (2.37%) at 30 degree and C-C (25.3%) at 45 degree got maximum atomic percentage were present all over. The atomic percentage of both oxygen (22.95% - 25.5%) and zinc (19.59% - 20.29%) for ZnO were almost stable. But C-C carbon concentration varies about 10% between 14.58% to 25.3%. The hydroxide having variation of 4% both in O 1s (16.11% - 12.37% and in Zn 2p (10.26% - 6%). The carbon monoxide and water were with 2% and all other aluminium, aluminium oxide, hydrocarbon, carbon trioxide, zinc hydro carbonate were with 1%.

4.4.4.1 Contaminations

The major contaminants on ZnO surface were carbon, hydrogen and their compounds. On exposure of any surface to atmosphere will adsorb the carbon, which applies for ZnO surface too. The hydroxides, water were mainly adsorbed form atmosphere and as well as inside UHV chamber as ZnO is reactive surface [37]. The contamination analysis graph (expect nanorods) for carbon is shown in figure 4.18 and for hydroxide is shown in figure 4.19. First from figure 4.18 strong contamination of (C-C) carbon is seen from 60% - 10%. IPA treated Zn metal sheets have the large amount of 58.92%, and after annealing 200 °C of IPA treated sample only reduced to 52.08% of carbon. So instead of cleaning the metal surface, IPA treatment contaminate the surface. On other hand, scraped metal got increase in (C-C) carbon from 21.94% 29.78% after annealing treatment. Among ZnO crystals, (0001)-Zn terminated surface adsorbed more carbon of 32.62%, next (11-20) - 21.96% later (000-1)-O and (10-10) have less ≈10% only. The thin films only have less amount of carbon(C-C) of 12.84% - 16.25%. Then irrespective of any processing, ZnO pellets have constant amount of ≈30% (C-C) carbon. On seeing carbon based oxides (C=O and O-C=O) it ranges from 0 - 7.52%. The metal samples, (0001)-Zn crystal have high level of approx. 4% - 7% and other all samples only have between approx. 0% - 3%.

On seeing figure 4.19, the high amount of hydroxide contamination is found ≈24% on air exposed ZnO sintered pellets. Initially, as made pellet have 8% of OH on surface,

ZnO XPS atomic %														
Element	**Peak / compound**	**Native oxide on Zn metal**				**ZnO Crystal**				**ZnO Thin films**		**ZnO Powder**		
		IPA Clean £	**IPA Clean + 200°C**	**Scraped**	**Scraped +100°C$**	**(0001)-Zn**	**(000-1) -O**	**(10-10)**	**(11-20)**	**E-Beam**	**PLD**	**Pellet**	**Sintered**	**Ageing**
Carbon	C-C	58.9	52.1	21.9	29.8	32.6	10.9	11.8	22.0	12.8	16.3	29.7	28.0	30.6
	C-O	7.5	4.1	3.3	3.1	4.5	1.9	1.4	0.8	1.6	2.5	1.9	2.2	3.3
	O-C=O	6.9	2.9	5.0	3.5	2.9	0.7	1.0	0.0	2.5	1.9	0.0	0.0	3.8
Oxygen	O-Zn	6.6	20.8	23.3	41.2	22.5	53.4	27.5	32.6	25.9	35.9	22.6	23.7	7.8
	O-H	10.9	10.9	19.1	15.8	12.8	5.0	9.0	6.9	10.9	13.7	8.0	6.7	24.0
	H_2O/CO_x	7.2	8.2	11.0	5.5	3.7	0.0	3.4	1.1	1.4	5.2	2.9	2.8	3.0
Zinc	Zn-O	0.0	0.7	11.8	0.2	15.9	25.4	36.4	30.1	30.5	18.7	28.4	30.3	22.5
	Zn-O-H	1.2	0.2	3.9	0.0	4.1	1.9	7.6	5.2	10.0	4.8	5.6	5.5	3.9
	Zn_x	0.2	0.1	0.7	0.2	0.9	1.0	1.9	1.2	4.4	1.1	0.8	0.9	1.2

Note: **£** - IPA clean sample having Zn-O-H-C of 0.48%, **$** - Scraped and annealing at 100°C having Zn metal about 0.71%

Table 4.4 The XPS atomic concentration analysis of various different forms of ZnO

ZnO nanorod Atomic % by angle resolved XPS						
Peak	**Element/ Compound**	**0 degree**	**15 degree**	**30 degree**	**45 degree**	**60 degree**
Aluminium - Al2p	Al	3.97	2.79	2.63	1.22	0.89
Gold - Au4f	Au	0.01	0.68	0.71	0.55	0.37
Carbon - C1s	C-H	1.1	0.69	0.45	0.22	0.58
	C-C	14.58	22.22	24.13	25.3	19.08
	C-O	2.19	2.26	2.37	2.12	2.06
	O-C=O	1.78	1.06	1.05	1.01	1.18
Oxygen - O1s	O-Al	0.99	0.62	0.42	0.99	0.69
	O-Zn	25.55	25.01	24.89	24.54	22.95
	O-H	16.11	12.87	12.37	14.27	16.04
	H2O/COx	3.89	3.67	2.95	2.19	3.15
Zinc - Zn2p	Znx	1.62	1.32	1.21	1.06	1.3
	Zn-O	19.82	19.76	19.93	19.59	20.29
	Zn-O-H	7.5	6.29	6.14	6.32	10.26
	Zn-C-O-H	0.89	0.76	0.77	0.62	1.18

Table 4.5 The angle resolved XPS atomic concentration of ZnO nanorods on sapphire substrate

further annealing at 400 °C as sintering process OH reduces little to 6.65% but made surface with more oxygen dangling bonds. Finally, exposure of these sintered pellets makes adsorption of hydrogen on the dangling oxygen bonds, a sudden increase of OH to 24%. In zinc metal, IPA treated samples have uniform ≈10%, but scraped sample have ≈18% and by annealing little reduces to ≈16%. Among crystal samples, from high to low (0001)-Zn surface - 12.5%, (10-10) - 9.03%, (11-20) - 6.2% and for (000-1)-O is very less of 4.95%. Again in crystals, Zn-terminated (0001) surface is more reactive to hydroxide similar to carbon contamination. In thin films, even though polycrystalline surface E-beam grown films have 10.88% and PLD sample have little high OH coverage of 13.71%.

The water (H_2O/CO_x) contamination on these ZnO surfaces was mostly below 5%. For metal samples only above 5% is seen. Similar to hydroxide, the scraped metal piece have high amount of water - 19.07% and by annealing drops to 15.79%. In crystals (0001)-Zn, (10-10) surface have nearly ≈3.5%, (11-20) has only 1.1% and no more water detected on (000-1)-O surface. On thin films, PLD grown have high 5.23% and E-beam gown have 1.3%. ZnO pellets have nearly equal to 3% for all processing.

From Table 4.4 examining hydroxide ($Zn(OH)_2$) bonded with zinc atom from Zn 2p3/2 core level. Zinc hydroxide found in metal sample before annealing is 1.19% to

3.92% had completely reduced to 0% - 0.2% after annealing. This shows by UHV annealing, zinc hydroxide cane removed from surface. Then in crystals, high level is at (10-10) - 7.56%, (0001)Zn and (11-20) surfaces have nearly 5% and (000-1) had very less 1.87%. E-beam grown thin film has 10% of $Zn(OH)_2$, but PLD grown films have half of it 4.77%. For ZnO pellets found about 5.6% expect air exposed pellet was 3.89%. This reduction pellet was due to increase of OH seen O 1s core level peak.

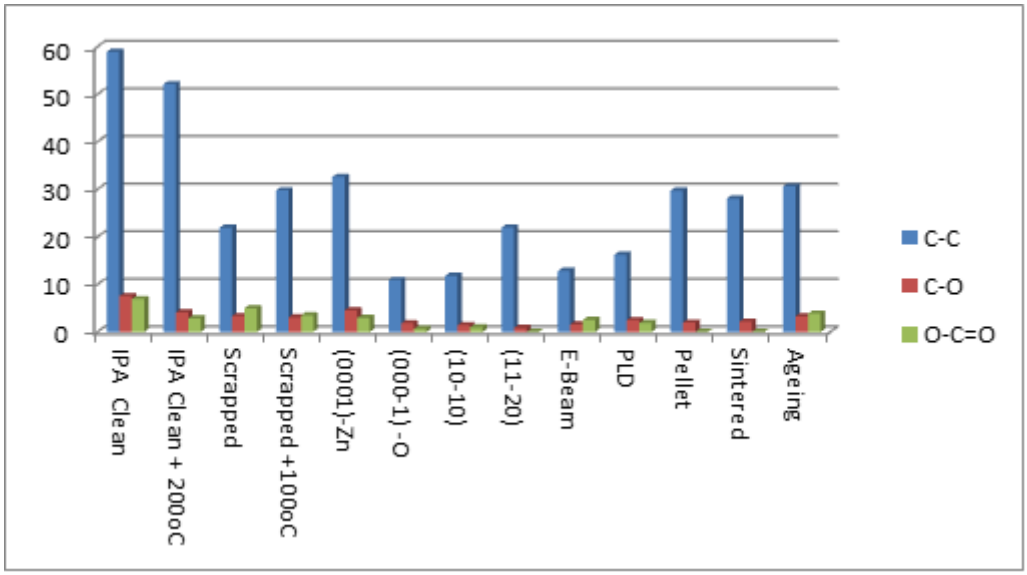

Figure 4.18: Carbon contaminations on ZnO surfaces.

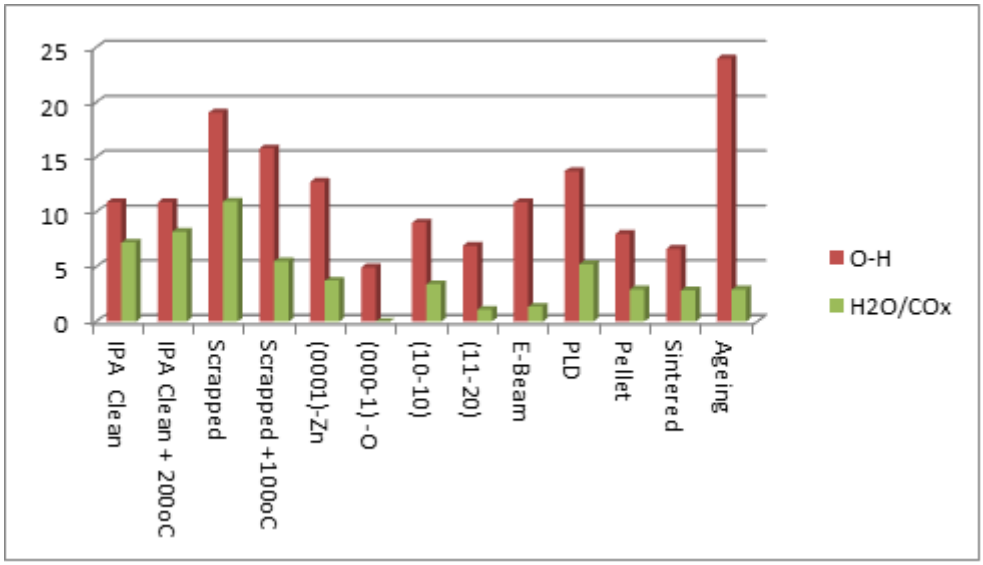

Figure 4.19: Hydroxide and water contamination analysis of ZnO surfaces from O 1s core level.

4.4.4.2 Stoichiometry (Zn:O)

Pure ZnO is composed of zinc and oxygen atoms in the ratio of 1:1; hence the stoichiometry zinc oxide in atomic percentage will be 50:50 of zinc and oxygen.

Stoichiometry – ZnO (%)														
Element	**ZnO Single crystal surfaces**				**ZnO thin films**		**ZnO powders**			**ZnO nanorods**				
	(0001)	**(000-1)**	**(10-10)**	**(11-20)**	**E-beam**	**PLD**	**Pellet**	**Sintered**	**Aging**	**0°**	**15°**	**30°**	**45°**	**60°**
Zinc – Zn%	42.21	32.22	57.04	47.99	54.09	34.22	55.73	56.13	74.35	43.68	44.13	44.46	44.38	46.91
Oxygen – O%	57.79	67.78	42.96	52.01	45.91	65.77	44.27	43.87	25.64	56.33	55.87	55.54	55.61	53.08

Table 4.6 The ZnO stoichiometry for single crystals, thin film, powders and nanarods

From XPS atomic percentage, the value for oxygen atoms from O 1s peak and for zinc atoms from Zn 2p peak were then compared to 100% and tabulated in Table 4.6. On seeing the tabulated values, there is no ideal stoichiometry of 50:50 are found for any of ZnO samples. This is consistent with previous results reported [38] normally O to Zn ratio is either in 60:40 or other way opposite 40:60, over all with 10% variation. But the values obtained here have mostly the variation 10% between zinc and oxygen. Initially in ZnO crystals, mostly oxygen is found greater than zinc in (0001)-Zn, (000-1)-O and (11-20) surfaces, expect (10-10) surface. This is due to the adsorbed hydroxide in oxygen is reason. Even though the careful peak fit fails to distinguish the closely associated hydroxide with zinc oxide. This is also similar to XPS compositional study of polar and non-polar ZnO surface recently reported [33]. Then very less amount of Zn - 32.22% is found at (000-1)-O terminated surface. E-beam films have more zinc than oxygen is because during the e-beam evaporation of ZnO pellets, the oxygen loss is occurred. But in PLD growth process, during the deposition and in post-deposition annealing of sample were done at oxygen atmosphere. So presence of oxygen is more than zinc in PLD thin films. The consistent zinc richness is seen in ZnO pellets irrespective of their processing shows significant loss of oxygen and surface oxygen got hydroxide too. ZnO nanrods have more oxygen than zinc and which consistent with different photoemission angles. This is similar case to the ZnO crystal surfaces. So over all in this study, the stoichiometry of Zn to O is between (32.22% 74.35%) and (25.64% - 67.78%).

4.5 Conclusion

A complete XPS characterisation of differently prepared ZnO surfaces (zinc metal, single crystals, powders, thin film and nanorods) has been undertaken. The calibration and optimisation of binding energy, peak shapes and fitting parameter were obtained and presented for ZnO surfaces. From zinc metal surface characterisation, transition of the metallic Zn state to oxidised ZnO state were clearly found in Zn LMM and Zn 2p peaks. The clear distinction of binding energy difference between Zn, ZnO, $Zn(OH)_2$ and $Zn(CO)_x$ were also found for complex and surface sensitive Zn 2p core level peak. Asymmetric nature of zinc peaks and new surface state peak (Zn_x) at lower B.E. of all zinc peaks is obtained. From Angle resolved XPS (ARXPS) study, the photoemission angle at 30 degrees was found as a suitable angle to collect all surfaces chemical composition of vertically aligned nanorods. Carbon based contamination were found high in IPA cleaned metal surface, (0001)-Zn crystal surface, ZnO powders. Hydroxide based contamination were high on scraped metal surface, (0001)-Zn surface, PLD grown thin films and ZnO powders. In general, the chemical composition ZnO surface was estimated as carbon and related - 23%, oxygen - 32%, zinc - 27%, hydroxide - 15%, water - 3%. The stoichiometry of crystals surfaces (0001)-Zn, (10-10), (11-20), E-beam and nanorods have almost ideal stoichiometry. Oxygen terminated (000-1)

crystal surface, PLD grown thin film have more oxygen atoms and ZnO powder have high zinc concentration.

4.6 Bibliography

[1] M. W. Allen C. H. Swartz, T. H. Myers, T. D. Veal, C. F. McConville, and S. M. Durbin, Phys. Rev. B 81 (2010) 075211.

[2] K. Ozawa, and K. Mase, Phys. Rev. B 83 (2011) 125406.

[3] C. Woll, Prog. Surf. Sci. 82 (2007) 55.

[4] L. Fiermans, E. Arijs, J. Vennik, and W. Maenhout-Van Der Vorst, Surf. Sci. 39 (1973) 357.

[5] V. Avrutin, G. Cantwell, J. Zhang, J. J. Song, and D. J. Silversmith, IEEE Proceeding 98 (2010) 1339.

[6] D-K. Hwang, M-S Oh, J-H Lim and S-J Park, J. Phys. D: Appl. Phys. 40 (2007) R387.

[7] M. Willander, O. Nur, Q. X. Zhao, L. L. Yang, M. Lorenz, B. Q. Cao, J. Zuniga Perez, C. Czekalla, G. Zimmermann,M. Grundmann, A. Bakin, A. Behrends, M. Al-Suleiman, A. El-Shaer, A. Che Mofor, B. Postels, A. Waag, N. Boukos, A. Travlos, H. S. Kwack, J. Guinard and D. L. Si Dang, Nanotechnology 20 (2009) 332001.

[8] L. S. Dake, D. R. her and J. M. Zachara, Surf. Interface Anal. 14 (1989) 71.

[9] B. Mutel, A. Ben Taleb, 0. Dessaux, P. Goudmand, L. Gengembre, J. Grimblot, Thin Solid Films 266 (1995) 119.

[10] M. F. Guimon, G. Pfister-Guillouzo, M. Bremont, W. Brockmann, C. Quet, J.Y. Chenard, Appl. Surf. Sci. 108 (1997) 149.

[11] G. Ballerini, K. Ogle, M.-G. Barthes-Labrousse, Appl. Surf. Sci. 253 (2007) 6860.

[12] S. Noothongkaew, R. Supruangnet, W. Meevasana, H. Nakajima, S. Limpijumnong, P. Songsiriritthigul, Appl. Surf. Sci. 256 (2009) 980.

[13] S. Ben Amor, M. Jacquet, P. Fioux, M. Nardin, Appl. Surf. Sci. 255 (2009) 5052.

[14] M. C. Biesinger, L. W. M. Lau, A. R. Gerson, R. St. C. Smart, Appl. Surf. Sci. 257 (2010) 887.

[15] P. J. Cumpson, M. P.seah and S. J. Spencer, Spectroscopy Europe 10 (1998) 2.

[16] A. V. Naumkin, A. Kraut-Vass, S. W. Gaarenstroom, and C. J. Powell, NIST Standard Reference Database 20, Version 4.1 (web version), http://srdata.nist.gov/xps/, 2012.

[17] J. F. Moulder, W. F. Stickle, P. E. Sobol, K. D. Bomben, Handbook of X-ray Photoelectron Spectroscopy, Perkin-Elmer Corp., Eden Prairie, MN, 1992.

[18] J. Grabowska, K.K. Nanda, E. McGlynn, J.-P. Mosnier, M.O. Henry, Surf. Coat. Technol. 200 (2005) 1093.

[19] A. Herrera-Gmez, A. Hegedus and P. L. Meissner, Appl. Phys. Lett., 81 (2002) 1014.

[20] F. J. Himpsel, F. R. McFeely, A. Taleb-Ibrahimi, and J. A. Yarmoff, Phys. Rev. B 38 (1988) 6084.

[21] A. Molle, M. N. K. Bhuiyan, G. Tallarida, and M. Fanciulli, Appl. Phys. Lett. 89 (2006) 083504.

[22] D. Briggs, Faraday Discuss. Chem. Soc., 60 (1975) 81.

[23] G. E. Hammer and R.M. Shemenski, J. Vac. Sci. Technol. A 1 (1983) 1026.

[24] V. Sirtori, F. Zambon, and L. Lombardi, J. Electron Mat. 29 (2000) 463.

[25] D. Guo, M. Xue, Q. Guo , K. Wu, J. Guo, E.G. Wang, Appl. Surf. Sci. 255 (2009) 9015.

[26] B. Veincent Christ, Hand book of XPS Monochromatic spectra Vol.2 (Commercially pure binary oxides), XPS International LLC, 2007.

[27] H. Morkoc and U. Ozgur, Zinc Oxide fundamentals, materials and device technology, first ed.,Wiley-VCH, 2009.

[28] J. W. Rasmussen, E. Martinez, P. Louka and D. G. Wingett, Expert Opin. Drug Deliv. 7 (2010) 1063.

[29] M. Opel, S. Geprags, M. Althammer, T. Brenninger and R. Gross, J. Phys. D: Appl. Phys. 47 (2014) 034002.

[30] Y. F. Lu, H. Q. Ni, Z. H. Mai, and Z. M. Ren, J. Appl. Phys. 88 (200) 498.

[31] Y. Y. Tay and S. Li, C. Q. Sun, P. Chen, Appl. Phys. Lett. 88 (2006) 173118.

[32] D. C. Look, H. L. Mosbacker, Y. M. Strzhemechny, L. J. Brillson, Superlatt. Microstruct., 38 (2005) 406.

[33] M. W. Allen, D. Y. Zemlyanov, G. I. N. Waterhouse, J. B. Metson, T. D. Veal, C. F. McConville, and S. M. Durbin, Appl. Phys. Lett. 98 (2011) 101906.

[34] I. Sakaguchi and S. Hishita, Surf. Interface Anal. 36 (2004) 645.

[35] J-C. Dupin,D. Gonbeau, P. Vinatier and A. Levasseur, Phys. Chem. Chem. Phys., 2(2000) 1319.

[36] J. C. Vikerman, Surface Analysis - The Principal Techniques, John Wiley and Sons, (1997).

[37] T.G.G. Maffeis, M.W. Penny, A. Castaing, O. J. Guy, S. P. Wilks, Surf. sci. 606 (2012) 99.

[38] R. Heinhold and M. Ward Allen, J. Mater. Res. 27 (2012) 2214.

Chapter 5

XPS and SRPES studies of thermal cleaning and *in-situ* atomic hydrogen cleaning of ZnO(0001) surface

5.1 Introduction

Cleaning of semiconductor surfaces is a critical step in the fabrication of any optimized reliable semiconductor device. About 30% to 40% of the steps involved in the semiconductor device fabrication processes are related to surface cleaning of the semiconductor substrates. This is carried out both in front-end-of-line (FEOL) and back-end-of-line (BEOL) stages of each process to minimise the contamination and keep the device yield high [1]. Effective surface cleaning enhances the electrical properties of semiconductor devices by improving the reliability of both ohmic and Schottky contacts as well as facilitating subsequent epitaxial growth.

One of the problems encountered during the fabrication process of ZnO devices is the difficulty in achieving rectifying Schottky contacts. While an ohmic contact to n-type ZnO is readily achievable, the formation of reliable Schottky contact still remains a technological challenge [2]. The surface contamination of ZnO by carbon and hydroxide species has been reported to produce an electron rich ZnO surface which favours ohmic contact formation [17]. The quality of homo (or) hetero epitaxial layer growth on ZnO substrate is also found to be improved by the surface cleaning of the substrate [19]. Many cleaning processes have been reported for the ZnO surface such as, argon ion sputtering [5], organic solvent cleaning [10], high temperature oxygen annealing [7], ozone [8] and oxygen and helium plasma cleaning treatments [9]. Ar

ion sputtering followed by annealing in vacuum as well as in an oxygen atmosphere have been shown to be effect at removing carbon from the ZnO(0001) surface, but a residual sub-monolayer coverage of hydroxide remained [9]. High temperature oxygen annealing at 1100 °C has been reported to increase the n-type conductivity on both (0001)-Zn and (000-1)-O terminated surfaces along with the formation of atomic steps on the polar surfaces [7]. However, an Ar ion sputtering treatment coupled with high temperature oxygen annealing led to the desorption of zinc atoms from both the (0001)-Zn and (000-1)-O surfaces and the segregation of impurities like Ca, K, Al, Ga with a substantial change in the surface morphology [5]. Organic solvent cleaning treatments have been shown to reduce the concentration of surface contaminates such as carbon and hydroxide [10], while ozone cleaning is effective at removing the surface carbon contamination but not the hydroxide species [9]. In summary, the development of an effective cleaning strategy for the ZnO surface has proved to be challenging due to strong bonding of O-H groups.

Ultra high vacuum (UHV) thermal annealing of a semiconductor surface can be used to remove loosely bonded atoms or molecules from the surface such as water, hydroxide, and hydrocarbons [10]. After initial surface cleaning by wet chemical treatments or *in-situ* ion bombardment, thermal annealing treatments have been successfully applied to many semiconductor surfaces [10, 11]. This has been achieved primarily for oxide contaminant removal from elemental semiconductors such as Si [12] and Ge [13] and III-V compound semiconductors [14]. Annealing of a ZnO surface was previously reported as controlling defects [15], enhancing the electrical conductivity [16] and creating steps on the surface [17]. Annealing in controlled gaseous atmospheres was used as the ZnO substrate preparation procedure for subsequent homoepitaxy [18], heteroepitaxy [19] growth and the production of acceptor carriers [20] in ZnO crystals. High temperature oxygen annealing of ZnO crystals at 700 °C was also investigated as a method of surface cleaning leading to the removal carbon contamination [9]. In this study, we report the UHV annealing of ZnO surfaces at lower temperatures up to 500 °C.

Recently, atomic hydrogen cleaning (AHC) has become an important tool for surface cleaning of III-V semiconductor surfaces [21]. A study of the interaction of atomic hydrogen with MBE grown GaAs surfaces reported that it was effective at producing a clean surface with enhanced semiconducting properties [22]. The atomic hydrogen treatment of the native oxide covered GaAs substrate at 400 °C and a partial H_2 pressure of 10^{-7} mbar resulted in the removal of carbon and surface oxides [23]. Another reported study showed that it was possible to remove the surface carbon contamination by this method at 200 °C while surface oxides were decomposed at 40 °C [24]. The mechanism of the interactions which occur during AHC resulting in the removal of the surface oxides has also been suggested [25]. Efficient designs for an ultra-high vacuum AHC source with either tungsten or tantalum filaments have been published [26, 27]. As well as finding wide application for III-V semiconductors [27],

AHC has been applied to other materials including CdTe, GaN and Al_2O_3 [28–30]. For Al_2O_3, the surface cleaning temperature was reduced from 1050 °C to 600 °C compared to thermal cleaning with a measured reduction in the root-mean-square surface roughness [30]. More recently, AHC procedures have been employed as part of the processing for *in-situ* GaAs wafer bonding [31], Extreme Ultraviolet (EUV) multilayer cleaning [32], copper interconnects and *in-situ* cleaning of ICs [33]. In comparative studies of hydrogen cleaning with simple thermal cleaning, the benefits of AHC include lower sample temperatures and reduced surface roughness [34]. Furthermore, comparing hydrogen plasma cleaning and AHC of Si, it was found that the atomic hydrogen was effective at cleaning the Si at 500 °C while hydrogen plasma cleaning required a temperature of 700 °C [35]. Also, for atomic hydrogen, the time to produce a clean surface was found to decrease, when the temperature was increased.

Interaction of hydrogen with ZnO polar (Zn O-terminated) and prismatic (mixed terminated) surfaces has been reviewed by Woll et al [36] and Monakhov et al [37]. Atomic hydrogen was generated either by the conventional flow of H_2 gas in the presence of a hot tungsten filament [24, 26] or by an electron cyclotron resonance plasma source [23]. In these studies hydrogen was reported to interact with the ZnO surfaces and enhance the n-type conductivity by creating an electron accumulation layer at the surface. Recent studies on the interaction of atomic hydrogen with ZnO surfaces by in-situ ellipsometry [38] and photoemission [39] measurements show that the reactivity is high on the ZnO(0001)-Zn surface with the formation of zinc hydride, while it is less reactive on the ZnO(000-1)-O surface where hydroxide is formed. The reactivity of atomic hydrogen is also found to be sensitive to the termination and the polarity of the surface. Implementation of AHC on ZnO surfaces could be an effective single step cleaning process as an industrially viable technique in terms of low cost, low temperature and *in-situ* processing.

The present work focuses on a comparative study of UHV annealing and atomic hydrogen cleaning of the ZnO (0001) surface. For the UHV annealing study the ZnO surface was characterised by *in-situ* conventional XPS. The low temperature (up to 600 °C) atomic hydrogen cleaning of the ZnO (0001) zinc terminated surface was investigated using *in-situ* synchrotron radiation photoemission (SRPES) spectroscopy.

5.2 Experimental details

5.2.1 For XPS study

A ZnO(0001) Zn-terminated polished crystal of dimensions 1 cm x 1 cm from Crystal GmbH, Germany was loaded into the vacuum system without any pre-treatment. The crystal was clamped in a sample holder and UHV annealing was performed through a resistive heated sample holder. The temperature was measured using a chromel-alumel thermocouple connected with the sample holder. The ZnO crystal surface was annealed for 30 minutes at a range of temperatures (100 °C, 200 °C, 250 °C, 300 °C,

350 °C, 400 °C, 450 °C, 500 °C, 600 °C) and after cool down to room temperature, XPS spectra were recorded. All XPS spectra were recorded by a VG photoelectron spectrometer using Al-Kα radiation (1486.6 eV) as the X-ray excitation source at a pressure of 10^{-9} mbar. The calibration of binding energy scale was performed with the C 1s line (285 eV) from the carbon contamination layer. The XPS core levels were analyzed by using AAanlyser [40] in which a Shirley background is assumed and peak fitting of experimental curves were defined by mixed singlet combinations of Gaussian and Lorentzian line shapes.

5.2.2 For SRPES study

A ZnO(0001) Zn-terminated polished crystal of dimensions 0.5 x 0.5 cm from Crystal GmbH was loaded into the vacuum system without any pre-treatment. The sample was mounted on the holder by tantalum strips and a chromel-alumnel thermocouple was attached. The sample heating was achieved by e-beam bombardment from a tungsten filament at the backside of the holder. An Oxford Applied Research® thermal gas cracker was used for the production of atomic hydrogen. The gas-cracker design uses e-beam heating of a tungsten capillary tube to thermally dissociate the flowing gas. A quasi-equilibrium condition is established as the hydrogen molecules interact with hot capillary walls. The cracking efficiency is then determined by the equilibrium thermodynamics of the dissociation of hydrogen molecules into atoms. For capillary temperatures of 1400 °C or more and pressures below 10^{-8} mbar, the cracking efficiency is in excess of 95% [41]. The H-cracking was carried out throughout the experiment at a hydrogen partial pressure of 1 x 10^{-7} mbar. The working distance between the H source and the sample was 20 cm. The standard operating procedure involved exposure of the ZnO surface to atomic H for 30 minutes at a range of temperatures (300 °C, 400 °C, 500 °C, 600 °C) and recording photoemission spectra at room temperature after each anneal. The synchrotron photoemission experiments were carried out on the SX700 beamline at the Astrid Synchrotron in the University of Aarhus in an ultrahigh vacuum (UHV) system (2 x 10^{-10} mbar). The system was equipped with a hemispherical (VG-CLAM2) electron energy analyser of fixed 100 mm mean radius which was operated at a pass energy of 30 eV.

Photoemission spectra of the following core levels were acquired at the indicated photoelectron energies: O 1s (600 eV), Zn 3p (140 eV and 300 eV) and C 1s (390 eV). The photon energies of 600 eV for O 1s and 140 eV for Zn 3p were chosen so that the kinetic energies of the photoemitted electrons from the core levels were similar (i.e for O 1s, the electron kinetic energy is 600 eV − 532 eV = 68 eV and for Zn 3p, 140 eV − 90 eV = 50 eV, where 532 eV and 90 eV are the binding energies of O 1s and Zn 3p core levels, respectively) which ensures that the sampling depths were comparable. This makes a direct comparison of the intensity ratios meaningful for the determination of relative elemental composition of the surface. The Fermi level of the spectrometer was set to zero by measuring the Fermi level position of a reference gold

sample and the accuracy of the photon energies used in the study were cross checked by acquiring spectra with second order light. Then Zn 3d core level peak was used as a binding reference after the surface carbon signal was removed by surface cleaning.

5.3 Results and Discussion

5.3.1 XPS studies of UHV annealing of ZnO (0001)-Zn surface

In this UHV thermal cleaning of ZnO (0001) surface the survey spectra and the core level spectra of C 1s, O 1s, Zn 2p were recorded for every annealing temperature including the as received sample. Survey spectra for 300 °C and 500 °C annealing temperatures are shown in figure 5.1. The binding energy of the peaks are as follows: Zn 3d - 9.75 ± 0.25 eV, Zn 3p - 88.65 ± 0.15 eV, Zn 3s - 139.65 ± 0.15 eV, Cl 2p - 199.5 eV, C 1s - 285 ± 0.15 eV, Zn LMM - 476 ± 0.5 eV & 499 ± 0.5 eV, O 1s - 532 ± 0.5 eV, and Zn 2p - 1024.5 ± 0.75 eV. There is a reduction in the carbon signal with anneal and this results in an increase in the intensity of the ZnO substrate peaks.

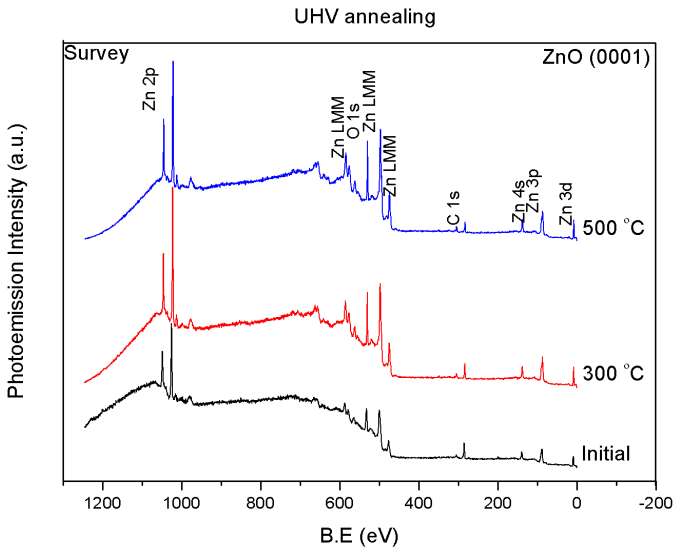

Figure 5.1: Survey spectra of UHV annealed ZnO (0001)-Zn surface.

Zinc LMM Auger peaks for these annealing temperatures are shown in figure 5.2. Annealing at 300 °C and above results in the Zn LMM peak moving from 986.91 eV to 989.27 eV consistent with reports for surfaces with reduced contamination [42,43].

The peak fitted C 1s core level spectra for the same annealing temperatures are shown in figure 5.3. The primary C-C peak is at 285 eV, while additional higher binding energy peaks are present (C-O) at 286.7 ± 0.2 eV and O-C=O at 288.5 ± 0.5 eV. Higher temperature anneals to 500 °C do not result in any significant change in the peak profile, but there is a reduction in intensity which will be discussed in chapter 7.

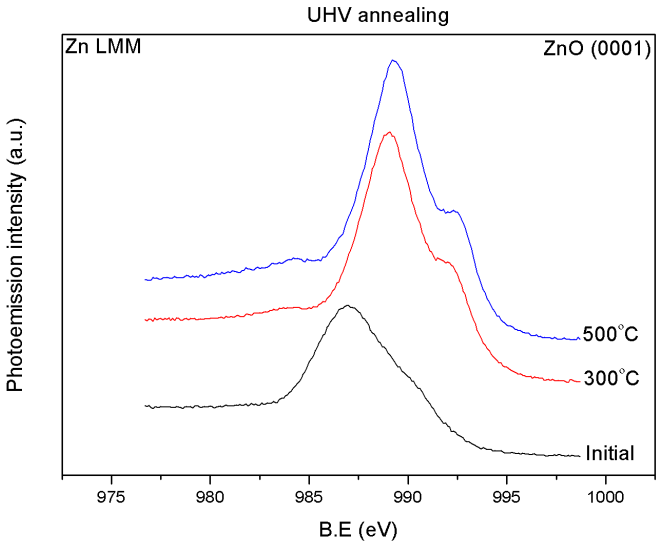

Figure 5.2: Zinc Auger peak - Zn LMM spectra for successive annealing temperatures.

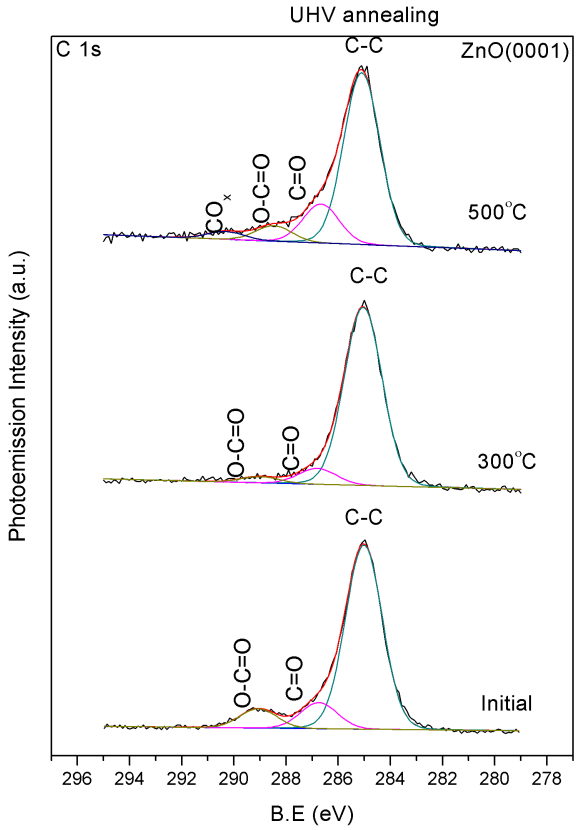

Figure 5.3: C 1s core level spectra with peak fitting for as received and following a 500 °C anneal in UHV.

The oxygen peak for ZnO(0001) surface is shown in figure 5.4 and can be curve fitted with the following component peaks O-Zn - 530 ± 0.1 eV, OH - 531.5 ± 0.3

eV and H_2O - 532.4 ± 0.1 eV. By annealing at higher temperatures (>100 °C) the hydroxide component peak is reduces while the water related peak was completely removed at 300 °C. Overall there is a significant reduction in the surface hydroxide signal with anneal reflecting the removal of the surface contamination layer.

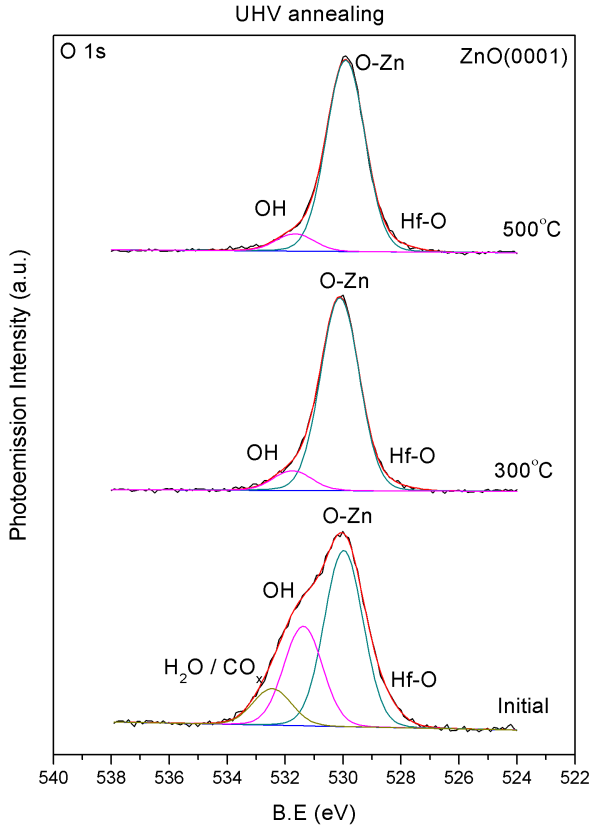

Figure 5.4: O 1s core level peaks fitted with ZnO, OH, H_2O peaks for the as received surface and following a 500 °C anneal.

The chlorine is an electronegative contaminant naturally found on the ZnO surfac [42]. The change in intensity of the Cl 2p core level peak following a 500 °C anneal is shown in figure 5.5. In this chlorine doublet peak, the binding energy Cl 2p 3/2 peak is 199 ± 0.1 eV. Up to an annealing temperature of 300 °C there is very little change in the peak profile, however annealing at 500 °C completely removed the contaminant from the ZnO(0001) surface.

Figure 5.6 shows the Zn 2p core level for UHV annealed ZnO(0001)-Zn surface. Zn 2p is a surface sensitive peak because of its high binding energy (>1000 eV). The Zn 2p core level peak profile is curved fitted with a primary ZnO peak, a secondary hydroxide peak, a Zn surface state peak and an additional contamination of zinc carbonate. The binding energies are, Zn_x - 1020.7 ± 0.2 eV, ZnO - 1022 ± 0.1 eV, $Zn(OH)_2$ - 1023 ± 0.1 eV and $ZnCO_x$ - 1024.5 ± 0.5 eV. No significant change in the chemical species occurs in the annealing cycle, but there is a reduction in the

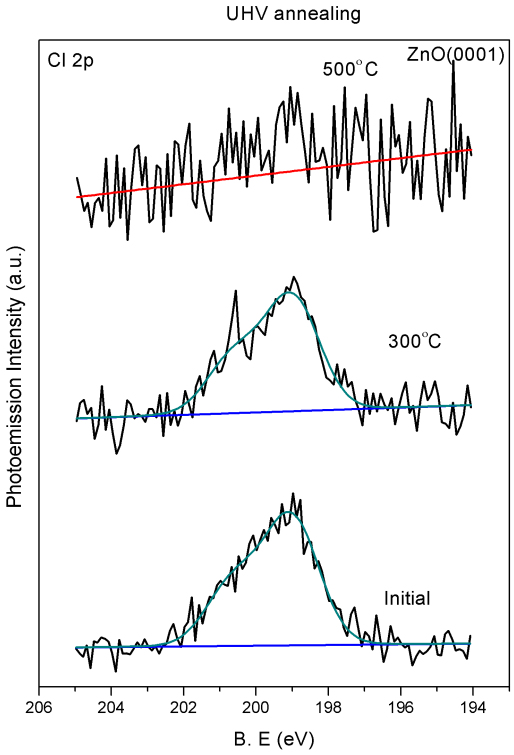

Figure 5.5: Cl 2p core level peak on ZnO surface for as received and following a 500 °C anneal.

$Zn(OH)_2$ peak at the 500 °C anneal.

The XPS chemical composition analysis of the ZnO (0001) surface for UHV annealing at different temperatures is shown in figure 5.7. The XPS atomic percentages were calculated by dividing the area of peak with the appropriate relative sensitive factor (RSF) for the particular element. There is a clear trend showing the reduction in intensity of the surface contaminants of carbon, hydroxide, water and chlorine, however, there is still substantial surface contamination present following the 500 °C anneal. An alternative approach of atomic hydrogen cleaning of ZnO at similar temperatures was then undertaken.

5.3.2 SRPES studies of atomic hydrogen cleaning of ZnO (0001)-Zn surface

The survey spectra, acquired at a photon energy of 600 eV for the different temperatures during the atomic hydrogen exposure of the ZnO (0001)-Zn surface are shown in figure 5.8. The photoelectron peaks of Zn 3d (11 eV), Zn 3p (90 eV), Zn 3s (141 eV), C 1s (286 eV) and O 1s (532 eV) are identified in the spectra and clearly display the reduction in the surface carbon signal as a function of higher exposure temperature. The Zn and O related photoemission features become more pronounced as the surface carbon contamination layer, estimated to be between 1 - 2 nm is effectively removed

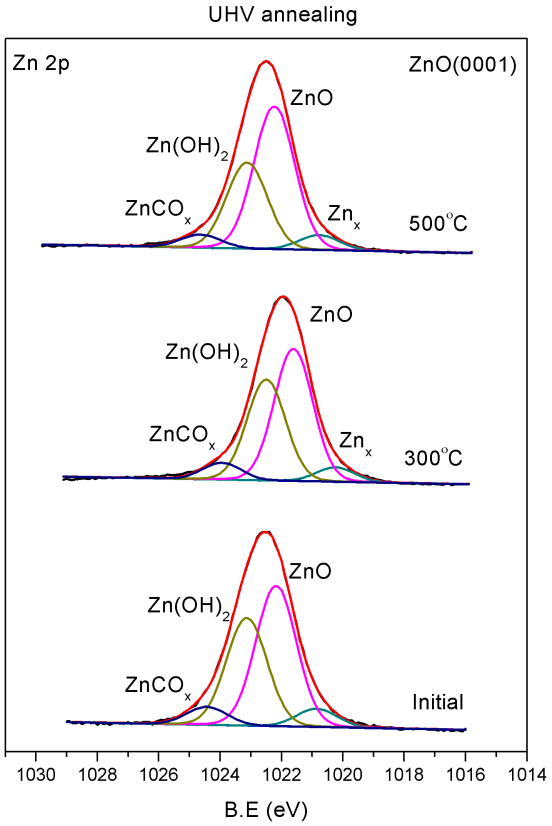

Figure 5.6: Zinc peak - Zn 2p core level for as received and following a 500 °C anneal.

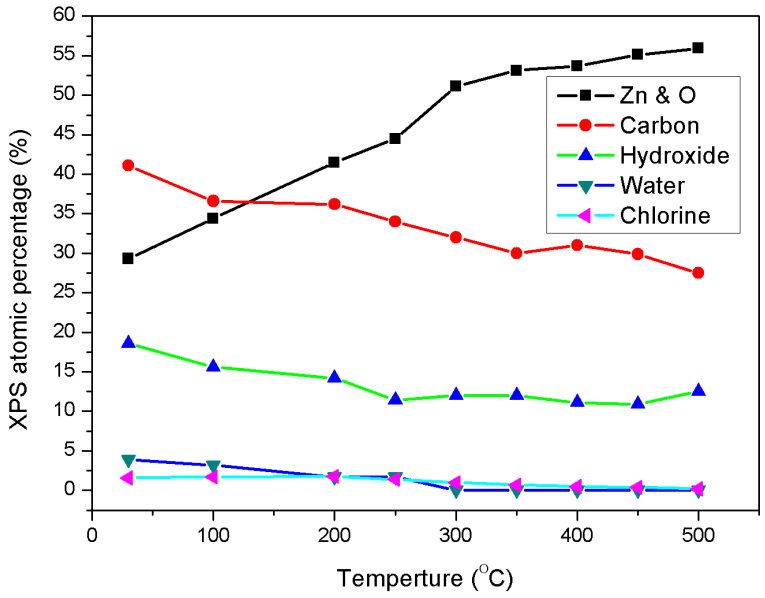

Figure 5.7: Chemical composition (atomic %) of ZnO(0001) surface for different UHV annealing temperatures.

at 600 °C. The binding energy difference between the O 1s and Zn 3p for the cleaned surface is 442.0 eV which is in agreement with the expected value for ZnO [42].

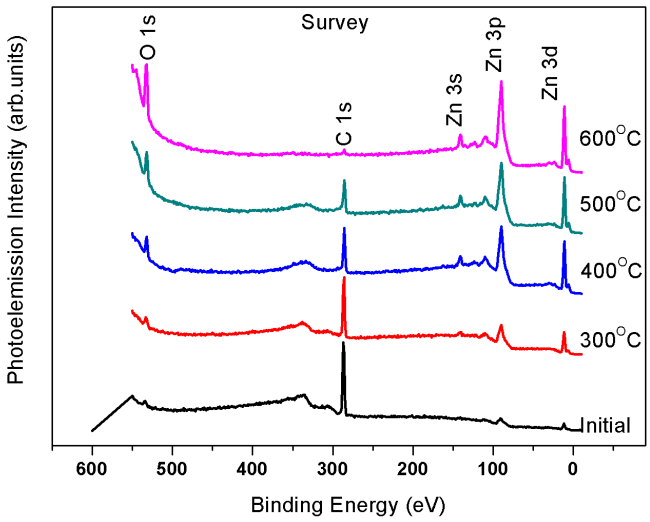

Figure 5.8: ZnO survey spectra of the as received and atomic hydrogen treated surface as a function of annealing temperature acquired at a photon energy of 600 eV.

For narrow scans of the C 1s, shown in figure 5.9, a photon energy of 390 eV was chosen in order to enhance the surface sensitivity. The spectra show a trend of the change in intensity of the C 1s signal as a function of the temperature at which the atomic hydrogen cleaning was performed. The spectra have been curve fitted with four component peaks which have binding energies consistent with carbon C-C bonds (285 eV), carbon monoxide C-O (286 eV), carbon dioxide C=O species (286.2 eV) and carboxyl species O-C=O (288 eV) [44]. In the as-received condition and following the 300 °C atomic hydrogen exposure, the ambient adsorbed C-C and C-O bonds can be detected. Further oxidation of carbon into C=O and O-C=O is observed at annealing temperatures of 400 °C and 500 °C. This is attributed to the dissociation of C-C bonds and subsequent carbon reacting with oxygen atoms dissociated from water or hydroxide species adsorbed on the ZnO surface. A significant reduction (40%) in the carbon contamination only begins to become apparent following hydrogen cleaning at 500 °C, while at 600 °C the complete removal of carbon contamination, to within the photoemission detection limit is attained.

The O 1s core level spectrum of the as-received surface shown in figure 5.10(a) is an extremely weak signal and confirms the contaminated nature of the as-received surface especially in this very surface sensitive measurement mode with minimized sampling depth. A small signal for adsorbed water is seen at 534.8 eV binding energy on the as-received surface and following the 300 °C anneal. Following the 400 °C anneal, it is apparent that there are two component peaks in the spectrum which were curve fitted using (1) an O-Zn bond at 532.4 eV and (2) a hydroxide bond at

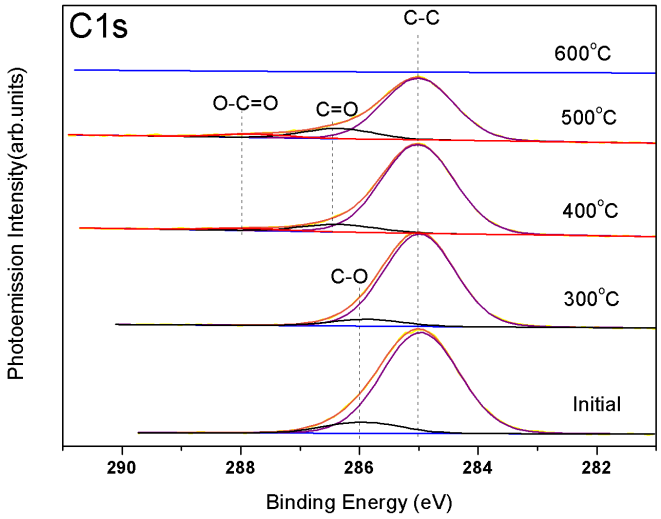

Figure 5.9: C 1s core level spectra of atomic hydrogen cleaning from as received to 600 °C.

533.8 eV binding energy. With increasing temperature, the intensity of the oxygen signal in the ZnO bonding configuration increases as displayed in the O 1s peak area analysis graph in figure 5.10(b) showing that there is no reduction of the relative hydroxide component peak intensity. This demonstrates the stability of the hydroxide bonding to the ZnO(0001) surface. However, the extreme surface sensitivity of these measurements means that the signal associated with the surface hydroxide component is accentuated compared with conventional XPS studies. This result is also consistent with previous reports of the atomic hydrogen cleaning of Si substrates in which it was effective at the removal of carbon but not at breaking Si-O bonds [35]. It is also in agreement with recent reports which showed that even in remote oxygen plasma cleaning of ZnO(0001)-Zn and ZnO (000-1)-O surfaces, the removal of H on O-terminated surface is not completely achieved [9, 45]. The estimation of thickness of hydroxide component peak on ZnO surface following the 600 °C anneal is considerably below 1 atomic layer and may well reflect the recontamination of the cleaned surface by residual oxygen in the chamber, even at UHV.

The Zn 3p core level (BE = 90 eV) spectra shown in figure 5.11(a) were acquired at 140 eV and curve fitted with two principle component peaks separated by 1 eV attributed to ZnO at 88.5 eV and the surface $Zn(OH)_2$ at 89.6 eV consistent with previous reports in the literature [46] and a small component at lower binding energy (87.5 eV), attributed to a surface state related feature, becomes apparent following the 300 °C anneal [47]. The increase in the area of Zn 3p peak as a function of the annealing temperature shown in the figure 5.11(b) confirms the inability of this surface preparation treatment to desorb the surface hydroxide component despite its effectiveness at removing the surface carbon contamination. Following the 300 °C atomic hydrogen treatment there is no subsequent change in the Zn 3p to O 1s in-

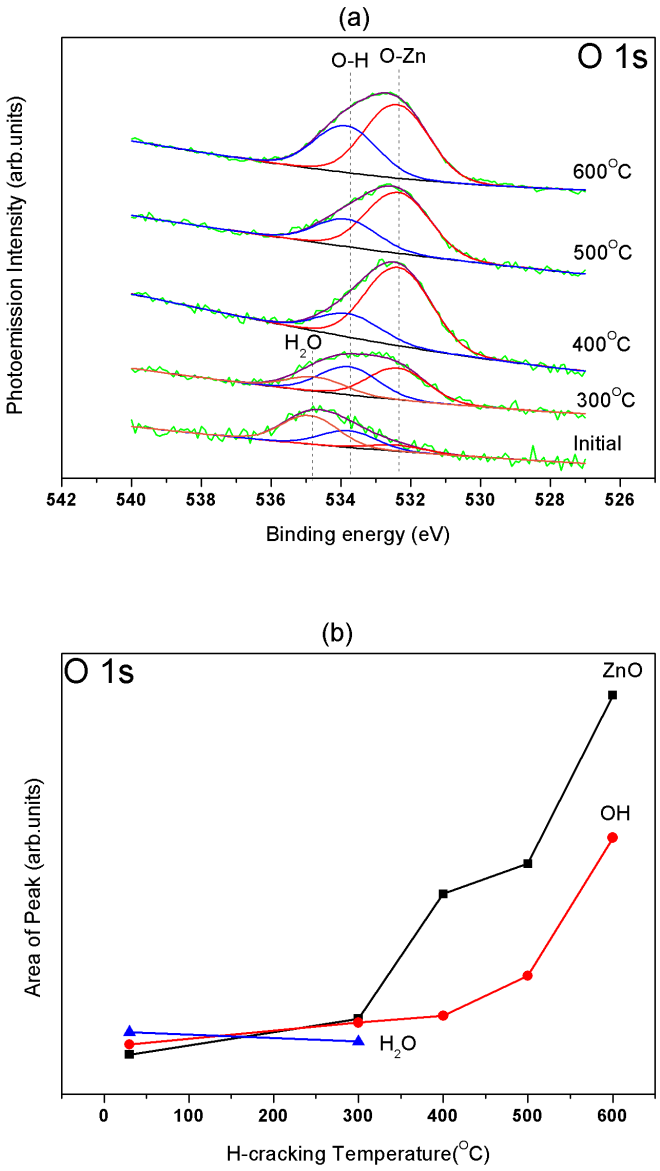

Figure 5.10: (a) O 1s core level spetra from the as received surface to the 600 °C atomic hydrogen treated surface and (b) quantitative area analysis graph for O-Zn, hydroxide and C-O as a function of treatment.

tensity ratio indicating that the removal of surface contamination is not impacting on the stoichiometry of ZnO.

The ratios of C 1s to Zn 3p and Zn 3p to O 1s peak intensities as a function of cleaning temperature are shown in figure 5.12. The almost complete removal of C 1s signal following the 600 °C anneal is clearly observed. But this surface cleaning does not substantially impact on the Zn 3p to O 1s ratio which is basically constant indicating that the hydrogen cleaning is not impacting on the stoichiometry of ZnO. Figure 5.13 shows a plot of the estimated thickness of the surface carbon contamination layer which was calculated from the changes in the intensity of the Zn 3p peak with hydrogen cleaning by considering the inelastic mean free paths given in the NIST

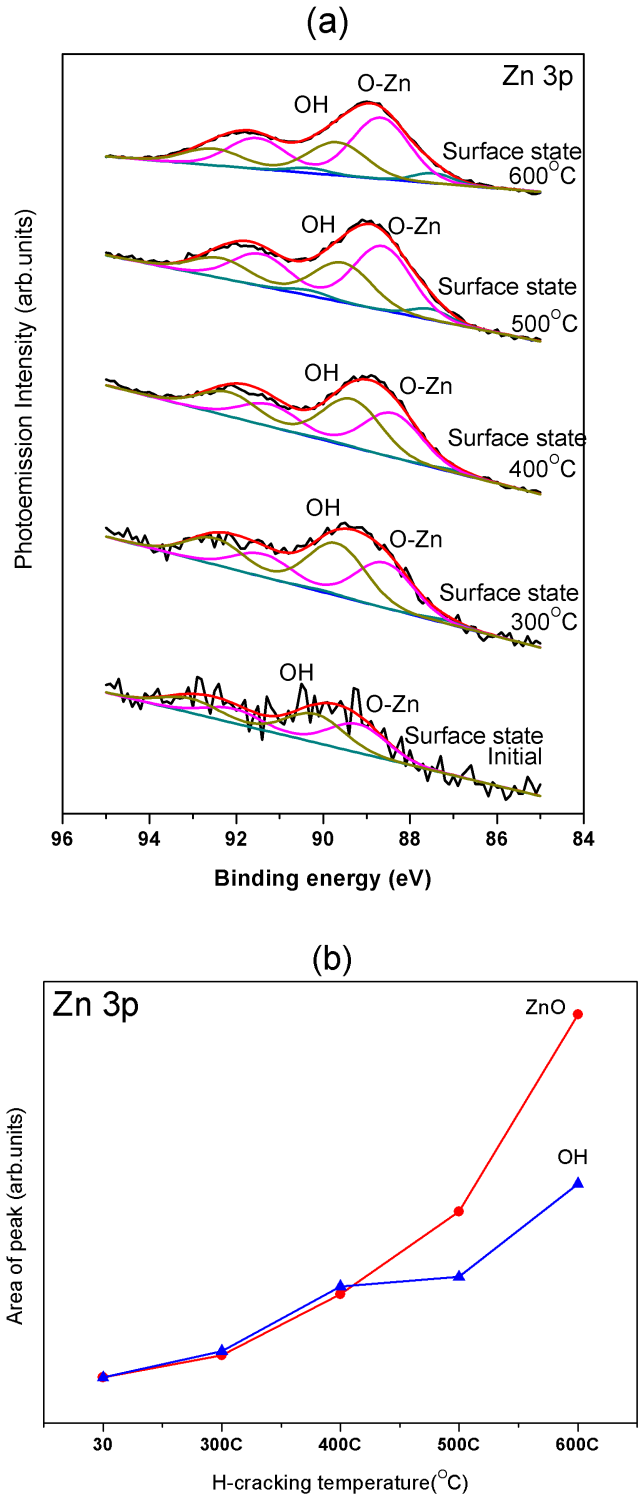

Figure 5.11: (a) Peak fitted Zn 3p core level spectra as a function of annealing temperature with prominent ZnO and Zn-OH spectral features and evidence of a surface state component at lower binding energy and (b) quantitative area analysis for the change in intensity of the zinc oxide and zinc hydroxide component peaks with increasing treatment temperature.

database [48].

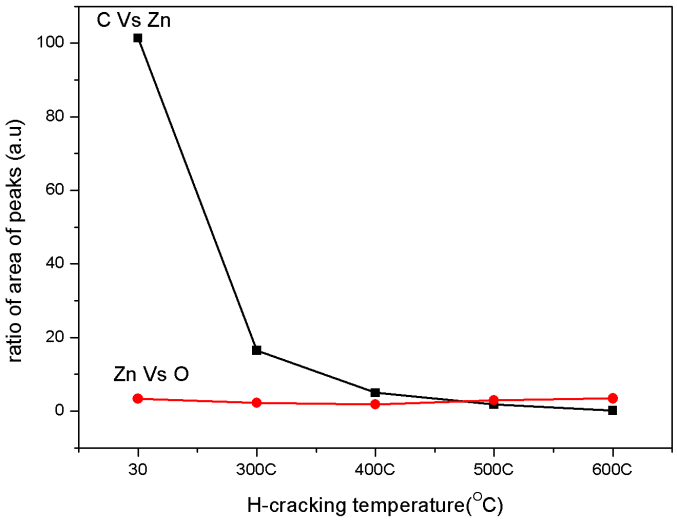

Figure 5.12: Area ratios of carbon vs zinc and zinc vs oxygen as function of atomic hydrogen cleaning temperature

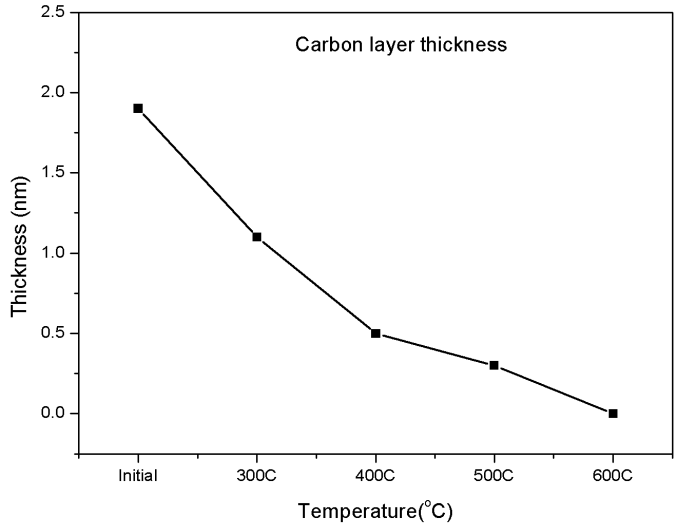

Figure 5.13: Area ratios of carbon vs zinc and zinc vs oxygen as function of atomic hydrogen cleaning temperature

These results differ from a previous atomic hydrogen study using Kelvin probe measurements [49] and a more recent synchrotron radiation photoemission study on atomically clean ZnO(10-10), ZnO(000-1) and ZnO(0001) surfaces [39, 50, 51]. They reported that the atomic hydrogen readily bonded with both the ZnO(10-10) Zn(000-1) surfaces resulting in a metallic surface as the Fermi level moves into the conduction band. For the Zn terminated ZnO(0001) surface, the interaction with hydrogen re-

sulted in a zinc hydride termination. This different behaviour with atomic hydrogen is attributed to the fact that the exposed surfaces in these studies were atomically clean rather than covered with an ambient contamination layer. Previously studies of both oxygen plasma and ozone cleaning treatments of ZnO surfaces reported the presence of hydroxide after the removal of the surface carbon contamination layer [9, 46]. A schematic model of the removal of surface carbon contamination by the atomic hydrogen induced formation of volatile hydrocarbon species and the formation of a hydroxide terminated surface is shown in figure 5.14.

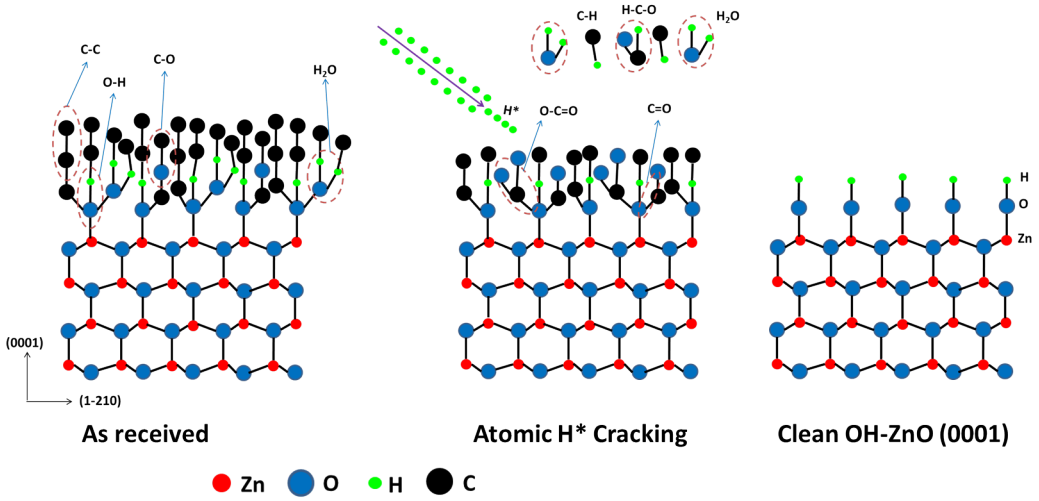

Figure 5.14: Schematic diagram of the atomic hydrogen removal of the ZnO surface contamination layer and the formation of a hydrogen terminated surface

The valance band (VB) spectra acquired at a photon energy of 60 eV shown in figures 5.15 reveal that surface contamination dominates the observed spectral features prior to the atomic hydrogen treatment. The VB spectrum for the as received sample shows a carbon related feature at 7 eV B.E. with the emergence of the Zn 3d peak (10-11 eV) and a distinct Zn 4p - O 2p feature at 4.65 eV appearing following the 300 °C and 400 °C atomic hydrogen treatments, respectively. As the surface contamination is removed with hydrogen cleaning between the 500 °C and the 600 °C treatments, there is an increase in the binding energy of the Zn 3d peak, of approximately 0.2 eV. This peak shift is attributed to the movement of the Fermi level towards the conduction band reducing the band bending present on the contaminated surface. The spectra of the 600 °C cleaned surfaces indicate that the valence band maximum is at 2.8 eV from the Fermi level position (0 eV on the x-axis). The valence band spectra for the 400 °C and 500 °C treatments show clear evidence of occupied states in the bandgap i.e. above the clean surface valence band maximum and below the Fermi level. The fact that the core level peak positions do not move by any appreciable extent during the cleaning process which clearly removes the surface contamination as evidenced by the attenuation of emission from energy states above the ZnO valence band maximum illustrates the difficulty in moving the Fermi level position in the bandgap.

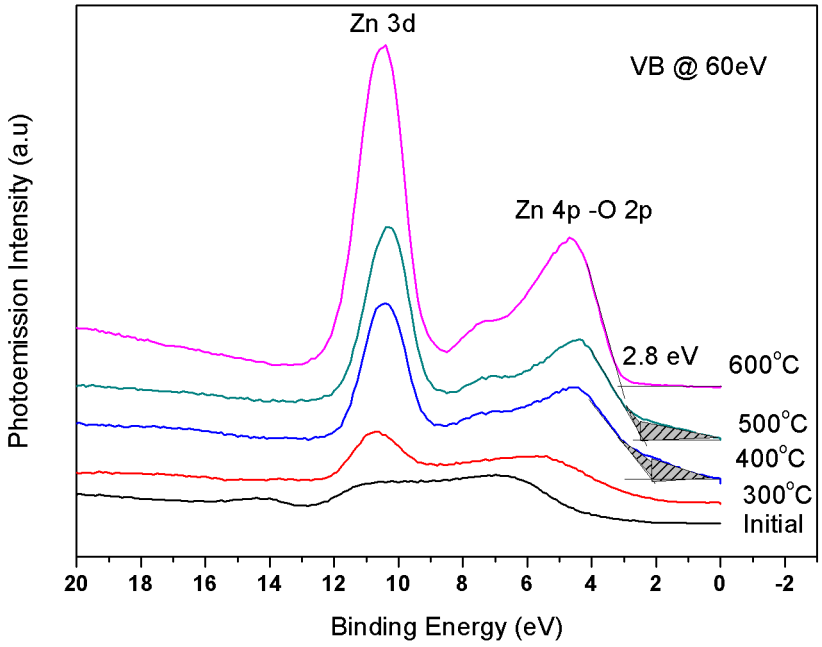

Figure 5.15: Valance band spectra acquired at a photon energy 60 eV for the as-loaded Zn(0001) surfaced and as a function of atomic hydrogen treatments up to 600 °C annealing temperature.

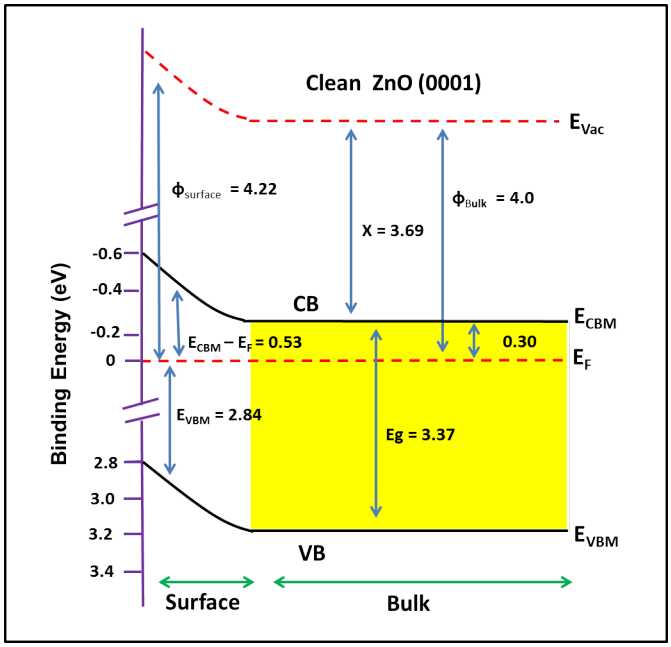

Figure 5.16: Schematic diagram of the band alignment on the clean ZnO(0001) surface after atomic hydrogen cleaning

In figure 5.16 a schematic energy band diagram for the cleaned ZnO(0001) surface is shown. The band gap (Eg) of ZnO is taken as 3.37 eV, the electron affinity as 4.0 eV and the measured work function of the cleaned surface was 4.2 eV. The location

of the valence band maximum with respect to the Fermi level position indicates that there is upward banding of 0.53 eV at the cleaned ZnO surface. The changes in the morphology of the ZnO (0001) surface induced by the hydrogen cleaning was characterized by atomic force microscopy measurements made in non-contact mode in air and are shown in figure 5.17. The RMS surface roughness values reduced from 4 nm to 2.1 nm following hydrogen cleaning and confirmed that this treatment does not increase surface roughness as is the case with argon bombardment treatment.

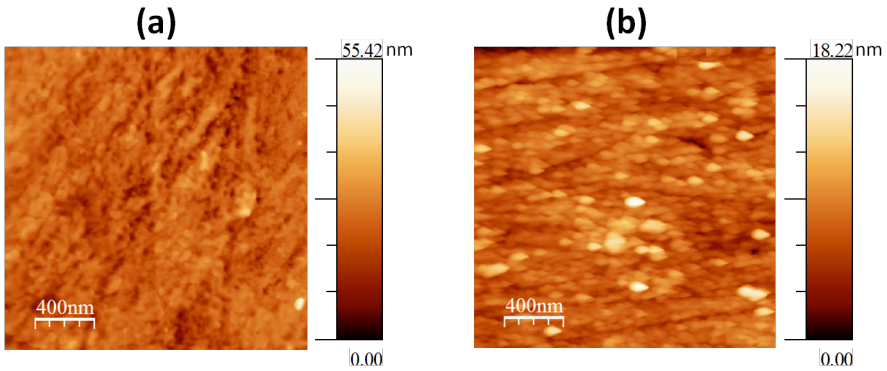

Figure 5.17: Schematic diagram of the band alignment on the clean ZnO(0001) surface after atomic hydrogen cleaning

5.4 Conclusions

The XPS study of UHV annealing of the ZnO (0001)-Zn surface up to 500 °C, removed some of the surface contamination, but was not successful in achieving the objective of producing a clean surface. The photoemission study of the atomic hydrogen cleaning of the ZnO(0001) Zn-terminated surface from room temperature to 600 °C was carried out to determine the optimum treatment to remove surface contaminants and not impact on the surface stoichiometry. At 600 °C, the surface carbon contamination is removed, however, there is a residual hydroxide termination of the surface. This may well be as a result of recontamination of the cleaned surface even in UHV due to the high reactivity of this surface, Valence band spectra show that the cleaning process results in the removal of defect states degenerate with the ZnO bandgap however, this does not result in any substantial movement in the Fermi level position which resides 0.53 eV from the conduction band minimum.

5.5 Bibliography

[1] Leading Edge Semiconductor Cleaning Technologies. Sony Corp.CX-News 36 (2004).

[2] C. Jagadish and S. J. Pearton(Eds.), Zinc Oxide bulk, thin films and nanostructures, first ed., Elsevier, 2006.

[3] L. J. Brillson and Y. Lu, J. Appl. Phys., 109 (2011) 121301.

[4] T. Nakamura, K. Masuko, A. Ashida, T. Yoshimura, N. Fujimura, J. Cryst. Growth, 318 (2011) 516.

[5] R. Lindsay, C. A. Muryn, E. Michelangeli, G. Thornton, Surf. Sci., 565 (2004) L283.

[6] J. Dumont, T. Seldrum, S. Couet, C. Moisson, D. Turove, R. Sporken, J. Vac. Sci. Technol. B, 24 (2006) 2124.

[7] S. Graubner, C. Neumann, N. Volbers, B. K. Meyer, J. Blsing and A. Krost, Appl. Phys. Lett., 90 (2007) 042103.

[8] K. Ip, B. P. Gila, A. H. Onstine, E. S. Lambers, Y. W. Heo, K. H. Baik, D. P. Norton, S. J. Pearton, S. Kim, J. R. LaRoche, F. Ren, Appl. Surf. Sci., 236 (2004) 387.

[9] B. J. Coppa, C. C. Fulton, P. J. Hartlieb, R. F. Davis, B. J. Rodriguez, B. J. Shields, R. J. Nemanich, J. Appl. Phys., 95 (2004) 5856.

[10] L. K. E. Ericsson, H. M. Zhang, K. O. Magnusson, Surf. Sci., 612 (2013) 15.

[11] U. Diebold, L. Vogel Koplitz, O. Dulub, Appl. Surf. Sci., 237 (2004) 336.

[12] A. Ishizaka and Y. Shiraki, J. Electrochem. Soc., 133 (1986) 666.

[13] D. Wang, Y-L Chang, Q. Wang, J. Cao, D. B. Farmer, R. G. Gordon, and H. Dai, J. Am. Chem. Soc., 126 (2004) 11602.

[14] Z. Liu, Y. Sun, F. Machuca, P. Pianetta, W. E. Spicer, and R. F. W. Pease, J. Vac. Sci. Technol. B, 21 (2003) 1953.

[15] Z. Q. Chen, S. Yamamoto, M. Maekawa, A. Kawasuso, X. L. Yuan and T. Sekiguchi, J. Appl. Phys., 94 (2003) 4807.

[16] D-C Oh, H-J Ko, S-K Han, S-K Hong, W-G Jeong, and T. Yao, Appl. Phys. Express, 5 (2012) 075801.

[17] X. Gu, M. A. Reshchikov, A. Teke, D. Johnstone, and H. Morkoc B. Nemeth and J. Nause, Appl. Phys. Lett., 84 (2004) 2268.

[18] C. Neumann, S. Lautenschlger, S. Graubner, J. Sann, N. Volbers, B. K. Meyer, J. Blsing, A. Krost, F. Bertram, and J. Christen, Phys. Stat. Sol. (b), 244 (2007) 1451.

[19] T. Suzuki, C. Harada, H. Goto, T. Minegishi, A. Setiawan, H. J. Ko, M-W Cho, T. Yao, Curr. Appl. Phys., 4 (2004) 643.

[20] N. Y. Garces, N. C. Giles, and L. E. Halliburton, G. Cantwell and D. B. Eason, D. C. Reynolds and D. C. Look, Appl. Phys. Lett., 80 (2002) 1334.

[21] B. Brennan, K. Kumarappan, G. Hughes, Phys. Stat. Sol. (RRL), 7 (2013) 989.

[22] R. Z. Bachrach, R. D. Bringans, J. Phys. Colloques, 43 (1982) C5-145.

[23] A. Takamori, S. Sugata, K. Asakawa, E. Miyauchi, H. Hashimoto, Jpn. J. Appl. Phys., 26 (1987) L142.

[24] T. Sugaya, M. Kawabe, Jpn. J. Appl. Phys., 30 (1991) L402.

[25] M. Yamada, Y. Ide, Jpn. J. Appl. Phys., 33 (1994) L671.

[26] A. Sutoh, Y. Okada, S. Ohta, M. Kawabe, Jpn. J. Appl. Phys., 34 (1995) L1379.

[27] C. Eibl, G. Lackner, A. Winkler, J. Vac. Sci. Technol. A, 16 (1998) 2979.

[28] G. R. Bell, N. S. Kaijaks, R. J. Dixon, C. F. McConville, Surf. Sci., 401 (1998) 125.

[29] Y. Luo, D. A. Slater, M. Levy, R. M. Osgood, Appl. Surf. Sci., 104 (1996) 49.

[30] Y. Okamoto, S. Hashiguchi, Y. Okada, M. Kawabe, Jpn. J. Appl. Phys., 37 (1998) L1109.

[31] T. Akatsu, A. Plossl, H. Stenzel, U. Gosele, J. Appl. Phys., 86 (1999) 7146.

[32] S. Graham, C. Steinhaus, M. Clift, L. Klebanoff, S. Bajt, Proc. SPIE 5037 (2003) 460.

[33] A. Izumi, T. Ueno, A. Tsukinari, A. Takada, ECS Meeting Abstracts. 502 (2006) 793.

[34] L. S. Hirsch, Z. Yu, S. L. Buczkowski, T. H. Myers, M. R. Richards-Babb, J. Electron. Mater., 26 (1997) 534.

[35] A. ABmuth, T. Stimpel-Lindner, O. Senftleben, A. Bayerstadler, T. Sulima, H. Baumgrtner, I. Eisele, Appl. Surf. Sci., 253 (2007) 8389.

[36] C. Woll, Prog. Surf. Sci., 82 (2007) 55.

[37] E. V. Monakhov, A. Y. Kuznetsov and B. G. Svensson, J. Phys. D: Appl. Phys. 42 (2009) 153001.

[38] M. Losurdoa and M. M. Giangregorio, Appl. Phys. Lett. 86, (2005) 091901.

[39] K. Ozawa, and K. Mase, Phys. Rev. B, 83 (2011) 125406.

[40] A. Herrera-Gmez, A. Hegedus and P. L. Meissner, Appl. Phys. Lett. 81 (2002) 1014.

[41] Thermal Gas Cracker, http://www.oaresearch.co.uk/

[42] John F. Moulder, William F. Stickle, Peter E. Sobol, Kenneth D. Bomben, Jill Chastain, Handbook of X-ray Photoelectron Spectroscopy, Perkin-Elmer Corporation, 1992.

[43] L. S. Dake, D. R. Baer and J. M. Zachara, Surf. Interface Anal. 14 (1989) 71.

[44] www.lasurface.com/database/elementxps.php(XPS Database).

[45] H. L. Mosbacker, Y. M. Strzhemechny, and B. D. White, P. E. Smith, D. C. Look, D. C. Reynolds, C. W. Litton, and L. J. Brillson, Appl. Phys. Lett. 87, (2005) 012102.

[46] J. Robertson, Papers from the international conference on silicon dielectric interfaces, 3 ed., AVS, Raleigh, NC (USA), 2000, pp. 1785.

[47] Y.Y. Tay, S. Li, C.Q. Sun, P. Chen, Appl. Phys. Lett. 88 (2006) 173118.

[48] http://www.nist.gov/srd/nist71.cfm, 2009.

[49] H. Moormann, D. Kol and G. Heiland, Surf. Sci., 80 (1979) 261.

[50] K. Ozawa, K. Mase, Phys. Stat. Sol. (a) 207 (2010) 277.

[51] R.T. Girard, O. Tjernberg, G. Chiaia, S. Soderholm, U.O. Karlsson, C. Wigren, H. Nylon, I. Lindau, Surf. Sci.373 (1997) 409.

Chapter 6

XPS and SRPES studies of effect of *ex-situ* organic solvent cleaning of ZnO polar and non-polar surfaces

6.1 Introduction

Wet chemical surface cleaning procedures for semiconductor wafers are well established and widely used in semiconductor device manufacturing. The advantages of wet chemical surface cleaning are that it is generally cost-effective, applicable to large scale and large area wafers, availability of wide range of highly pure chemicals and the selective removal of particular contaminants etc. Wet chemical cleaning is used in the industry to remove organic contaminants, ionic contaminants, native oxides, particles and metals from semiconductor surfaces [1]. One of the mostly widely used wet chemical cleaning process for surface cleaning of silicon was developed by Radio Corporation of America (RCA) in 1965 [2]. This RCA cleaning process is still employed as a basic silicon wafer cleaning method in research laboratories and IC manufacturing industries. Later, a modified RCA and an IMEC wet chemical cleaning process were developed for silicon wafers [3]. For III-V semiconductors, several wet chemical cleaning methods have been developed [4] and successfully employed in the device manufacturing process [5].

As previously mentioned in chapter 5, the surface cleaning of ZnO substrates is essential to explore the intrinsic optical and electrical properties of pure ZnO surfaces. It is also critical to making reliable Schottky contacts and preparing the surface for the growth of as well as heterostructures for the fabrication of optoelectronic devices. The different types of surface cleaning methods applied for ZnO surfaces were already discussed in chapter 5. For ZnO surface cleaning, several different wet chemical clean-

ing processes were employed with range of different chemicals. Earlier studies of ZnO surface cleaning investigated the use of phosphoric acid, hydrochloric acid and deionized water [6]. Then for making intimate metal contacts on ZnO, trichloroethylene, acetone and methanol were used as cleaning solvents [7–9]. In addition, deposited thin films [10] and metals [11, 12] deposited on ZnO [13] cleaned by acetone, dimethyl sulfoxide (DMSO) and toluene have been reported. Further wet chemical cleaning solvents like, trichloroethylene, methanol, alcohol, isopropyl alcohol, tetra methyl ammonium hydroxide(TAMH), dilute HCl, were used for surface cleaning of different crystallographic surfaces of ZnO prior to the metal deposition for both ohmic and Schottky contact studies [14–18]. ZnO surfaces have also been cleaned by NH_4-buffered HF (BHF) and ethanol for expitaxial growth of homo-structures [19].

The most commonly used chemicals for *ex-situ* surface cleaning of ZnO single crystals are, acetone, DMSO(dimethyl sulfoxide) and toluene were chosen for these XPS studies. Acetone will remove the carbon contamination and fluid layers from the surface [10]. The DMSO and toluene remove both polar and non-polar organic contaminants [10]. The aim of the present study is twofold. Firstly, to investigate the effect of surface cleaning by these organic solvents acetone, DMSO and toluene on three different single crystal ZnO surfaces, the polar Zn(0001) and O(000-1) and non-polar (10-10) surfaces and identifying the best one for each surface as measured by x-ray photoelectron spectroscopy. Secondly, examine the effect of ethanol surface cleaning on all four ZnO surfaces: (0001), (000-1), (10-10) and (11-20) as determined by synchrotron radiation photoemission spectroscopy (SRPES).

6.2 Experimental

Polished ZnO single crystal polar Zn(0001), O(000-1) terminated surfaces and non-polar (10-10), (11-20) mixed terminated surfaces were purchased from Crystal GmbH, Germany. For XPS studies 1.0 x 1.0 x 0.5 cm size of the crystals was used. Three organic solvents acetone (99.5%), dimethyl sulfoxide (DMSO) (99.99%) and toluene (99.5%) were used for wet chemical surface cleaning of ZnO crystals. Samples were ultrasonically cleaned in each solvent about 10 minutes and dried by flowing N_2 gas. They were then immediately loaded into the UHV preparation chamber through a load lock and pumped down to 10^{-6} mbar and kept in this vacuum for 3 hours prior to being transfered into the analysis chamber (1.0 x 10^{-9} mbar). XPS spectra were recorded for each separate cleaning in each solvents and following exposure to air for one week to record the recontamination. Finally the spectra were acquired for re-contaminated crystals which were cleaned in all solvents. The detailed experimental procedure for wet chemical cleaning was explained in chapter 3. XPS characterisation was done using a VG photoelectron spectrometer with Mg-Kα (1253.6 eV) radiation at a pressure of 10^{-9} mbar. The calibration of binding energy scale was performed with the C 1s line (285 eV) from the carbon contamination layer. XPS peak fitting

were done by AAanlyser [20] and XPS atomic percentage were calculated using the relative sensitive factors (RSF) from the XPS Handbook [21].

For synchrotron photoemission studies, 5 x 5 x 0.5 mm ZnO crystals were used and ethanol was used as the cleaning solvent. The samples were cleaned by ethanol solution for 6 minutes in an ultrasonic bath before being dried by flowing gas. The samples were then placed into the load lock and pumped down to a pressure of 2 x 10^{-5} mbar. After 5 hours, the samples were transferred to the analysis chamber which has a base pressure of 4 x 10^{-9} mbar. These photoemission experiments were carried out on the SX700 beamline at Institute for Storage Ring (ISA) in the University of Aarhus, Denmark in an UHV system (2 x 10^{-10} mbar) with a typical photon flux of 1 x 1010 photons per second. The system was equipped with hemispherical (VG-CLAM2) electron energy analyser which was operated at pass energy of 30 eV. Photoemission spectra of the following core levels were acquired at the indicated photoelectron energies: Survey and O 1s (600 eV), valence band Zn 3d (60 eV) and C 1s (390 eV).

6.3 Results and Discussion

6.3.1 XPS studies surface cleaning by acetone, DMSO, and toluene

Three different ZnO surfaces (0001)-Zn, (000-1)-O and (10-10) were used for this XPS wet chemical cleaning study.

6.3.1.1 Zn-terminated (0001) surface

For the Zn-terminated surface, narrow scan spectra for core levels of C 1s, O 1s and Zn 2p were recorded for as received, acetone cleaning, DMSO cleaning, toluene cleaning, exposed to air and cleaning in all solvents continuously are systematically shown in figure 6.1. The spectra shown in figure 6.1 were peak fitted based on the optimised binding energy values and FWHM obtained from previous XPS study of ZnO crystals in chapter 4. The C 1s core level was fitted with four synthetic peaks at binding energies C-C (285 eV), C-O (286.35 ± 0. 15 eV), O-C=O (288 ± 0.10 eV), C-H (283.5 ± 0.35 eV). In all cases carbon peaks the variation of binding energy is within 0.25 eV, expect the C-H peak which has 0.73 eV a high variation due to recontamination. For the O 1s core level, two peaks were fitted for ZnO, OH and an additional peak is for water was fitted for air exposed and continuous cleaned sample conditions. For as received and acetone cleaned conditions the binding energy for O-Zn is at 530.7 eV and OH is at 532.2 eV. After DMSO cleaning, the O-Zn peaks moves by 0.2 eV, OH peak moves about 0.4 eV to higher binding energy (i.e, O-Zn 530.9 eV, OH 532.6 eV) and afterwards no change in binding energy position was observed for all other processing. The water peak fitted at 534 eV for the air exposure and continuous cleaning conditions. The two peaks fitted for Zn 2p3/2 zinc peak, one for

ZnO 1022.45 ± 0.20 eV and other is $Zn(OH)_2$ 1024 ± 0.35 eV. Over all, the hydrogen bonded peaks C-H, O-H, Zn(OH)2 have shift more in binding energy by increase of ± 0.5 eV than the other peaks. The oxygen peak (O-Zn) and its hydroxide (O-H) were moved to higher binding energy of 0.2 eV, water moves higher by 1.0 eV, zinc hydroxide ($Zn(OH)_2$) also move higher by about 0.5 eV. These results show there is a stronger adsorption of hydroxide on the surface. Note that the zinc peak for (Zn-O) moves by 0.2 eV to lower binding energy.

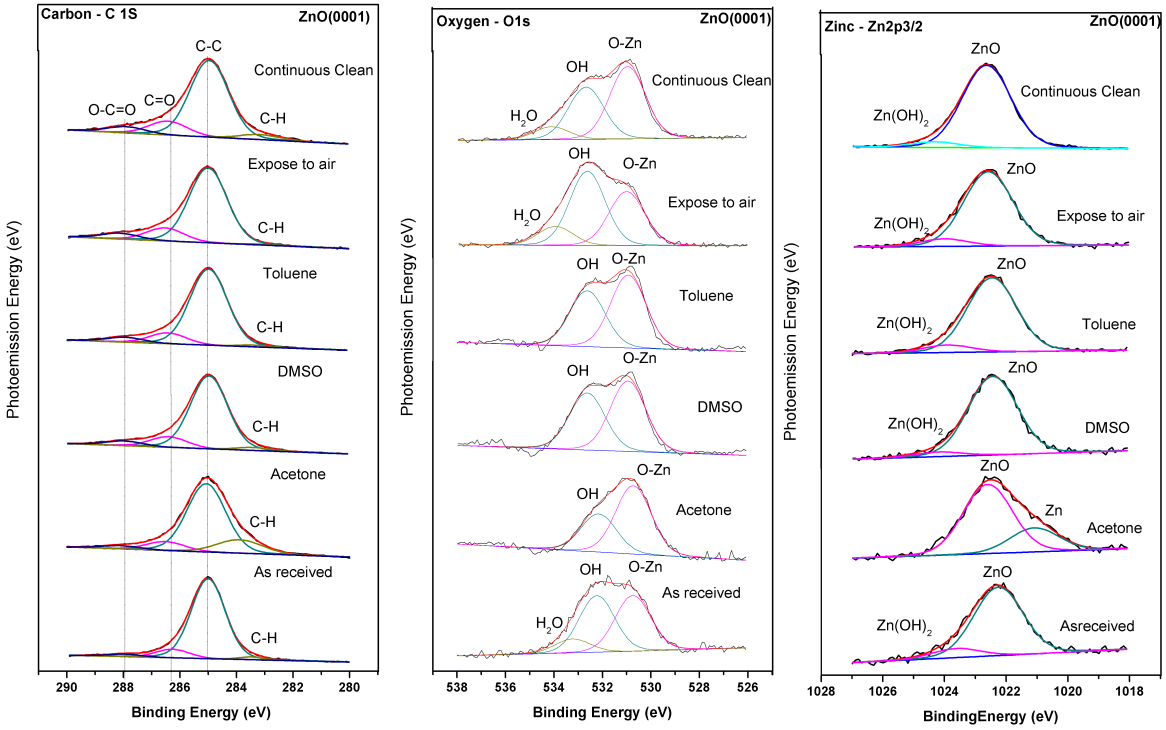

Figure 6.1: Peak fitted C 1s, O 1s, Zn 2p core level peaks for ZnO(0001)-Zn surface cleaned by organic solvents.

The contamination analysis of carbon and hydroxide with water for (0001)-surface as function of different solvent cleaning were plotted in figure 6.2 and figure 6.3. The amount of contamination shown in figure 6.2 and figure 6.3 were in atomic % were calculated using relative sensitive factors (RSF) as in chapter 4. From figure 6.2 the carbon contamination was in large range from 76.3% - 50.9% and the rest carbon dioxide, carbon trioxide, hydrocarbons were within 10% only. Upon cleaning by acetone reduces about 15% of adventitious carbon, but hydrocarbon increases from 2.1% to 14.3%. Then on DMSO treatment increased 6% of the carbon and reduced the hydrocarbon to 2.7%. The toluene cleaning does not made significant change expect 1.5% reduction of hydrocarbon. For (0001)-Zn surface after first set of cleaning exposed to air for a week, show no more growth of carbon contamination because the surface was fully covered by hydroxide and water (see figure 6.3 for air exposed condition). Finally after exposed to atmosphere, then cleaned in all three solutions

continuously shows similar reduction of carbon 8%, with hydrocarbon growth of 3%. So the acetone only plays a role of reducing the carbon contamination on (0001) surface greater than all other solvents.

The figure 6.3 shows the total amount of hydroxide and water contamination on (0001) surface was within 15%. Initial acetone cleaning completely removed the zinc hydroxide, water and reduced the hydroxide by 0.6%. The DMSO treatment again contaminated the surface with increase of hydroxide from 4.2% to 8.2% with traces of zinc hydroxide also. Toluene cleaning only reduces 2% of hydroxide. On exposure of surface to atmosphere for a week, doubled the amount of hydroxide (6.3% to 12.5%) and additional contamination of water also seen (3.2%). By continuous cleaning in all three solvents reduced only 3.3% of hydroxide and 1% of water. This re-contamination of hydroxide and water was very strong on exposed to atmosphere after initial cleaning in the solvents. Here toluene only reduce hydroxide based contaminates on (0001) surface.

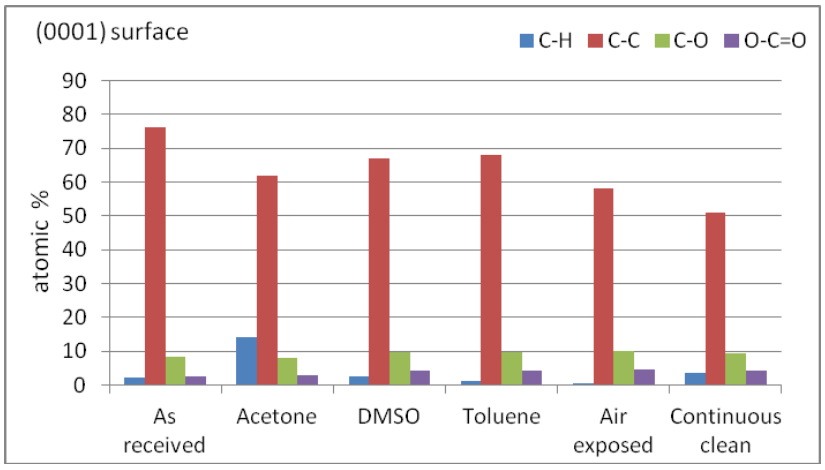

Figure 6.2: Carbon contamination analysis on ZnO(0001) surface for solvent treatments.

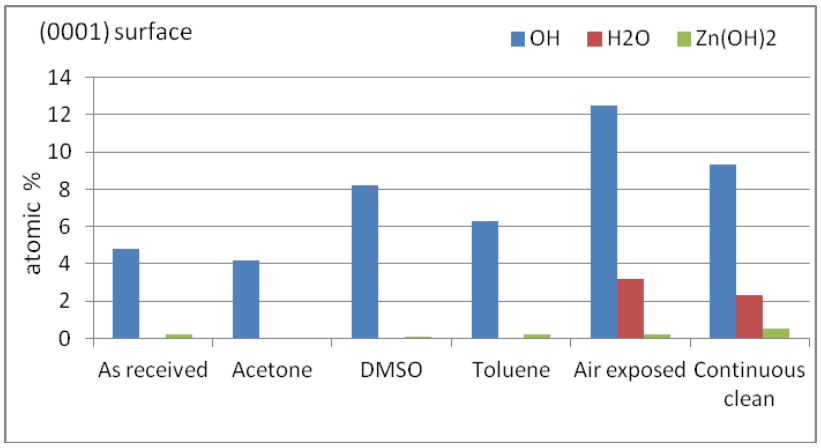

Figure 6.3: Hydroxide contamination analysis on ZnO(0001) surface for solvent treatments.

The stoichiometry analysis of Zn and O on the Zn(0001) surface was shown in figure 6.4. The surface mostly seems oxygen rich (90% 60%), initially zinc ratio was

very less (9%) and after final continues clean an more expected amount of 40% zinc is seen. This result implies the (0001) surface is mostly covered with oxygen atoms, contaminations and due to high amount hydroxide on surface the oxygen ratio was very high. The (0001)-Zn surface have special property of (1 x 1) oxygen coverage on surface were also recently reported [22] is also agreeable as ratio of oxygen is high here. This is also consistent with higher binding energy shift of oxygen and hydroxides peaks. Over all, poor stoichiometry is seen on this (0001)-Zn surface.

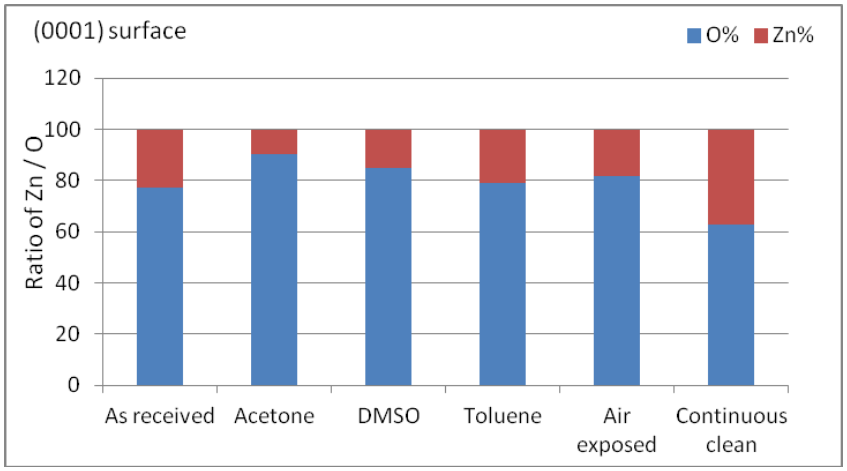

Figure 6.4: Stoichiometry analysis of ZnO(0001) surface as effect of solvent treatments.

6.3.1.2 O-terminated (000-1) surface

The survey spectra obtained for ZnO(000-1)-O surface also have usual three elements zinc, oxygen and carbon. The core level of C 1s, O 1s, Zn 2p peaks for (000-1) surface with respect to different solvent cleanings, air exposure and re-cleaning conditions are shown in figure 6.5. Similar to ZnO(0001) surface the binding energy positions and FWHM for peak fitting were obtained from chapter 4. The carbon spectrum was widened with increase in number of compound is seen. Hence C 1s core level is peak fitted with usual four peaks, C-H (283 ± 0.4 eV), C-C (285 eV), C=O (286.6 ± 0.2 eV), O-C=O (288.2 ± 0.3 eV) and an additional unknown carbon peak C_x (281.1 ± 0.5 eV). The variation of binding energy for C-H, C=O, O-C=O is between 0.2 - 0.4 eV and the C_x peak have high variation of 1.0 eV is a loosely bonded carbon on surface. The oxygen O 1s core level peak was fitted with three peaks (1) O-Zn at (530.5 eV - 531 eV), (2) OH at (532 eV - 532.5 eV), (3) water peak is at (533 eV - 534.3 eV) so the variation of binding energy for oxygen peak is about 0.5 eV expect the water peak variation is at 1 eV. The Zn 2p zinc peaks were also split into three peak as Zn_x (1020.6 ± 0.6 eV), ZnO (1022.4 ± 0.15 eV) and $Zn(OH)_2$ (1023.8 ± 0.25 eV). Similar to oxygen peaks, the zinc peaks binding energy variation was within 0.5 eV expect the Zn_x which have 1.0 eV B.E variation. From the binding energy analysis, the carbon and water peak movement were shows there is wide range of contaminations making different bonding on surface. The 0.5 eV higher binding

energy movement of oxygen and zinc peak is purely due to the hydroxide formation while the solvent cleaning and after.

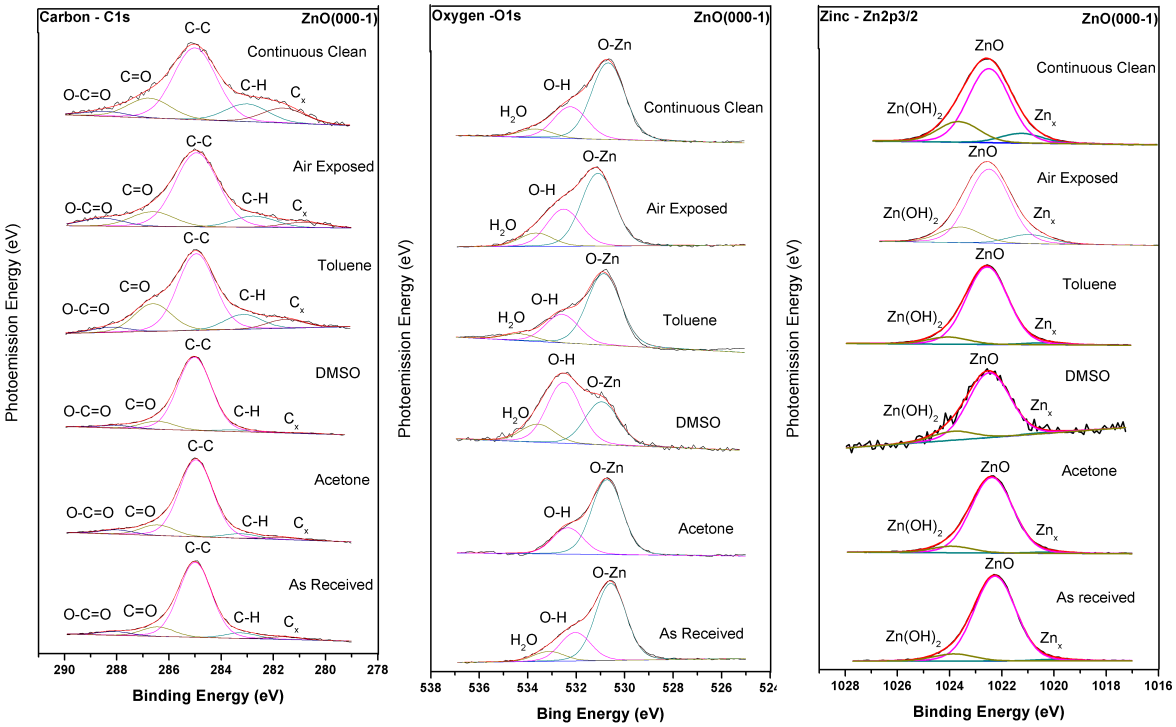

Figure 6.5: Peak fitted for C 1s, O 1s, Zn 2p core level peaks for ZnO(000-1)-O surface cleaned by organic solvents.

Analysis of carbon and hydroxide on ZnO (000-1) surface with respect to different organic solvents cleaning, re-contamination and complete cleaning were shown in figure 6.6 and figure 6.7 respectively. From figure 6.6, the amount of total carbon contamination varies between 71.2% to 32.7%. The acetone treatment does not affect the (C-C) primary carbon (50%) on this (000-1) surface. Further 10% of carbon contamination was increased by DSMO ultra sonication. The toluene treatment hugely reduced the (C-C) primary carbon from 60% to 22%, but with little increase of other compounds C-H (4.3%), CO (8%), C_x (2.6%). On air exposure of surface leads to recontamination of (C-C) carbon from 22% to 25% and 3% reduction of C-O is seen. As a final step of continuous cleaning in all solvents brought down the primary (C-C) carbon to 18%, with approx. increase of 2% loosely bonded hydrocarbon (CH) and unknown carbon (C_x). So the toluene only plays a role removing carbon contamination on (0001)-O surface.

From figure 6.7 the total hydroxide on (000-1) surface before and after solvent cleaning is between 19.7% to 7.4%. Initial cleaning by acetone completely removes the water on (000-1)-O surface as similarly happened in (0001)-Zn surface, but only small reduction 1% of hydroxide is seen. By DMSO treatment the re-contamination of water and 1% increase in both hydroxide (6.7% to 7.7%) as well as zinc hydroxide

(0.7% to 1.8%) were seen. On cleaning with Toluene leads to increase of all contaminations hydroxide (11%), water (2.7%) and zinc hydroxide remains same (1.7%). Later exposure to atmosphere re-contaminated the surface by approx. 2% increase of water and zinc hydroxide with no change in hydroxide. In final continuous cleaning in all solvents further increased the zinc hydroxide contamination from 4.6% to 7%, reduced the water about 1% and no change on hydroxide. On over all, no more solvent seems to be useful in removing or reducing total hydroxide contaminates on (000-1)-O surface, expect acetone particularly removes the water on the surface.

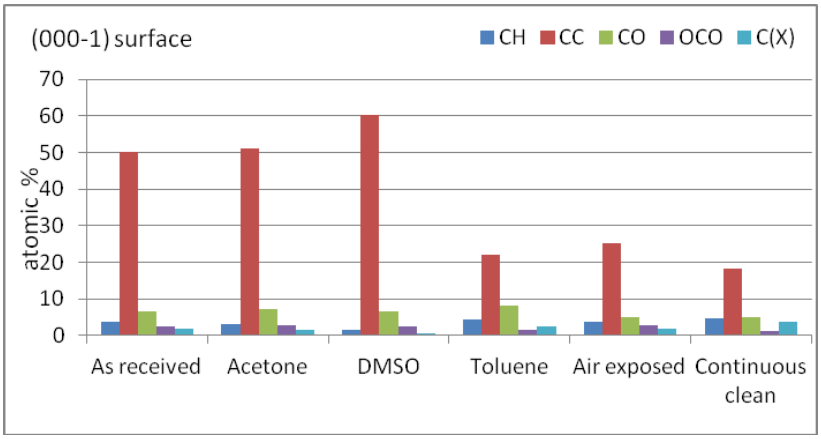

Figure 6.6: Carbon contamination analysis on (000-1) surface for solvent treatments.

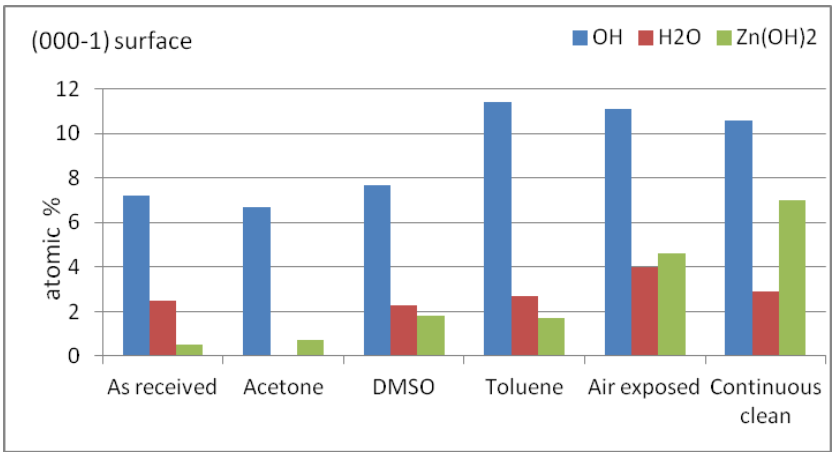

Figure 6.7: Hydroxide and water contamination analysis on (000-1) surface for solvent treatments.

The comparison of oxygen to zinc as stoichiometry analysis for (000-1) surface is shown figure 6.8. The variation of oxygen is 30% to 70%; zinc is 24% to 70% and mostly surface seems oxygen rich. Naturally the top surface termination is oxygen only, so the ratio of oxygen is higher than zinc. In as received and acetone cleaned condition the presence of zinc was very less of approx. 30%. The high amount of zinc was found at DMSO cleaned condition of 70% is unclear. ZnOs usual stoichiometry of 60% oxygen and 40% zinc was attained in Toluene cleaned condition. On air exposure, continuous cleaned conditions a good and ideal stoichiometry of 49% 50%

both oxygen and zinc is obtained.

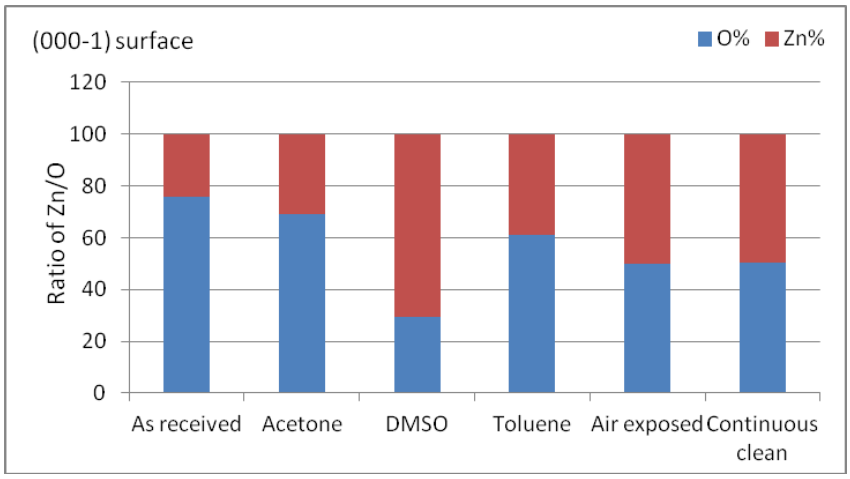

Figure 6.8: Stoichiometry analysis of ZnO (000-1) surface for solvent treatments.

6.3.1.3 Zn and Oterminated (10-10) surface

Similar to the (0001)-Zn and (000-1)-O surface the survey spectra obtained for (10-10) surface also shows the peaks for three elements of carbon, oxygen, and zinc. The narrow scans of core levels C 1s, O 1s and Zn 2p and with their peak fitting for different organic solvent cleaning were shown in figure 6.9. The wide carbon spectra was obtained for all cleaning conditions were fitted with five peaks with binding energies, C_x 281.4 ± 0.22 eV, C-H - 283 ± 0.2 eV, C-C - 285 eV, C=O - 286.7 ± 0.25 eV, O-C=O - 288.3 ± 0.5 eV. Mostly carbon peaks have binding energy variation of 0.4 eV and the tail peak O-C=O only has 1.0 eV. Oxygen O 1s core level have usual three peak fits with binding energies, O-Zn - 530.7 ± 0.2 eV, OH - 532 ± 0.2 eV, H_2O - 533 ± 0.2 eV. But in as received condition, all oxygen peaks were found 0.5 eV lower than standard values, O-Zn (530.04 eV), OH (531.45 eV), H_2O (532.45 eV). Similarly in Zn 2p core level also in as received condition the peaks moved 0.45 eV to lower binding energy, ZnO (1021.76 eV), $Zn(OH)_2$ (1023.03 eV) and Zn_x (1020.17 eV). For all organic solvent cleaning and air exposure conditions, binding energy position for zinc peaks were found at O-Zn - 1022.3 ± 0.15 eV, $Zn(OH)_2$ - 1023.6 ± 0.15 eV and Zn_x - 1020.6 ± 0.2 eV. As like in (000-1) surface due to hydroxide on surface both zinc and oxygen peaks move approx. 0.5 eV higher binding energy form the as received binding energy position.

The effect of different organic solvents in removal of carbon and hydroxide contaminations on (10-10) surface was shown separately in figure 6.10 and figure 6.11. Initially on referring 6.10, the range of total carbon contamination is from 56.4% to 26.1%. Ultrasonic cleaning in acetone increased C-C carbon contamination from 38% to 40% and C-H was reduced by 2%. Suddenly high amount of C-C carbon was removed by DMSO cleaning (40% - 16%) and C-O carbon by 2%. Again re-contamination was happened by toluene cleaning, C-C reduced carbon got increased

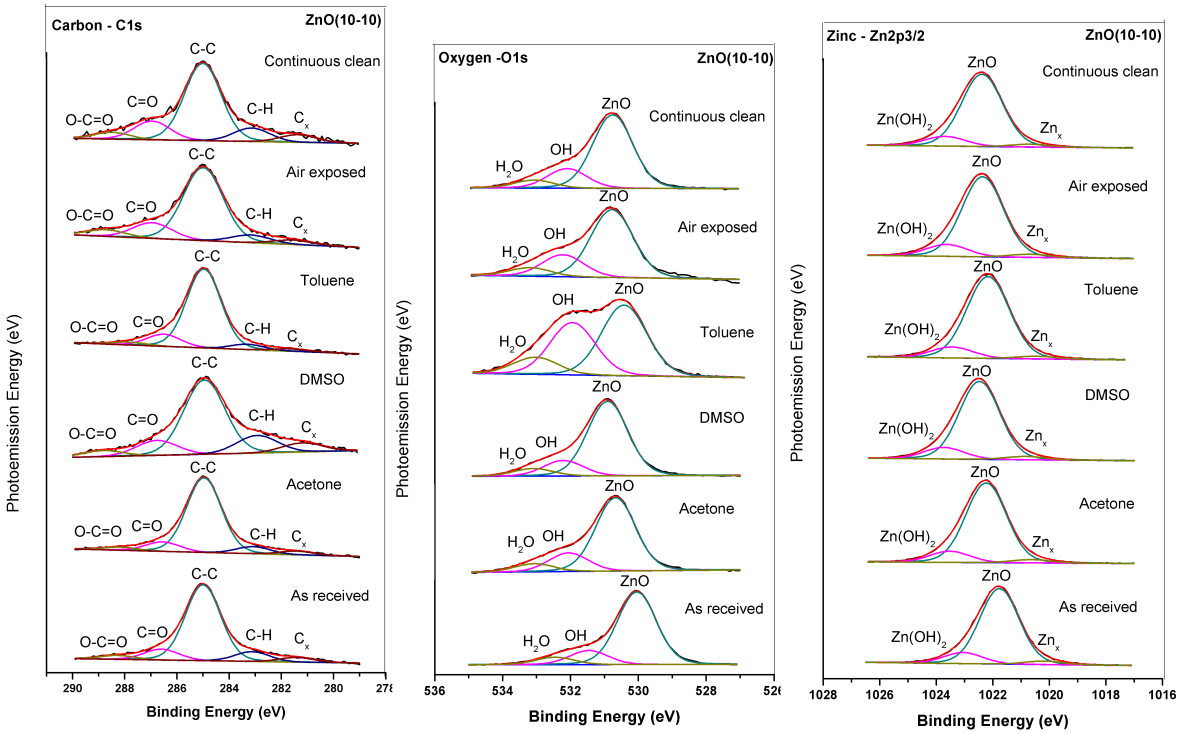

Figure 6.9: Peak fitted C 1s, O 1s, Zn 2p core level peaks for ZnO(10-10) surface cleaned by organic solvents.

from 16% to 44% and C-O also increased 3.4% to 6.7%. On exposing the (10-10) surface to ambient condition surprisingly reduced the carbon contaminations, C-C to 28%. Then on continuous cleaning all three solvents, reduced all carbon contaminations, C-C - 26%, C-O - 3.9%, O-C=O - 1.4%. On overall for (10-10) surface, DMSO only reduced large amount of carbon contamination.

The figure 6.11 meant for hydroxide and water contaminations on (10-10) surface show the total OH based contamination ranges from 17.9% to 10.2%. Initial acetone surface cleaning 1% of water only reduced, but no more change in other contamination is seen. By DMSO cleaning contaminations increased about 1% of OH, H_2O and 2% of $Zn(OH)_2$. High re-contamination happened in toluene treatment, increase of OH from 6.8% to 12.7%, H_2O (3.3% to 4.1%), but $Zn(OH)_2$ got reduced from 3.7% to 1.1%. Similar to carbon here also in air exposed condition, Hydroxide is reduced to 8.7% and zinc hydroxide increases to 2.5%. Further continuous cleaning in all solvents removed only small amount of hydroxide, water and further increased the amount of zinc hydroxide. On over all, no more solvent seems significantly cleaning hydroxide based contamination, especially toluene re-contaminate the (10-10) surface more instead of cleaning.

As seen in (0001)-Zn and (000-1)-O surface, here also the (10-10) surface have more amount of oxygen than zinc is seen in stoichiometry analysis (see figure 6.12). In as received condition, the ratio of zinc is only 10%, oxygen is 90%. Then cleaning

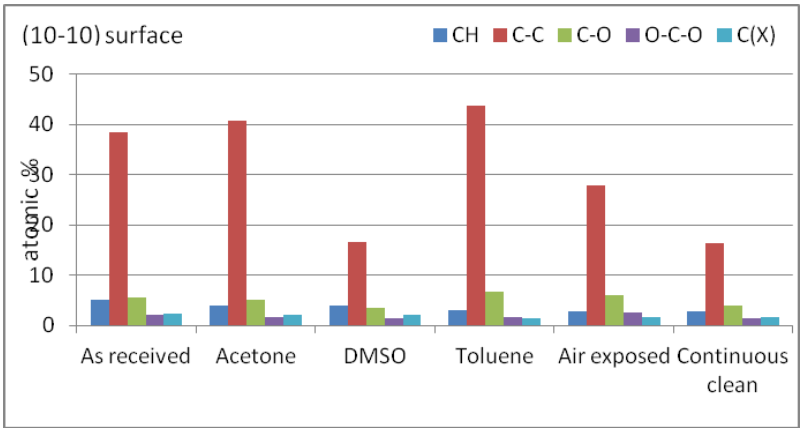

Figure 6.10: Amount of carbon contamination on (10-10) surface with solvent treatments.

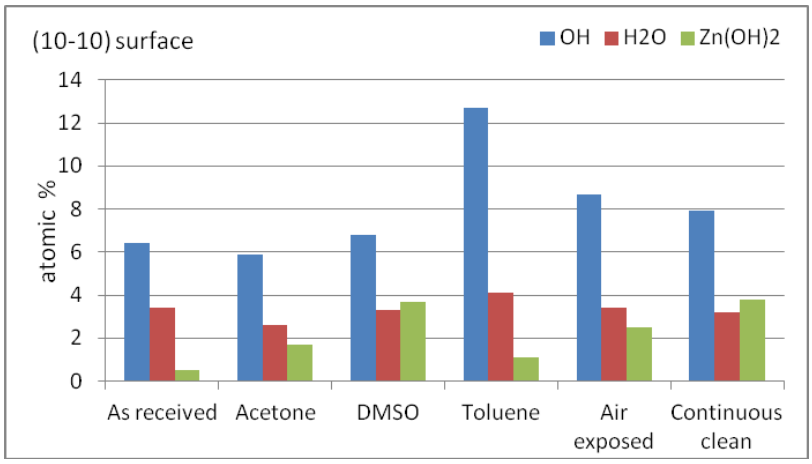

Figure 6.11: Amount of hydroxide and water on (10-10) surface with solvent treatments.

by acetone zinc ratio improves to 35%, on DMSO cleaning zinc ratio reaches 43%, in toluene cleaning as contamination were high zinc ration falls to 32.5%. The usual ZnO ratio of Zn - 38.6% and O 61% was attained at air exposed condition. The ideal stoichiometry of Zn - 49% and O - 51% is seen at continuous cleaning in all solvents.

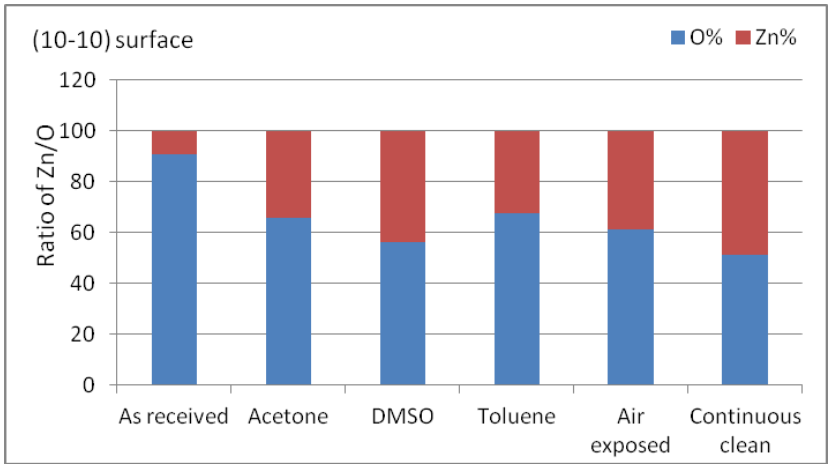

Figure 6.12: Stoichiometry of (10-10) surface after cleaning in different solvents treatments.

6.3.1.4 Comparison of three surfaces

This study showed that the organic solvent cleaning of the (0001)-Zn is less effective than either the (000-1)-O surface and the (10-10)Zn and O surfaces. The surface carbon contamination cannot effectively be removed by the combined cleaning process from the (0001)-Zn surface. There is no particular organic solvent that is effective in cleaning contamination on all surfaces. The model of hydroxide on three surfaces is shown in figure 6.13. On all three surfaces, amount of hydroxide is much high than in as received condition.

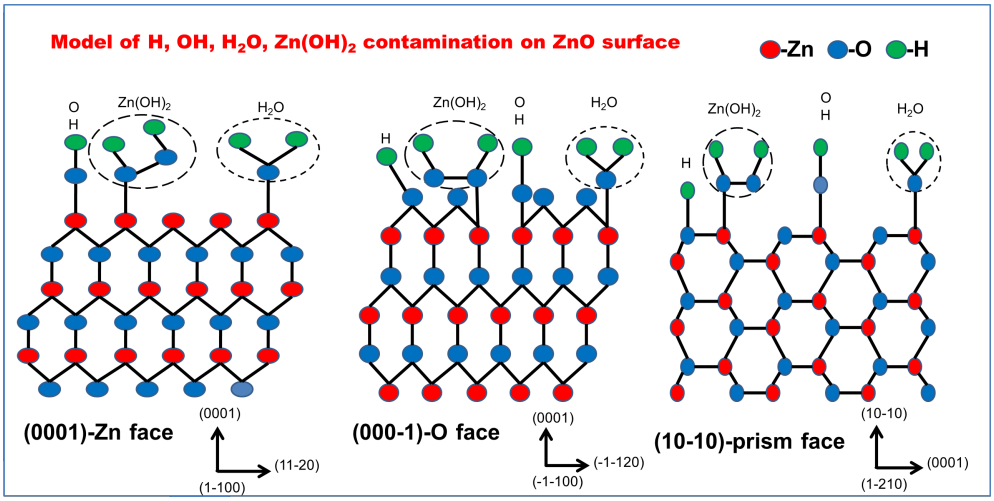

Figure 6.13: Hydroxide and water contamination model of three ZnO surfaces.

6.3.2 SRPES studies of surface cleaning of ZnO polar and non-polar surfaces by ethanol

In this study, both polar (0001)-Zn, (000-1)-O and non-polar (10-10), (11-20) ZnO surfaces were used to explore the effect of surface cleaning by ethanol. Initially the ZnO (00001) zinc terminated surfaces taken for feasibility study of ethanol surface cleaning. Photoemission spectra were recorded for as received condition and the ethanol cleaned condition. By using different photoemission energies the survey spectra (600 eV), core levels of C 1s (390 eV), O 1s (600 eV), and valence band spectra with Zn 3d (60 eV) were acquired and shown in figure 6.14. From the survey spectra for the as received and ethanol cleaned surface shown in figure 6.14, the following peaks were identified with the binding energies Zn 3d 12 eV, Zn 3p 91 eV, C 1s 287 eV, O 1s 534 eV. The dominant carbon peak seen in the as received sample is significantly reduced after ethanol cleaning with oxygen and zinc peaks becoming more prominent.

The C 1s narrow scan spectra, acquired at photon energy of 400 eV, shown in figure 6.14(b) illustrates the reduction in the intensity of the peak following ethanol cleaning. Curve fitting the C 1s spectrum after ethanol treatment required the fitting of additional Carbon peaks of C-O (288.15 eV) and O-C=O (290.35 eV). While the intensity of the O 1s core level shown in figure 6.14(c) prior to cleaning is difficult

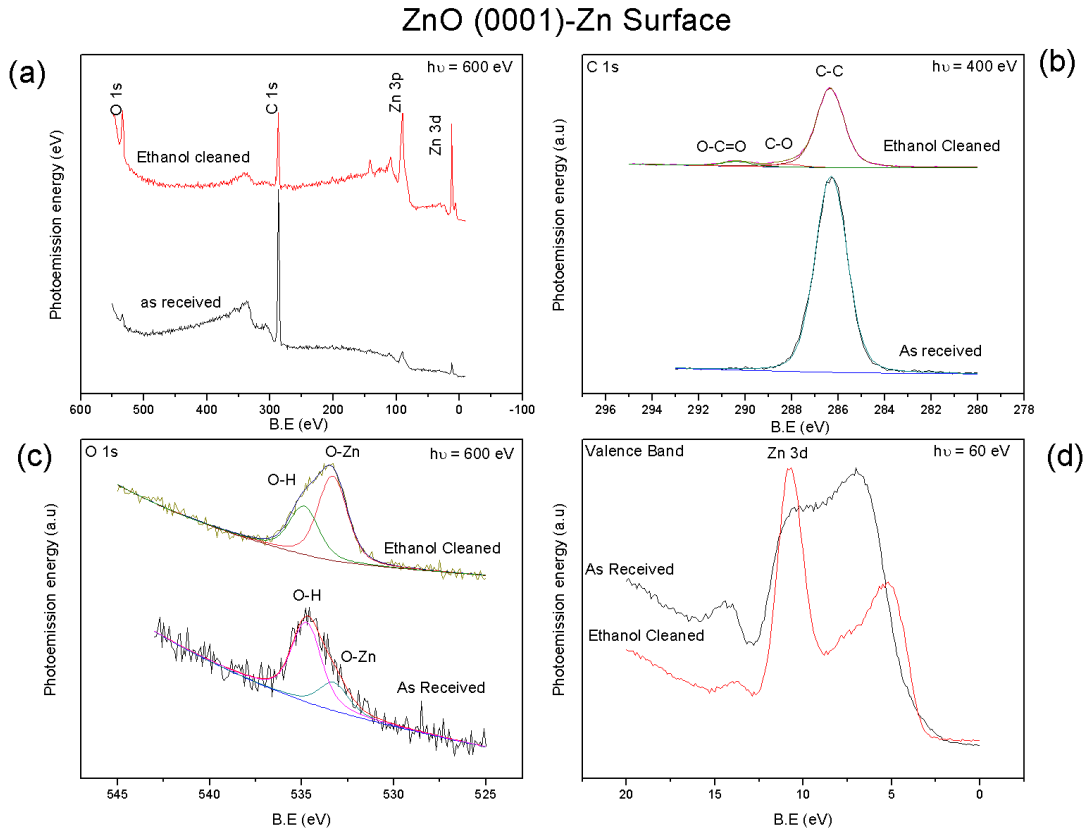

Figure 6.14: photoemission spectra before and after ethanol cleaning of ZnO(0001) surface: (a) survey spectra, (b) carbon C 1s, (c) oxygen O1s, (d) Valence band and Zn 3d.

to curve fitted with any degree of confidence due to its indistinct nature, following cleaning, it can be fit with a ZnO and hydroxide component peaks. For the valence band spectra, acquired at photon energy of 60 eV, shown in figure 6.14(d) as the surface cleaning results in the observation of the Zn 3d peak (12 eV). Therefore, while ethanol cleaning is not effective at completely removing the surface carbon contamination from the Zn terminated surface, the intensity of the Zn and O signals is significantly improved to allow curve fitting with a high degree of confidence.

The ethanol cleaning was also performed on the other three ZnO surface: (000-1), (10-10) and (11-20) with same procedure of 10 minutes ultra sonication in ethanol and dried in a flowing gas. Photoemission scans recorded for survey, C 1s, O 1s and valence band with same photoemission energies used for (0001) surface are shown in figure 6.15.

After ethanol cleaning the highest residual carbon contamination was found on (11-20) surface, with the other three surfaces, (0001) and (000-1) (10-10) displaying similar levels of carbon (see figure 6.16). Consistent peak fitting of the individual carbon components following cleaning shows the presence of carbon (C-C), carbon dioxide (C=O) and carbon trioxide (O-C=O) peaks. The normalised by number of scans and

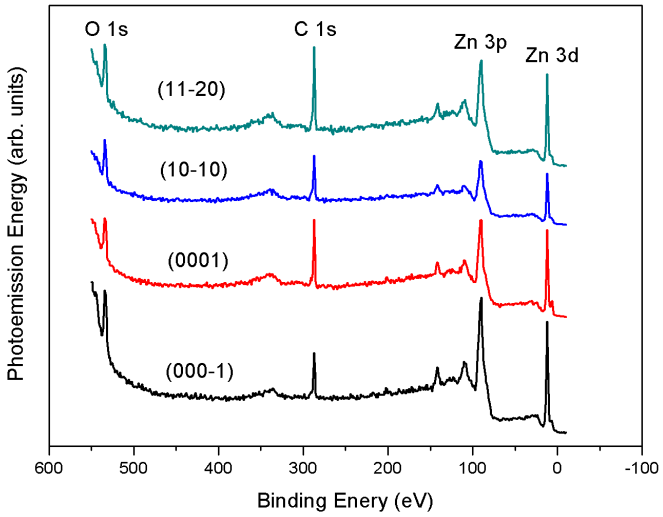

Figure 6.15: A comparative survey spectra for four different ZnO surfaces treated with ethanol solvent.

curve fitted O 1s spectra for all four ZnO surfaces are shown in figure 6.17. Along with a ZnO peak at 533.25 eV, a hydroxide component peak is observed at 534.93 eV B.E.. While there are variations in the relative intensities of these component peaks, it is difficult to attribute a definitive explanation given that the surfaces were exposed to air after the organic cleaning treatment.

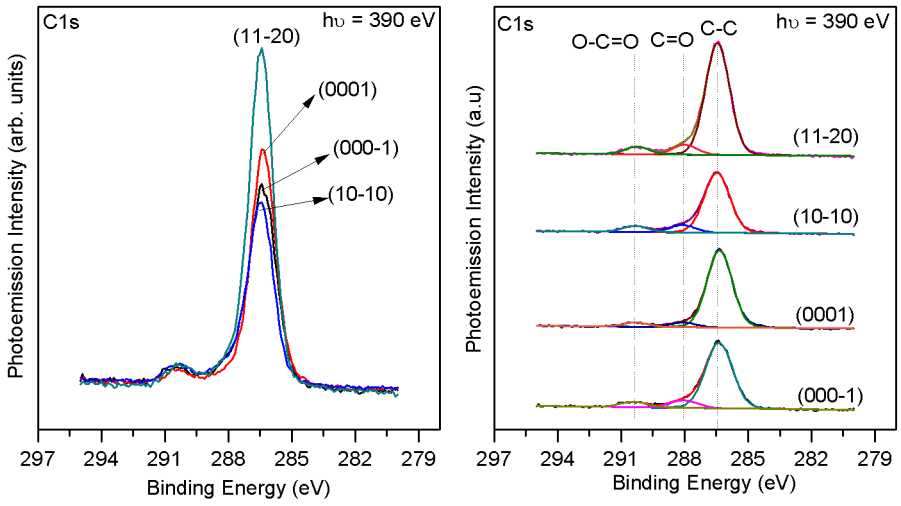

Figure 6.16: Carbon C 1s core level spectra comparison and peak fitting for ethanol cleaned different ZnO surfaces.

So here we use specific way of comparing area of core level peak areas. For hydroxide estimation, we compare the peak areas of O-H to O-Zn in oxygen O 1s core level. This is named the OH factor. Similarly for carbon contamination the peak areas of

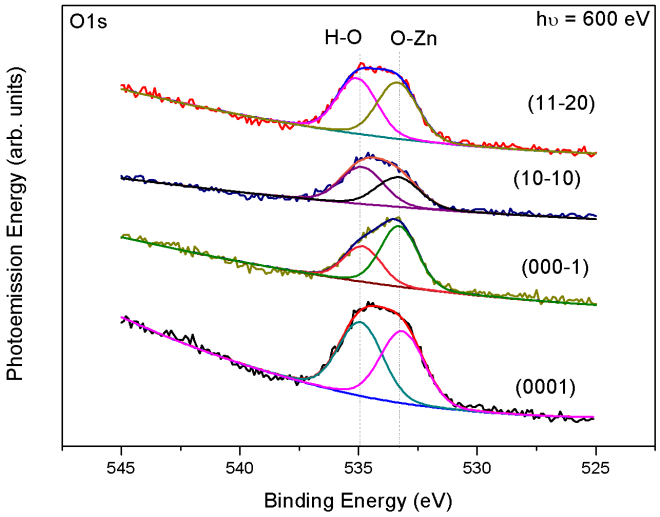

Figure 6.17: Oxygen O 1s core level as impact of ethanol cleaning of ZnO surfaces.

C-C peak in carbon C 1s core level to Zn 3d peak in valence band, named the CZ factor. For this ethanol cleaning of ZnO surfaces, the OH factor and CZ factor values were plotted in Figure 6.18. For the estimation of carbon contamination on ZnO surfaces, the CZ factor measurements were better than simply measuring the carbon peak intensity. From figure 6.18 the carbon contamination seems almost uniform on all surfaces with small variations. The more carbon is on (0001) surface and very less is seen in (000-1) surface. But the OH contamination has huge variations, on the (000-1) and (11-20) surfaces the hydroxide is equal to zinc oxide (OH factor is 1). More than zinc oxide was found on (10-10) surface and on (0001) surface the hydroxide nearly half to zinc oxide (OH factor is 0.5). So in overall, (10-10) surface have both carbon and hydroxide high amount. The (0001) surface has both less amounts of carbon and hydroxide contaminations. By ethanol cleaning hydroxide were seems high than carbon contaminations.

The valence band spectra of Zn 3d were recorded at the photoemission energy of 60 eV is shown in figure 6.19. The valence band maximum (VBM) were measured by extrapolating a line from the lower end of peak. The VBM values of all four surfaces were as follows: (0001) - 3.16 eV, (000-1) - 2.91 eV, (10-10) - 2.90 eV and (11-20) - 2.83 eV. The work function measurements were also found (see table 6.1) to be uniform for all three surfaces about 4.0 ± 0.3 eV expect the (11-20) surface which has a value of 4.65 eV due to the surface dipole moment between Zn and O atoms. As we seen already (chapter 1), the work function of ZnO was variable in range of 4 eV to 4.5 eV. So the high value obtained for (11-20) surface was acceptable and similar value also reported [23].The band bending (E_{BB}) was calculated by using valence band maximumm (E_{VBM}) values obtained from valence band spectra and the energy band gap of ZnO is well known, Then E_{BB} = Eg - E_{VBM} The (0001) surface got the flat

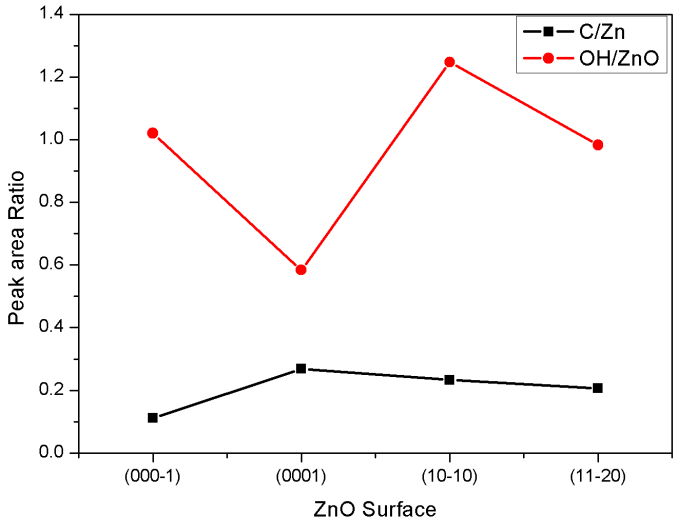

Figure 6.18: Ratio of peaks, OH factor and CZ factor for four ZnO surfaces after ethanol cleaning.

band after ethanol cleaning. But on all other surfaces got the upward band bending were shown in Figure 6.20. The band bending values are for (000-1) - 0.46 eV, (10-10) - 0.47 eV and (11-20) - 0.54 eV close agreement with previous reports [24]. Along with partial contamination of carbon and hydroxide on ZnO surface, obtaining the upward band bending after ethanol cleaning is the significant result.

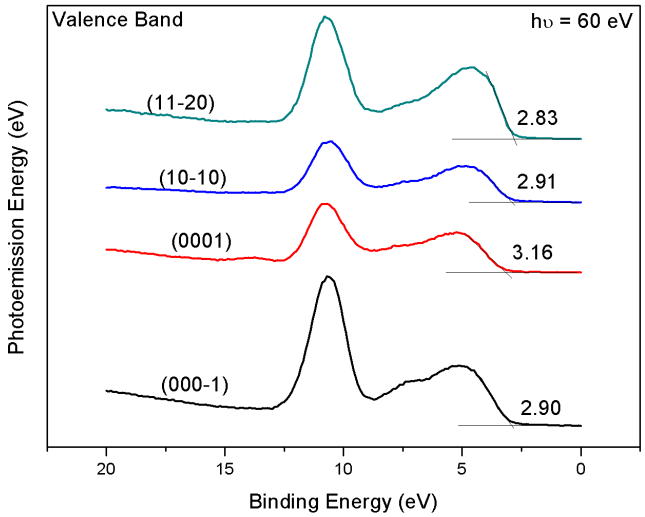

Figure 6.19: Valence band spectra for four different ZnO surfaces after ethanol cleaning.

Table 6.1: Work function measured after ethanol cleaning of ZnO surfaces.

ZnO Surface	Work Function
(000-1)	4.04 eV
(0001)	4.07 eV
(10-10)	4.12 eV
(11-20)	4.65 eV

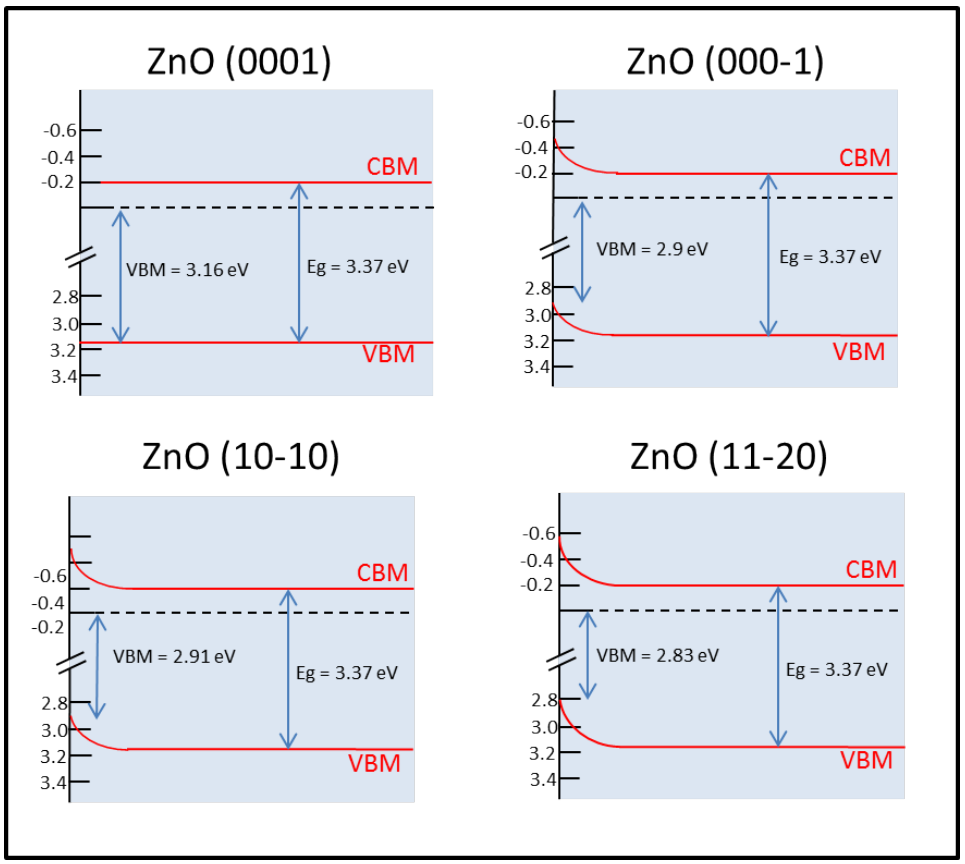

Figure 6.20: Energy level band diagram of ethanol cleaned ZnO (0001), (000-1), (10-10), (11-20) surfaces.

6.4 Conclusions

XPS study of wet chemical cleaning by acetone, DMSO and toluene shows these organic solvents differently react with different (0001), (000-1) and (10-10) ZnO surfaces. Particularly no more solvent is effective in consistent removal of a contamination in all three ZnO surfaces. Both the decrease in contamination as well as increase in contamination was seen in all surfaces by treating with these chemicals. Over all, after cleaning with these three solvents the carbon contamination was reduced and the hydroxide contamination increased. After cleaning in solvents the exposure of ZnO surfaces in atmosphere leads to strong re-contamination of hydroxide and wa-

ter. Synchrotron photoemission studies of ethanol cleaning shows the reduction of the carbon and hydroxide on four ZnO surfaces in various degrees. By ethanol cleaning the partial amount of surface contamination were removed and ZnO valence band is clearly seen. The flat band on (0001) surface due to strong bonding of carbon (as seen in chapter 5) and upward band bending on (000-1), (10-10), (11-20) surfaces were also obtained by ethanol cleaning.

6.5 Bibliography

[1] Werner Kern (Ed.), Handbook of semiconductor wafer cleaning technology, first ed., Noyes Publications, 1993.

[2] W. Kern, J. Electrochem. Soc., 137 (1990) 1887.

[3] Karen A. Reinhardt, and Werner Kern, Silicon wafer cleaning technology, 2nd ed., William Andrew, 2008.

[4] D. H. van Dorp, D. Cuypers, S. Arnauts, A. Moussa, L. Rodriguez, and S. De Gendt, ECS J. Solid State Sci. Technol. 2 (2013) 190.

[5] K. A. Reinhardt, R. F. Reidy, Handbook of Cleaning for Semiconductor Manufacturing - fundamentals and applications, first ed., John Wiley and Sons, (2011).

[6] R. C. Neville and C. A. Mead, J. Appl. Phys., 41 (1970) 3795.

[7] Han-Ki Kim, Sang-Heon Han, and Tae-Yeon Seong and Won-Kook Choi, Appl. Phys. Lett. 77 (2000) 1647.

[8] K. Ip, K. H. Baik, Y. W. Heo, D. P. Norton, S. J. Pearton, J. R. LaRoche, B. Luo, F. Ren and J. M. Zavada, J. Vac. Sci. Technol. B, 21 (2003) 2378.

[9] A. Y. Polyakov, N. B. Smirnov, E. A. Kozhukhova, V. I. Vdovin, K. Ip, D. P. Norton, and S. J. Pearton, J. Vac. Sci. Tech. A, 21 (2003) 1603.

[10] J. Dumont, T. Seldrum, S. Couet, C. Moisson, D. Turover, and R. Sporken,J. Vac. Sci. Technol. B, 24 (2006) 2124.

[11] F. D. Auret, S. A. Goodman, M. J. Legodi, W. E. Meyer, and D. C. Look, Appl. Phy. Lett., 80 (2002) 1340.

[12] H. von Wenckstern, E. M. Kaidashev, M. Lorenz, H. Hochmuth, G. Biehne, J. Lenzner, V. Gottschalch, R. Pickenhain, and M. Grundmann, Appl. Phys. Lett., 84 (2004) 79.

[13] T. Frank, G. Pensl, R. Tena-Zaera, J. Ziga-Prez, C. Martnez-Toms, V. Muoz-Sanjos, T. Ohshima, H. Itoh, D. Hofmann, D. Pfisterer, J. Sann, B. Meyer, Appl. Phys. A, 88 (2007) 141.

[14] U. Grossner, S. Gabrielsen, T. M. Brseth, J. Grillenberger, A. Y. Kuznetsov, and B. G. Svensson, Appl. Phys. Lett., 85 (2004) 2259.

[15] H. Endo, M. Sugibuchi, K. Takahashi, S. Goto, S. Sugimura, K. Hane, and Y. Kashiwaba, Appl. Phys. Lett., 90 (2007) 121906.

[16] Y. Dong, Z-Q. Fang, D. C. Look, G. Cantwell, J. Zhang, J. J. Song and L. J. Brillson, Appl. Phys. Lett., 93 (2008) 072111.

[17] L. J. Brillson, H. L. Mosbacker, M. J. Hetzer, Y. Strzhemechny, D. C. Look, G. Cantwell, J. Zhang, J. J. Songd, Appl. Surf. Sci., 254 (2008) 8000.

[18] R. Heinhold, G. T. Williams, S. P. Cooil, D. A. Evans, and M. W. Allen, Phys. Rev. B 88 (2013) 235315.

[19] T. Nakamura, K. Masuko, A. Ashida, T. Yoshimura, and N. Fujimura, J. Cryst. Growth, 318 (2011) 516.

[20] A. Herrera-Gmez, A. Hegedus and P. L. Meissner, Appl. Phys. Lett., 81 (2002) 1014.

[21] John F. Moulder, William F. Stickle, Peter E. Sobol, Kenneth D. Bomben, Jill Chastain, Handbook of X-ray Photoelectron Spectroscopy, Perkin-Elmer Corporation, 1992.

[22] C. M. Schleputz, Y. Yang, N. S. Husseini, R. Heinhold, H-S. Kim, M. W. Allen, S. M. Durbin and R. Clarke, J. Phys.: Condens. Matter 24 (2012) 095007.

[23] O. T. Hofmann, J-C. Deinert, Y. Xu, P. Rinke, J. Stahler, M. Wolf and M. Scheffler, J. Chem. Phys. 139 (2013) 174701.

[24] K. Ozawa, and K. Mase, Phys. Rev. B, 83 (2011) 125406.

Chapter 7

SRPES and XPS studies of *in-situ* surface cleaning of ZnO surfaces by molecular and atomic oxygen

7.1 Introduction

Zinc oxide surface reactivity towards the contaminants from ambient atmosphere is well known. The ex-situ organic solvents cleaning methods have been shown to be ineffective at removing all surface contamination (see chapter 6) and unable to avoid recontamination after cleaning. Hence *in-situ* surface cleaning studies were undertaken with all the surface processing being performed in an ultra-high vacuum environment. For a range of compound semiconductors a simple and easy way to preform surface cleaning is annealing the semiconductor surface to high temperature in an appropriate gaseous atmosphere. In case of nitride semiconductors, samples have been annealed in an NH_3 atmosphere [1] and similarly for oxide semiconductors, samples have been annealed in an oxygen atmosphere [2]. The oxygen annealing results in the oxygen reacting with surface hydrocarbons to form volatile gaseous species such as CO and CO_2. Another effective way of cleaning a metal oxide surface is by using atomic oxygen or ozone (O_3) which are more reactive than the molecular oxygen (O_2) [3]. Atomic oxygen can be generated either in an oxygen plasma [4–6] or specially designed atomic gas cracking source [7]. The use of highly reactive atomic oxygen reduces the annealing temperature required to remove surface contaminants.

There are several studies reported for annealing of ZnO surfaces in an oxygen atmosphere for different purposes such as surface cleaning [8], to enhance the optical property [9], improving crystalline quality with increase in electrical conductivity [10], growing homo-epitaxy [11], changing resistive material to conductive material [12] and reducing defects [13] . Previous oxygen annealing studies for surface cleaning of ZnO crystals show a significant reduction of carbon concentration on ZnO(000-1) surface observed at 600 °C [14] and another study reports that the maximum removal of carbon contamination on ZnO(000-1) surfaces happened in the 600 °C - 650 °C temperature range [8]. The surface cleaning of different ZnO (0001), (000-1), and (10-10) surfaces was also performed by Ar^+ sputtering (2 kV) followed by oxygen annealed at 775 °C - 825 °C [15].

Atomic oxygen is widely used for different material science applications such as surface activation and cleaning for electronic materials, ashing organic materials in electronics, ashing biological and medical samples, selective etching of composite materials and plasma deposition of thin films [5]. To restore some art works without any surface damage atomic oxygen has been employed in museums [16]. This technology was developed by NASA based on their study of atomic oxygen damage to spacecraft in the upper atmosphere [17]. Atomic oxygen was generated by oxygen plasma by different methods and used in the growth of ZnO thin films [18, 19] and surface cleaning of ZnO crystals [8, 20]. UV-ozone plasma was used for the surface cleaning of ZnO surfaces which removed the carbon contamination and resulted in the formation of rectifying contacts for both platinum and tungsten [21]. Similarly, Schottky barrier heights for Ag and Au contacts have been reported to increase after surface cleaning by ozone plasma [22]. The work function of ZnO based flexible transparent electrodes increase after treating with UV ozone plasma [23]. A pure O_2 plasma was also used for surface cleaning of ZnO:Ga thin films resulting in an increase in the work function by removal of contaminations [20]. The wettability change of ZnO nanowire surface from hydrophobic to super-hydrophilic was reported after treating with an oxygen plasma [24]. A remote oxygen plasma (20% He and 80% O) used for the surface cleaning of ZnO surfaces was successful at removing all surface carbon and almost removed all the surface hydroxides [8]. Combined He and O plasma treatments on ZnO surfaces resulting in a reduction of the green luminescence by suppression of hydrogenbonded exciton observed by photoluminescence [25]. Radio frequency (20% O and 80% Ar) oxygen plasma treatments also turn ZnO epitaxial thin films from displaying ohmic behaviour to rectifying for Au and In contacts [26].

The focus of this study is two folded; first to investigate the effect on the chemical composition of the different ZnO crystal surfaces resulting from surface cleaning by molecular oxygen (O_2) at a range of temperatures. These experiments were undertaken using synchrotron radiation based photoemission spectroscopy. Sec-

ondly, to explore the effect of atomic oxygen (produce by thermal gas cracker) on the surface chemical composition of ZnO thin films at both room temperature and high temperature as evaluated by conventional x-ray photoelectron spectroscopy.

7.2 Experimental

7.2.1 Molecular oxygen surface cleaning experiments

Polished ZnO single crystal (5 x 5 x 0.5 mm) polar Zn(0001), O(000-1) terminated surfaces and non-polar (10-10), (11-20) mixed terminated surfaces were ultrasonically cleaned by ethanol solvent for 6 minutes and then dried by flowing oxygen gas. The samples were then placed into the load lock and pumped down to a pressure of 2 x 10 $^{-5}$ mbar. After 5 hours, the samples were transferred to the analysis chamber which had a base pressure of 4 x 10^{-9} mbar. For the annealing studies, an oxygen partial pressure of 7.5 x 10^{-7} mbar for 30 minutes at temperatures ranging from 300 °C to 1000 °C were undertaken. After annealing, the samples were allowed to cool down to 30 °C and then characterised by photoemission spectroscopy. The photoemission experiments were carried out on the SX700 beamline at Institute for Storage Ring (ISA) in the University of Aarhus, Denmark in an UHV system (2 x 10^{-10} mbar) with a typical photon flux of 1 x 10^{10} photons per second. The system was equipped with hemispherical (VG-CLAM2) electron energy analyser which was operated at pass energy of 30 eV. The photoemission energies were carefully chosen for different core levels to ensure comparable sampling depths as previously explained in Chapter 5.

7.2.2 Atomic oxygen surface cleaning experiments

ZnO thin films were grown on pre-cleaned silicon substrates by pulsed laser deposition (PLD) as described in Chapter3. The thickness of the deposited films was determined to be approximately 550 nm. For the atomic oxygen surface cleaning studies an *in-situ* Oxford Applied Research® thermal gas cracker was used. The gas-cracker design uses e-beam heating of a tungsten capillary tube to thermally dissociate the flowing gas as explained in Chapter 3. The oxygen cracking was carried out throughout the experiment at an oxygen partial pressure of 1 x 10^{-7} mbar. The standard operating procedure involved exposure of the ZnO thin film surface to atomic oxygen for 30 minutes at a range of temperatures (100 °C, 200 °C, 30 °C, 400 °C) and recording XPS spectra at room temperature after each anneal. All XPS spectra were recorded by a VG photoelectron spectrometer using an Al-Kα radiation (1486.6 eV) source at a pressure of 10^{-9} mbar and emitted photoelectrons were analysed by a triple channeltron spectrometer

(resolution 1.0 eV). The calibration of the binding energy scale was performed with the C 1s line (285 eV) from the carbon contamination layer.

Both SRPES and XPS spectra were analyzed by using AAanlyser [27] in which a Shirley background is assumed and peak fitting of experimental curves is performed by a mixed singlet combination of Gaussian and Lorentzian line shapes.

7.3 Results and discussion

7.3.1 SRXPS studies of molecular oxygen thermal cleaning of ZnO surfaces at high temperatures

To explore the possibility of removing carbon and hydroxide contamination from both ZnO polar and nonpolar surfaces, high temperature oxygen annealing was investigated in UHV. Initially, the (0001)-O terminated surface was chosen to optimise the oxygen annealing temperature ranges from 300 °C to 1000 °C. Afterwards, oxygen annealing was carried out on the ZnO (0001), (10-10), (11-20) surfaces from 600 °C up to 1000 °C at an oxygen partial pressure of 7.5 x 10^{-7} mbar. The variation of surface chemical composition and electronic structure of each ZnO surface was characterised by synchrotron radiation photoemission spectroscopy.

7.3.1.1 (000-1)-O terminated surface

The oxygen terminated surface was chosen for an initial wide range of annealing temperatures (300 °C to 1000 °C) because it is a known reactive surface with more adsorbed hydroxide and water than the other surface terminations. Survey spectra acquired at a photon energy of 600 eV for different annealing temperatures are shown in figure 7.1. The binding energies of the main peaks in the spectra are Zn 3d - 11.99 eV, Zn 3p - 90.1 eV, Zn 3s - 141.5 eV, C 1s - 286.97 eV, and O 1s at 533 ± 1.0 eV. The carbon signal is completely attenuated (removed) for annealing temperatures above 600 °C. The 2p core level spectra of chlorine, a common contaminant in ZnO, shown in figure 7.2 indicate that it has been removed to below the photoemission detection limit after 600 °C oxygen anneal.

The carbon 1s core level spectra ($h\nu$ = 400 eV) for different oxygen annealing temperatures is shown in figure 7.3 and again indicates that above the 600 °C oxygen anneal, it has been reduced to below the detection limit. By peak fitting the carbon peaks (figure 7.3(b)), carbon bonded to oxygen component peaks were observed. The binding energy difference between the peaks O-C=O to C-C is 3.5 eV and O=C to C-C is 1.6 eV. The FWHM of all carbon peaks also varies between 1.45 to 1.5 eV.

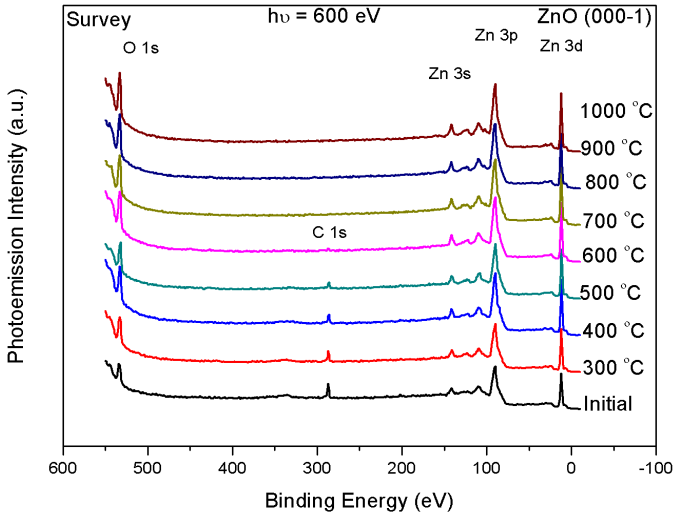

Figure 7.1: Survey spectra of ZnO (000-1) surface for different annealing temperature in O_2 atmosphere.

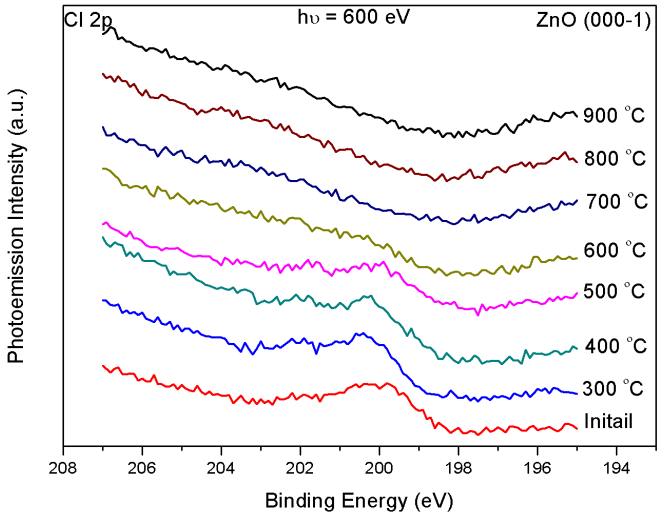

Figure 7.2: Chlorine - C l 2p core level spectra for (000-1) surface annealed in O_2 atmosphere.

Oxygen 1s core level spectra ($h\nu = 600$ eV) for different oxygen annealing temperatures are shown in figure 7.4(a). The curve fitted O 1s spectra (see figure 7.4(b)) for the as received sample and following the 500 °C and 1000 °C anneals show that once the initial surface contamination is removed, the relative intensity of the hydroxide and zinc oxide derived component peaks remains largely unchanged, displaying the thermal stability of this surface. The residual OH signal following these anneals is estimated to be below 1 monolayer on the ZnO(000-1) surface. The binding energy position of the fitted oxygen peaks was ZnO - 532.83 ± 0.2

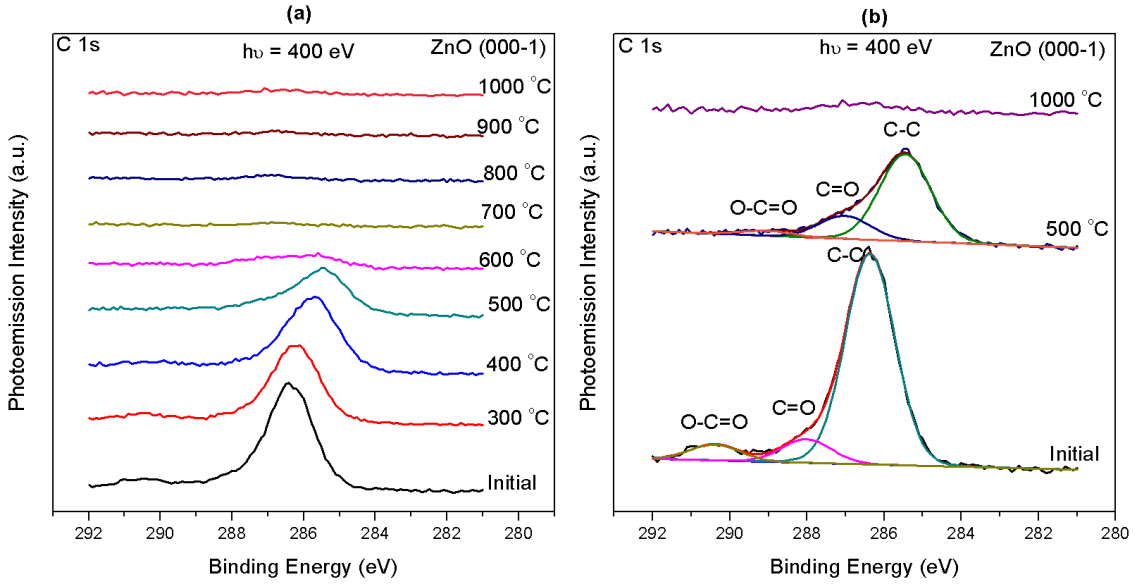

Figure 7.3: Carbon - C 1s core level spectra for (000-1) surface (a) comparison of spectra for different O_2 annealing temperatures (b) peak fitted spectra for selective oxygen annealing temperatures.

eV, OH - 534.57 ± 0.2 eV and water - 535.44± 0.2 eV and FWHM for all peaks was 2.1 eV.

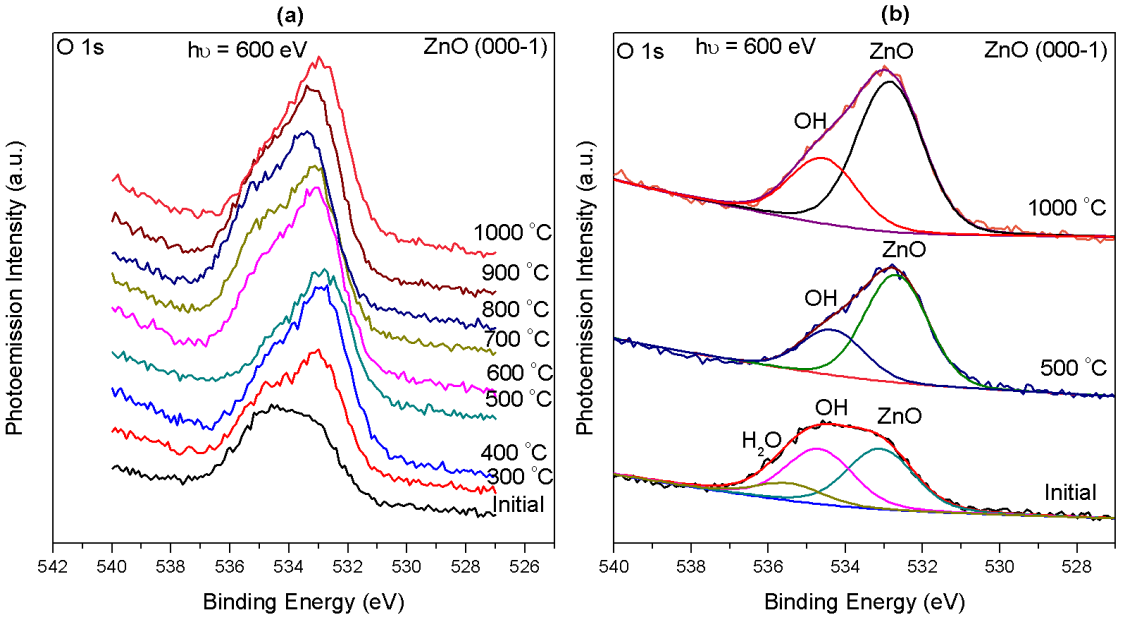

Figure 7.4: Oxygen O 1s core level spectra for (000-1) surface (a) Comparison of spectra for different O_2 annealing temperatures (b) peak fitted spectra for selective temperatures.

The corresponding zinc 3p core level spectra (hν = 400 eV) for different oxygen annealing temperatures are shown in figure 7.5(a) and again remain largely unchanged once the initial surface contamination has been removed. By fitting the zinc peak (see figure 7.5(b)) three components were identified, a surface state

peak Zn_x at 86.4 ± 0.2 eV, zinc oxide peak at 88.5 ± 0.2 eV, zinc hydroxide peak at 89.6 ± 0.2 eV. These B.E. values were consistent with previous photoemission spectra for ZnO (see chapter 5). The FWHM of all zinc peaks was 2.4 eV.

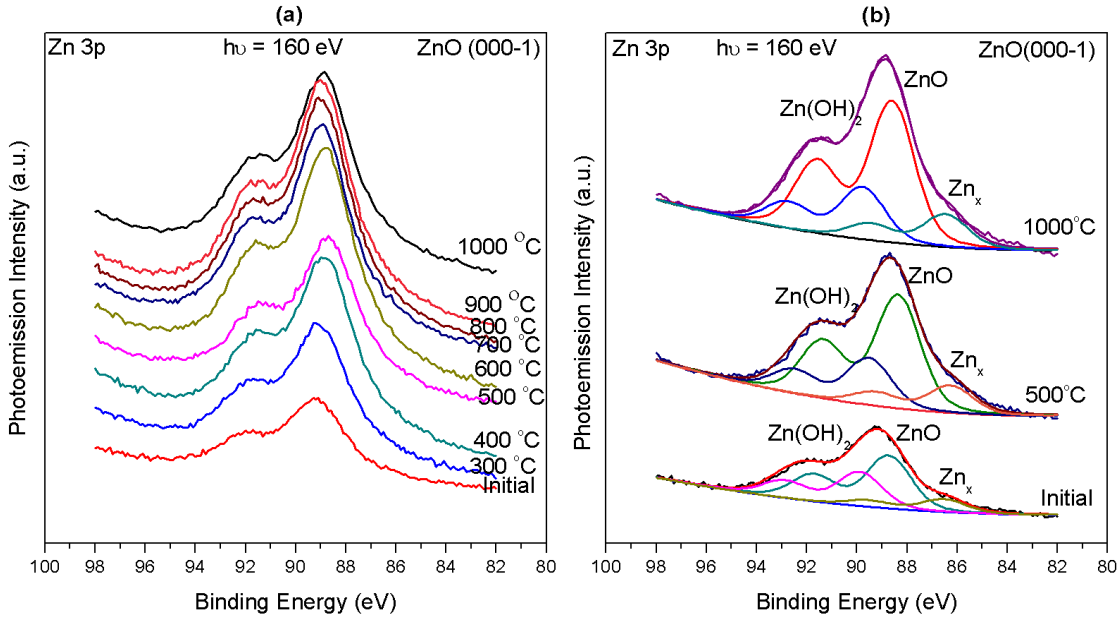

Figure 7.5: Zinc - Zn 3p core level spectra for (000-1) surface (a) Comparison of spectra for different O_2 annealing temperatures (b) peak fitted spectra for selective temperatures.

The Zn 3d core level and valence band spectra for the ZnO (000-1) surface for different oxygen annealing temperatures are shown in Figure 7.6(a). Valence band spectra were acquired at photoemission energy of 60 eV where the photoionization cross section of the zinc 3d core level is high [28]. The binding energy position of the Zn 3d peak as a function of annealing treatment is shown in figure 7.6(b). The position of the valence band maximum (VBM), determined by a linear extrapolation of the leading edge, is consistent with Zn 3d peak binding energy variation (see figure 7.6(b)). Up to an annealing temperature of 500 °C, there is a continuous reduction in the binding energies, consistent with the downward movement of the Fermi level in the ZnO bandgap. This is confirmed by the work function measurements shown in figure 7.7 which show a corresponding opposite but equal in magnitude change in value over the same temperature range.

The chemical composition and removal or reduction of contaminations can be quantified by using the area of the photoemission peaks. The removal of carbon contamination was measured by the peak area of C 1s core level spectra (see figure 7.8(a)). The primary (C-C) carbon was significantly reduced from the initial condition by the 600 °C oxygen anneal. Similarly, carbon trioxide (O-C=O) also reduced up to 600 °C, but carbon dioxide (C=O) slightly increased from 400 °C to 600 °C which is attributed to surface chemical reactions between the dissociating C-C bonds and surface oxygen. Finally at 700 °C the carbon

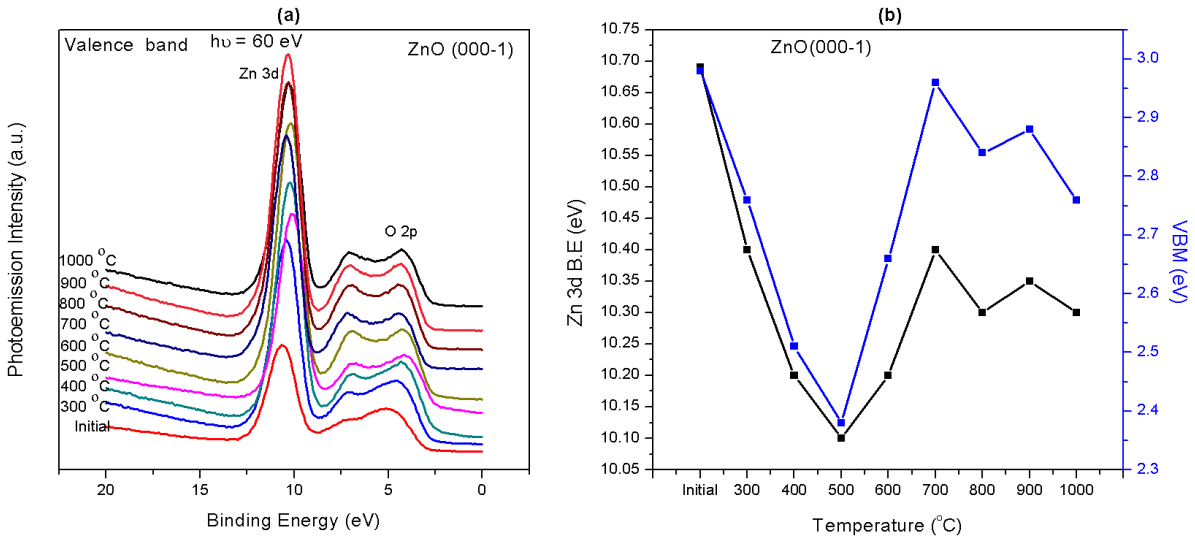

Figure 7.6: Valence band with Zn 3d core level spectra for (000-1) surface (a) Comparison of spectra for different O_2 annealing temperatures (b) Variation of valence band maximum (VBM) and binding energy of Zn 3d Peak for different annealing temperature in O_2 atmosphere.

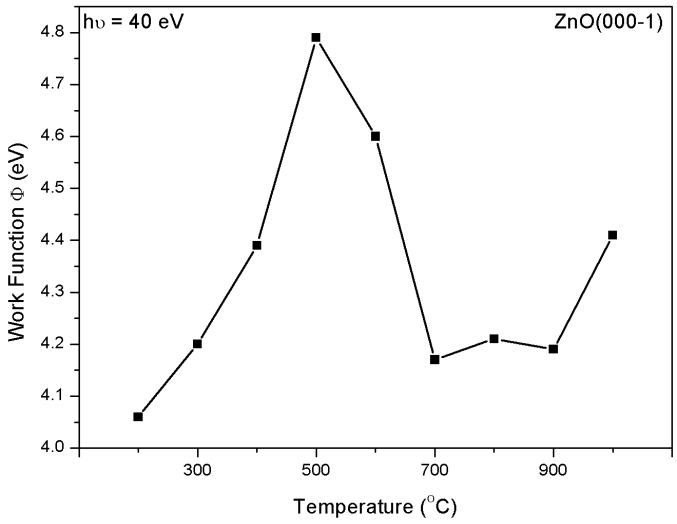

Figure 7.7: Work function (ϕ) measurements of ZnO (000-1) surface for different oxygen annealing temperatures.

signal is reduced below the detection limit of the measurement technique. The presence of hydroxide on ZnO surface was detected in both O 1s and Zn 3p peaks. But the photoemission sensitivity of O 1s core level peak is much higher than the Zn 3p peak and by peak fitting the hydroxide component peak can easily be distinguished in O 1s core level profiles.

The band diagrams at the different stages of oxygen annealed of the ZnO (000-1) surface are shown in figure 7.9. In the ZnO bulk, the reported Fermi level

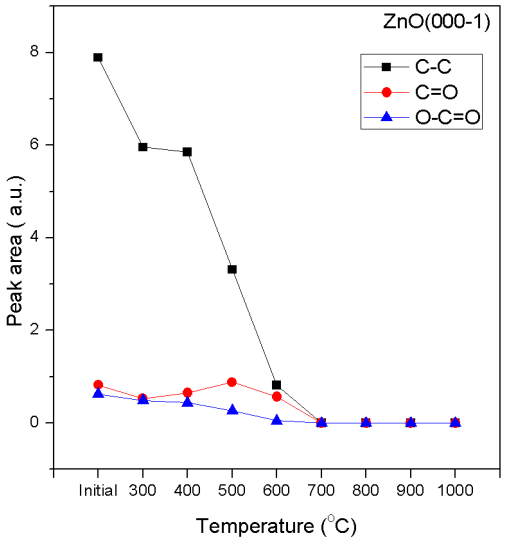

Figure 7.8: (a) Rate of removal carbon contamination on (000-1) surface with respect to oxygen annealing temperatures (b) Ratios of zinc to oxygen and hydroxide to zinc oxide for different annealing temperatures in O_2 atmosphere.

position is 3.1 eV above the VBM and work function is 4.0 eV [8, 15, 29]. The VBM and work function values for different steps in the present experiment (see figure 7.6 and figure 7.7) are determined with respect to these bulk values. In the initial condition the ZnO(000-1) surface has upward band bending of 0.38 eV. At 700 °C, ZnO(000-1) surface the carbon free surface has an upward band bending of 0.40 eV. Finally, at an oxygen annealing temperature of 1000 °C results in 0.6 eV upward band bending.

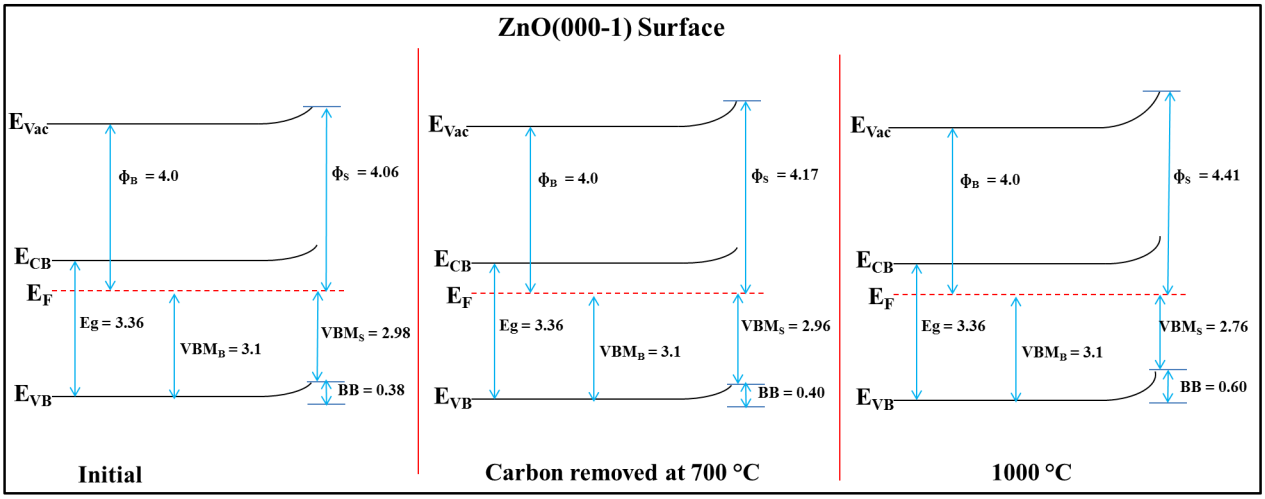

Figure 7.9: (Energy level band diagram of ZnO(000-1) surface for initial condition, after complete removal of carbon contamination at 700 °C, final stage of annealing at 1000 °C in oxygen.

7.3.1.2 (0001)-Zn terminated surface

Based on the previous oxygen annealing study of ZnO (000-1) O-terminated surface the optimised temperature for cleaning carbon from surface was found to be between 600 °C and 700 °C. So for oxygen annealing study of the ZnO(0001)-Zn terminated surface annealing temperature started at 600 °C up to 1000 °C. At the photoemission energy of 600 eV survey spectra were recoded for oxygen annealing temperatures as shown in figure 7.10. The peak binding energies were, Zn 3d - 11.99 eV, Zn 3p - 90 ± 0.5 eV, Zn 3s - 141.75 ± 0.25 eV, O 1s - 533.5 ± 0.5 eV, consistent with previous studies. There are trace signals of a residual C 1s component up to 800 °C while the Cl 2p core level peak shown in figure 7.11 is completely removed after oxygen annealing at 700 °C.

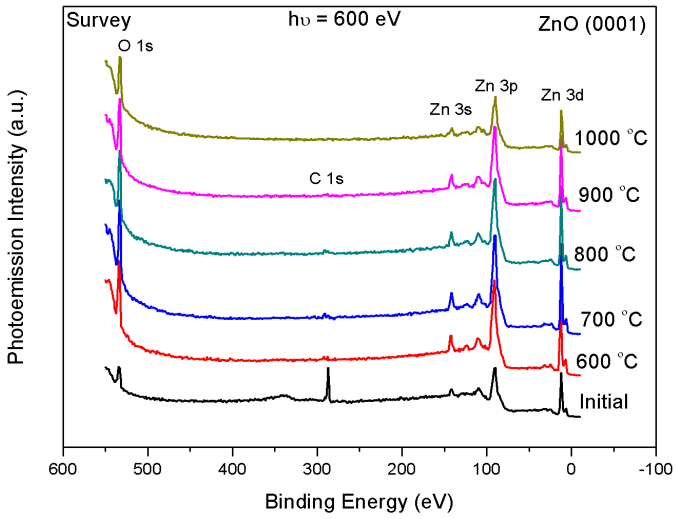

Figure 7.10: Survey spectra for ZnO(0001) Zn surface for oxygen annealing temperatures.

C 1s core level spectra for ZnO (0001) surface for oxygen annealing temperatures are shown in figure 7.12. On comparing the carbon spectra (see figure 7.12(a)) at different annealing temperatures, the main C-C attributed component peak is rapidly attenuated after annealing at 600 °C. Peak fitting of the carbon spectra (see figure 7.12(b)) reveal three peaks with binding energies, C-C - 286.4 ± 0.15 eV, C=O - 287.6 ± 0.4 eV and O-C=O - 290.5 ± 0.2 eV and FWHM of all peaks was between 1.1 eV to 1.54 eV. By further increasing the annealing temperatures to 1000 °C, the C-O bonding interactions are fully attenuated. The removal of carbon contamination only by 1000 °C annealing implies that bonding of carbon on Zn-terminated ZnO (0001) surface was very stronger.

O1s oxygen core level spectra for ZnO(0001) surface for various oxygen annealing temperatures are shown in figure 7.13(a). By peak fitting the oxygen core level spectra (see figure 7.13(b)), two peaks of ZnO at 533 ± 0.25 eV and OH at

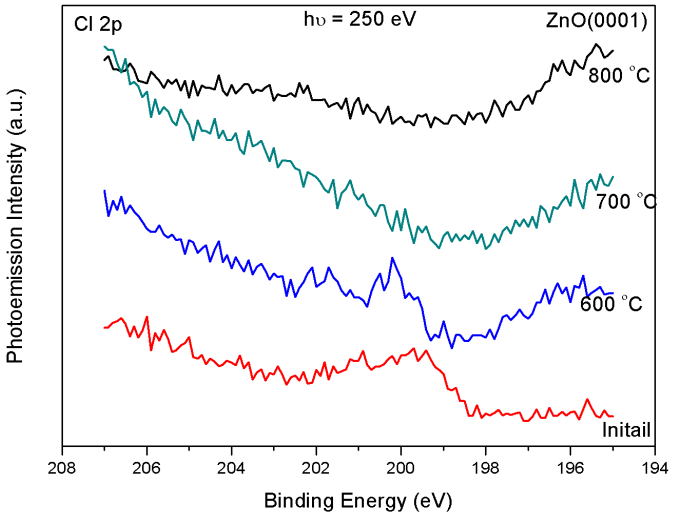

Figure 7.11: Cl 2p spectra of ZnO(0001) surface for oxygen annealing temperatures.

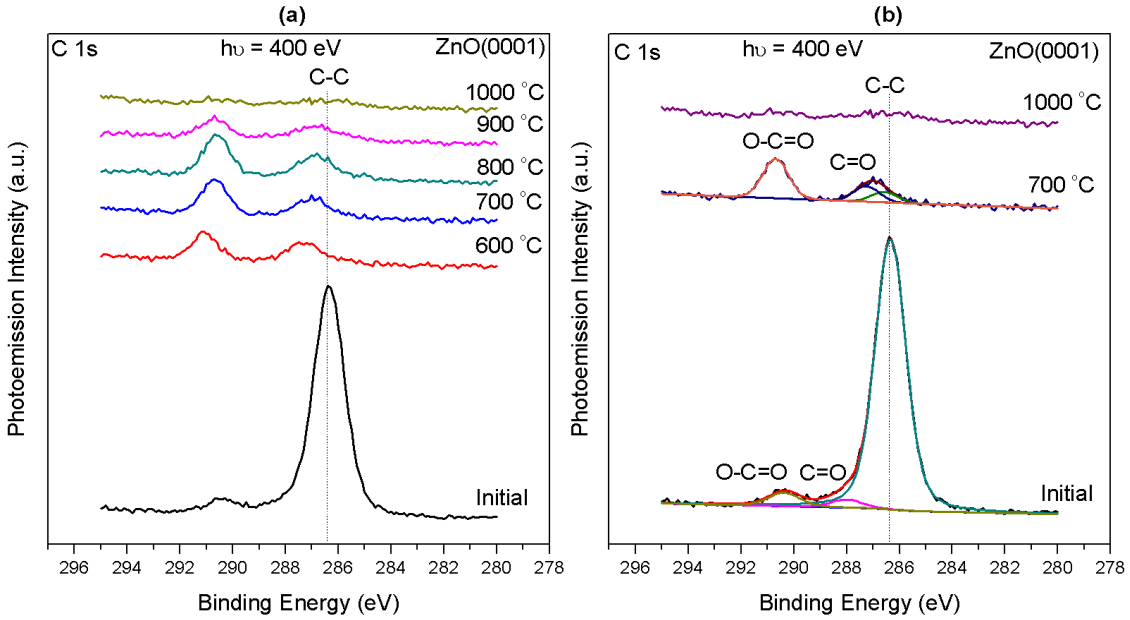

Figure 7.12: (a) Comparison of carbon C 1s core level spectra for ZnO (0001) surface for different oxygen annealing temperatures and (b) peak fitting for selected oxygen annealing temperatures.

534 ± 0.25 eV are consistently found and the relative intensity of these peaks is largely unaffected by the annealing process. The FWHM of all peaks was between 1.85 eV - 2.00 eV. The corresponding Zn 3p core level spectra for different oxygen annealing temperatures are shown in figure 7.14(a). From the peak fitting spectra (figure 7.14(b)), the usual three peaks were fitted with binding energy, Zn_x - 86.5 ± 0.3 eV, ZnO - 88.50 ± 0.3 eV and $Zn(OH)_2$ - 89.60 ± 0.25 eV. The $Zn(OH)_2$ hydroxide signal was found to be approximately equal to the oxygen signal from

the ZnO independent of annealing temperature. The FWHM of all zinc peaks is 2.1 eV

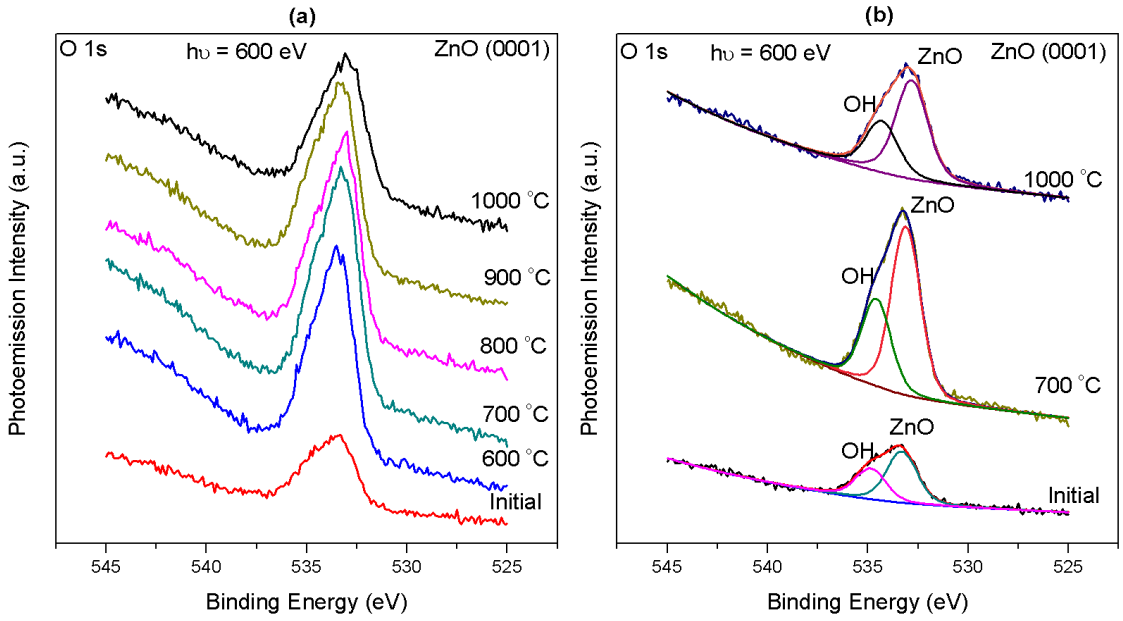

Figure 7.13: (a) Comparative O 1s core level spectra of ZnO (0001) surface different annealing oxygen temperatures and (b) peak fitting of oxygen spectra for selected oxygen annealing temperatures.

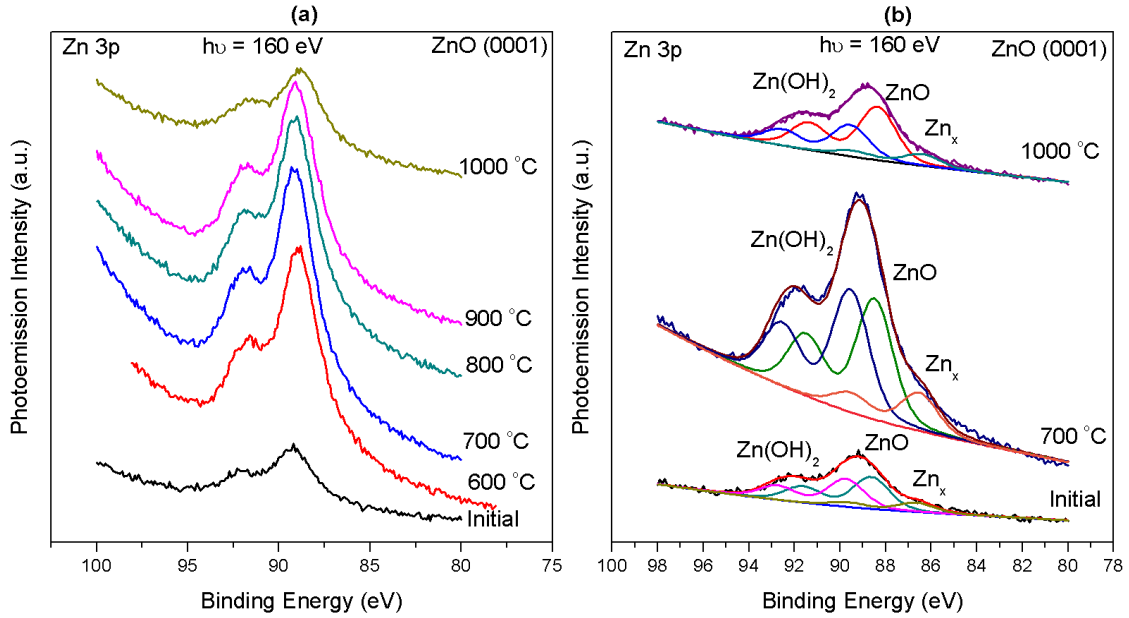

Figure 7.14: (a) Comparative Zn 3p zinc core level spectra for ZnO(0001) surface for different oxygen temperatures and (b) peak fitting of zinc spectra for selected annealing oxygen temperatures.

Valence band spectra for ZnO (0001) surface for different annealing temperatures are shown in figure 7.15(a). A sharp O 2p core level peak is seen. The VBM values and Zn 3d B.E. plotted for different annealing temperatures (see figure 7.15(b))

shows the same trend of variation confirming the Fermi level movement. By removing all carbon contaminations by oxygen annealing at 1000 °C Zn 3d B.E. and VBM reached a minimum value. The work function measurements for ZnO(0001) surface are shown in figure 7.16. The work function value varies from 4.0 eV - 4.61eV, which reflects the corresponding equal but opposite change in the VBM position over the same temperature range.

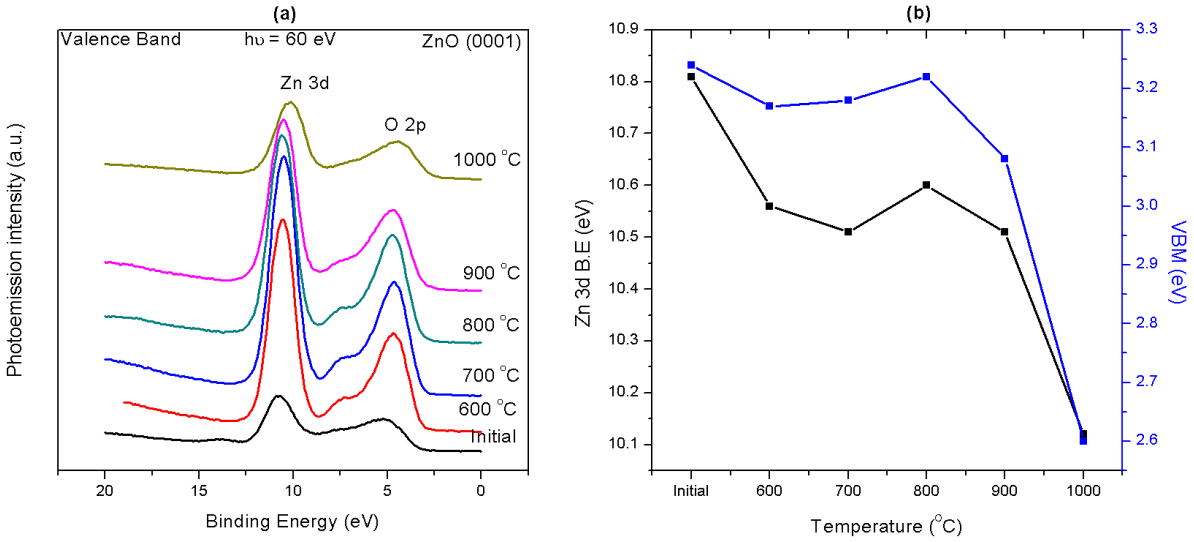

Figure 7.15: (a) Valence band spectra for ZnO(0001) surface for different oxygen annealing temperatures with Zn 3d Core level and (b) variation of VBM and Zn 3d binding energy with respect to oxygen annealing temperatures.

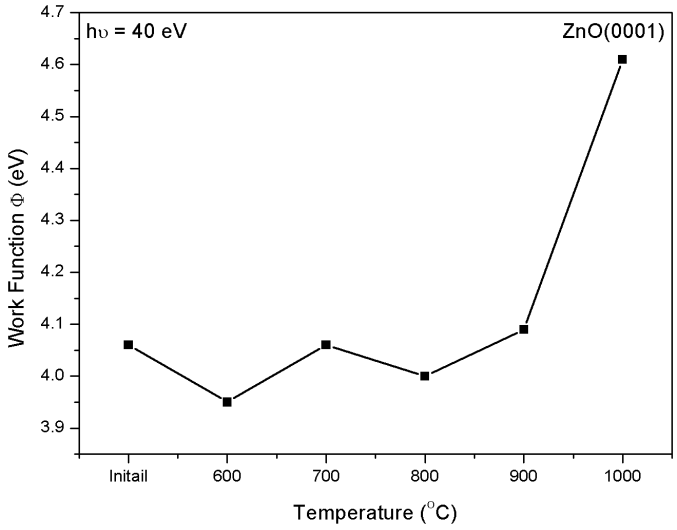

Figure 7.16: Work function measurements of ZnO (000-1) surface for different oxygen annealing temperatures.

The removal of carbon, the ratio of OH to ZnO, and the ratio of Zn to O on ZnO(0001) surface for different annealing temperatures in an oxygen atmosphere

is shown in figure 7.17. Graph for carbon removal (figure 7.17(a)) shows that oxygen annealing at 600 °C significantly reduces the C-C carbon with a small increase in the C=O and O-C=O bonds as previously observed. The ratio of OH/ZnO (figure 7.17(b)) is almost uniform for all annealing temperatures showing that hydroxide contamination was very stable on ZnO(0001) surface. The stoichiometry Zn/O is almost uniform for all annealing temperatures.

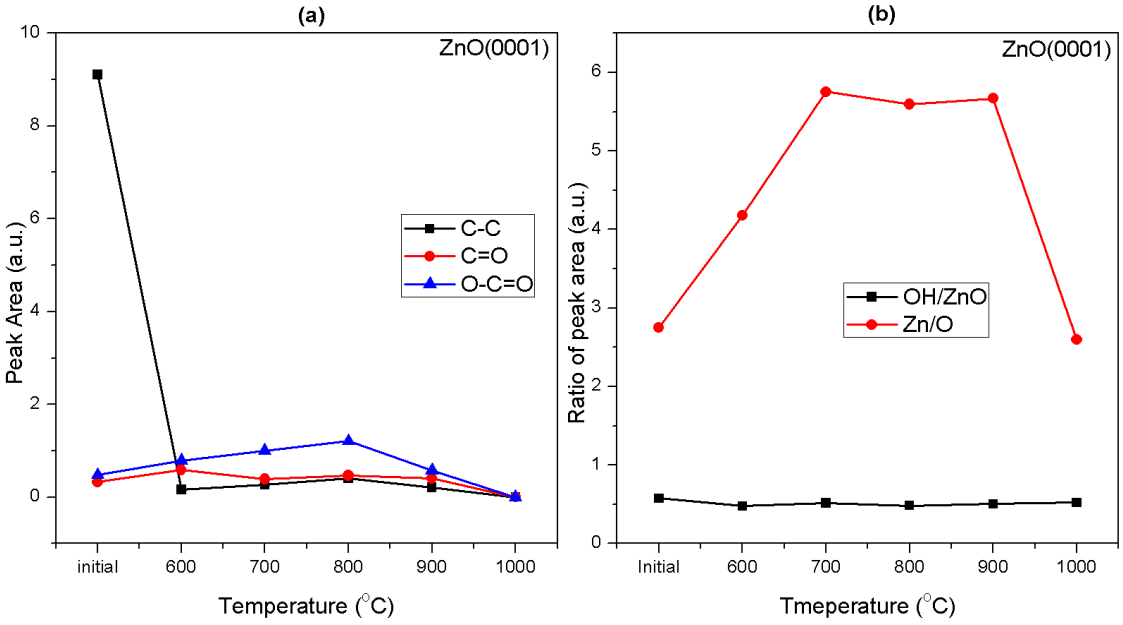

Figure 7.17: The effect of annealing ZnO(0001) surface in oxygen atmosphere (a) the removal of carbon contamination, (b) ratio of hydroxide to zinc oxide in oxygen core level and ratio of ZnO in Zn 3p core level to ZnO in O 1s core level.

The electronic band alignments of ZnO(0001)-Zn surface deduced from these measurements for the as received condition and final oxygen anneal at 1000 C are shown in figure 7.18. The VBM and work function values were obtained from experiment (refer figure 7.15 and figure 7.16). The band bending is calculated from the difference between ZnO energy band gap to VBM value. In the initial condition Fermi level was very close to conduction band with downward band bending. At 1000 °C ZnO (0001) surface became carbon free the Fermi level was away from conduction band with upward banding of 0.76 eV. So the removal of carbon contamination on ZnO (0001) surface by oxygen annealing turns the downward band bending into upward band bending. Carbon on ZnO (0001) surface plays an important role in change in band bending.

7.3.1.3 (10-10)-Zn and O terminated surface

For the ZnO(10-10) surface the oxygen annealing temperature range was chosen to be 600 °C to 900 °C. The survey spectra for ZnO(10-10) surface for different oxygen annealing temperatures is shown in figure 7.19. For this surface the

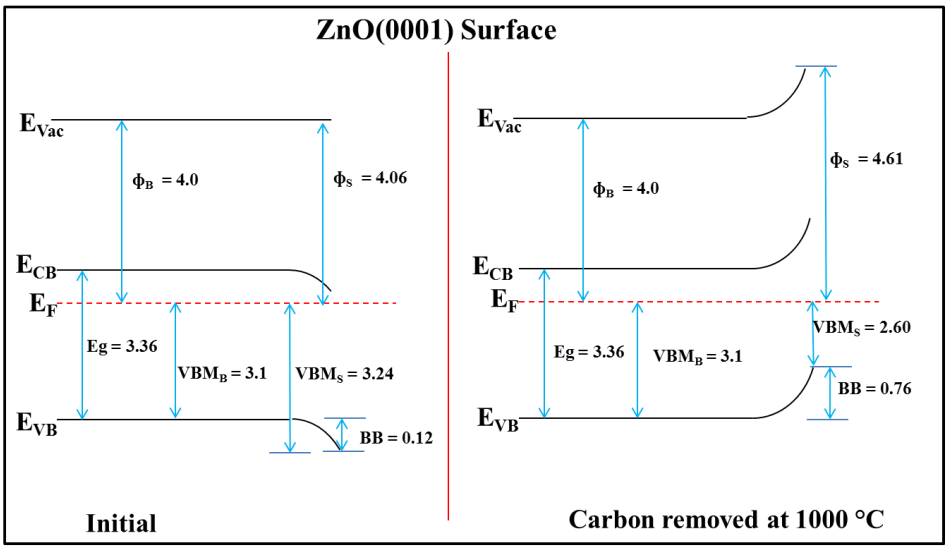

Figure 7.18: Energy level band diagram of ZnO(0001) surface at initial condition and after annealing at 1000 °C in oxygen atmosphere.

600 °C oxygen anneal was sufficient to completely attenuate the carbon signal. The narrow scans for carbon, C 1s core level shown in figure 7.20 for the different oxygen annealing temperatures were curve fitted with the same three component peaks as reported above. The peak fitting of carbon spectra with peaks, C-C - 286.45 eV, C=O - 288.04 eV, O-C=O - 290.32 eV and the FWHM of all peaks was 1.5 eV

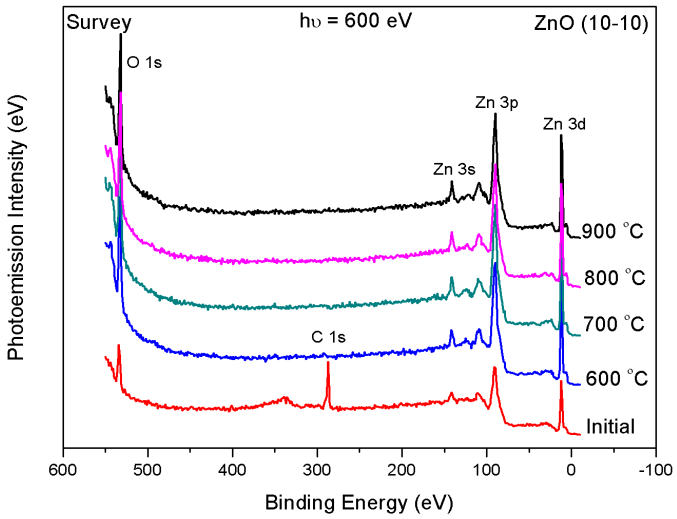

Figure 7.19: Survey spectra for ZnO(10-10) surface for various oxygen annealing temperatures .

Narrow scans for the O 1s core level for the different annealing temperatures displayed in figure 7.21(a) show that once the surface contamination layer is re-

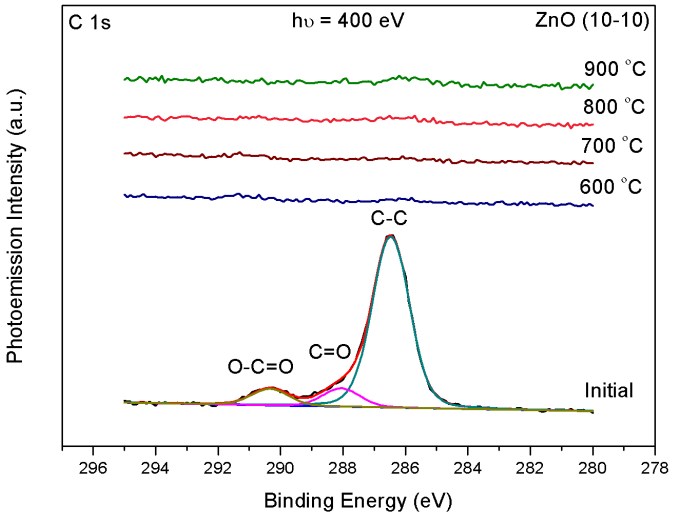

Figure 7.20: C 1s - Carbon core level spectra for ZnO(10-10) surface for various oxygen annealing temperatures.

moved, the spectrum profile remains largely unchanged. The curve fitted spectra in figure 7.21(b) show that annealing removes the H_2O related component and the hydroxide peak is reduced in intensity relative to the ZnO peak between the 700 °C and 900 °C anneals. The binding energy of peaks was ZnO - 532.8 ± 0.4 eV, OH - 534.45 ± 0.25 eV and H_2O - 536.19 eV. The FWHM of peaks for initial condition is 1.99 eV and for annealing condition is 2.11 eV. The narrow scans for the Zn 3p core level for different annealing temperatures are shown in figure 7.22(a). Again, once the surface contamination layer is removed, the peak profile remains largely unchanged. The curve fitted spectra shown in figure 7.22(b) display the same peaks as previously observed.

The valence band spectra for the ZnO(10-10) surface for different annealing temperatures are shown in figure 7.23(a). The variation of Zn 3d B.E. and VBM (see figure 7.23(b)) from initial to 900 °C is approximately 0.5 eV which reflects the Fermi level movement. The work function (ϕ) of ZnO(10-10) surface for different oxygen annealing temperatures is plotted in figure 7.24. The work function value varies from 4.13 eV - 5.32 eV as the annealing temperature is increased. The increase in work function to values above 5 eV after the 800 °C has been attributed to the presence of a surface dipole [30] between surface terminated Zn and O atoms on ZnO(10-10) surface as the Fermi level doesnt move by this amount in the bandgap.

The graph for change in hydroxide signal for different oxygen annealing temperatures is shown in figure 7.25 in terms of OH/ZnO ratios. Similarly stoichiometry analysis of Zn and O is plotted as the ratio of Zn/O. There is a decrease in the OH/ZnO ratio following the 600 °C anneal and further gradual decrease with

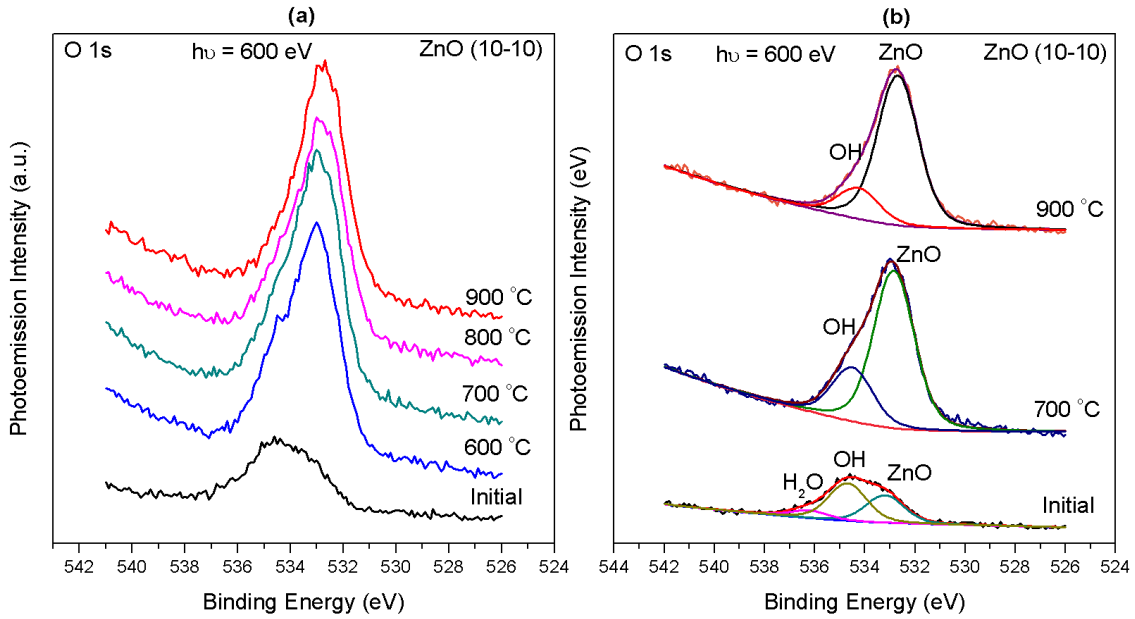

Figure 7.21: O 1s - Oxygen core level spectra for ZnO(10-10) surface (a) Comparative oxygen spectra for various oxygen annealing temperatures and (b) peak fitting of oxygen spectra for selected oxygen annealing temperatures.

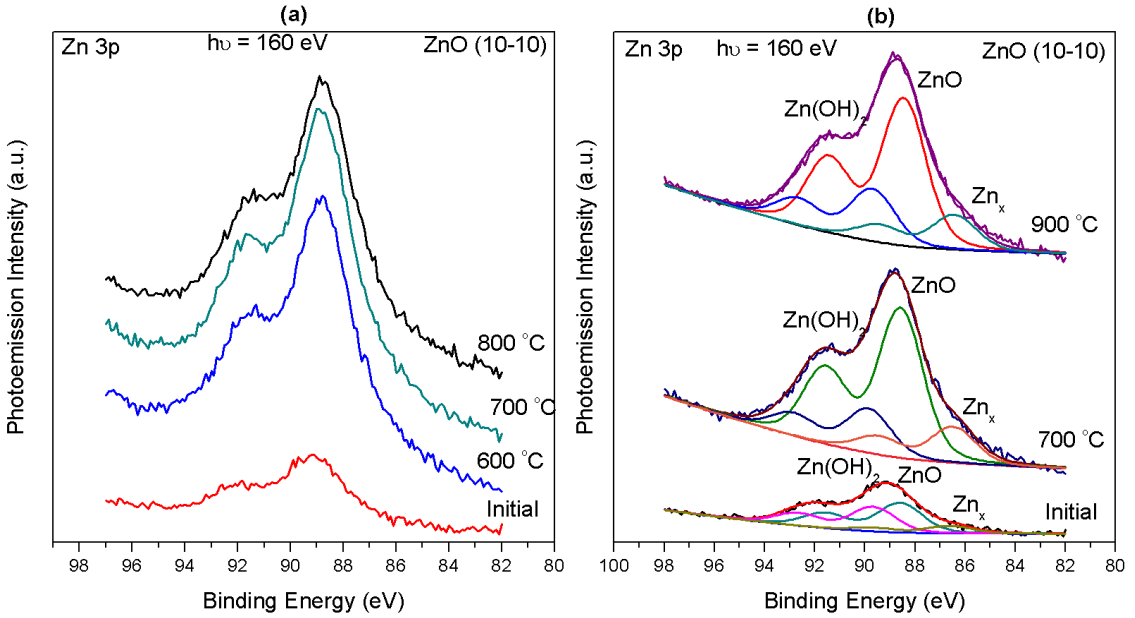

Figure 7.22: Zn 3p - Zinc core level spectra for ZnO(10-10) surface (a) comparative zinc spectra for various oxygen annealing temperatures and (b) peak fitting of zinc spectra for selected oxygen annealing temperatures.

increase in annealing temperature. This variation resembles the change in work function and the VBM values of ZnO(10-10) surface as a reduction in hydroxide results in an increase in the work function and a decrease in the VBM value.

The electronic structure of ZnO(10-10) surface from initial to different oxygen annealing conditions is shown in figure 7.26. The work function and VBM values

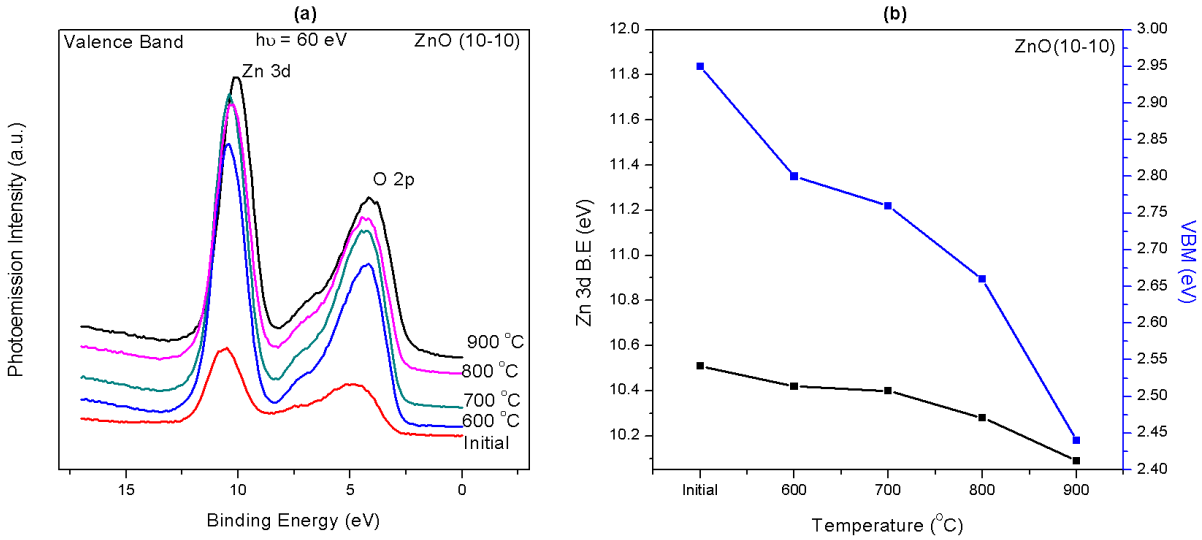

Figure 7.23: (a) Valence band spectra for ZnO(10-10) surface for various oxygen annealing temperatures and (b) Variation of VBM values and Zn 3d B. E. with respect to annealing temperatures.

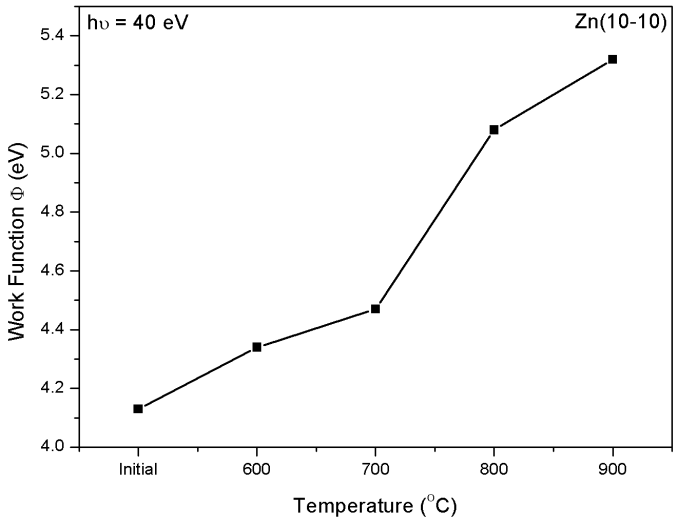

Figure 7.24: Work function of ZnO(10-10) surface for different oxygen annealing temperatures.

were obtained from previous graphs (see figure 7.23 and figure 7.24). The band bending and electron affinity (χ) values were calculated from VBM, work function and the known ZnO band gap. In the initial condition 0.41 eV of upward band bending was observed with presence of carbon and hydroxide contamination. Then following the 600 °C oxygen anneal resulting in the complete removal of carbon upward band bending increased to 0.56 eV. On final annealing at 900 °C, a maximum upward band bending of 0.92 eV is measured and an increase in work function to 5.32 eV which is attributed to a surface dipole between Zn and O

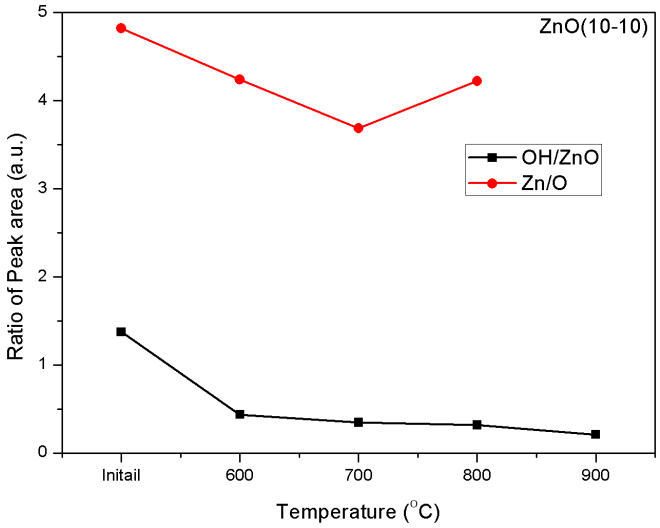

Figure 7.25: Ratio of OH/ZnO in O 1s oxygen core level for ZnO(10-10) surface and ratio of ZnO component in Zn 3p core level to ZnO component in O 1s core level for different oxygen annealing temperatures.

atoms.

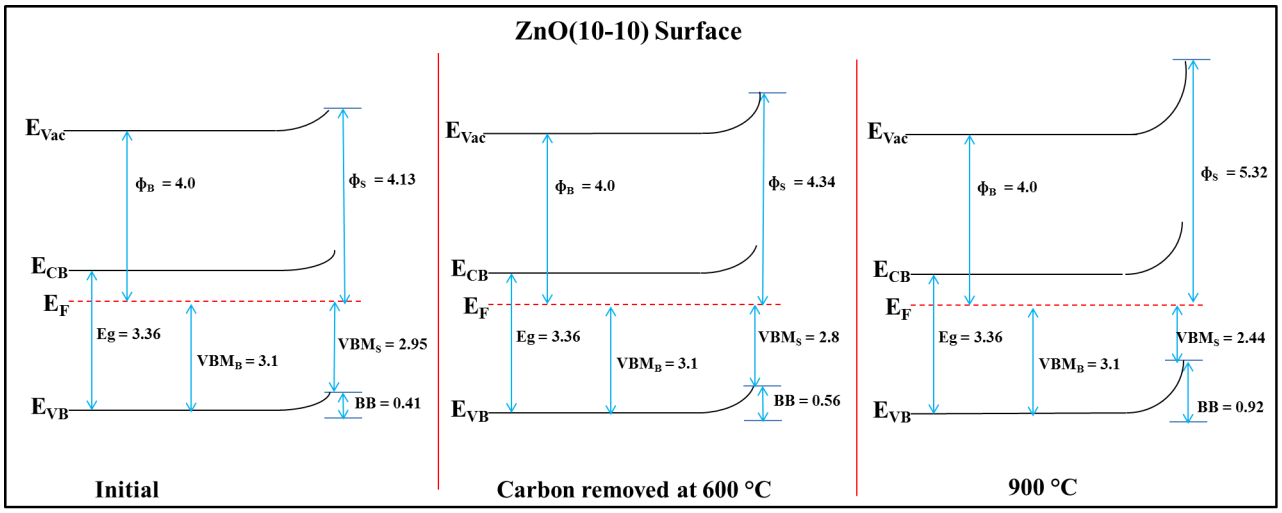

Figure 7.26: Energy level band diagram of ZnO(10-10) surface for surface for initial condition, after complete removal of carbon contamination, final stage of annealing at 1000 °C in oxygen.

7.3.1.4 (11-20)-Zn and O terminated surface

For the (11-20) surface, selective oxygen annealing temperatures of 600 °C, 750 °C and 900 °C were chosen based on previous studies of the other ZnO surfaces. Survey spectra for ZnO (11-20) surface for oxygen annealing temperatures are shown in figure 7.27. Three zinc peaks with one oxygen and carbon with binding

energies: Zn 3d - 12 ± 0.05 eV, Zn 3p - 90 ± 0.05 eV, Zn 3s - 14.7 ± 0.3 eV, C 1s - 286.99 eV and O 1s - 533.95 (initial), 532.99 eV (annealing). Following the 600 °C anneal the carbon signal was completely attenuated with the detailed curve fitted C 1s signal shown in figure 7.28 with the same peak fitted components as previously reported.

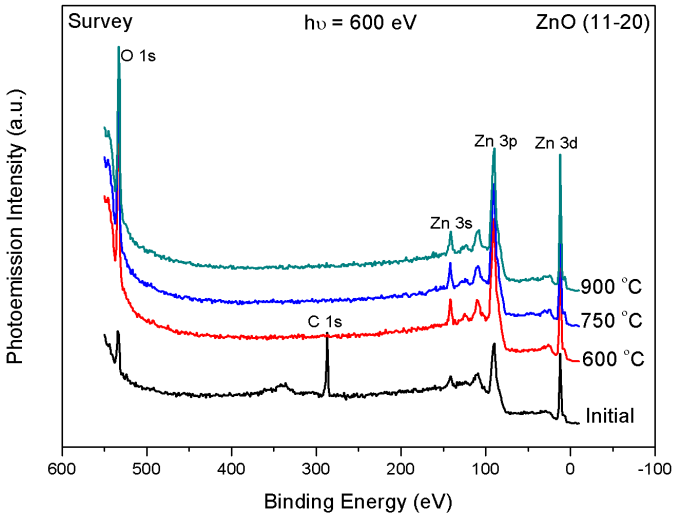

Figure 7.27: Survey spectra for ZnO(11-20) surface for various oxygen annealing temperatures .

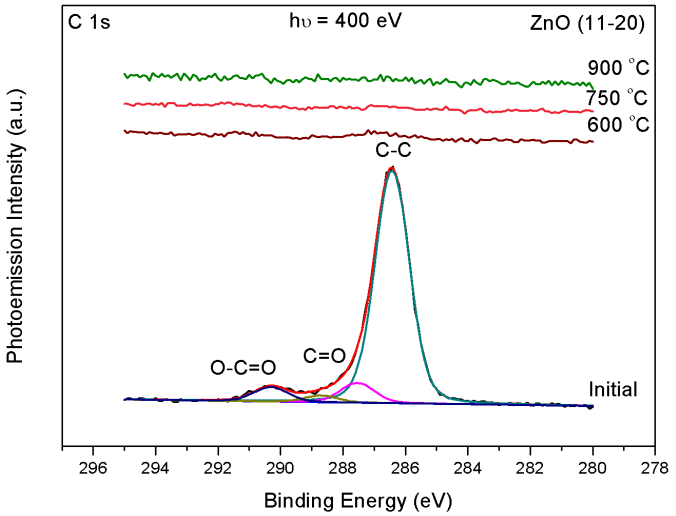

Figure 7.28: C 1s - Carbon core level spectra for ZnO(11-20) surface for various oxygen annealing temperatures.

The O 1s core level spectra of the ZnO (11-20) surface for different annealing temperatures are shown in figure 7.29(a) and (b). Following the pattern observed

on previous surfaces, once the initial contamination layer is removed, the peak profile can be fitted with ZnO and OH derived component peaks, the relative intensity of which remains primarily unaltered by annealing temperature. The binding energy of the peak was ZnO - 533.2 eV, OH - 534.8 eV and H_2O - 535.8 eV and FWHM of all peaks is 2.0 eV.

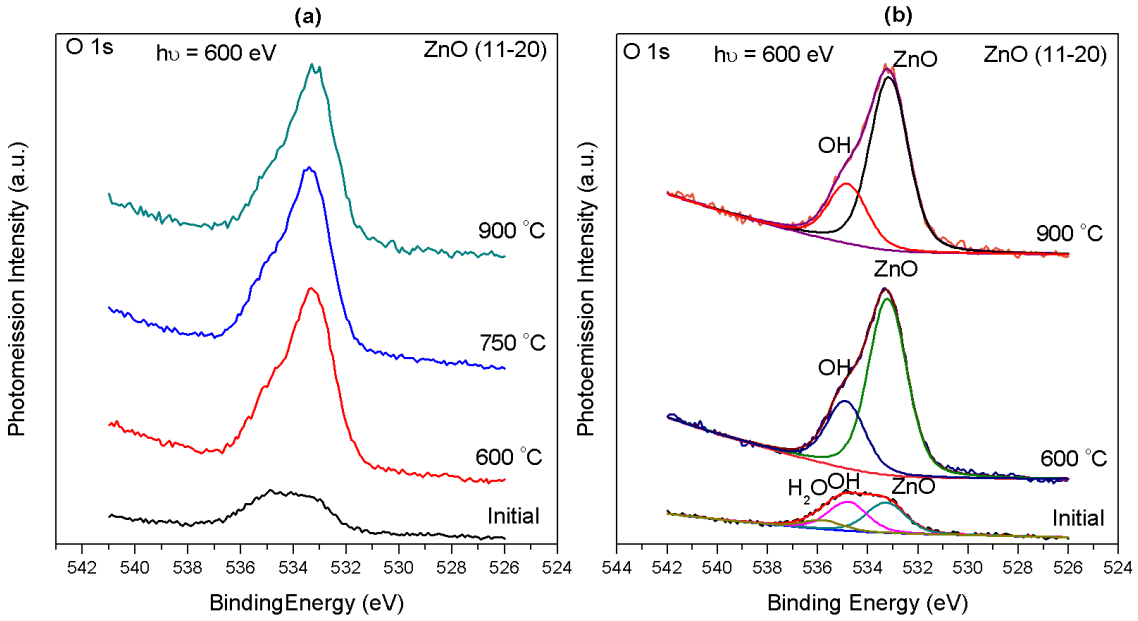

Figure 7.29: O 1s - Oxygen core level spectra for ZnO(11-20) surface (a) comparative oxygen spectra for various oxygen annealing temperatures and (b) peak fitting of oxygen spectra for selected oxygen annealing temperatures.

The Zn 3p core level spectra for the ZnO (11-20) surface for different annealing temperatures are shown in figure 7.30(a). Three peaks were fitted for Zn 3p core level with binding energies(see figure 7.30(b)), Zn_x - 86.50 ± 0.25 eV, ZnO - 88.6 ± 0.2 eV and $Zn(OH)_2$ - 89.75 ± 0.25 eV. The FWHM of all zinc peaks is 2.3 eV. The curve fitted spectra for the annealed surface show two component peaks for ZnO and $Zn(OH)_2$. The Zn3d core level and valence band spectra for the ZnO (11-20) surface of different oxygen annealing temperatures are shown in figure 7.31(a) and display a strong O 2p signal after removal of the surface contamination layer. The variation of Zn 3d binding energy and VBM values are plotted in figure 7.31(b) essentially show that there is very little Fermi level movement with annealing cycle.

The change in the work function (ϕ) values for the ZnO (10-10) surface displayed in figure 7.32 show that once the initial surface contamination layer is removed, there is no significant change from the measured value of 4.0 eV. The OH/ZnO and Zn/O elemental ratios plotted in figure 7.33 show that once the surface contamination is removed the chemical composition remains unaltered. Similar to work function, the Zn/O ratios as well as OH/ZnO ratios were high at the

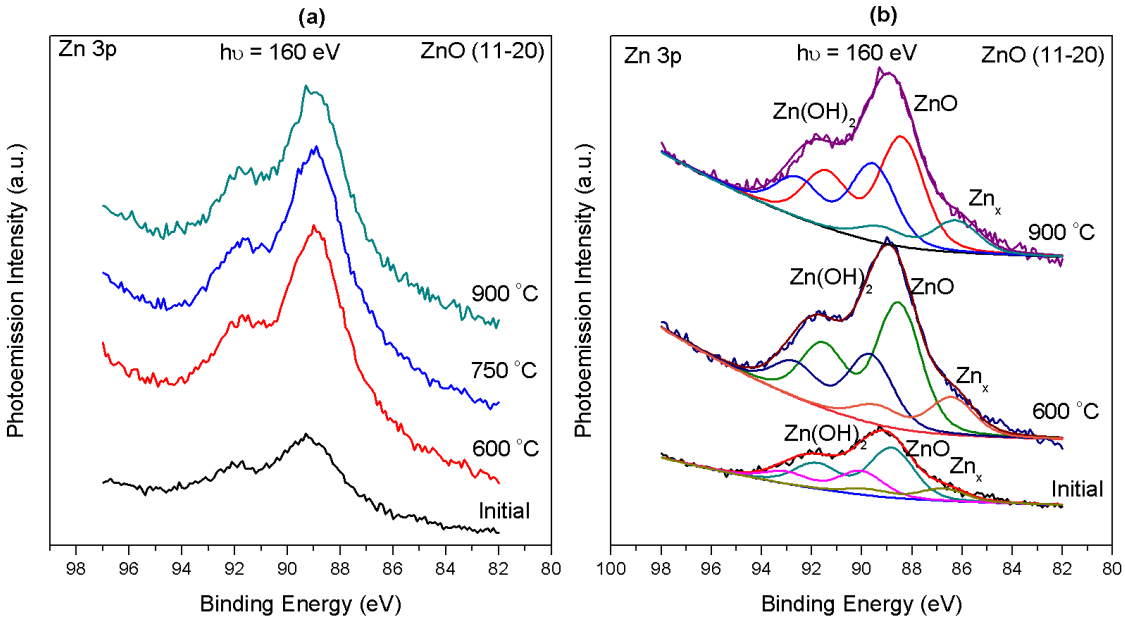

Figure 7.30: Zn 3p Zinc core level spectra for ZnO(11-20) surface (a) comparative zinc spectra for various oxygen annealing temperatures and (b) peak fitting of zinc spectra for selected oxygen annealing temperatures.

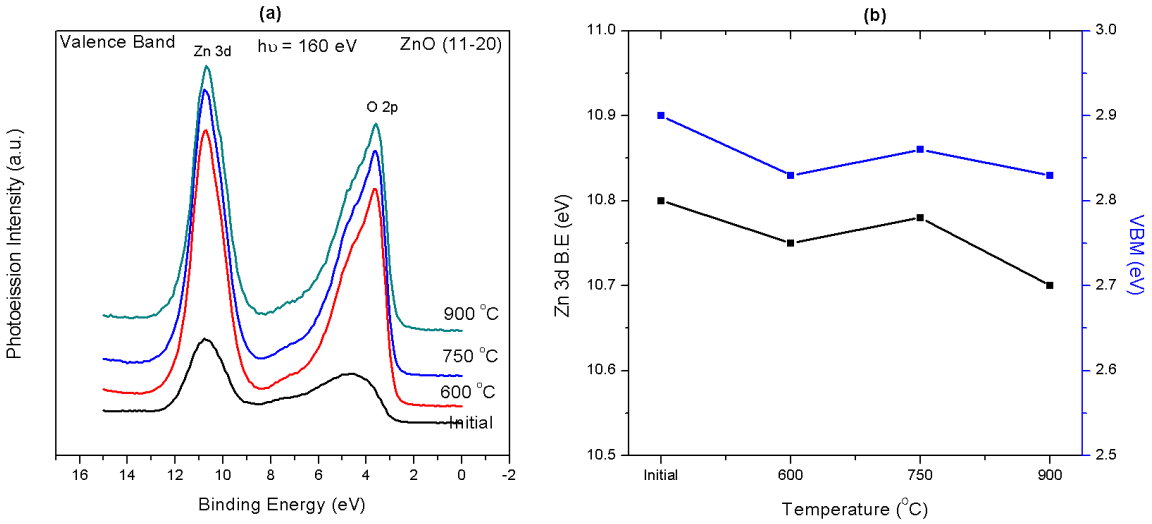

Figure 7.31: (a) Valence band spectra for ZnO(11-20) surface for various oxygen annealing temperatures and (b) Variation of VBM values and Zn 3d B. E. with respect to annealing temperatures.

initial condition. Then for annealing temperatures the ratio remains constant and shows no more change resulting from oxygen annealing on the ZnO (11-20) surface.

Electronic structure of ZnO(10-10) surface before and after oxygen annealing is shown in figure 7.34. The VBM and work function values were obtained from previous figures (see figure 7.31 and figure 7.32). In the initial condition the surface displays a large work function value 4.65 eV and 0.46 eV upward band

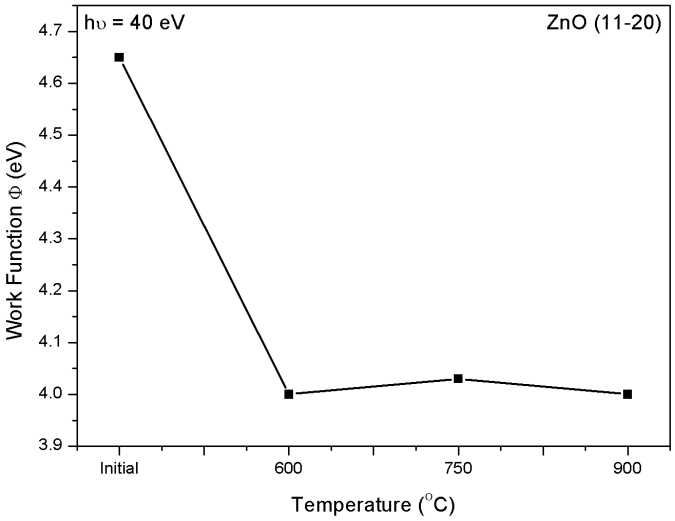

Figure 7.32: Work function of ZnO(11-20) surface for different oxygen annealing temperatures.

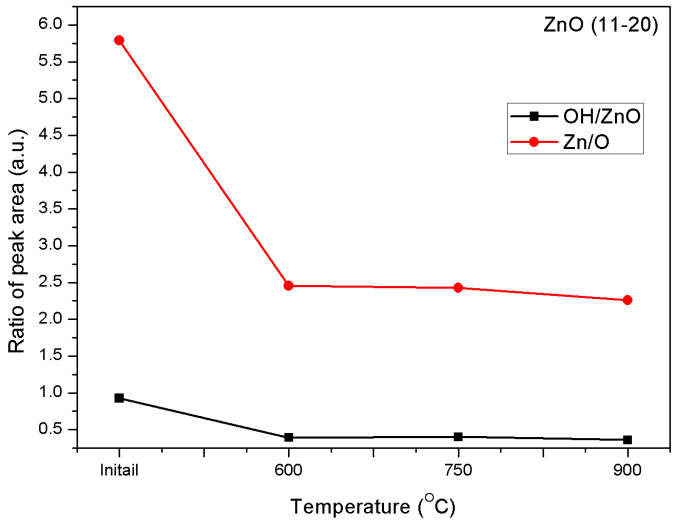

Figure 7.33: Ratio of OH/ZnO in O1s oxygen core level for ZnO(11-20) and ratio of ZnO component in Zn 3p core level to ZnO component in O 1s core level for different oxygen annealing temperatures.

bending. After removal of carbon from the surface the band bending increased by 0.1 eV to 0.56 eV while the work function decreased to 4.0 eV. After the final oxygen anneal at 900 °C no subsequent changes are observed. As mentioned earlier, in initial condition the high work function is due to surface dipole [30] resulting from the presence of surface contamination. The oxygen annealing of the ZnO (11-20) surface removes the carbon from the altering the work fucntion, but doesnt impact significantly on the Fermi level position in the band gap.

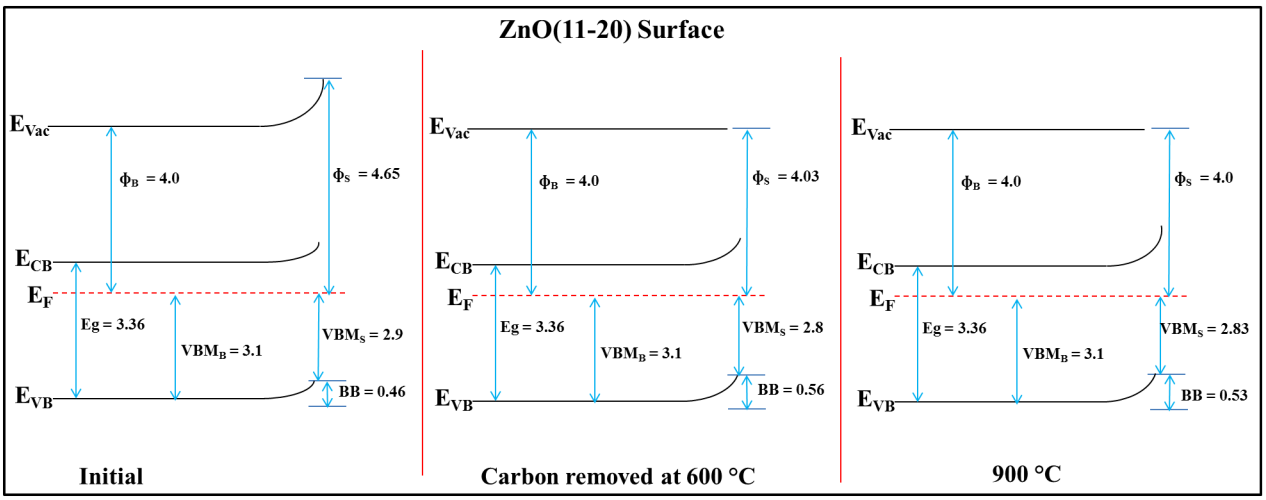

Figure 7.34: Energy level band diagram of ZnO(11-20) surface for surface for initial condition, after complete removal of carbon contamination, final stage of annealing at 1000 °C in oxygen.

7.3.1.5 Comparative analysis

Binding energy, FWHM and Contamination Analysis: On comparing the binding energy variation between all four ZnO surfaces for different core levels, for Zn 3p the variation is no more than 0.1 eV, while for oxygen and carbon the variation in BE position is between 0.5 - 1.0 eV. This large variations of peak BE peak are attributed to surface chemical reactions of carbon, carbon bonded oxides, hydroxide and water. When comparing FWHMs very standard values Zn 3p - 2.3 eV, O 1s - 2.1 eV, C 1s - 1.5 eV were found for ZnO(0001), ZnO(10-10) and Zn(11-20) surfaces. Only the ZnO(0001) surface has a smaller FWHM value of Zn 3p - 2.1 eV, O 1s - 1.8 eV and C 1s - 1.1 eV. Quantitative analysis of the surface carbon contamination on the different ZnO surfaces is displayed in figure 7.35. These carbon thicknesses were calculated using the NIST database [31]. Overall about 4 Å - 5.5 Å of carbon was seen on the ZnO surfaces after initial cleaning by organic solvents.

The amount of hydroxide on the different ZnO surfaces in the initial condition and after oxygen annealing are plotted in figure 7.36 in terms of OH/ZnO ratio of oxygen O 1s core level peak. For the ZnO(10-10) surface the highest hydroxide signal was observed, but this surface also displayed the lowest hydroxide signal following the oxygen anneal. The ZnO(000-1) and (11-20) surfaces display similar initial concentrations of hydroxide and the post treatment surfaces also display similar reduced concentrations to below half the original values. For the ZnO(0001) surface the initial concentration of hydroxide is significantly lower than on the other surfaces and the oxygen annealing treatment make almost no change in this concentration.

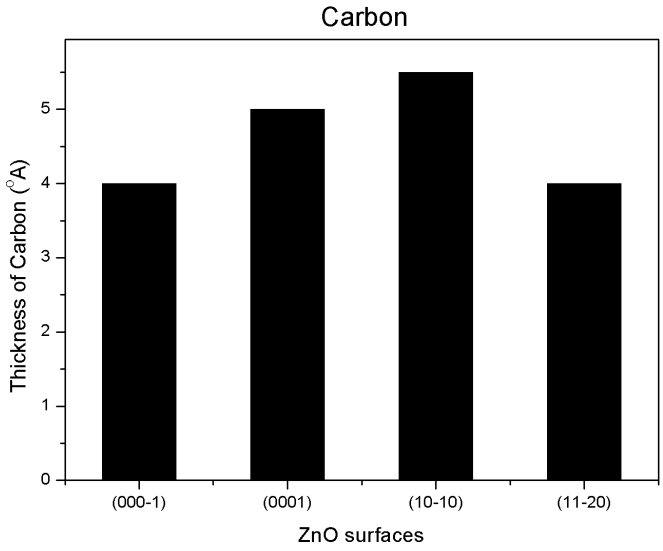

Figure 7.35: Thickness of carbon on different ZnO crystal surfaces prior to vacuum annealing.

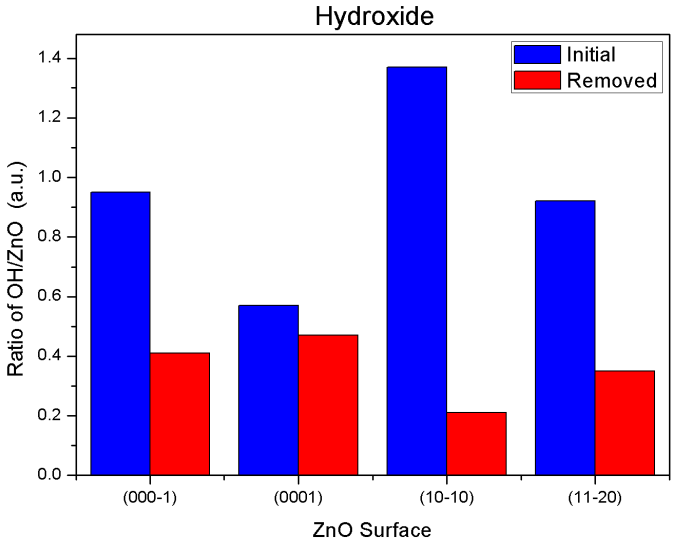

Figure 7.36: Amount of hydroxide on different ZnO surfaces in the initial condition and following the oxygen annealing treatments.

Band bending in different ZnO surfaces: The band bending values for four different Zno surfaces were tabulated in table 7.1. In initial (ethanol cleaned) condition for all ZnO surfaces, upward band bending was observed expect for the Zn-terminated (0001) surface which displayed downward band bending. After the complete removal of carbon contamination the (000-1) and (11-20) surfaces have a small increase (0.02 eV, 0.1 eV, respectively) in upward band bending. For the Zn-terminated (0001) surface the treatment results in a reversal of the

band bending from slightly downward to upward band bending of 0.76 eV. At the high annealing temperature of 1000 °C the band bending increased 0.2 eV for the ZnO (000-1) surface, 0.36 eV for the ZnO (10-10) surface at 900 °C and there was no change observed for the ZnO (11-20) surface.

Table 7.1: Upward band bending values of different ZnO surfaces before and after surface cleaning by oxygen annealing (*downward band bending).

ZnO surface	Sample Condition	Band bending (eV)
(000-1)	Initial	0.38
	700 °C (carbon removed)	0.4
	1000 °C	0.6
(0001)	Initial	0.12*
	1000 °C (carbon removed)	0.76
(10-10)	Initial	0.31
	700 °C (carbon removed)	0.56
	900 °C	0.92
(11-20)	Initial	0.46
	700 °C (carbon removed)	0.56
	900 °C	0.53

Identification of different ZnO surface termination by photoemission: The surface termination on ZnO crystals is commonly determined by observing the etching behaviour in a dilute hydrochloric acid solution. For example the (0001)-Zn terminated surface appears more polished following this etch test while the (0001)-O termination has an opaque appearance [32]. A non-destructive method to find a ZnO crystals surface termination is by making X-ray diffraction measurements [33]. Valence band spectra of the cleaned ZnO surfaces acquired in this study by synchrotron radiation based photoemission measurements show clear differences depending on the surface termination as shown in figure 7.37. At the photoemission energy of 60 eV the shape of the valence band spectra (O 2p peak) is distinctly different for the different surface terminations which is consistent with previous photoemission studies of different ZnO surfaces [15, 34].

7.3.2 XPS studies of atomic oxygen cleaning of ZnO surfaces

This XPS study investigated the effectiveness of atomic oxygen at surface cleaning of pulse laser deposited (PLD) grown ZnO thin films. Studies of both room temperature and elevated temperature exposures to atomic oxygen were undertaken.

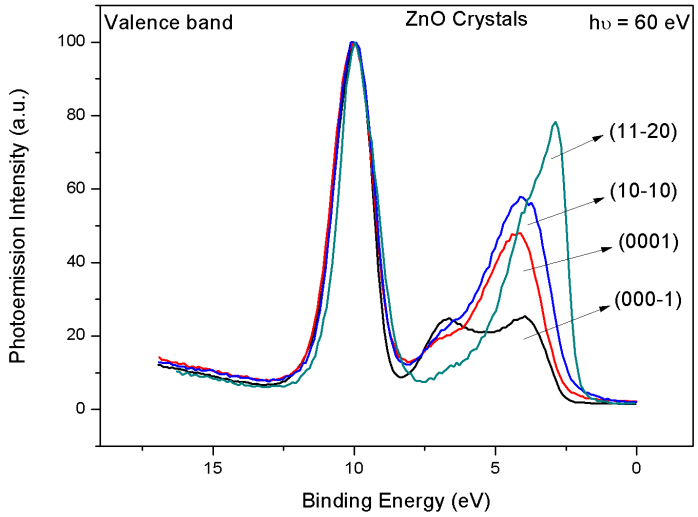

Figure 7.37: Valence band spectra for the different ZnO crystal surfaces acquired after annealing in an oxygen atmosphere at 900 °C.

7.3.2.1 Atomic oxygen cleaning of the ZnO surface at elevated temperatures

The atomic oxygen cleaning of ZnO thin film surfaces was carried out at annealing temperature up to 500 °C and the survey spectra are shown in figure 7.38. Core level photoemission and Auger peaks for zinc, oxygen and carbon are observed. The surface carbon contamination signal was removed for annealing temperatures above 100 °C. The narrow scans of the zinc LMM Auger peak shown in figure 7.39 indicate that the removal of the surface carbon contamination does not impact on the peak profile which is very sensitive to the surface chemical composition [35].

The carbon core level spectra shown in figure 7.40 indicate that the atomic oxygen treatment is effective at removing the carbon contamination at low temperature. The peak fitting of the carbon peak for the as received surface and following 100 °C atomic oxygen treatment shows the usual carbon bonded oxides with binding energies: C-C - 285 eV, C=O - 286.6 eV, O-C=O - 289 eV. The oxygen core level spectra were shown in figure 7.41(a)and(b) indicate that the higher binding energy hydroxide component peak is significantly attenuated by the atomic oxygen treatment.

The zinc 2p core level spectra shown in figure 7.42(a) have a BE position of zinc peak at 1022.7 ± 0.1 eV. The peak fitted spectra (figure 7.42(b)) show that the hydroxide component is attenuated following atomic oxygen treatment confirming the results observed in the O 1s core level spectra. The contamination analysis of the atomic oxygen cleaned ZnO thin film is shown in figure 7.43(a) and (b).

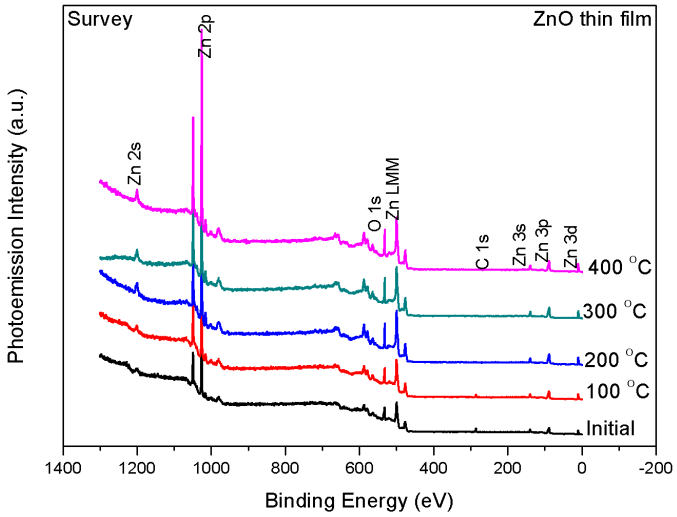

Figure 7.38: Survey spectra of PLD grown ZnO thin films for atomic oxygen cleaning at elevated temperatures.

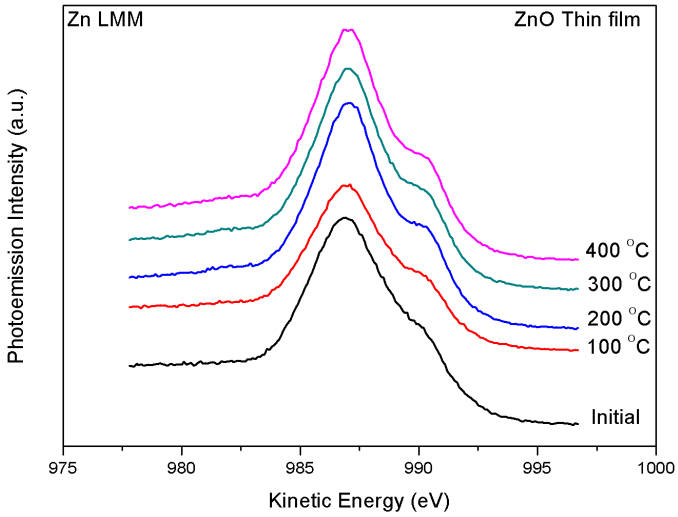

Figure 7.39: Zn LMM - Zinc Auger spectra for atomic oxygen cleaning of ZnO thin films at elevated temperatures.

7.3.2.2 Room temperature atomic oxygen cleaning ZnO surface

From a previous study of atomic hydrogen cleaning of GaAs by Kurt. G. Eyink et al [36], they reported that increasing the exposure time to atomic oxygen allowed the the cleaning temperature to be reduced. Therefore, the possibility of removing carbon contamination at room temperature by atomic oxygen was explored. Survey spectra for room temperature atomic oxygen cleaning of ZnO thin film are shown in figure 7.44. Only after a 180 minutes exposure to atomic

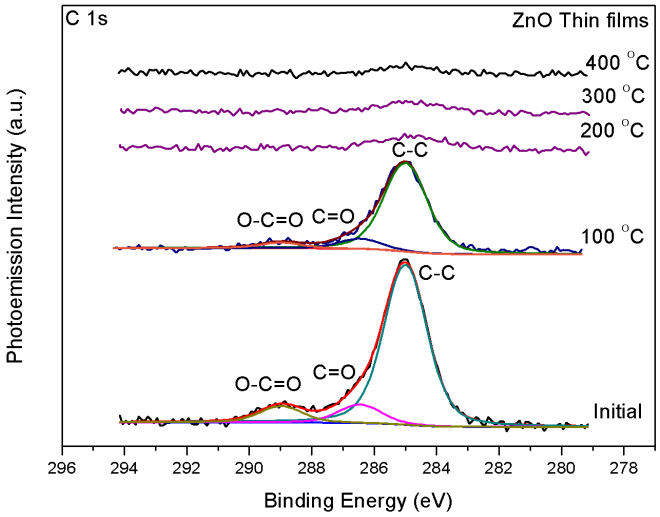

Figure 7.40: C 1s - Carbon spectra for atomic oxygen cleaning of ZnO thin films at elevated temperatures.

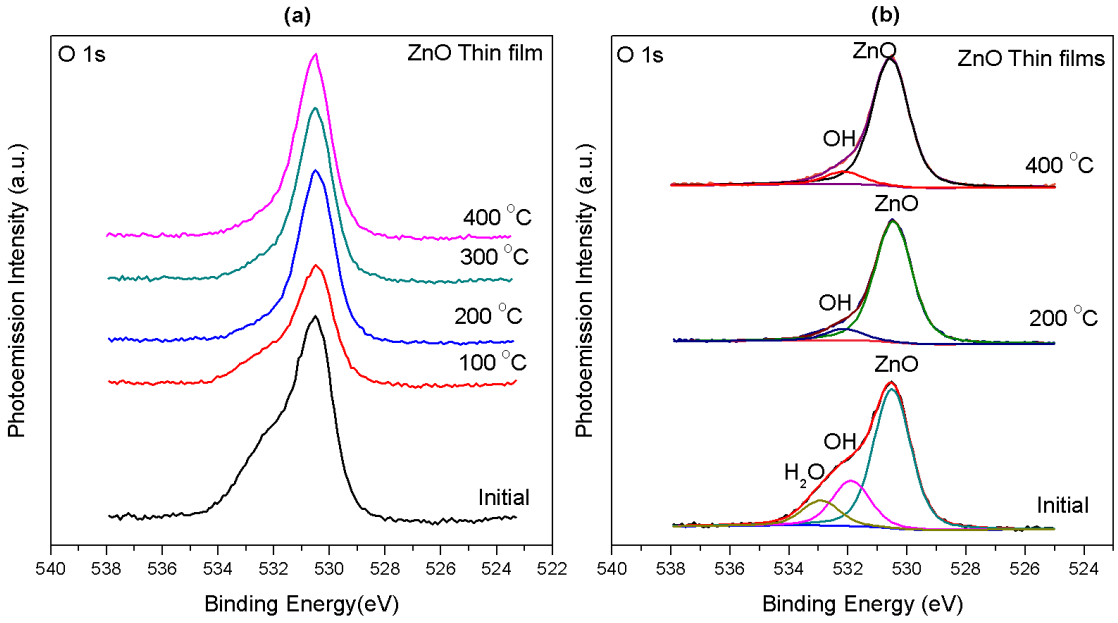

Figure 7.41: O 1s - Oxygen spectra for atomic oxygen cleaning of ZnO thin films at elevated temperatures: (a) comparison of raw oxygen spectra and (b) peak fitted oxygen spectra.

oxygen did the surface carbon contamination signal reduced significantly. The profile of the Zn LMM Auger peak is shown in figure 7.45 and is same as for the atomic oxygen treatment at elevated temperature.

The C 1s carbon spectra for the room temperature atomic oxygen cleaning of ZnO thin films are shown in figure 7.46(a) and (b). A successive reduction of carbon peak intensity is observed with increased atomic oxygen exposure time, but it is never reduced below the detection limit.

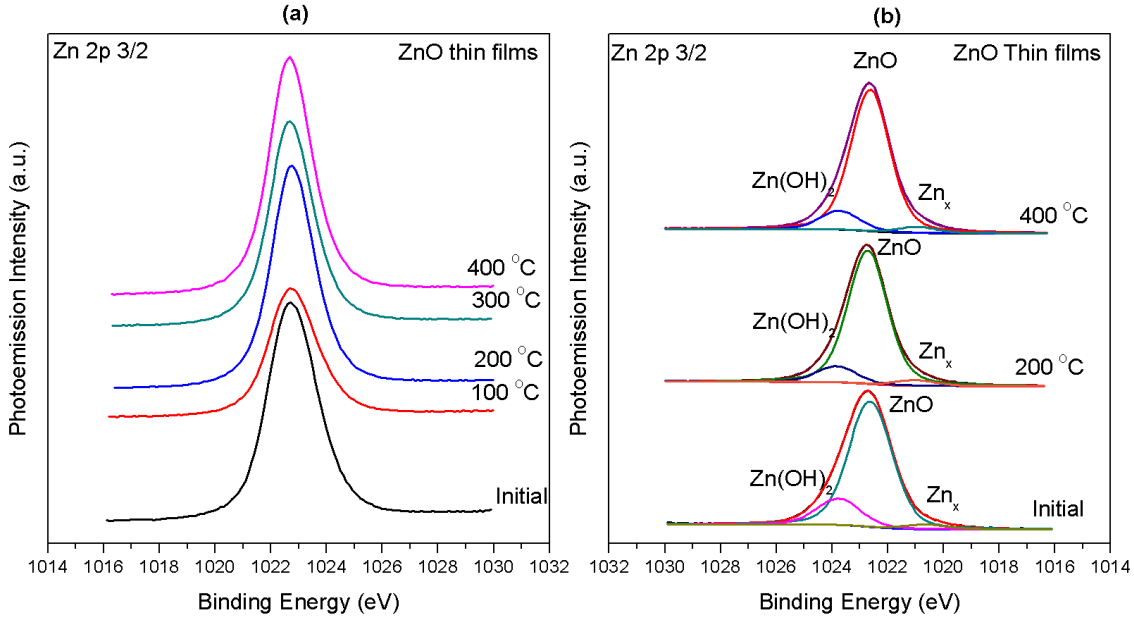

Figure 7.42: Zn 2p3/2 spectra for atomic oxygen cleaning of ZnO thin films at elevated temperatures: (a)) comparison of raw zinc spectra and (b) peak fitted zinc spectra.

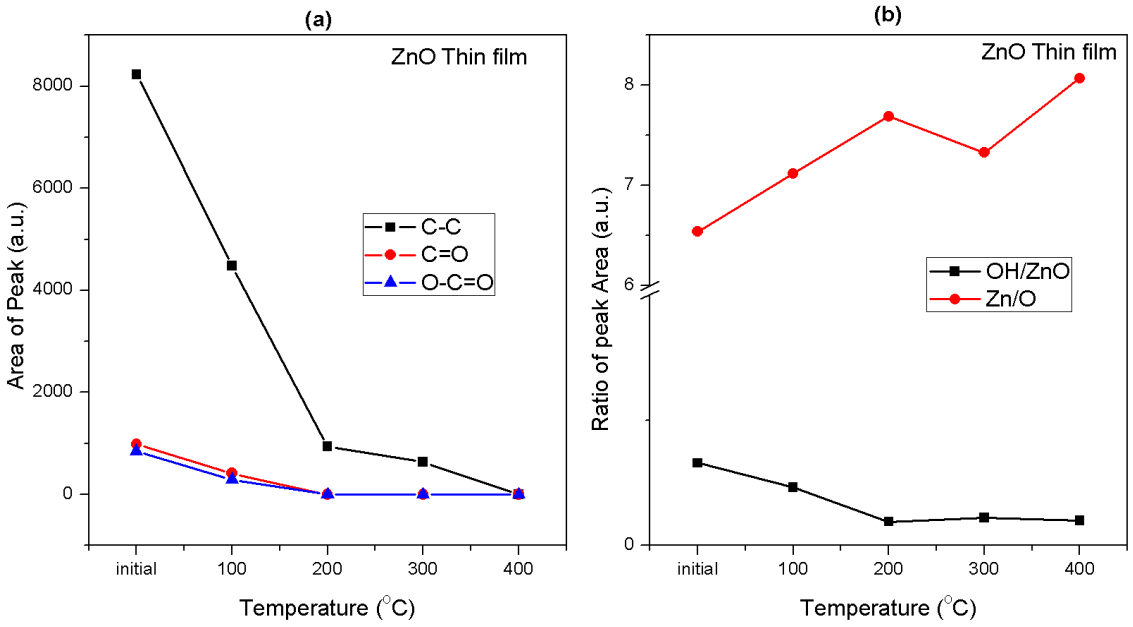

Figure 7.43: (a) Area of carbon peak with respect to atomic oxygen cleaning temperatures, (b) ratio of OH to ZnO in oxygen spectra and ratio of Zn to O for different atomic oxygen cleaning temperatures.

The O 1s oxygen spectra for room temperature atomic oxygen cleaning of ZnO thin films are shown in figure 7.47. From initial condition to the final 180 minutes exposure of atomic oxygen there is no observation impact on the peak profiles displayed in figure 7.47(a). The peak fitted data shown in figure 7.47(b) also shows the existence of water and hydroxide peak from initial to final cleaning stage. The binding energies are ZnO - 531 ± 0.1 eV, OH - 532.5 ± 0.2 eV and

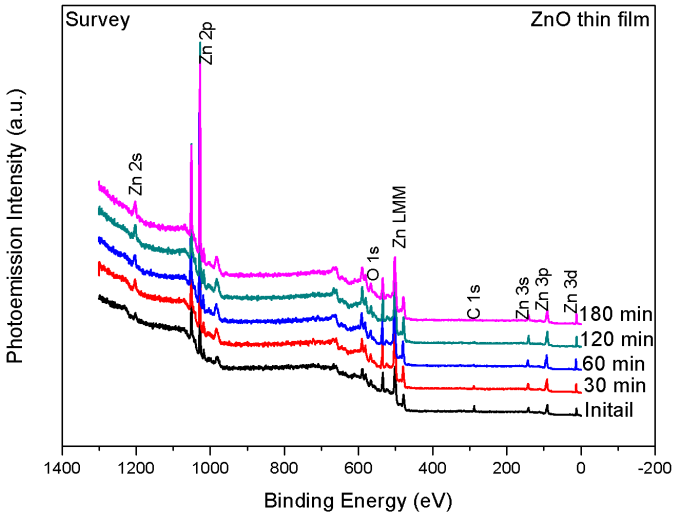

Figure 7.44: Survey spectra of PLD grown ZnO thin films for atomic oxygen cleaning at room temperatures.

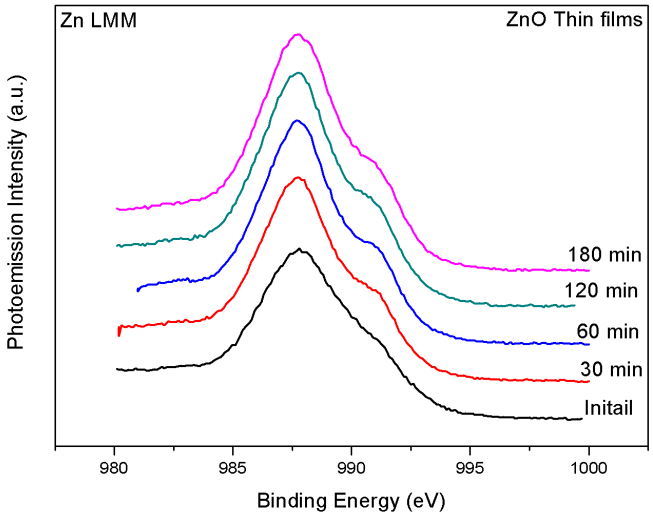

Figure 7.45: Zn LMM Auger spectra for atomic oxygen cleaning of ZnO thin films at room temperatures.

H_2O - 533.5 ± 0.2 eV and FWHM values vary between 1.5 eV - 1.9 eV. This indicates that the room temperature atomic oxygen cleaning cannot even remove the absorbed moisture or water on ZnO surface. The difference from the elevated temperature study is that a residual water component is apparent in the O 1s profile. Zn 2p zinc spectra for room temperature atomic oxygen cleaning of ZnO thin films are shown in figure 7.48(a). The increase in intensity of zinc peak with increased atomic oxygen exposure is seen in the raw spectra of figure 7.48(a).

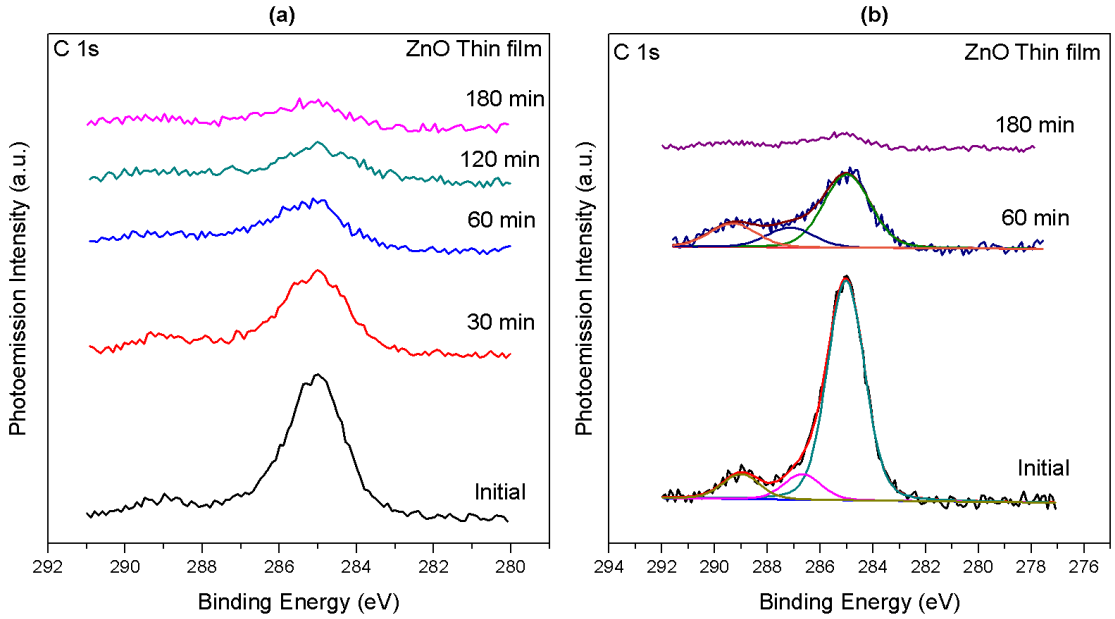

Figure 7.46: C 1s - Carbon spectra for atomic oxygen cleaning of ZnO thin films at room temperatures (a) Comparison of raw carbon spectra and (b) Peak fitted carbon spectra.

This increase is directly related to the removal of carbon on ZnO surface. As previously observed, three peaks were fitted (see figure7.48(b)) as follows Zn_x - 1020.75 ± 0.25 eV, ZnO - 1022.7 ± 0.1 eV and $Zn(OH)_2$ - 1024.2 ± 0.1 eV and FWHM vary between 1.8 eV - 2.1 eV.

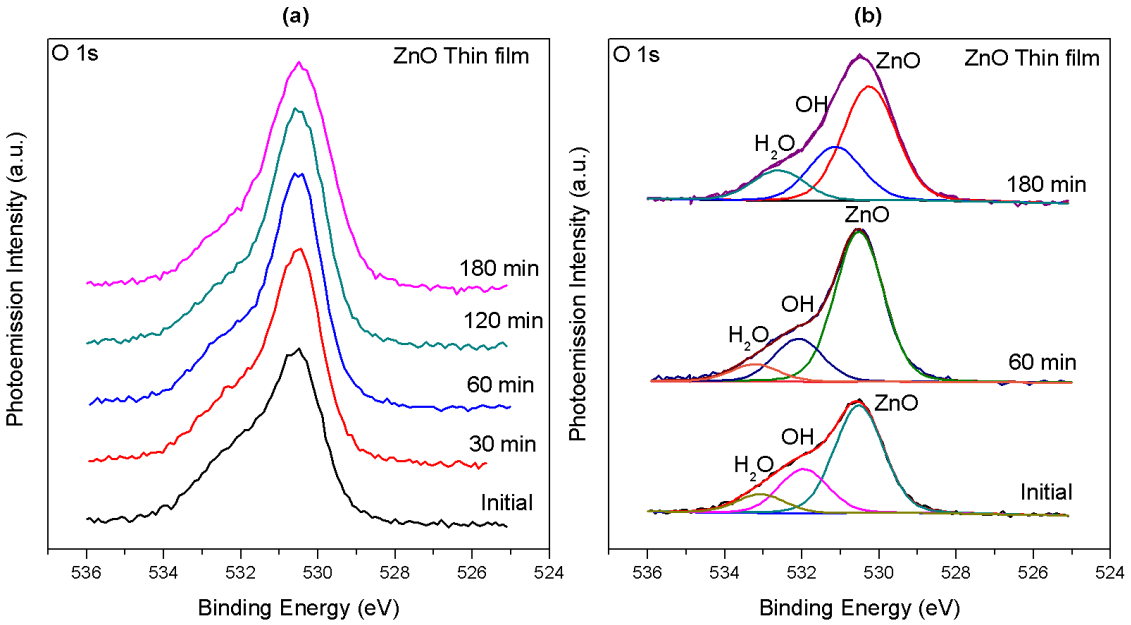

Figure 7.47: O 1s - Oxygen spectra for atomic oxygen cleaning of ZnO thin films at room temperatures: (a) Comparison of raw oxygen spectra and (b) Peak fitted oxygen spectra

To explore the removal of surface contamination and changes in the surface stoichiometry of the ZnO thin films as a function of atomic oxygen cleaning at room

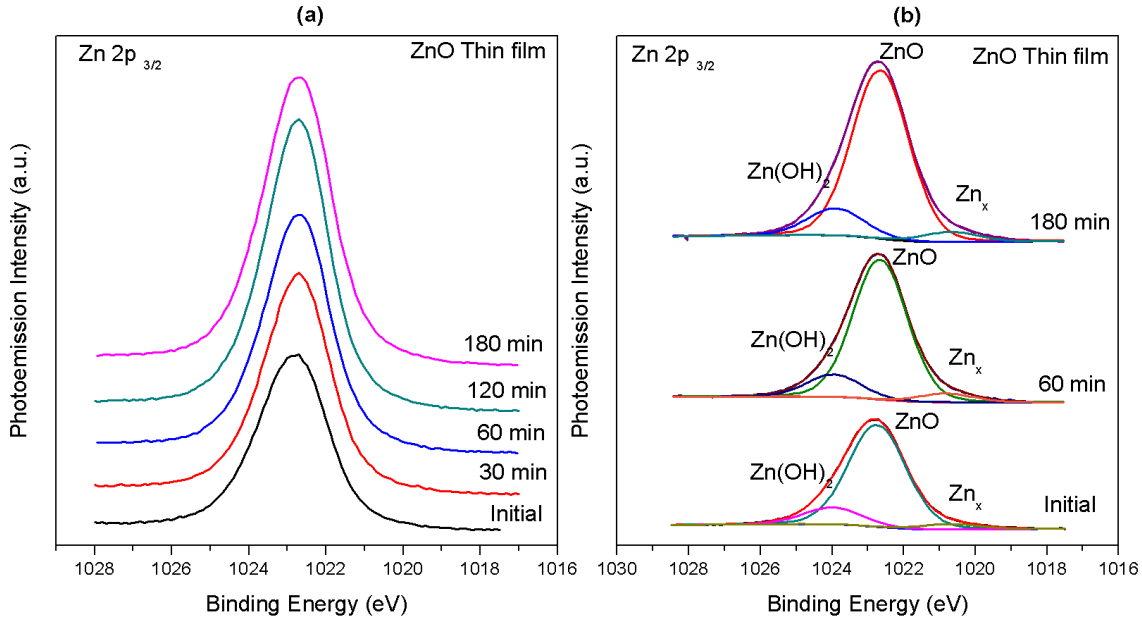

Figure 7.48: Zn 2p 3/2 zinc spectra for atomic oxygen cleaning of ZnO thin films at room temperatures: (a) Comparison of raw zinc spectra and (b) Peak fitted zinc spectra.

temperature, the areas of carbon peak and ratio of OH/ZnO and Zn/O are plotted in figure 7.49(a) and (b). The treatment is effective in removing the carbon signal without changing the surface stoichiometry by any significant amount.

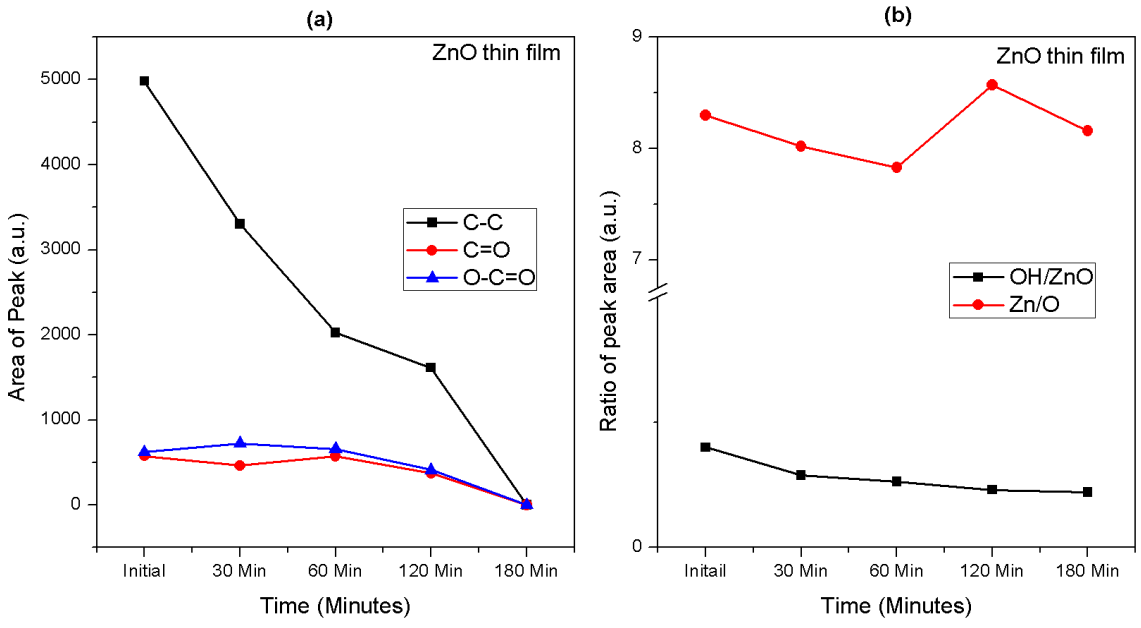

Figure 7.49: (a) Area of carbon peak with respect to atomic oxygen cleaning with increase in time, (b) ratio of OH to ZnO in oxygen spectra and ratio of Zn to O for different atomic oxygen cleaning with increase in time..

7.4 Conclusions

In SPRES study, similar levels of carbon contamination were detected on all ZnO surfaces prior to oxygen treatment. Hydroxide contamination was detected on all surfaces with the (10-10) surface displaying the highest concentration, the (000-1) and (11-20) surfaces showing less with the least amount observed on the (0001) surface. The carbon and water surface layers were successfully removed by molecular oxygen thermal annealing on all the ZnO surfaces at temperatures between 700 °C and 1000 °C. The hydroxide contamination could not be removed completely from any of these surfaces under the annealing conditions studied. The residual OH is estimated to be below 1 monolayer on all four ZnO surfaces and its presence may well reflect the re-adsorption of hydroxide groups in the UHV environment.

In an XPS study of atomic oxygen cleaning at elevated temperatures the surface carbon contamination was successfully removed from a ZnO thin film surface. For atomic oxygen cleaning at elevated temperature the carbon contamination was completely removed at 400 °C and water was removel at 100 °C. For room temperature cleaning 180 minutes of exposure atomic oxygen failed to remove all carbon contamination. The overall finding is that atomic oxygen treatment is effective at removing surface contamination at a lower temperature than molecular oxygen.

7.5 Bibliography

[1] S. W. King, J. P. Barnak, M. D. Bremser, K. M. Tracy, C. Ronning, R. F. Davis,and R. J. Nemanich,J. Appl. Phys., 84 (1998) 5248.

[2] H. Zama, Y. Ishii, H. Yamamoto and T. Morishita, Jpn. J. Appl. Phys. 40 (2001) L465.

[3] M. de Ridder, R. G. Van Welznis, and H. H. Brongersma, Surf. Interface Anal. 33 (2002) 309.

[4] A. Anders, G. Y. Yushkov, Rev. Sci. Instrum. 78 (2007) 043304.

[5] M. Naddaf, V. N. Bhoraskar, A. B. Mandale, S. R. Sainkar, and S. V. Bhoraskar, Plasma Sources Sci. Technol. 11 (2002) 361.

[6] T. Koide, T. Shidara, K. Tanaka, A. Yagishita and S. Sato, Rev. Sci. Instrum. 60 (1989) 2034.

[7] G. B. Hoflund and J. F. Weaver, Meas. Sci. Technol. 5 (1994) 201.

[8] B. J. Coppa, C. C. Fulton, P. J. Hartlieb, R. F. Davis, B. J. Rodriguez, B. J. Shields, R. J. Nemanich, J. Appl. Phys. 95 (2004) 5856.

[9] K. Ogata, K. Sakurai, Sz. Fujita, Sg. Fujita, K. Matsushige, J. Crystal Growth 214/215 (2000) 312.

[10] S. Graubner, C. Neumann, A. Krost, J. Blsing, and B. K. Meyer, Phys. stat. sol. (b) 244 (2007) 1490.

[11] C. Neumann, S. Lautenschlger, S. Graubner, J. Sann, N. Volbers, B. K. Meyer, J. Blsing, A. Krost, F. Bertram, and J. Christen, Phys. stat. sol. (b) 244 (1997) 1451.

[12] S. Graubner, C. Neumann, N. Volbers, and B. K. Meyer, I. Blasing and A. Krost, Appl. Phys. Lett. 90 (2007) 042103.

[13] X. Q. Wei , B. Y. Man, M. Liu, C. S. Xue, H. Z. Zhuang, C. Yang, Physica B 388 (2007) 145.

[14] H. Jacobs, W. Mokwa, D. Kohl, and G. Heiland, Surf. Sci. 160 (1985), 217.

[15] K. Ozawa, and K. Mase, Phys. Rev. B, 83 (2011) 125406.

[16] http://www.nasa.gov/centers/glenn/business/AtomicOxRestoration.html

[17] B. A. Banks and S. K. Rutledge, "Process for non-contact removal of organic coatings from the surface of paintings", US Patent, 5560781 (May 8, 1995)

[18] Y. Chen, D. M. Bagnall, H-J. Koh, K-T. Park, K. Hiraga, Z. Zhu, J. Appl. Phys. 84 (1998) 3912.

[19] S. Yamauchi, H. Handa, A. Nagayama, T. Hariu, Thin Solid Films345 (1999) 12.

[20] E. W. Forsythe and Y. Gao, L. G. Provost and G. S. Tompa, J. Vac. Sci. Technol. A 17 (1999) 1761.

[21] K. Ip, B. P. Gila, A. H. Onstine, E. S. Lambers, Y. W. Heo, K. H. Baik,D. P. Norton, and S. J. Pearton, S. Kim, J. R. LaRoche, and F. Ren, Appl. Phys. Lett. 84 (2004) 5133.

[22] K. Ip, B.P. Gila, A.H. Onstine, E.S. Lambers, Y.W. Heo, K.H. Baik, D.P. Norton, S.J. Pearton, S. Kim, J.R. LaRoche, F. Ren, Appl. Surf. Sci. 236 (2004) 387.

[23] Y. Kato, M-C Jung, M. V. Lee, Y. Qi, Org. Electron. 15 (2014) 721.

[24] X.Q. Meng, D.X. Zhao, J.Y. Zhang, D.Z. Shen, Y.M. Lu, L. Dong, Z.Y. Xiao, Y.C. Liu, X.W. Fan, Chem. Phys. Lett. 413 (2005) 450.

[25] H. L. Mosbacker, Y. M. Strzhemechny, B. D. White, P. E. Smith, D. C. Look, D. C. Reynolds, C. W. Litton, L. J. Brillsonb, Appl. Phys. Lett., 87 (2005) 012102.

[26] B. Angadi, H. C. Park, H. W. Choi, J. W. Choi and W. K. Choi, J. Phys. D: Appl. Phys. 40 (2007) 1422.

[27] A. Herrera-Gmez, A. Hegedus and P. L. Meissner, Appl. Phys. Lett., 81 (2002) 1014.

[28] A. W. Fliflet and H. P. Kelly, Phys. Rev. A 13 (1976) 312.

[29] R. Heinhold, G. T. Williams, S. P. Cooil, D. A. Evans, and M. W. Allen, Phys. Rev. B 88 (2013) 235315.

[30] F-L. Kuo, Y. Li, M. Solomon, J. Du and N. D. Shepherd, J. Phys. D: Appl. Phys. 45 (2012) 065301.

[31] http://www.nist.gov/srd/nist71.cfm

[32] O. Dulub, L. A. Boatner, U. Diebold, Surf. Sci. 519 (2002) 201.

[33] J. R. Williams, Masaaki Kobata, I. Pis, E. Ikenaga, T. Sugiyama, K. Kobayashi, N. Ohashi, Surf. Sci. 605 (2011) 1336.

[34] E. I. Solomon1 and V. E. Henrich, Surf. Sci. Spectra, 5 (1998) 186.

[35] L. S. Dake, D. R. her and J. M. Zachara, Surf. Interface Anal. 14 (1989) 71.

[36] K. G. Eyink and L. Grazulis, J. Vac. Sci. Technol. B 23 (2005) 554.

Chapter 8

Conclusions

The primary goal of the thesis was surface cleaning of (0001)-Zn, (000-1)-O, (10-10) and (11-20) ZnO surfaces. The exploration of new surface cleaning methods for ZnO surfaces and their impact on the electronic properties were studied in detail. The evaluation of surface cleaning and experimental study of surface electronic properties were carried out using both XPS and SRPES techniques. Except for a few wet chemical procedures, the most of surface cleaning methods investigated in the study were carried out in-situ to avoid recontamination prior to measurement. The different cleaning characteristics for the different ZnO surfaces subjected to the same surface cleaning procedures were also studied. The key results in terms of the successful removal of carbon contaminants, the challenges in removing the surface hydroxide and the change in surface band bending are summarised in this chapter.

8.1 XPS characterisation of ZnO

Prior to start of the surface cleaning studies of the ZnO surfaces, a detailed XPS study of different types of ZnO samples was performed. Some of the ZnO samples were directly purchased (ZnO crystals, ZnO powder, zinc metal sheet) and some were exclusively grown (thin films, nanorods) for this study. From an initial study of surface oxidised zinc metal foil, unique binding energy positions for the Zn 2p peak for Zn, ZnO, $Zn(OH)_2$ and $ZnCO_3$ were established along with the respective O 1s peak binding energy positions. From ZnO crystals, thin films, powders and nanorods photoelectron spectra obtained for core levels peaks for carbon, zinc and oxygen displayed similar binding energy positions. Similarly the FWHMs of the photoemission peaks were almost the same for all ZnO samples with a variation within 0.3 eV while the carbon peak had a higher variation

from sample to sample (0.5 eV). A peak classified as an asymmetric peak - Zn_x was found in Zn 2p and Zn 3p core level profiles for all ZnO sample at a lower binding energy position than the bulk peak. From angle resolved XPS (ARXPS) measurements, the photoemission angle at 30 degrees was found as a suitable angle to collect all surfaces chemical composition of vertically aligned nanorods. In all ZnO samples the contamination of carbon, hydroxide and water was found. The high amount of carbon contaminations were seen on IPA cleaned zinc metal sheets, (0001)-Zn crystal surface and ZnO powders. High amount of hydroxide was present on scrapped metal sheets, (0001)-Zn surface, PLD grown thin films and ZnO powders. Based on XPS analysis of different ZnO samples, the surface chemical composition of a typical ZnO surface exposed to atmosphere was found to be as follows: 27% of zinc, 32% of oxygen, 23% of carbon, 15% of hydroxide and 3% of water. In the Zn to O stoichiometry (excluding the contamination) the ideal stoichiometry (50% Zn and 50% oxygen) was found for the sample: ZnO crystals surfaces (0001)-Zn, (10-10), (11-20), E-beam thin films and nanorods. Oxygen rich stoichiometry was found for (000-1) ZnO crystal surface, PLD grown thin films. Finally, the ZnO powders were found to be richer in zinc than in oxygen. The optimised binding energy position of photoelectron peaks and their peak width (FWHM) obtained from this study were used as a reference for analysing the ZnO photoemission spectra of all other work.

8.2 *Ex-situ* surface cleaning of ZnO surfaces

For the XPS study the wet chemical cleaning of ZnO crystal surfaces (0001), (000-1) and (10-10) by organic solvents including acetone, dimethyl sulfoxide (DMSO) and toluene was systematically studied. Neither separate cleaning in the individual solvents nor sequential cleaning in all solvents were not successful at completely removing the surface contaminants. A general observation for these treatments was that the *ex-situ* organic cleans resulted in only a small reduction in the carbon contamination signal and a corresponding increase in hydroxide signal. The cleaned ZnO surfaces were very reactive in nature and exposure of the surface to atmospheric conditions after treating with the solvents leads to recontaminations. In SRPES study,the ethanol cleaning of all the ZnO surfaces (0001), (000-1), (10-10) and (11-20) reduced the surface contamination but in different rates, depending on the surface termination. A similar amount of carbon was removed from the (0001), (10-10) and (11-20) surfaces with the cleaning of the (000-1) surface being noticeably more effective. For the (000-1) and (11-20) surfaces the hydroxide signal were similarly reduced while it was more effectively removed from the (10-10) surface. From the valence band spectra and work function measurements upward band bending was observed for the (000-1), (10-10), (11-20) surfaces while a flat band condition was seen for the

(0001) surface. The overall conclusion is that *ex-situ* wet chemical cleaning was not effective or suitable for surface cleaning of ZnO surfaces.

8.3 *In-situ* surface cleaning of ZnO surfaces

An explorative study of atomic hydrogen cleaning of the ZnO(0001)-Zn terminated surface at a range of temperatures (300 °C to 600 °C) was undertaken. At 600 °C this treatment was shown to be effective at completely removing the surface carbon contamination. No difference in the hydroxide signal intensity was observed indicating that this surface was hydroxide terminated. As the result of atomic hydrogen cleaning the upward band bending of 0.53 eV is obtained for (0001) surface.

The high temperature molecular oxygen thermal cleaning of ZnO (0001), (000-1), (10-10) and (11-20) surfaces was carried out at a range of temperatures from 300 °C to 1000 °C. The carbon and water contamination were removed from all ZnO surfaces. The carbon removal annealing temperature was 700 °C for all ZnO surface expect (0001) where it was at 1000 °C. The hydroxide signal on all surfaces was attenuated by this treatment, but remained present again indicating a hydroxide surface termination was dominant. As the result of molecular oxygen thermal cleaning more than 0.5 eV of upward band bending is achieved. The attained band bending values for ZnO surface as follows: (0001) surface - 0.76 eV, (000-1) surface - 0.6 eV, (10-10) surface - 0.92 eV and (11-20) surface - 0.53 eV.

Another explorative study of surface cleaning of ZnO thin film surfaces by atomic oxygen cleaning at a range of temperatures was undertaken. The carbon and water contamination were successfully removed at 400 °C and 100 °C, respectively for atomic oxygen treatment at higher temperature. At room temperature, only the carbon contamination signal was reduced below the XPS detection limit. Hydroxide contamination stays same on the ZnO thin film surface.

Among all surface cleaning methods employed here atomic oxygen cracking at higher temperature seems to be suitable method for surface cleaning for all ZnO surfaces. Next the atomic hydorgen cracking at higher temperatures also suitable to attain a maximum clean ZnO surfaces, while the wet chemical cleaning and UHV annealing were not beneficiary for ZnO surface cleaning.

The overall conclusion drawn from all three *in-situ* cleaning methods employed for ZnO surfaces show the carbon contamination can be easily removed however, the hydroxide signal persists indicating that it is the preferred termination of these surface. The residual OH is estimated to be below 1 monolayer on all four ZnO surfaces after surface cleaning and its presence may well reflect the re-adsorption of hydroxide groups in the UHV environment. But by the result of removing

carbon contamination on ZnO surfaces, the surface downward banding is turned into upward band bending of more than 0.5 eV is achieved. The attainment of (>0.5 eV) upward band bending by surface cleaning makes the ZnO surface suitable for making schottky contacts.

Appendix A

SIMS characterisation of ZnO thin films

A.1 Introduction

Dynamic-Secondary Mass Ion Spectroscopy (D-SIMS) has been used to acquire a chemical depth profile of e-beam deposited ZnO thin films. SIMS has been used previously to detect elemental impurities in ZnO [1, 2] and to detect the presence of residual gold in ZnO nanorod grown by the VPT process [3]. In this study SIMS is used to identify the surface contamination on ZnO surface, obtain a depth profile of the thin film chemical composition and study the interface composition with a silicon substrate in order to derive a depth profile model.

A.2 Experimental

The ZnO films, 25 nm thick were deposited by e-beam evaporation of ZnO (99.9%) pellets purchased from ABCR GmbH & Co. KG, Germany onto native oxide covered silicon (100) substrates. The distance from the e-beam source to both the substrate surface and the thin film quartz crystal monitor was ≈15 cm. The base pressure in the vacuum system before deposition was 5 x 10^{-7} mbar, while during evaporation the pressure typically rose to 7 x 10^{-5} mbar. For e-beam settings of 5 kV and beam current of 26.3 mA, the measured deposition rate was 0.01 nm/second. Both positive and negative SIMS depth profiles were acquired using an incident neutral 5 kV Ar beam. The sample current was measured to be 40 nA, which resulted in an etching rate of approximately 0.85 nm/minute. The SIMS spectra were acquired at a background chamber pressure of 1x10^{-7}mbar

argon. The physical profile of the crater formed by the SIMS depth profiling was measured with a Tencor P-2 profilometer.

A.3 Result and Discussion

Dynamic SIMS profiles were acquired for ZnO thin films with an estimated thickness of 25 nm grown on silicon substrates. Mass spectra were initially acquired from different regions of silicon surface with and without the ZnO film. The SIMS bar analysis as shown in figure A.1 reflects the profile of the native oxide covered silicon surface with the detection of the isotopes of silicon ($^{28}Si^{+}$, $^{29}Si^{+}$, $^{30}Si^{+}$) and oxides of silicon SiO(m/z = 44), Si_2O (m/z = 72). This spectrum is consistent with the abundance of Si isotopes and oxide species of a standard reference of silicon oxide [4] and was measured to ensure correct operation of the instrument.

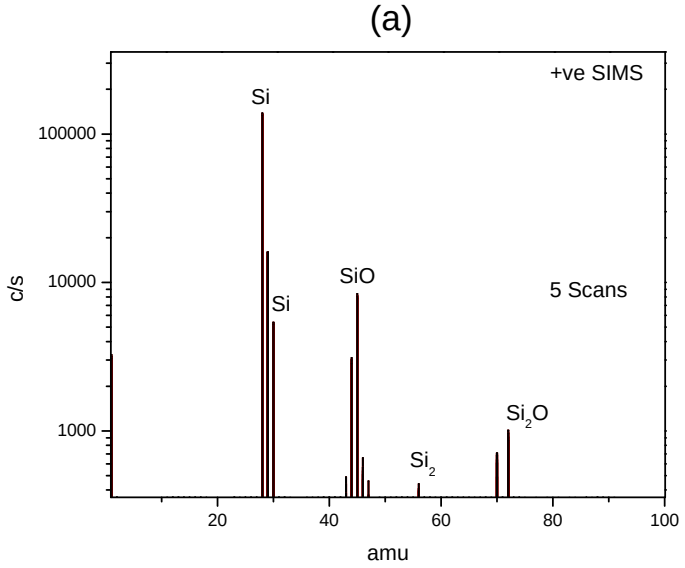

Figure A.1: Mass spectrum for Silicon substrate

Figure A.2 shows the mass profile when the SIMS argon beam is incident on the edge of the sample as it displays the presence of both ZnO related species with isotopes of Zn (mass = 64, 67 & 70) and O (m/z = 16) as well as less intensity substrate related silicon Si(m/z = 28), Si_2(m/z = 56) its oxides $^{28}Si^{+16}O^{-}$, $^{44}Si_2^{+32}O^{-}$. The absence of a ZnO(m/z = 80) peak maybe evidence of the poor growth of ZnO in edge of sample. Common contaminants widely detected in many SIMS profiles of a wide range of materials such as $^{1}H^{+}$, $^{12}C^{+}$, $^{13}C^{+}$, $^{23}Na^{+}$, $^{39}K^{+}$, $^{40}Ca^{+}$ are clearly observed in the film composition. When the primary Ar^{+} ion is moved fully onto the ZnO film, high intensity mass spectra for Zn ion and zinc oxide compounds are clearly observed in figure A.3. The commonly detected

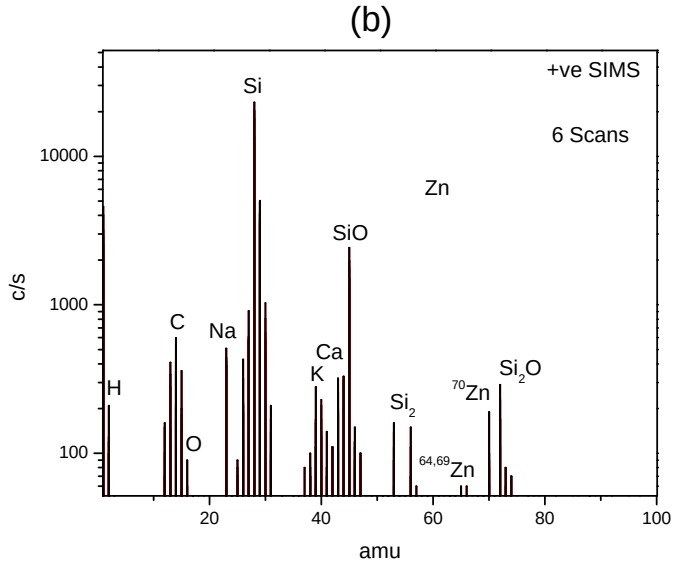

Figure A.2: Mass spectrum of edge of the sample

natural contaminant of chlorine in ZnO material is present in this spectrum as its isotopes $^{35}Cl^-$ and $^{37}Cl^-$ are seen. The SIMS-intensity distribution for pure ZnO target matched well with the natural abundance of Zn and O combinations previously reported by Meyer et al [5]. Again the substrate silicon and other basic contaminants $^{1}H^+$, $^{12}C^+$,$^{13}C^+$, $^{23}Na^+$, $^{39}K^+$, $^{40}Ca^+$, were found. The mass spectrum shown in figure A.4 displays very high intense peaks for both Zn isotopes $^{64}Zn^+$, $^{66}Zn^+$, $^{67}Zn^+$, $^{68}Zn^+$, $^{70}Zn^+$ and all mass region of zinc oxide $^{64}Zn^{+16}O^-$, $^{66}Zn^{+16}O^-$, $^{67}Zn^{+16}O^-$, $^{68}Zn^{+16}O^-$, $^{70}Zn^{+16}O^-$, even double ZnO species such as $^{128}Zn^{+32}O^-$, $^{132}Zn^{+32}O^-$, $^{136}Zn^{+32}O^-$, $^{140}Zn^{+32}O^-$ are detected. These results are consistent with reported SIMS spectra for ZnO [6]. A depth profile analysis of zinc isotopes was performed to detect the high abundance isotopes in the ZnO thin films and as shown in figure A.5, the $^{64}Zn^+$ isotope which had the highest abundance was subsequently used for depth profile analysis.

Depth profiles were undertaking by monitoring the intensity of $^{2}H^+$ for adsorbed hydroxide(OH) on ZnO surface, $^{64}Zn^+$ abundance isotope for ZnO and $^{28}Si^+$ abundance isotope for silicon substrate. The bombarding was carried out at a base pressure of 1 x 10^{-7} mbar with constant argon flow. The depth profile rate of 0.85 nm/min was estimated from a number of different experimental runs on identically prepared films where the depth of the generated crater was measured by profilometry. The depth profile through the ZnO film shown in figure A.6 allows a chemical composition model to be developed. The increase in the silicon signal intensity at the interface between the ZnO film and the silicon substrate is indicative of interface oxidation which reflects the presence of the native oxide on the surface. The pure silicon substrate is seen after bombarding the sample

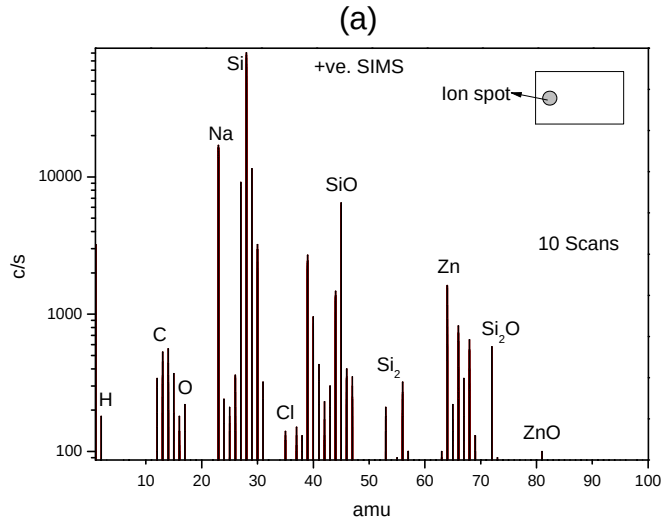

Figure A.3: Mass spectra of (edge of film)ZnO thin film

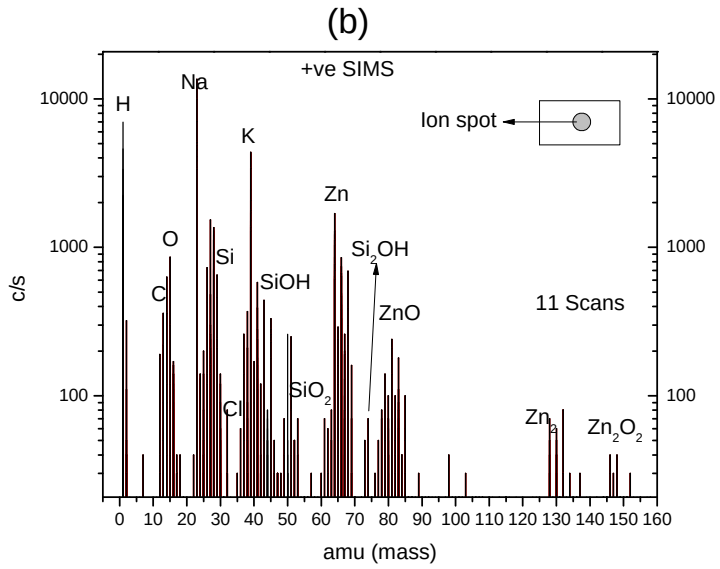

Figure A.4: abundance region (Centre of sample, uniform film) of ZnO film

for 43 minutes (36.5 nm). The depth profile model of this ZnO thin film is shown in figure A.7. The surface topography of the SIMS depth profiled ZnO thin films were characterised by profilometer in order to obtain the etch rate. The SIMS generated crater is circular in shape with a diameter of 1.5 to 2 mm and has uniform depth which was measured to determine the etch rate.

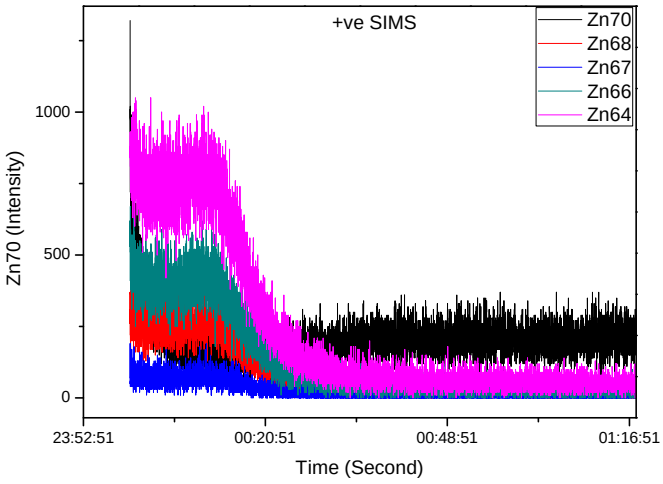

Figure A.5: Isotope analysis of Zinc element for detection of abundance

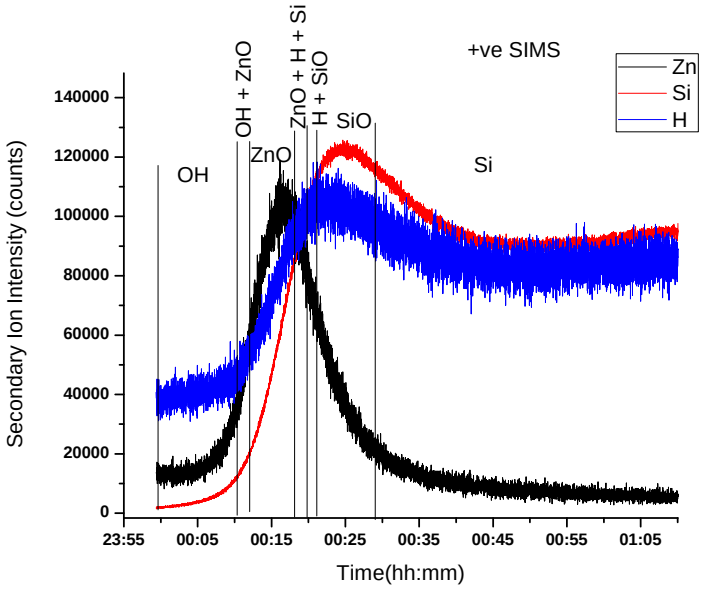

Figure A.6: Depth profile of H, Zn & Si in ZnO(25 nm) grown on Si(100) [where H & ZnO signal were multiplied by 20

A.4 Conclusion

SIMS analysis of e-beam deposited ZnO thin films on native oxide covered silicon surfaces has been undertaken. Details of the surface chemical composition and the chemical depth profile have been deduced. The surface topography of the SIMS craters generated during the depth profiling showed uniform ion milling and good consistency with film thickness (25 nm) measured by SIMS depth profile (25.4 nm).

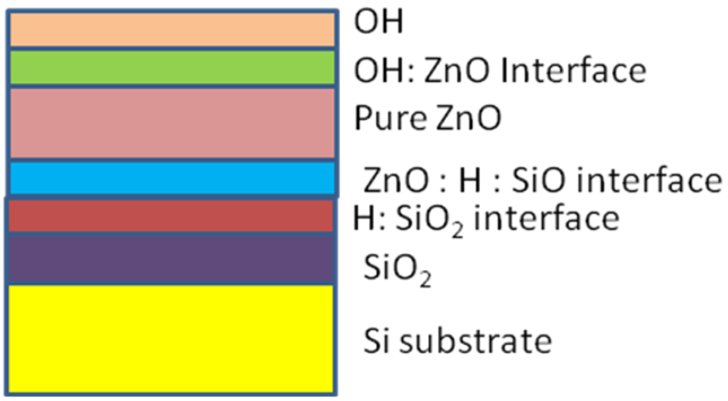

Figure A.7: SIMS depth profile model of ZnO(25 nm)/ Si(100) thin film

A.5 Bibliography

[1] I. Sakaguchi and S. Hishita, Surf. Interface Anal., 36 (2004) 645.

[2] M. D. McCluskey and S. J. Jokela, Physica B, 401 - 402 (2007) 355.

[3] R. J. H. Morris, M. G. Dowsett, S. H. Dalal, D. L. Baptista, K. B. K. Teo, and W. I. Milne, Surf. Interface Anal., 39 (2007) 898.

[4] C. W. Magee, R.G. Wilson, F.A. Stevie. Secondary Ion Mass Spectrometry - A practical handbook for depth profiling and bulk impurity analysis. John Wiley Sons, 1989.

[5] B. K. Meyer, H. Alves, D. M. Hofmann, W. Kriegseis, D. Forster, F. Bertram,J. Christen, A. Hoffmann, M. Straburg, M. Dworzak, U. Haboeck, and A. V. Rodina. Phys. Status Solidi B, 241 (2004) 231.

[6] M. Sumiya, S. Fuke, A. Tsukazaki, K. Tamura, A. Ohtomo, M. Kawasaki, and H. Koinuma, J. Appl. Phys., 93 (2003) 2562.